Ph.D. Thesis

Université de Limoges

University of Limoges

ED 610 - Sciences et Ingénierie des Systèmes, Mathématiques, Informatique (SISMI)

XLIM CNRS UMR-7252 Fiber photonics and coherent sources
ISL, French-German Research Institute of Saint-Louis

A thesis submitted to University of Limoges
in partial fulfillment of the requirements of the degree of
Doctor of Philosophy
High Frequency Electronics, Photonics and Systems

Presented and defended by
Maxime Pinaud

On November 24, 2021

Phase Change Materials (PCM) for the reconfiguration of terahertz devices

Thesis supervised by Aurelian Crunteanu, Georges Humbert, Bernd Fischer and Sebastian Engelbrecht

JURY:

Reporters
M. Vincent Laur, Professor, Université Bretagne Occidentale
M. Frédéric Garet, Professor, Université Savoie Mont Blanc

Examiners
M. Jan C. Balzer, Professor, Doctor, Duisburg-Essen University
M. Patrick Mounaix, CNRS Research Director, Université de Bordeaux
M. Aurelian Crunteanu, CNRS Research Director, Université de Limoges
M. Georges Humbert, CNRS Researcher, Université de Limoges
M. Bernd Fischer, Professor, Doctor, French-German Research Institute of Saint-Louis
M. Sebastian Engelbrecht, Doctor, French-German Research Institute of Saint-Louis

I dedicate this manuscript to my loved ones
A. F. F. T.

Acknowledgements

First, I would like to acknowledge the French German institute of Saint-Louis (ISL) for funding half of my PhD. I would also like to acknowledge the University of Limoges for funding the second half of my PhD.

Secondly, I would like to thank M. Vincent Laur and M. Frédéric Garet for thoroughly reviewing my manuscript and the other members of the jury as well for being part of my PhD defense.

I would like to express my deepest gratitude to my supervisors, Dr. Georges Humbert and Dr. Aurelian Crunteanu in Xlim laboratory, and Pr. Dr. Bernd Fischer and Dr. Sebastian Engelbrecht, in ISL, for their guidance and support during my PhD. I would like to thank them for allowing me to be a part of this project and for their countless advice during my PhD.

In the ISL, I would like to extend my sincere thanks to Lionel Merlat for welcoming me and his help during my PhD. I would also thank the member of the RIM division for welcoming me with open arm during my stay in the ISL.

In Xlim laboratory, I would like to thank all the people who helped in a way or another during my PhD. A special thanks to the clean room team for their help, advice and their sympathy, especially Jehison, Cyril, Areski and Ling Yan. Thanks should also go to the photonic A team for their warm welcome and their support, this list is, of course, non-exhaustive: Philippe, Raphaël, Geoffroy, Baptiste, Romain, Marie Alicia, Colman and all those I will inevitably fail to mention...

On a more personal note, specials thanks to Flavien, Hugo, Etienne, Lova, Thomas and Gabin for the coffee breaks, their good mood, their jokes and the unforgettable moments during my PhD. Thank you also to the nice people I met during my years of study who will recognize themselves.

I cannot begin to express my thanks to my parents for their unconditional love and support. Finally, I would like to extend my gratitude to my sister for her support and help to improve my English skill.

Rights

This creation is available under a Creative Commons contract:

« Attribution-Non Commercial-No Derivatives 4.0 International »

online at https://creativecommons.org/licenses/by-nc-nd/4.0/

Table of Contents

List of Figures

List of Tables

General introduction

General introduction

Wireless telecommunications have experienced unprecedented growth during the last years. The development of new connected devices integrating new applications in all aspects of daily life (augmented reality, virtual reality, self-driving cars, smart cities, etc), require real-time data flow, and new communications standards. The new communication systems need to be more performant, more compact and requires multiple functionalities for reducing the cost and the complexity of a specific subsystem.

Current existing solutions propose to use millimeter-waves (frequencies between 26.5 GHz and 60 GHz) in order to increase the bandwidth and the data traffic. This range of frequency corresponds to the 5G technologies. 5G is expected to support data rates ranging from one to a few Gbps. However, the continuous increase of users and the multiplication of smart communication devices will lead the extension of the telecommunication frequencies to the terahertz (THz) band, corresponding to the frequencies of the electromagnetic spectrum from 0.1 THz to 30 THz.

THz frequency spectrum holds very promising applications not only for high-speed wireless communication but also for imaging or security screening, chemical identification or non-destructive sensing. Nevertheless, over the last two decades, the development of practical applications has been hindered due to the difficulties to generate, detect and modulate the terahertz waves.

For telecommunications, THz waves is referred as *beyond 5G* technologies and can achieve Terabits per second (Tbps) data rates and a latency inferior to 1 ms. A prerequisite to the extensive development of terahertz telecommunications is the development of sources, detectors and reconfigurable devices such as filters, spatial light modulators, frequency selective surfaces, which enable to control the properties of electromagnetic waves such as their amplitude, phase, polarization and/ or spatiotemporal distribution of their wave fronts.

Reconfiguration strategies and the associated technologies based electronic components already employed in the microwave and optical domains are difficult or ineffective to transpose to THz domain since microwave wavelengths are too long and optical wavelengths are too short compared to terahertz field wavelengths. For the realization of reconfigurable devices (such as switches, modulators, reconfigurable filters, etc), current approach consists to integrate active devices (semiconductors, MEMS, liquid crystal, etc) in artificially engineered metasurfaces or metamaterials composed of two-dimensional arrays of sub-wavelength metallic resonators. However, most of these agile elements have volatile-type

responses requiring permanent optical or electrical bias and complex electrical/ optical control schemes when integrated over large-area.

Our approach for the realization of reconfigurable THz devices is to use phase change materials (PCM) as an active media integrate in passive metamaterials but also for the development of PCM-only THz devices where the PCM is used to realize non-volatile and reconfigurable metallic structures which can modulate incident THz waves. PCM such as GeTe (germanium telluride) or $Ge_2Sb_2Te_5$- GST (germanium antimony telluride) are chalcogenide materials which undergo a non-volatile phase transition on nanosecond timescales from an amorphous (insulating) state to a crystalline (metallic) one. Their electrical and optical properties are drastically changed upon the onset of the phase change through the application of thermal, electrical or optical stimuli. These PCM capabilities have been exploited over the years for realizing optical memory disks and non-volatile memories and, more recently, for the realization of high performance, bi-stable switching devices in the microwaves/ millimeter waves domains. It holds high-promises for future multi-reconfigurable telecommunication systems. Their most interesting property which justifies our choice to use them as reconfiguration elements within a THz device is their bistability. Indeed, they retain their state (amorphous or crystalline) even after removing the specific excitation, allowing low energy consumption compared to other reconfiguration methods. The PCM properties are still under investigation in the terahertz domain, and need supplementary research to fully assess their capabilities to manipulate THz waves.

The principal objectives of this thesis are to realize and characterize thin PCM films at the THz domain, and then to designed, realized, and characterized functional reconfigurable THz devices based on PCM.

This manuscript is composed of three chapters. The **chapter I** presents a state of the art of different technologies to realize reconfigurable THz devices. After the presentation of the terahertz domain and its potential applications, we will focus on the existing technologies for the realization of reconfigurable terahertz devices. In a second step, we will introduce an overview the PCM properties, their different applications and address the challenges for their integration as tuning elements in reconfigurable THz devices. The **chapter II** is dedicated to the realization and electrical characterization of GeTe thin films along with their THz properties. Finally, we will detail the principle of optical activation of GeTe film between amorphous and crystalline phase using short laser pulses. The **chapter III** will be devoted to the development and the study of different reconfigurable THz devices integrating the GeTe material. As a first step, we will design and characterize a split ring resonator (SRR) based metamaterial integrating GeTe patterns which can achieve strong modulation of the THz waves when the GeTe integrating the SRRs will change its phase using optical irradiation. As a second step,

considering the significant differential amplitude response of the GeTe film's transmission at THz frequencies when optically switched between the amorphous and the crystalline states, we will present for the first time to the best of our knowledge an all-dielectric THz device realized using solely GeTe. device which can actively control the polarization state of the incident THz waves. Finally, we will demonstrate the possibility to inscribe resonant metallic structures in a bare amorphous GeTe films using optical activation for the realization of reconfigurable and multifunctional THz devices. We will conclude by given several directions in the continuity of this research work.

This thesis is a collaboration between the XLIM research Institute in Limoges and the French-German Research Institute of Saint-Louis (ISL) under the supervision of Dr. Aurelian Crunteanu (XLIM- RF-Elite Department), Dr. Georges Humbert (XLIM- Photonics Department), Dr. Sebastian Engelbrecht (ISL- THz Technologies RIM) and Pr. Dr. Bernd Fischer (ISL- head of division "Protection technologies, Security, Situational Awareness").

Chapter I : Interest of phase change materials for terahertz reconfigurable devices

Chapter I.   Interest of phase change materials for terahertz reconfigurable devices

Introduction

In this first chapter we will present the terahertz domain and challenges associated with it, notably for the realization of reconfigurable THz devices. Terahertz (THz) frequency spectrum holds very promising applications such as security screening, chemical identification, non-destructive sensing and high-speed wireless communication [1]. This last application has attracted a real interest with the future development of "beyond 5G" technologies.

Since the start of the wireless communications, we observed a continuous increasing demand for lower latency communication capabilities, faster data rate and increase of the available bandwidth. To overcome these issues a solution is to increase the operating frequency (carrier frequency) which leads the scientific community to develop applications for the frequencies situated at millimeter waves (26.5-100 GHz). However, with the future development of the internet of things (smart cities, self-driving cars…), millimeter wave technology cannot fulfill the demand alone for such a high data rate since there is only 9 GHz bandwidth for available data transmission [2]. In this way, terahertz band (between 300 GHz and 3 THz) seems to be a good candidate for the development of the internet of things, the high frequency of THz can increase the data rate of communication systems to the terabyte per second. However, for the development of these applications it is necessary to develop news sources and reconfigurable devices compatible with this range of frequency. Reconfigurable, multifunctional devices can replace similar individual components performing only one function.

Through this first chapter we will present the terahertz domain its potential and the challenges for the development of THz applications. Reconfigurable devices are key components to develop terahertz applications with low cost. In a second part, we will present different methods to realize reconfigurable structures, illustrated by several examples. Then, we will focus our work on chalcogenide phase change materials (PCMs) as potential candidates to realize new reconfigurable THz devices. PCMs such as germanium antimony telluride (GST) or germanium telluride (GeTe) undergo a non-volatile phase transition between amorphous and crystalline phase. This transition occurs with a large change of their electrical and optical properties. This part will be the opportunity to study the different deposition techniques of thin PCMs films. Then, the use of PCMs in other domains for prospective and also industrial applications to achieve strong modulations of optical and radio waves will be introduced. Different techniques to control the phase transition using electrical or optical excitation will be presented. Finally, we will investigate the state of the art regarding the use of PCMs in the terahertz domain and address the remaining challenges.

I.1. Introduction to the terahertz domain

I.1.1. Presentation and interest

Frequencies of the electromagnetic spectrum such as radio waves, microwaves, optical spectrum or X-rays are commonly used and well known for their "general public" applications like wireless telecommunication with radio waves or medical imaging of the human body and security scan using X-rays. The terahertz frequencies are also part of the electromagnetic spectrum, nevertheless, they are still under-exploited. The terahertz domain corresponds to the frequency domain between the microwaves and the infrared (Figure I-1). In terms of frequency values, it generally corresponds to the frequencies between 100 GHz and 30 THz, which corresponds to the wavelength between 3 mm and 10 μm and an energy range between 0.41 meV and 123 meV.
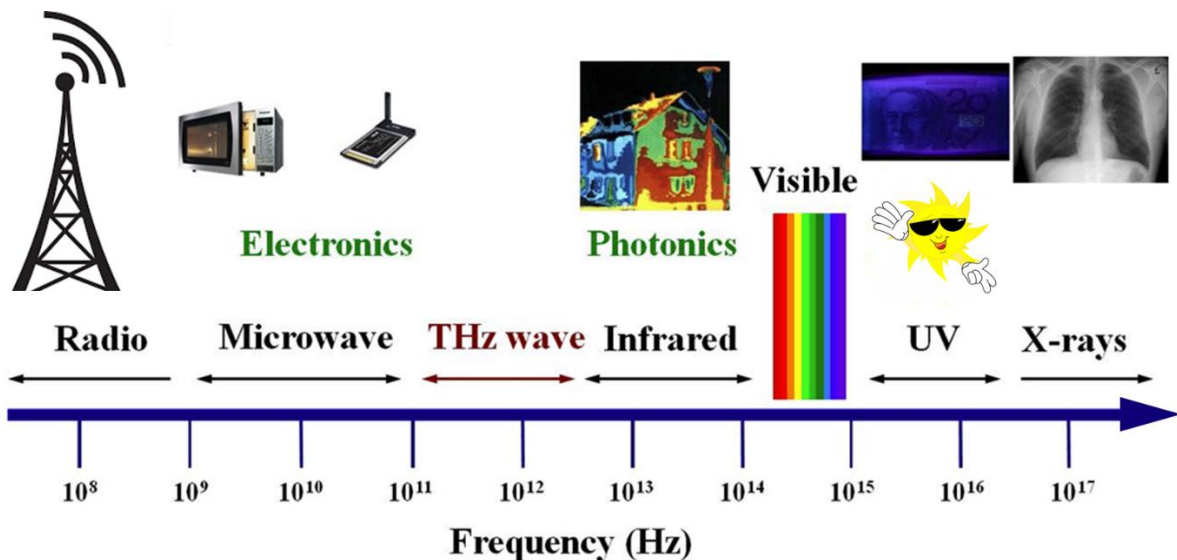
Figure I-1: Place of the terahertz-frequency domain in the electromagnetic spectrum.

Each electromagnetic wave interacts with matter in different ways depending on their specific frequency. In this case, the interactions of terahertz waves make them hold very promising applications as presented on Figure I-2 [1].
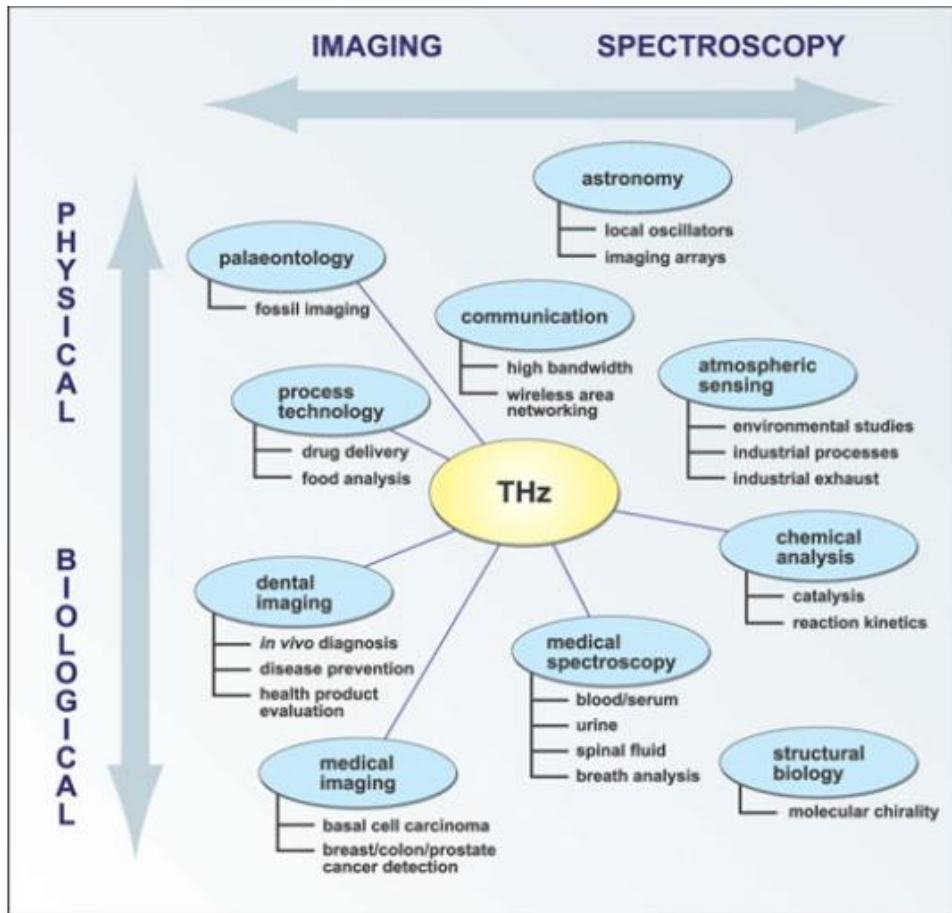
Figure I-2 : Presentation of the different applications of terahertz domain [3].

One of the first applications is the terahertz spectroscopy. The terahertz frequency range has the advantage of being able to probe matter by accessing the rotational type resonances of molecules observed in the microwave range and the vibrational type resonances characteristic at the infrared frequencies (Figure I-3). Thus, numerous molecules have absorption lines at terahertz frequencies and can be easily identified. Terahertz waves can be used in astronomy to determine the chemical composition of a planet's atmosphere or in biochemistry to analyze DNA or determine the composition of an unknown substance [4].
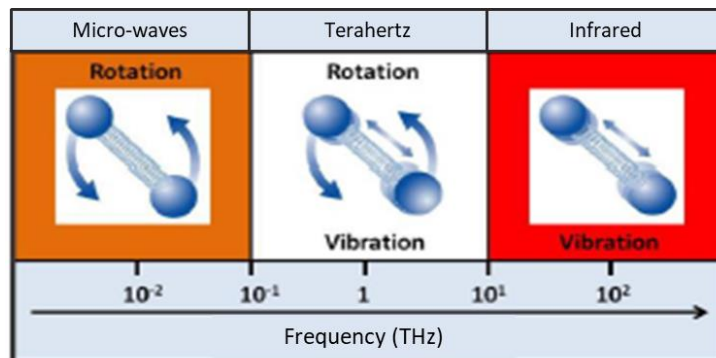
Figure I-3: Different vibration mode of molecules in different domains.

Another application is terahertz imaging. Some materials like paper, plaster or semiconductors which are opaque to other frequencies ranges are transparent to the terahertz waves. On the contrary, some materials such as water absorb terahertz waves. Additionally, terahertz waves are non-ionizing radiation due to their low photon energy (between 0.41 meV and 123 meV); thus, they can be used in medical imaging systems to analyze fragile biological cells, contrary to X-rays (energy above 10 keV). However due to the water absorption terahertz imaging will be limited to superficial scanning of biological tissues (Figure I-4). These systems are also used in security and defense domain, notably in airports to detect dangerous components which are harder to detect with other usual techniques.
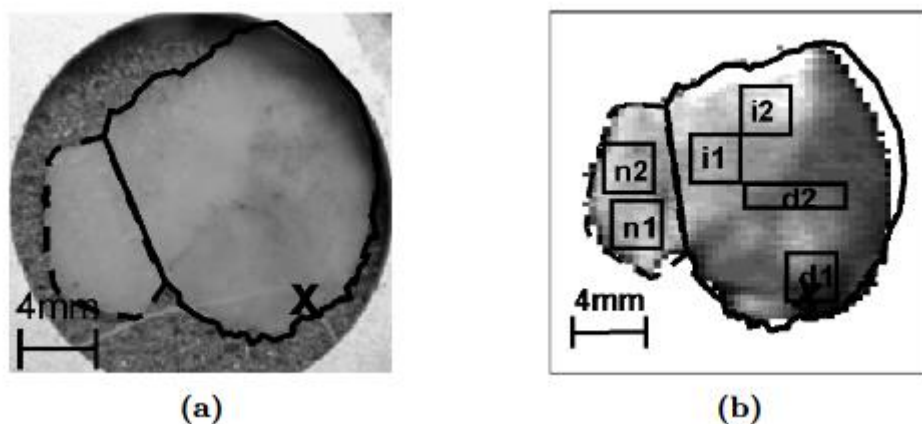
Figure I-4: (a) Image in the visible domain of cancerous tissues (full lines) and healthy tissues (dashed lines) (b) same image realized in the terahertz domain [5].

Another application we can quote is wireless telecommunication. With the advent of new "smart" applications such as smart city, smart home, self-driving cars and augmented reality, the available frequency spectrum reaches its limits. Indeed, billions of devices will need wireless connectivity to the Internet, and many of these devices (cameras, sensors, ...) require real-time data flow. To respond to the demands for lower latency communication capabilities and faster data rate to sustain these applications, we are currently witnessing the development of millimeter-wave communications (26.5-100 GHz) with 5G [6]. The current 5G, limited to the frequencies below 30 GHz (60 GHz in the future), can increase the data rate to several Gbit/s. As the next step of 5G development, terahertz telecommunications start to receive considerable attention. The terahertz frequency band between 0.1-10 THz could increase the data flow to the terabyte per second by a simple increase of the carrier frequency [7, 8]. Hence, the bandwidth supplied is one order of magnitude above millimeter-wave systems. However, the strong absorption of the terahertz waves by water in the atmosphere limits terahertz telecommunication to a short-range wireless telecommunication similar to Wi-Fi or to space communications (satellite to satellite or satellite to space probe). Even so, the strong absorption of terahertz radiation can also be an advantage to increase the security of the

communication, since the range of the network will be limited to a building or a room area because the terahertz waves will be absorbed by water vapors and the walls.[9]

I.1.2. Development of terahertz technologies

Even if the potential applications of terahertz waves are known since a long time, the difficulties to realize components in this domain hindered the development of THz technologies and favored the development of technologies in adjacent domains (optical and micro-waves).

Consequently, the electromagnetic waves were historically divided in two categories, the photonics and the electronic domain. Each domain has its own principles, methods and tools. Nevertheless, terahertz cannot be classified in these groups, they are halfway between the two and the approximations used for adjacent domains are hardly applied in the terahertz domain.

As an example, for the terahertz sources, the traditional solid state sources used for microwave generation cannot follow the fast oscillation of the terahertz field because of the saturation velocity of the carriers (typically 10^5 m/s) in the device [10]. On the other hand, the optical sources exhibit a decrease in optical power with the decrease of the frequency. This is due to lack of photon energy to meet the band-gap requirements for most of the sources. Additionally, the terahertz photon energy is of the same order of magnitude as the ambient temperature thermal energy (black-body radiation), which hindered the terahertz field measurements.

Therefore, to develop terahertz applications, it has been necessary to develop new technologies and tools. During the last decades, we have seen a real explosion of research on development of THz detectors and sources [11]. We can differentiate two different approaches, the first consists of using microwave technologies and transpose them in the terahertz domain by increasing the operating frequency. It leads to the development of diode oscillators and electronic tubes [12-14]. The second approach consists of using the optical technologies and transpose them to the terahertz. We can quote quantum cascade lasers, doped silicon lasers or even photomixer antennas for the realization of mono-frequency terahertz sources [15-19]. Nowadays, we can find a lot of commercial systems based on these technologies. The Figure I-5 illustrates the different existing THz sources and their output power.
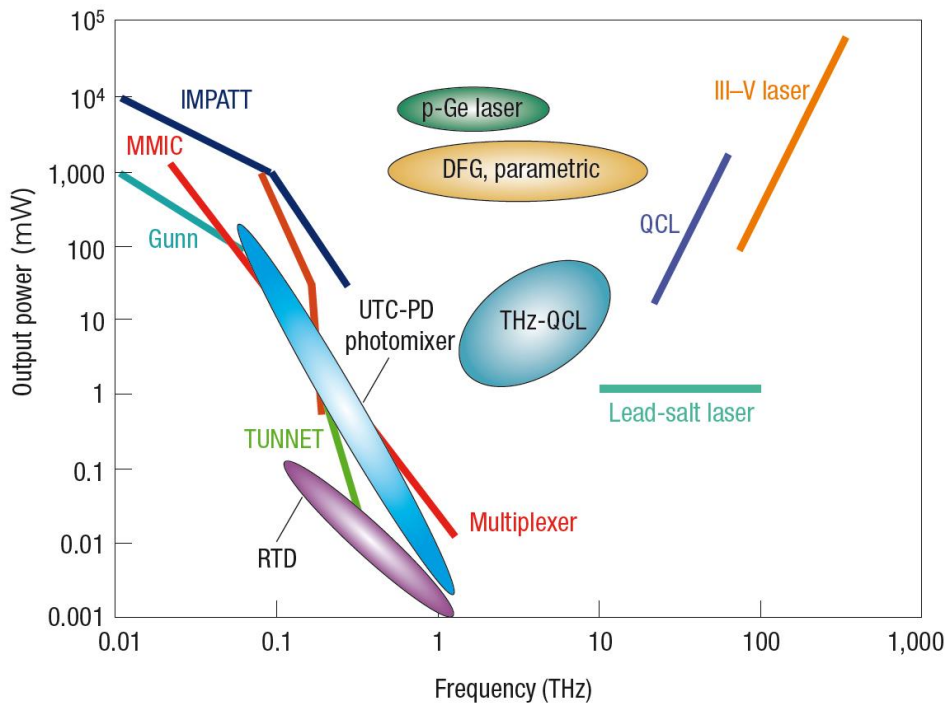
Figure I-5 : THz-emission power of THz sources as a function of frequency. Solid lines are for the conventional THz sources and oval denoted new THz sources [1].

With the apparition of new sources, the realization of terahertz applications becomes possible. Nevertheless, for the development of these applications, it appears necessary to develop new components such as filters, spatial light modulators, frequency selective surfaces to control the properties of THz waves such as their amplitude, phase, polarization and/ or spatiotemporal distribution of their wave fronts. The active component development is hindered because of the lack of natural materials capable to strongly modulate THz waves. If some devices have been proposed, most of them have to face large volume, high costs, and fabrication issues, which restrict their applications in terahertz scenarios. More recently, in the search for a material compatible with terahertz applications, we are witnessing the emergence of 2D resonators such as metallic grating structures or metamaterial (artificial structured materials) which can achieve strong modulations of terahertz wavefront [20].

However, these structures are passive structures and after the fabrication process it is not possible to modify the THz response of the structure. Although passive devices can be useful for specific applications (beam deflection, objects cloaking, focusing, absorbing and polarization converting), active devices are highly required to reduce the size of terahertz systems and for the development of more complex terahertz systems and applications such as high-speed telecommunications and spatial light modulators (SLM) to actively control the amplitude, phase, and polarization of terahertz waves. Nevertheless, active devices are high consumption and with the increase of the functionalities it appears necessary to reduce the size and the consumption of devices. In this context, THz reconfigurable components

represent a promising solution. The purpose of using these components is to replace similar individual components performing the same function but with different operating ranges. As an example, we can substitute several different filters composing a transmission line of a terahertz telecommunication system by a reduced numbered of reconfigurable filters, whose properties (center frequency, operational bandwidth) can match those of the replaced filters. The complexity and the space requirement of the system are thus reduced, and we can realize devices with potentially better performance and lower consumption (by reducing the number of active components). In the last years, numerous studies focused their work on means to make 2D reconfigurable structures.

I.2. Method to realize reconfigurable Terahertz devices

I.2.1. Presentation and introduction

To realize reconfigurable devices most of the main methods consist to integrate active elements in a fixed 2D passive structure. Generally, the 2D passive structure consists of a metamaterial which is an artificial structured material. This artificial material is composed of an arrangement of sub-wavelength periodic inclusions (dielectric or metallic) in a host material. Metamaterials exhibit strong resonances in the THz domain and can be used to control THz in free space for the realization of passive filters, flat lenses, absorbents, etc. Figure I-6 presents different shapes of 2D metamaterials and the typical transmission and real permittivity of this type of structures [21].

(a)   (b)
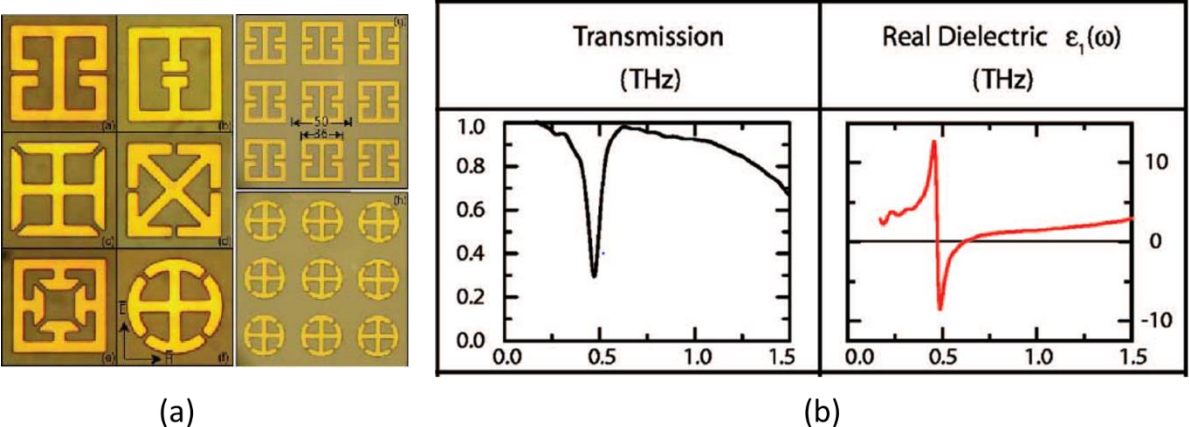
Figure I-6 : (a) Different kinds of metamaterial designs. On the left different shapes of unit cells and on the right examples of metamaterials composed of several unit cells. (b) Typical transmission and permittivity of the metamaterial depending on the frequency [21].

The response of the metamaterial structure is determined by the shape/dimensions and dielectric environment of the unit cell of the structure. Thus, by integrating an active media in each unit cell composing the metamaterial it is possible to actively modify the response of the metamaterial and use them to realize reconfigurable metamaterials.

In the THz domain, reconfigurable metamaterials can have large number of potential applications such as switches, modulators, reconfigurable filters, etc. to control the amplitude the phase, the polarization of incident waves which is essential for the realization of transmission line for THz telecommunication.

In the next parts, different technics to integrate active media in 2D structures for the realization of reconfigurable THz devices will be presented.

I.2.2. Semiconductors for reconfigurable terahertz devices

One of the first methods is the use of semiconductors. Semiconductor materials have electrical properties between insulating materials and conducting materials. According to the band theory, they are materials with a small bandgap ΔE (~ 1 eV). Applying a stimulus (electrical or optical), electrons from the valence band can be easily excited to the conduction band, creating a decrease of the resistivity and thus an electrical current. The resistivity and current value can be tuned by introducing impurity in small quantity (doping). If the impurities introduced in the semiconductors are electron donors, the doping is called N-type doping, if the impurities introduced in the semiconductors are electron acceptors, the doping is called P-type doping.

By joining a metal in contact with a semiconductor, we obtain a Schottky junction. When a reverse polarization (negative voltage) is applied, the capacitance of the junction varied according to the applied voltage [22]. Chen *et al.* proposed to integrate a semiconductor to a double split ring resonator (SRR) structure [23]. The SRR structure was fabricated on a substrate which is an n-type gallium arsenide (GaAs) layer grown on a semi-insulating gallium arsenide (SI-GaAs) wafer (Figure I-7). The metal and the n-GaAs form the Schottky junction. The equivalent circuit of the device is an RLC resonator (Figure I-7-b). Without voltage bias applied on the SRR structure (Figure I-7-c), the capacitance formed by the gap of the SRR is shorted by the substrate free charge carriers in the gap of the SRR structure. Thus, there is no LC resonance in the structure. However, when a gate bias is applied, a depletion area is created in the GaAs substrate (Figure I-7-d), which reduces the conductivity and restores the LC resonance (Figure I-7-e). The variable resistance in the equivalent circuit (Figure I-7-b) corresponds to the losses due to the substrate free carrier absorption within the split gap.

This type of design does not allow the shift of the resonance frequency because the bias current does not affect the value of the capacity but just shunts it. Due to their low-tuning time at the microsecond or nanosecond timescale semiconductor technologies cannot perform high frequency modulation. Additionally, they have low resonance strength and high insertion losses due to the inherent resistive loss of the semiconductors. Thus, insertion losses of 4.3 dB

and modulation depths of 45 % and 52% have been reported for these types of devices [24, 25].
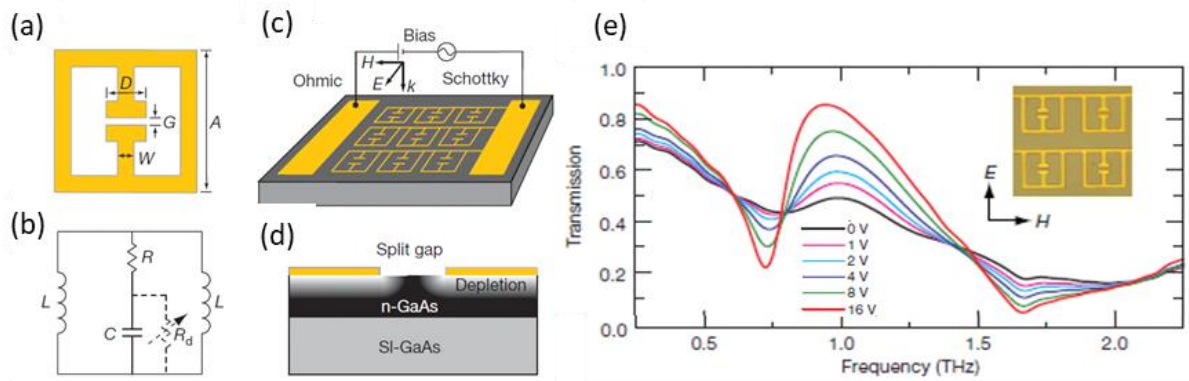
Figure I-7: (a) Geometry and dimensions of the SRR unit cell A=36 µm, G=2 µm, D=10 µm and W=4 µm. (b) Equivalent circuit. (c) The pattern of the metamaterial. (d) Cross-section of the device. (e) Transmission of the device for E parallel to the gap [23].

I.2.3. Microelectromechanical systems (MEMS) for reconfigurable terahertz devices

Another solution to realize reconfigurable THz device is to use microelectromechanical systems (MEMS). A MEMS is constituted by a moving part in the form of a suspended bridge with one or more anchors (Figure I-8). This bridge can be moved under stimuli (thermal, electrical, magnetic…) to create variable capacitances or switching functions.
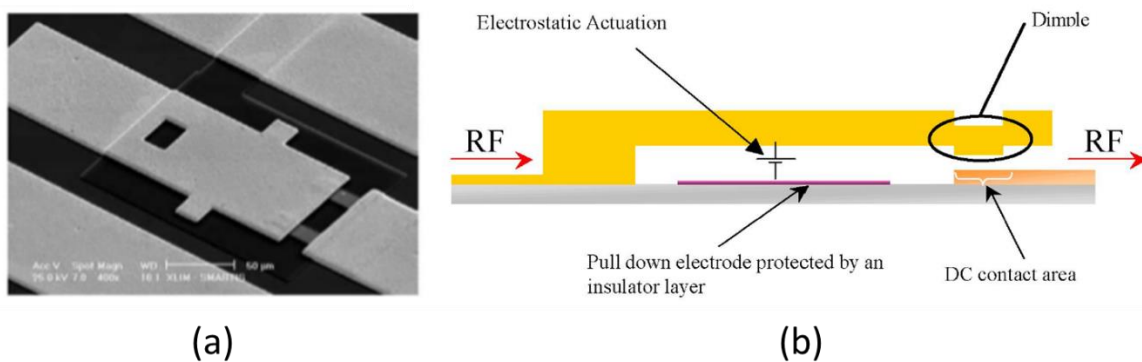
Figure I-8 : (a) MEMS component made at Xlim and (b) its corresponding schematic [26].

MEMS technologies have been used in the microwave domain for the realization of switches, filters, phase shifters or impedance matching circuits [27-29]. In analogy, by integrating MEMS devices in a terahertz metamaterial, the dimension/shape of the metamaterial can be actively controlled and, consequently, the response of the device changes.

Zhengli Han *et al.* proposed a design where the unit cell of the metamaterial is composed of a RF-MEMS capacitor embedded in the center of a SRR structure (Figure I-9-a).[30] When a voltage beyond the actuation voltage is applied to the electrodes, the MEMS-SRR move from the upper, OFF-state to the lower ON-state. This action closes the air gap and increases the capacitance of the SRR, lowering the resonance frequency of the SRR resonator (Figure I-9-b).
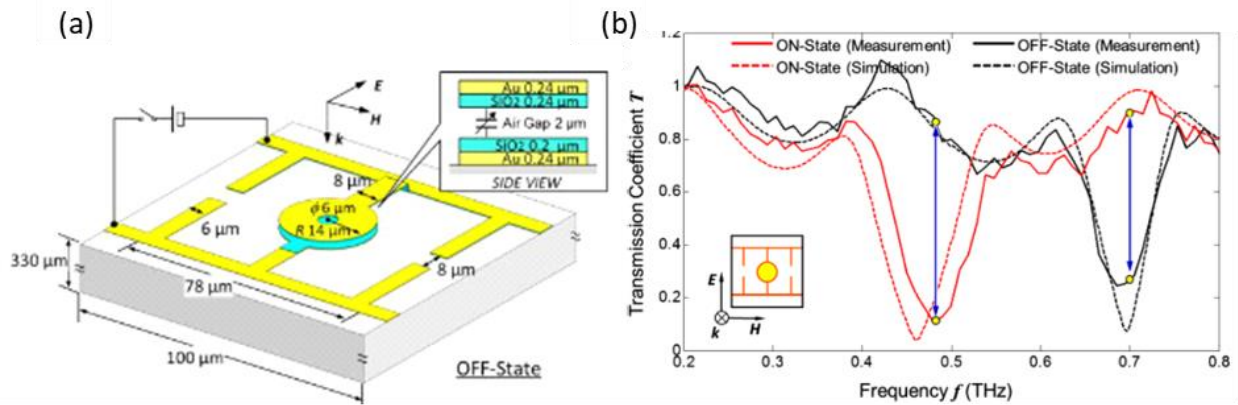
Figure I-9: (a) MEMS reconfigurable SRR design at OFF-state (b) Normalized transmission spectra for the MEMS-SRR device with polarization perpendicular to the electrical interconnect lines.[30]

Devices based on MEMs can achieve better amplitude and polarization modulations of terahertz waves than semiconductor technologies and have very low insertion losses in OFF state. By using MEMS technologies Zhengli Han *et al.* reported a modulation of 80%. Nevertheless, due to the mechanical process of the modulation (bridge moving up and down), MEMs technologies tend to have a slow tuning time at the microsecond timescale and shorter lifetime than other technologies.

I.2.4. Liquid crystals technology for reconfigurable terahertz devices

Liquid crystals are well known tunable permittivity materials which are extensively used in panel displays [31]. They are anisotropic materials in the form of a mesophase which have the particularity to be both solid and liquid [32]. The molecules in the liquid crystals present a certain order characteristic of a solid at low temperature and disorder characteristic of a liquid at high temperature. Depending on the degree of disorder, the properties of the liquid crystals more or less approach those of a liquid or solid. Using external stimuli (electric field, temperature…) it is possible to control the disorder of the liquid crystal and thus switch the different states of the liquid crystal.

In the case of the liquid crystal display technology (LCD), thermotropic liquid crystals with rod shape are used. Due to their elongated shape, they have an anisotropic permittivity which creates a polarization effect in the lengthwise direction. In the nematic state (liquid), the

molecules are unaligned, and each molecule blocks different polarizations of the incident wave. Therefore, the transmission of each polarization is weakly affected. When an electric field is applied, the molecules line up and block a unique polarization of the incident wave and its transmission is strongly attenuated (Figure I-10).
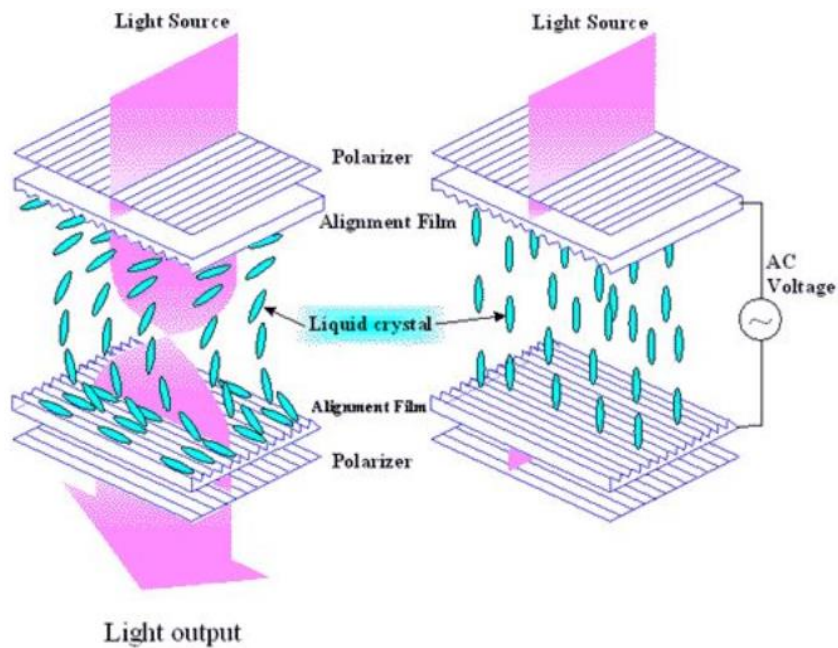
Figure I-10: Operating principle of a liquid crystal display (LCD) showing the alignment of the liquid crystal depending on the electric field [31]

LCD screens are not the only application, liquid crystal can be easily combined with metallic layers to provide tuneability for the realization of reconfigurable terahertz devices. For example, Zografopoulos and Beccherelli proposed a liquid-crystal tuneable fishnet metamaterials structure composed of a liquid crystal layer placed between two periodic gold square patch arrays (Figure I-11) [33]. By applying a voltage on the gold patch, it will change the alignment of the liquid crystals and thus, will change the response of the device. With this structure, a modulation depth of the THz transmitted amplitude of 70% at 0.890 GHz can be achieved, and also a shift of the resonance frequency by more than 150 GHz.
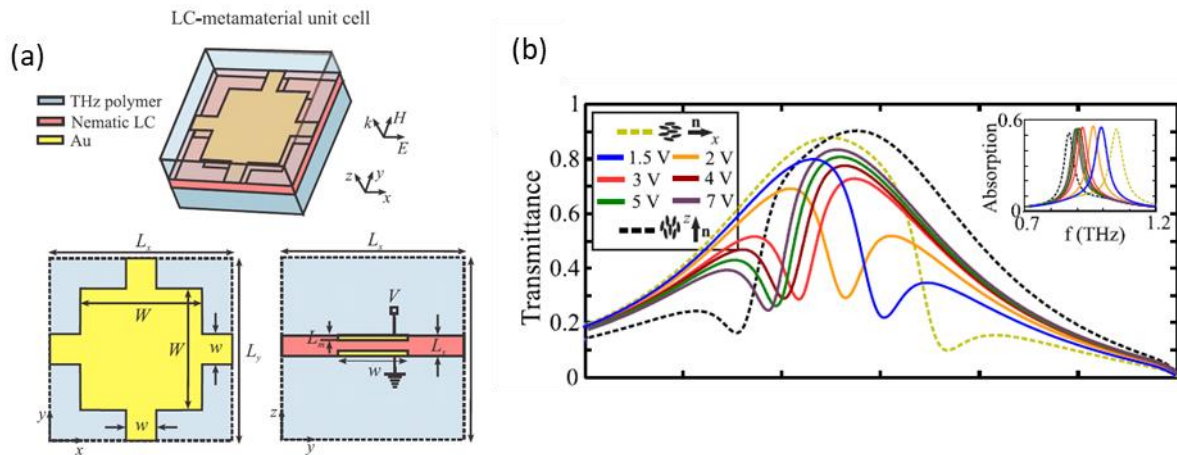
Figure I-11: (a) Schematic layout and geometrical parameter definition of the proposed LC-tunable fishnet (b) Transmittance of the LC-THz metamaterial for various values of applied voltage. The limiting cases of resting and fully switched LC molecules are shown in dashed lines. The inset shows the corresponding absorption spectra, indicating a shift of the metamaterial resonance for increasing voltage values.[33]

This principle can be used to realize terahertz spatial light modulator [34] or to realize multifunctional terahertz devices [35]. Liquid crystal is a good candidate for the realization of compact reconfigurable devices thanks to the possibility to make multifunctional devices. They have low insertion losses (1.16 dB) [36] and good modulation depth (70%) in the THz range. However, like MEMs technology, liquid crystals have a slow switching time at the millisecond or microsecond timescale.

I.2.5. Ferroelectric materials for reconfigurable terahertz devices

Ferroelectric materials are nonlinear dielectrics which present a structural change from a high symmetry structure to a non-centrosymmetric state composed of permanent electric dipole moments. This transition is controllable using thermal and electrical stimuli with a response time between the microsecond and the nanosecond timescale. The phase transition is mainly related to the strong polar soft lattice vibrational mode existing in the high temperature phase [37].

When an electric field is applied on the material, an electric polarization of the material can be induced. As we can see on Figure I-12 when the applied electric field increases, the overall polarization in the crystal increases as the polarization in different dipolar regions are aligned until it reaches the saturation of the polarization. When the electric field is removed, the material keeps a remanent polarization state (P_r). This phenomenon results in the presence of a hysteresis cycle [37].
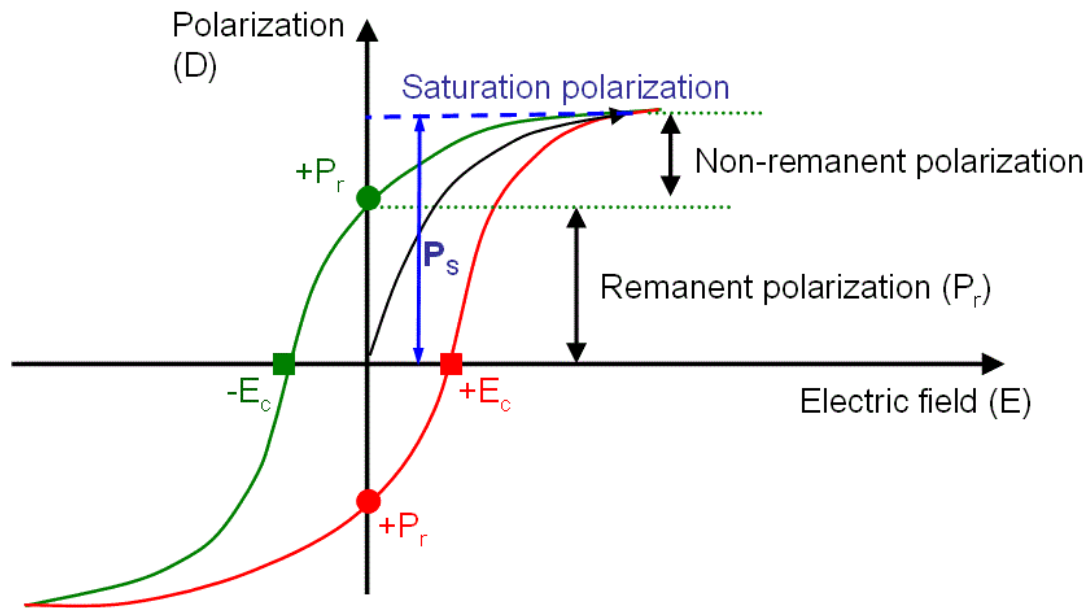
Figure I-12 : ferroelectric hysteresis loop

This polar state only exists on a specific range of temperature. When the temperature increases, for a limit temperature called Curie temperature, the material goes from a polar, ferroelectric phase to a non-polar, non-ferroelectric phase (paraelectric phase).

This phenomenon enables the tuning of the dielectric permittivity [38] and thus to control incident electromagnetic waves. The most common ferroelectric materials are the metal oxides knows as perovskites (ABO_3 type) such as titanates ($BaTiO_3$, $PbTiO_3$, …) and niobate ($KNbO_3$). The first method of integration and control of ferroelectric layers consists of using a temperature modulation. Singh et al. demonstrate the possibility to tune the resonance frequency of a SRR structure using ferroelectric materials. The proposed structure is composed of a gold SRR deposed on a bulk single crystal strontium titanate (STO) (Figure I-13) [39]. When the temperature decreases from 409 K to 150 K, the resonance frequency progressively redshift up to ≈50% with a small variation in the resonance amplitude due to the variation of the refractive index of the STO substrate.
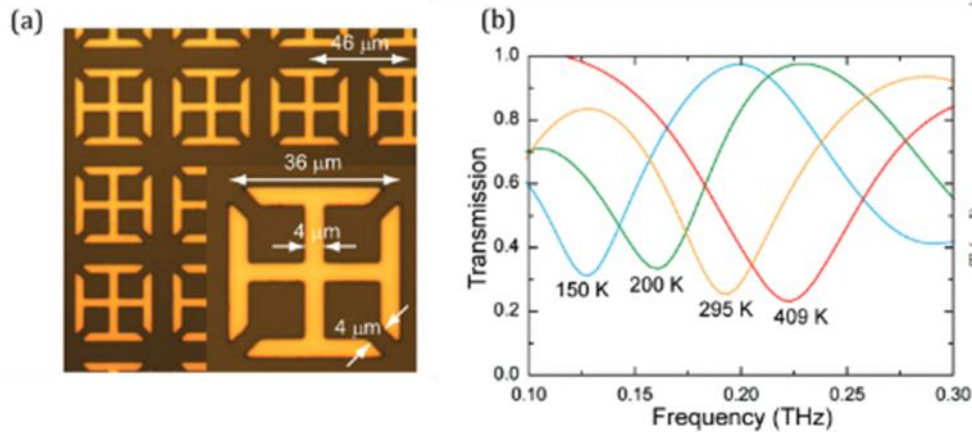
Figure I-13 : (a) Microscopic image of a gold SRR deposed on a STO substrate. (b) Terahertz transmission of the metamaterial normalized by the bare STO substrate depending on the temperature [39].

Another metamaterial composed of a series of grooves drilled in a thick STO wafer exhibiting a tunable range of negative effective permeability in the terahertz spectral region (0.2–0.36 THz) has been reported [40]. With this structure Nemec et al. demonstrated the possibility to shift the resonance of the structure from 0.36 THz at 300 K down to 0.20 THz at 120 K.

The use of thermal activation limits the achievable tuning speed. For practical terahertz applications, high tunability using an external bias voltage at room temperature is required. Therefore, ferroelectric materials with a Curie temperature near-room temperature is required to allow electrical tuning of ferroelectric materials. Under this constraint, metamaterials based on barium strontium titanate (BST) and potassium tantalite ($KTaO_3$, KTO) have proven high capacity to modulate terahertz waves [41-43]. However, these materials tend to have high losses, the maximum transmission of the structure proposed by Wu *et al.* is around 70%, and they have a response time around 0.1 µs.

I.2.6. 2D materials for reconfigurable terahertz devices

1. Graphene based reconfigurable devices

Graphene is a two-dimensional allotrope of carbon which has been isolated and characterized in 2004 [44]. It is formed by a single atomic layer of carbon in a hexagonal lattice. If we look at the band theory, metal and insulator present clearly different properties (Figure I-14). In the case of a metal, the conduction band is partially full of electrons and the valence band is completely full. Whereas for an insulator, the conduction band is empty of electrons and separate from the valence band by a gap. If we are now interested in the Fermi level which corresponds to the highest energy level occupied by the electrons of the system at

the temperature of 0 K. The Fermi level of metal is situated in the conduction band of the metal whereas the Fermi level of insulator is situated in the gap.
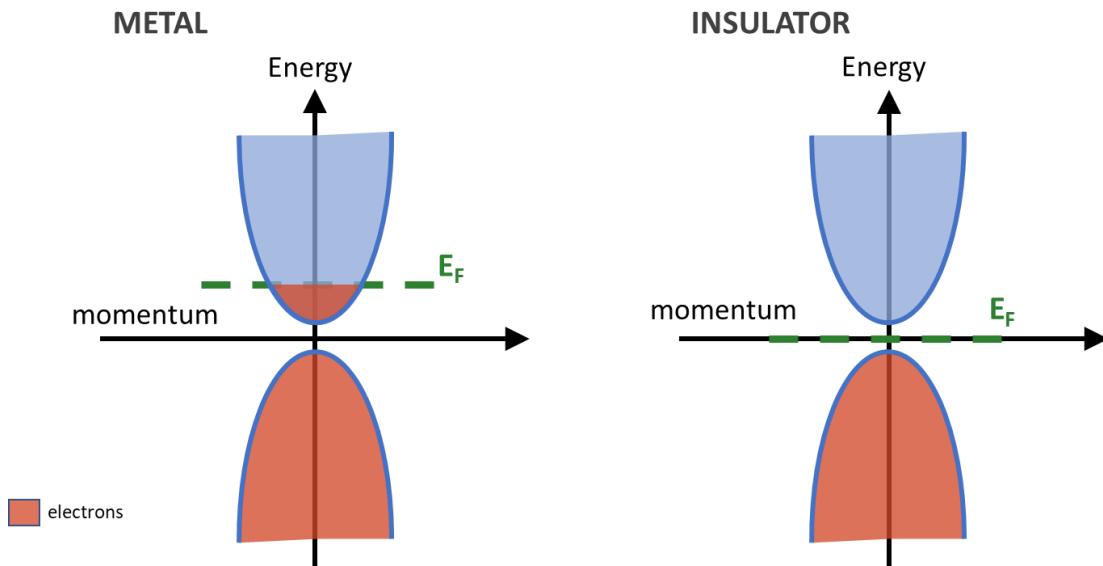
METAL

INSULATOR

Figure I-14: Schematic of the energy band of the electrons depending on their momentum in the case of a metal and an insulator. E_F corresponds to the Fermi level.

In the case of graphene, a very uncommon behavior can be observed. The valence and the conduction band form two cones (Dirac cones) joined in one point called Dirac point (Figure I-15) [45]. This band structure makes the properties of graphene a mix between semiconductors and metal. The electrons have all the same velocity and have no inertia, it is as if they were massless.
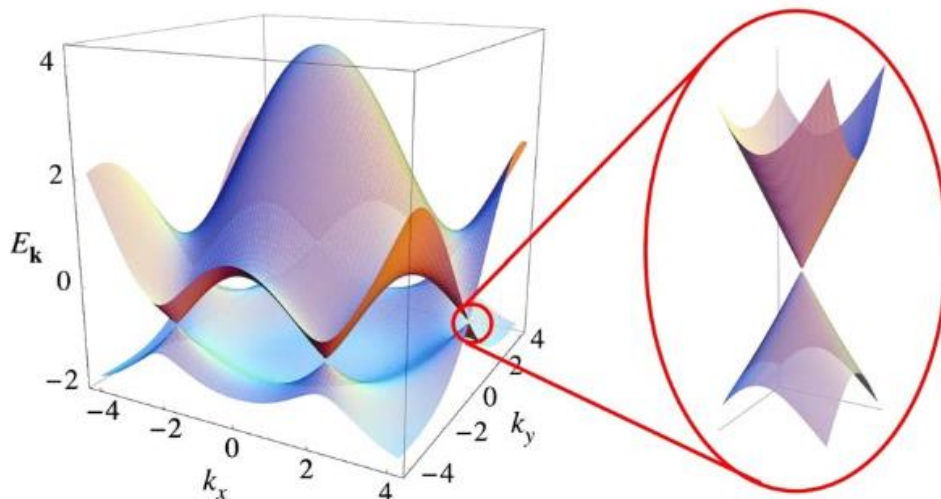
*Figure I-15: Graphene band structure. **right:** Enlargement of the band structure close to the Dirac point [45].*

The value of the Fermi level can be tuned using an electrostatic gating or chemical doping to modify the properties of graphene [46, 47].

In the terahertz domain, the graphene can be integrated in plasmonic structures to enable tuneability. For example, Lee *et al.* proposed a design made with an atomically thin graphene layer, an artificially constructed meta-atom array and a metallic wire gate electrode array (Figure I-16-a) [47]. The electrodes are designed to not perturb the incident terahertz waves. By applying a gate voltage on an electrode, the carrier density (conductivity) of the graphene will change and thus the transmission of the terahertz wave through the metamaterial will be modulated (Figure I-16-b). A modulation depth of 47 % and a phase shift of 32.2° is achieved at 0.62 THz for a variation of the voltage ΔV = 850 V. It is interesting to note that a hysteresis behavior is observed (Figure I-16-c), thus it allows the realization of graphene-based memory metadevice operations. Additional, graphene can achieve fast modulations at nanosecond timescale [48].
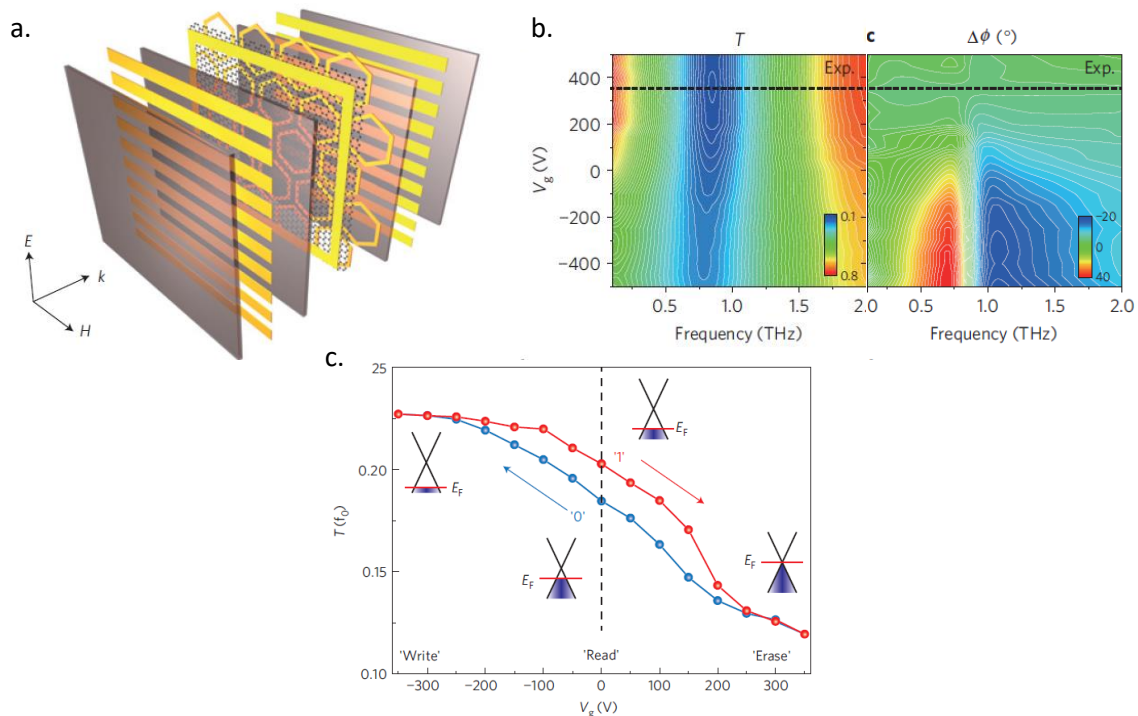
Figure I-16: (a) Gate-controlled active graphene metamaterial schematic composed of a single layer graphene deposited on a layer of hexagonal metallic meta-atoms and top/bottom electrodes embedded in a dielectric material. Metallic patterns and dielectric materials are represented by yellow and gray, respectively (b) measured transmission (T) and phase change (ΔΦ) in function of the gate voltage. The blue corresponds to lower value of transmission and phase whereas the red corresponds to higher values (c) Hysteresis behavior for a cyclic change of the gate. The graphene Fermi level is schematically illustrated for each of the operating points [47].

More recently, a device based on graphene with a modulation frequency range of 0.25-1 THz, a modulation depth of 94%, and a modulation speed of 200 kHz has been reported

using optical activation(1.55 μm laser with power ≈800 mW) [49]. Insertion losses of 2 dB have been reported [50].

Graphene-based technologies seem to be very promising for the development of reconfigurable devices. However, they tend to have narrow tuning spectral range due to the weak change of properties when switched from an OFF state to an ON state and the fabrication of graphene requires expensive procedures which slow down the development of large-scale applications.

2. Transition metal dichalcogenides (*TMDs*) for reconfigurable devices

With the success of graphene technologies, research started to focus on other existing 2D materials. Transition metal dichalcogenides (TMDs) are semiconductors of the type MX_2, where M is a transition metal atom (such as Mo or W) and X is a chalcogen atom (such as S, Se or Te). They provide a good alternative to graphene technologies. The most used TMD is the molybdenum disulfide (MoS_2). Monolayer MoS_2 is a direct band gap semiconductor which possesses 2 different phases and each phase has their own properties [51]. As a semiconductor it is possible to modify its carrier density/properties using electrical or optical pumping [52]. In the THz domain, TMDs have been integrated in THz resonance structures. Cao et al. proposed in a recent study to use THZ modulator based on MoS_2 doped by oxygen (Figure I-17). To dope the MoS_2 layer they heat the material to 300 °C in air atmosphere.
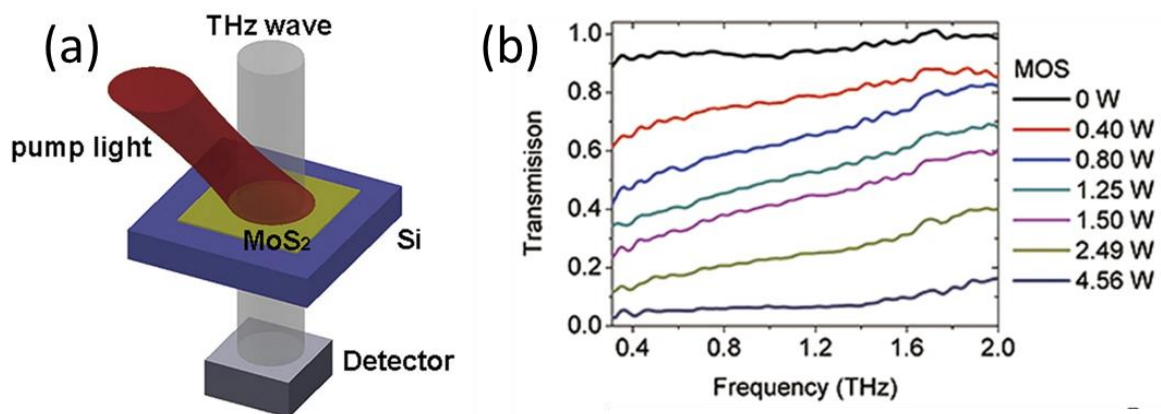
Figure I-17 : (a) Schematic of the device under optical pumping. (b) Corresponding transmission of the device after oxygen doping [52].

With this device, it was demonstrated that THz transmission could be modulated up to 87% at 0.9 THz by changing the power of the pumping laser up to 4.56 W.

As in graphene-based technologies, the transition of MoS_2 is volatile and requires a constant bias energy to maintain its properties.

I.2.7. Phase transition materials (PTM) for reconfigurable terahertz devices

Recently, many studies focus on phase transition metal oxides for the realization of reconfigurable terahertz devices. Some metal oxides have the particularity to present a metal-insulator transition (MIT) which occurs at a specific transition temperature, with a large change in their electrical, optical or dielectric properties. The resistance variation during MIT can be fast, with a large variation of material's electric properties and can be achieved using thermal heating, electrical bias or optical activation. As we can notice in Table I-1, it exists a wide variety of phase transition metal oxides characterized by their transition temperature which goes from 70 K for V_8O_{15} to 1081 K for NbO_2 [53].

Table I-1 : Metal-insulator transition temperature value for some metal oxides [53].

Oxide	T_{IMT} [K]	Oxide	T_{IMT} [K]
V_8O_{15}	70	$NdNiO_3$	201
Fe_3O_4	121	V_4O_7	250
VO	126	VO_2	340
V_5O_9	135	$SmNiO_3$	403
$PrNiO_3$	135	Ti_3O_5	448
V_6O_{13}	150	$LaCoO_3$	500
V_2O_3	165	Ti_2O_3	400–600
V_6O_{11}	177	NbO_2	1081

Among these MIT metal oxides, the most investigated is the vanadium dioxide (VO_2) due to its MIT occurring near-room temperature ($\approx$ 340 K). During the MIT, the VO_2 goes from a monoclinic insulating state to a tetragonal rutile conductive state with a variation of the electrical resistivity by four orders of magnitude [54]. In the case of the VO_2, the transition can be achieved by heating [55, 56], electrical activation [57, 58], optical activation [59] and even under pressure or external stress [60] with a fast transition time at the femtosecond time scale.

In the terahertz domain, this transition can also be observed. When the VO_2 is in insulating state, it is almost transparent to the terahertz waves, whereas when it is in metallic state, it is opaque to terahertz waves. The terahertz conductivity of the material varies by several orders of magnitude [61]. By combining VO_2 with a plasmonic terahertz structure, a functional reconfigurable terahertz device can be obtained. Reconfigurable THz devices using thermal heating which operate near room temperature and can actively control the transmission and polarization state of THz waves have been demonstrated [62, 63]. However, if thermal activation is a convenient way to investigate the MIT process of vanadium, it does

not provide fast and precise controlled transition and its integration and control for practical applications remains difficult. Another mechanism to control the MIT of VO_2 is the use of electrical bias. After the plasmonic structure is deposited on VO_2, additional electrodes can be added to the structure to electrically control the VO_2 [64, 65]. Even if this method is not considered as a pure electrical phenomenon (thermal heating due to joule effect) it can show fast switching speed on nanosecond timescales. For example, different wire grid structures deposed on VO_2 have been proposed to realize a broadband terahertz modulation (Figure I-18.a-d) [65]. When no electric bias is applied on the structure, it will act as a polarizer structure, the terahertz waves with a polarization parallel to the grating will be reflected whereas the perpendicular polarization will be transmitted. When a bias voltage is applied on the metallic grating, a conductive path will be created in the VO_2 film and modulation of the perpendicular polarization can be achieved. The parallel polarization is still reflected. For voltage values under 6 V, the modulation depth will be affected by the design of the line (Figure I-18.e-f), a modulation depth of 85 % is achieved. To decrease the activation voltage and increase the switching speed, VO_2 wires can be used instead of the VO_2 film (Figure I-18.d, h).
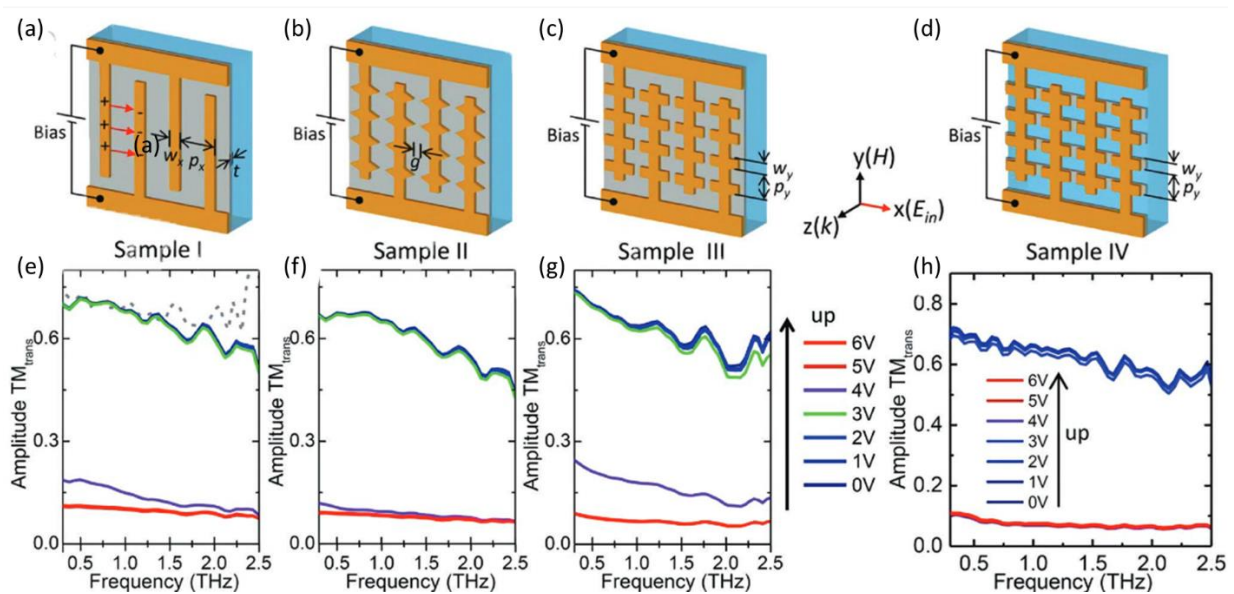
Figure I-18: a–d) Design of the four types of electrically driven hybrid bowtie antenna-VO_2 devices: Sample I, Al wires on VO2 film; Sample II, Al wires with triangle bowties on VO2 film; Sample III, Al wires with square bowties on VO_2 film; and Sample IV, Al wires with square bowties on VO_2 wires. Red arrows in (a) indicate the electric field built through the charge accumulations on two neighboring wires. e–h) Measured amplitude transmission for the TM mode for Samples I–IV when the applied voltage is increased [65].

Continuous wave lasers can also be used to trigger VO_2 MIT. This method is interesting because the MIT can be controlled without any direct mechanical contact on the structure

(electrode) [66]. By combining VO$_2$ with a plasmonic structure, ultrafast fast modulation can be achieved using optical pulses at 1 ps timescale (Figure I-19) [67].
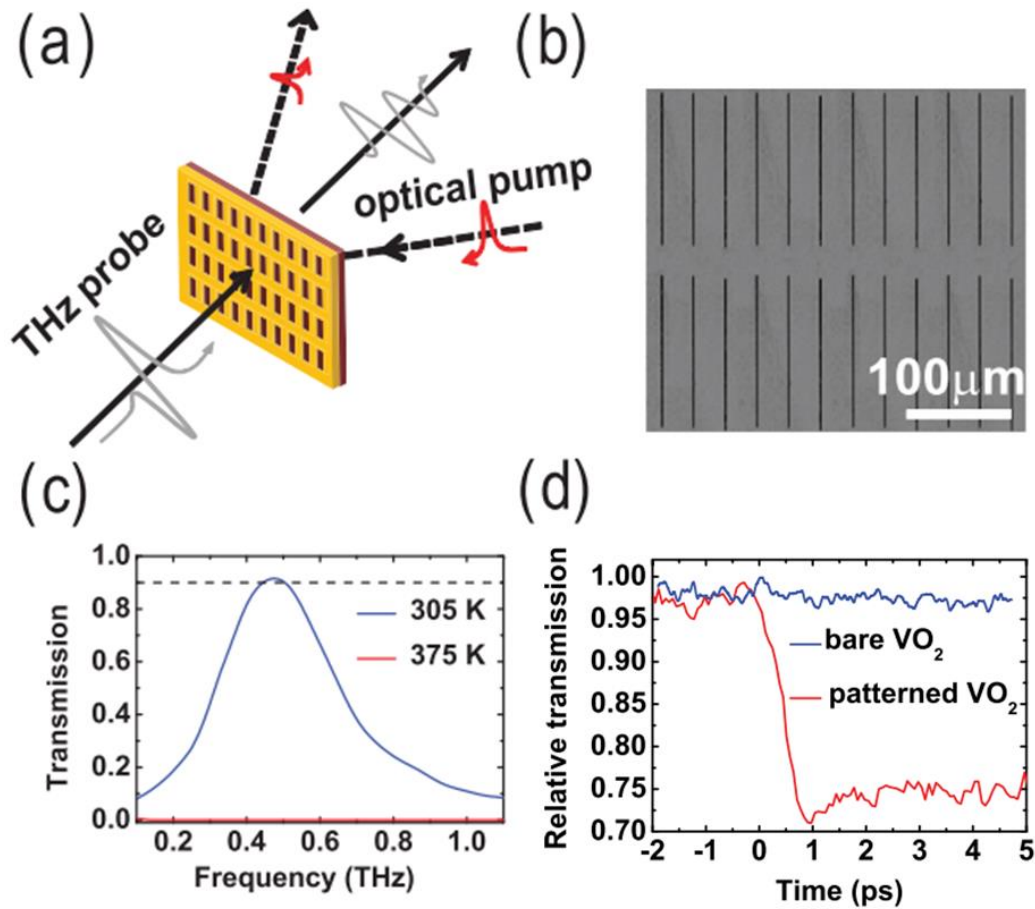
Figure I-19: (a)Schematic diagram of the nano-resonator sample (array of rectangular holes deposited on the VO$_2$ films) under optical pump and THz probe. The array of rectangles has a vertical period of 180 μm and horizontal period of 100 μm. The length and the width of each rectangle are 150 μm and 450 nm, respectively. (b) Scanning electron microscopy image of the sample. (c) Transmission spectra of patterned sample at the insulator and metal state of VO$_2$. (d) THz switching time measurements for a bare VO$_2$ film (blue line) and VO$_2$ film with the metallic structure (red line) with excitation of optical pump pulse at 0 ps. For bare VO$_2$ film no switch is observed because the energy density of the used optical pumping is too low [67].

I.2.8. Summary of the different techniques for the realization of reconfigurable THz devices

The main characteristics of the previously presented technologies to realize reconfigurable terahertz devices are shown on

Table I-2.

Table I-2 : Comparative table between the different active media.

	Semiconductor	MEMS	Liquid crystal	Ferroelectric materials	Graphene/ TMP	Phase transition materials
References	[24, 25]	[30]	[33, 34] [35] [36]	[40-43]	[48, 49] [50] [52]	[65, 66] [67]
Activation method	Electrical/ Optical	Electrical	Electrical	Thermal/ Electrical	Electrical/ Optical	Thermal/ Electrical/ Optical
Transition type	Volatile	Volatile	Volatile	Volatile	Volatile	Volatile
Switching time	µs-ns	µs	ms-µs	ms-ns	ns-ps	ns-ps
Fabrication	Simple	Complex	Complex	Simple	Complex	Complex
Modulation depth	50%	80%	70%	17%-70%	47-97%	85%
Insertion losses	4.3 dB	0.65 dB	1.16 dB	-	2 dB	<0.5 dB

Depending on the desired application, some technologies are more suitable than others to realize reconfigurable THz devices. As examples, MEMS and liquid crystal technologies have a low switching time. On contrary, graphene and VO2 technologies have proven very high switching time with high modulation depth which make them very suitable for the realization of fast terahertz modulators. Nevertheless, these agile elements have a volatile-type response which requires a permanent optical or electrical bias and a complex integration technology with electrical/ optical control schemes over large-area.

In my thesis I investigated phase change materials (PCMs) as an alternative of these technologies to realize bistable (non-volatile) terahertz devices. We investigated the properties of the PCMs at THz frequencies and the possibility to integrate them in fixed different topologies (metadevices' subwavelength resonators) for the realization of reconfigurable THz devices. Additionally, we explored the possibility to use them without any additional metallic structure for realizing resonant structures using solely PCMs.

I.3. Phase change materials (PCMs) presentation

I.3.1. Introduction to PCMs

Like phase transition materials, PCMs present a variation of their resistance which can be activated using a thermal, an electrical or an optical stimulus. In the case of PCMs, the resistance variation is due to a phase change between an amorphous, insulating state to a

crystalline, metallic-like state. In this thesis we develop the PCMs from chalcogenide family, which correspond to material based on chalcogens. Chalcogens correspond to the VI-B group from the Mendeleev classification. These elements are sulfur, selenium and telluride. However, for practical applications, PCMs are generally composed of materials like germanium (Ge), telluride (Te) and/or antimony (Sb) in different proportions. The ternary diagram in Figure I-20 summarizes the most used composition in the literature.
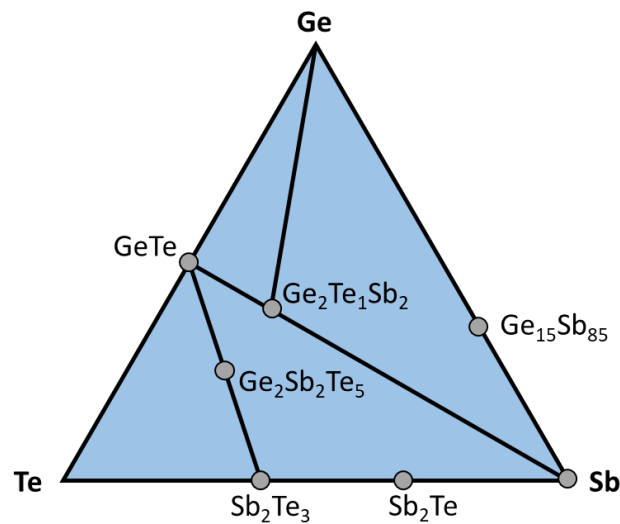
Figure I-20: Ternary diagram Ge-Sb-Te with the most common phase change materials.

PCMs have been discovered by Alan Tower Waterman from Yale University in the beginning of the 20th century [68]. Through his work on the thermionic emission of materials like chalcogenides, he demonstrated that these materials can be present in two different states: one α-state with a high resistivity and one β-state with low resistivity. Besides the direct heating, the change between these two states can be achieved with Joule effect using electrical excitation or with optical activation using photon injection. However, due to the lack of analyzing system (X-ray crystallography), he cannot infer the structural change of the material which can explain the change of resistivity. Starting from 1968, the phase change in chalcogenides was re-evaluated by Ovshinsky [69]. In 1973, he demonstrated the optical memory effect and its potential applications [70]. Thus, he demonstrated that Ge-Sb-Te compounds can be switched reversibly from an amorphous unstructured phase to a crystalline structured phase using either an electrical or an optical stimulus. Generally, the two states in PCMs have large, dissimilar electrical and optical properties. In the amorphous phase, the material has a high resistivity and a low optical reflectivity, whereas in the crystalline phase, it has a low resistivity and a high optical reflectivity (Figure I-21). This process is detailed in the next part.
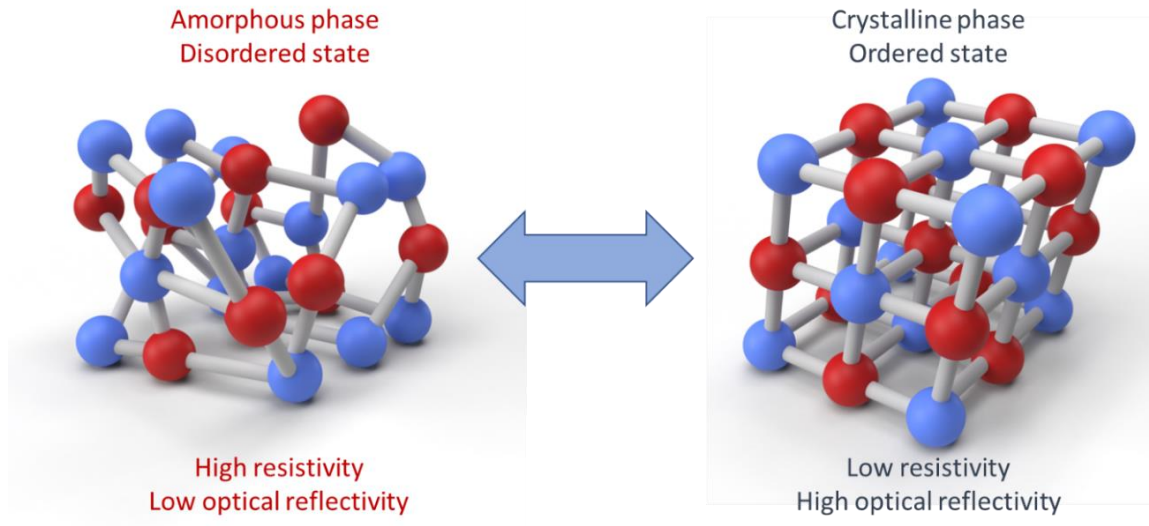
Figure I-21 : Different properties between amorphous and crystalline phase in chalcogenide materials.

I.3.2. Mechanism of the phase change

On Figure I-22, a typical example of PCM phase by thermal heating is presented. The material is initially amorphous (high resistivity state). When heating (using heating plate) until its specific crystallization temperature, abrupt decrease of the resistivity is observed which corresponds to the transition towards a crystalline phase (low resistivity state). Compared to phase transitions materials, PCMs phase change is non-volatile, when the material is cooled, it retains its amorphous state until ambient temperature (without any applied external stimuli), allowing bistable mode operation.
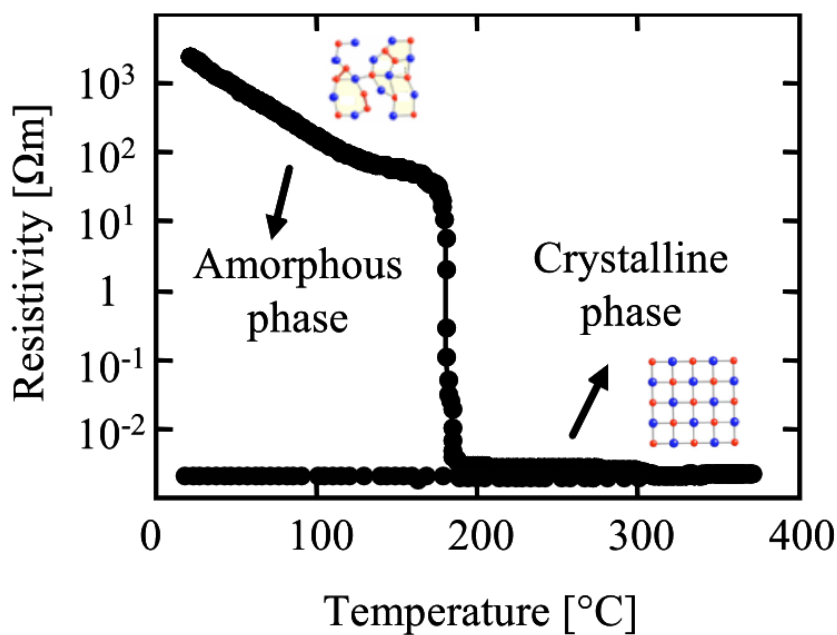
Figure I-22 : PCM resistivity variation depending on the temperature.

If direct heating highlights the bistability of the phase change, it is not suitable for the realization of PCM based devices. Current PCM devices are based on a fast thermal transformation (quenching) from a crystalline phase to an amorphous phase, passing by a liquid phase. Using direct thermal heating, it is practically impossible to obtain fast enough cooling to achieve this phase change. The fast and reversible phase change between amorphous and a crystalline state can be achieved using optical or electrical pulses [69, 71, 72]. The phase change principle is illustrated on Figure I-23.

To go from amorphous to crystalline phase, a low amplitude pulse (electrical or optical) is required to heat the material above its crystallization temperature (T_c). To allow the organization of atoms and thus the material crystallization the pulse duration must be long enough.

The reverse transition (from crystalline to amorphous phase) is achievable by heating the material above its melting temperature (T_f) to melt the crystalline structure and then, rapidly cool it to quench the material and freeze the atoms in a disordered state. During this process, the cooling process should be fast enough to avoid the crystallization of the material. A high amplitude pulse with a short pulse duration is therefore required.
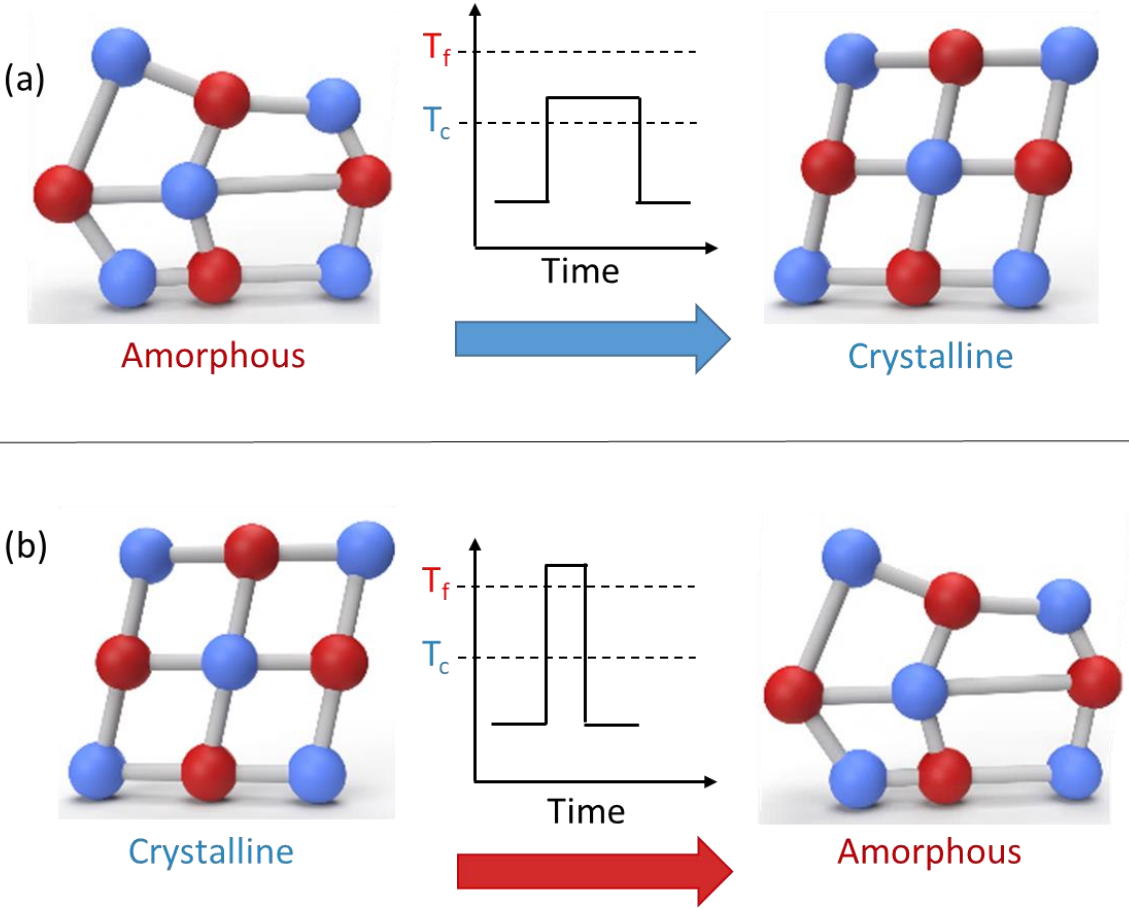
Figure I-23 : Principle of phase-change control using electrical or optical pulses: (a) from amorphous to crystalline and (b) from crystalline to amorphous.

I.3.3. Presentation of PCMs properties and activation schemes

The principal properties of PCM films (time transition, amorphous and crystalline resistance values) mainly depend on the composition of the PCM. As an example, in the case of Ge_xSb_x compounds, the slight increase of Ge concentration increases the phase change speed. In the case of GeTe and $Ge_xSb_xTe_x$ (GST) compounds, the increase of the Ge concentration leads to better thermal stability of the amorphous phase (higher phase change temperature) and can be used for high temperature applications (provided that the working temperature is lower than the crystallization temperature) [73-75]. Numerous studies have also proven the possibility of doping GST and GeTe PCMs with dopants such as nitrogen, carbon, silicon, oxygen, tungsten and indium for modifying the phase change temperature and the speed of the phase change, the stability or the resistivity values in the amorphous state [76-81]. However, the improvement of one characteristic often results in the degradation of a different one. As an example, the increase of the thermal stability of the amorphous phase always leads to the increase of the switching time.

Among the different PCMs, GeTe and GST are the most common materials, they can provide low switching time (at the nanosecond timescale), long-term stability of their different phases (>10 years) and a number of switching cycle (activation from amorphous to crystalline phase following by the reverse transition) between 10^5 and 10^{12} [82]. On Figure I-24, the resistivity and optical reflectivity variation of 100 nm thick layers of GST and GeTe protected by a 10 nm SiN layer during a heating/cooling cycle is shown.
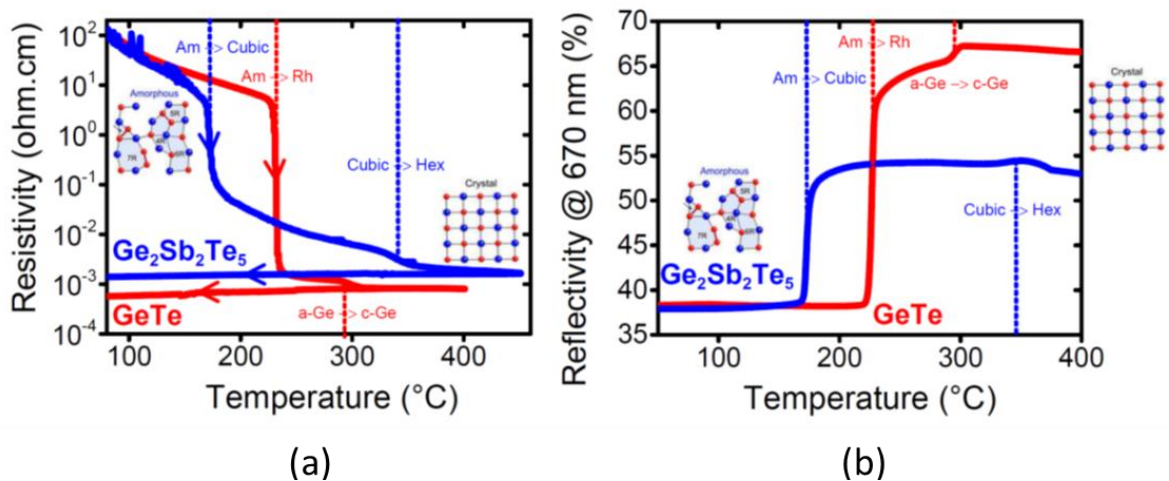
Figure I-24 : (a) Resistivity and (b) reflectivity measurements depending on the temperature for 100 nm GeTe and GST films deposited by DC magnetron sputtering on SI substrate and capped in situ with a 10 nm SiN protective layer [83].

If we look at the GST case (blue curve), we notice that when the temperature increases, the resistivity decrease progressively until 170 °C where a first transition occurs. The GST

goes from an amorphous phase to a cubic crystalline phase. After the first transition, a second smaller transition occurs around 340°C which corresponds to a change from the cubic crystalline phase to a hexagonal crystalline phase. After cooling back to ambient temperature, the resistance does not increase, the GST stays in it low resistive (crystalline) phase. Regarding the optical reflectivity at 670 nm, it increases from 38% to 54% when the GST goes from amorphous to crystalline phase. Amorphous-to crystalline transition timescales of GST films in the order of nanoseconds and picoseconds have been reported [72, 84].

In the case of GeTe (red curve), the same behavior is observed, however, only one transition is observed at 230°C (for the specific layers presented in[83]). The GeTe goes from an amorphous phase to a rhombohedral crystalline phase. Additionally, the resistivity variation between amorphous and crystalline phase is higher for GeTe than for GST. The same phenomenon is observed for the optical reflectivity of GeTe, which is higher (65%) than the optical reflectivity of GST (54%) in the crystalline state.

More generally, the crystallization of bare GeTe occurs between 150 °C and 200°C, whereas the melting temperature is between 500° C and 1000 °C [85]. Some studies reported a crystallization temperature of 180 °C and a melting temperature of 725 °C. However this value can be tuned by changing the proportion of Te in a GeTe alloy (Figure I-25) [86].
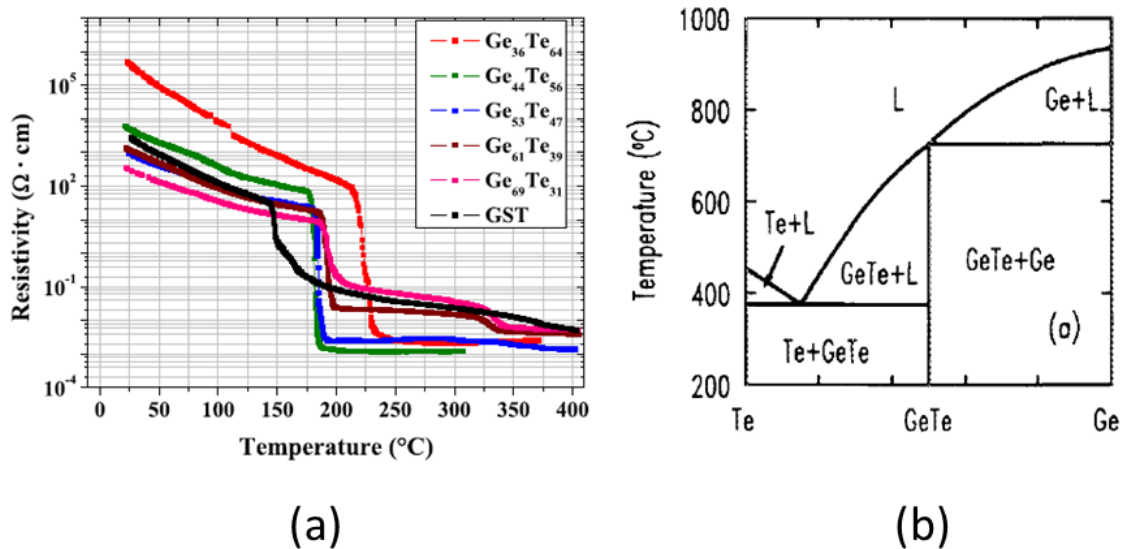
Figure I-25 : (a) Resistivity measurement depending on the temperature of a 100 nm thick Ge_xTe_{100-x} films. [86] (b) Phase diagram for binary GeTe system (L corresponds to liquid phase) [73].

By increasing the percentage of Te in the Ge_xTe_{100-x} compositions, the resistivity contrast increases as well as the crystallization temperature (Figure I-25). Nevertheless, the crystallization time will increase, the $Ge_{36}Te_{64}$ has a transition time in the microseconds range whereas a stochiometric compound has a transition time in the nanoseconds timescale. On the other hand, compounds with high germanium concentration show lower resistivity contrast between amorphous and crystalline state and do not show improvement of the transition speed

compared to the Ge:Te -50:50 compound. Moreover, compounds with high germanium concentration do not show stable amorphization, after several cycles, the material remaining in the crystalline state due to Ge segregation. Thus, high Ge concentration alloys do not show sufficient reliability to be integrated in reconfigurable devices. Depending on the composition, a resistivity variation from 4 to 8 order of magnitude is observed (Figure I-25) [73].

The crystallization time has been measured in another study, as a function on the composition of the GeTe film [87]. 30-nm thick amorphous GeTe films grown on Si substrate and covered by a 30 nm Al_2O_3 were crystallized using 670 nm laser pulses. Raoux et al. measured a crystallization time from 30 ns for the $Ge_{0.5}Te_{0.5}$ compound to ≈200 µs for the $Ge_{0.28}Te_{0.72}$ compound. It confirms that compounds with high Te concentration have slower switching time (Figure I-26). It is also interesting to note that after one melt-quenched cycle, the crystallization time is shorter than an as deposit amorphous film.
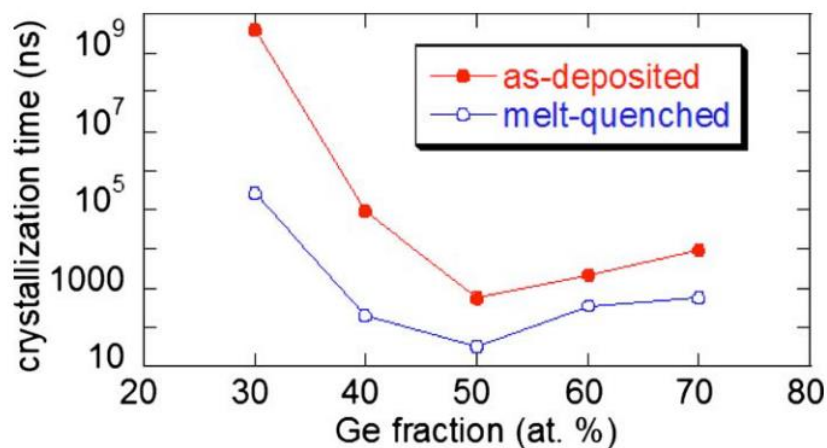
Figure I-26 : Crystallization time as a function of Ge fraction for a first crystallization after deposition (red curve) and after several switching cycles (blue curve) Ge–Te materials (30 nm)

If we compared GeTe and GST, the GeTe has a resistivity variation up to 7 orders of magnitude, higher than the GST (5 order of magnitude), and a crystallization temperature higher than the GST, which allows the GeTe to have a better stability in its amorphous state. Additionally, GeTe have a fast crystallization switching time, at the nanosecond timescale. [71, 88-90].

To bring back the film in the amorphous state, a high thermal energy is required to heat the material beyond its melting temperature and quench it afterwards. Thus, a high energy and short impulsion (from 10 ns to 100 ns) are required. During the cooling, the temperature must be dissipated very quickly, under its crystallization temperature in less than 1 µs (≈10^9 K/s) to quench the material in its amorphous phase [91]. To illustrate this phenomenon the time-temperature-transformation (TTT) diagram of a PCM is shown on Figure I-27 [92]. If the cooling is fast enough (orange curve), crystallization can be avoided (blue area) and we obtained an

amorphous film. On contrary, if the cooling is too slow, even if the maximum temperature is superior to the melting temperature, the temperature will go through the blue area of the diagram corresponding to the crystalline phase and the material will recrystallize and keep its metallic state.
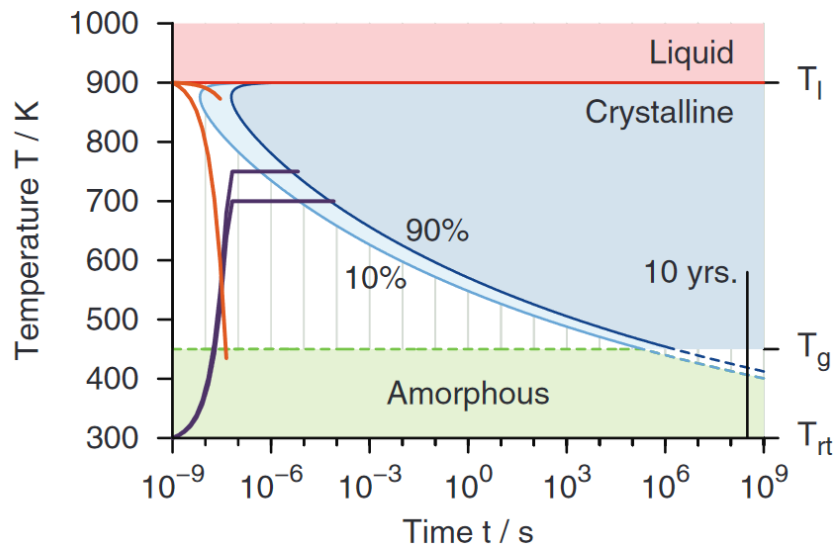
Figure I-27: Time-temperature-transformation (TTT) diagram for a PCM. The orange curve shows successful quenching process and the purple curve successful crystallization process [92].

As explained before crystallization and amorphization processes require either electrical or optical pulses. Regarding the electrical scheme, Figure I-28 presents an example of a switch integrating a 50 nm thick GeTe film activated with electrical pulses applied on a heating element (tungsten, W) placed under the film and separated from the film by a AlN barrier. [93]
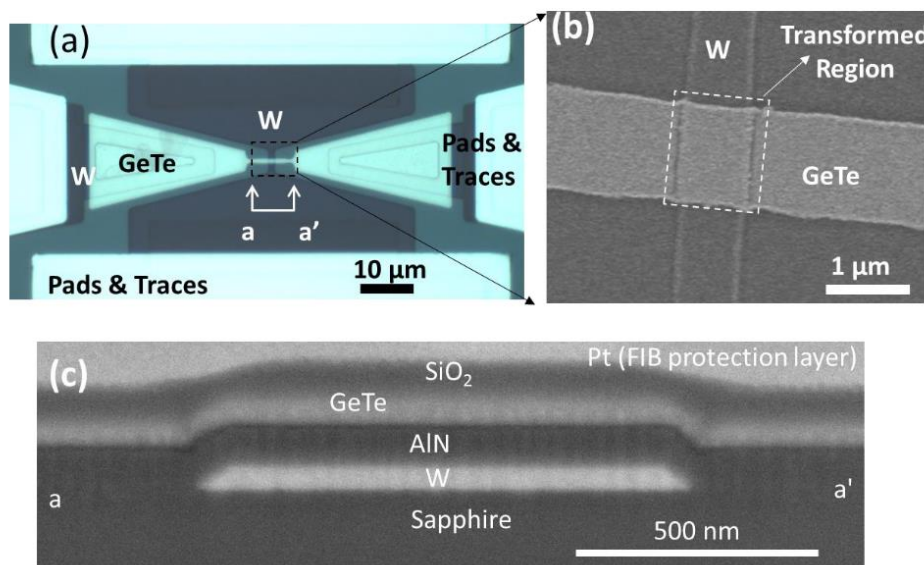
Figure I-28 : (a) microscopic image of a switch integrating GeTe and controlled by electrical pulses (b) zoomed image of the switch (c) cross section of the structure [93].

Initially the GeTe is crystalline. The different temperature transition times of the amorphization process were determined experimentally by measuring the different cooling times between 10 ns and 1µs (Figure I-29). The results show critical quenching time (CQT) of 317 ns for a successful amorphization. Above this CQT the GeTe film remains in crystalline phase.
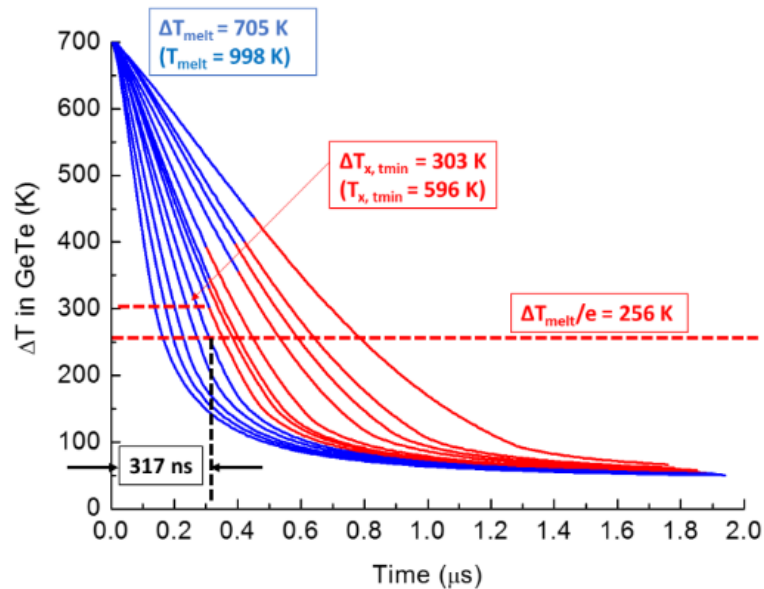
Figure I-29 : Temperature transients generated by pulses with different fall time. Blue represents successful amorphization (OFF state) and red crystallization of GeTe (ON state) [93].

To re-crystallize the GeTe voltage between 1.6 V and 2.3 V have been used to generate temperatures below the GeTe melting temperature. Crystallization times from 105 µs to 1.02 µs have been reported for a variation of the voltage from 1.6 V to 2.3 V, respectively (Figure I-30).
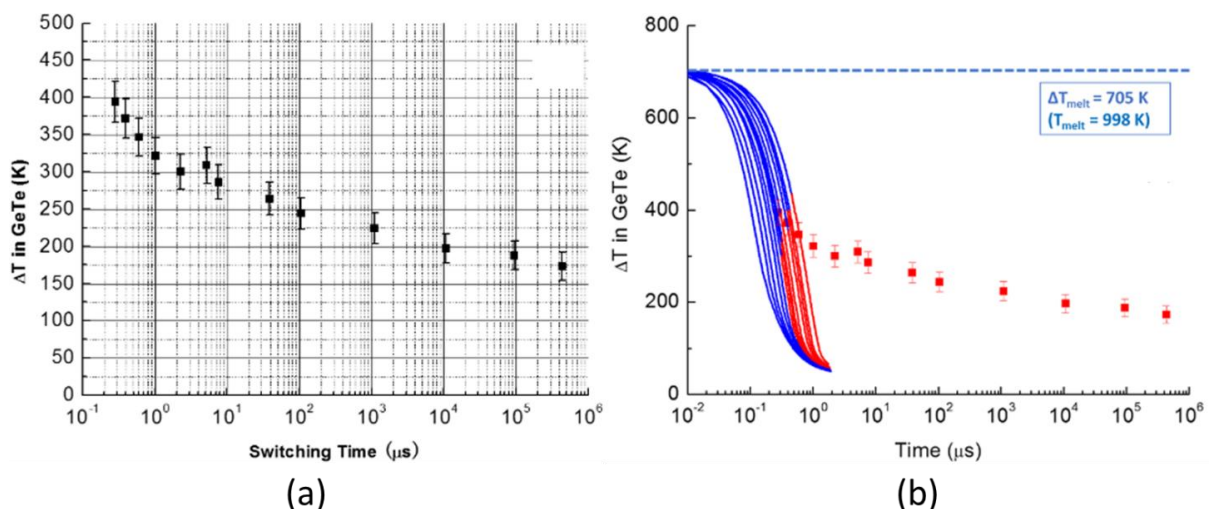
Figure I-30 : (a) GeTe TTT diagram determined from the crystallization measurements (b) Temperature transients generated by pulses with different fall time combined TTT diagram. Blue represents OFF-state and red represents ON-state [93].The second activation scheme is optical activation. To achieve correct crystallization or amorphization of GeTe film, the wavelength, the pulse duration, the pulse energy and the laser beam shape are critical parameters [94].

In Figure I-31 the reflectivity of a GeTe film during specific optical activation cycles is compared, when using laser pulses with durations of 8 ns (Figure I-31 a) and 120 fs (Figure I-31 b), at 800 nm, with similar fluences (≈74 mJ/cm^2 for amorphization and ≈25 mJ/cm^2 for crystallization) [71]. The film is initially crystalline, a single pulse (74 mJ/cm^2) is used to amorphized the GeTe film (SP1). In a second step, the film is crystallized using multiple pulses with a fluence of 25 mJ/cm^2 (MP1). Then the process is repeated, a single pulse (SP2) is applied to amorphize the GeTe following by multiple pulses (MP2) to crystallize the film.
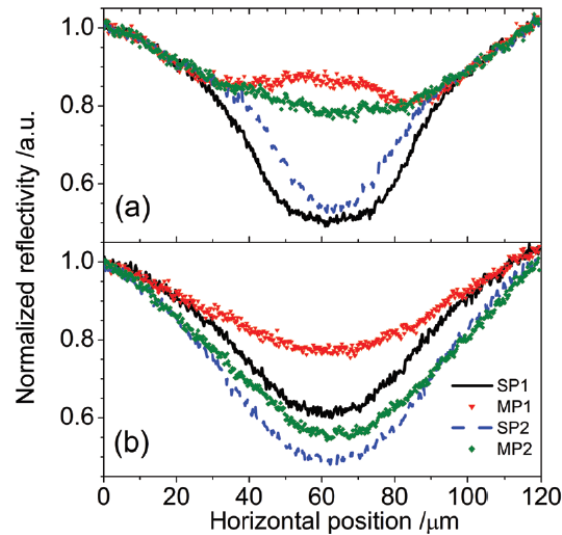
Figure I-31: Spatial reflectivity profiles of 20 nm GeTe films at 532 nm irradiated with (a) ns and (b) fs laser pulses. SP1 and SP2 correspond to a single pulse exposition and MP1 and MP2 correspond to multi-pulses exposition. The reflectivity difference between the laser-induced amorphous phase (SP1) and the recrystallized (MP1) state defines the optical contrast [71].

As observed, the reflectivity difference between laser-induced amorphous and crystalline phases upon fs irradiation gradually decreases. On the other side, with ns pulses the optical contrast is maintained. Femtosecond pulses seem to have a too fast heating/cooling rate in contrary to ns pulses which present considerably better switching capabilities. It can be expected that complete crystallization with a single laser pulse is achievable only with pulses >30 ns [87]. To achieve crystallization with shorter pulses an optimization of the overall heat flow is required. One method consists of using several pulses instead of one pulse which leads to increase of the heat load on the surface and increase the cooling time above the CQT to ensure proper crystallization.

The crystallization phenomenon of an initially amorphous PCM film is the result of the combination of two different processes, the nucleation process and the interface grow process. Depending on the composition of the film, the crystallization process can be different, one mechanism can dominate the other one. However, both mechanisms are always simultaneous present. If we take the example Figure I-32, a crystalline (blue area) film which has been

partially amorphized by a laser pulse (yellow area) is subsequently recrystallize by the same laser beam.
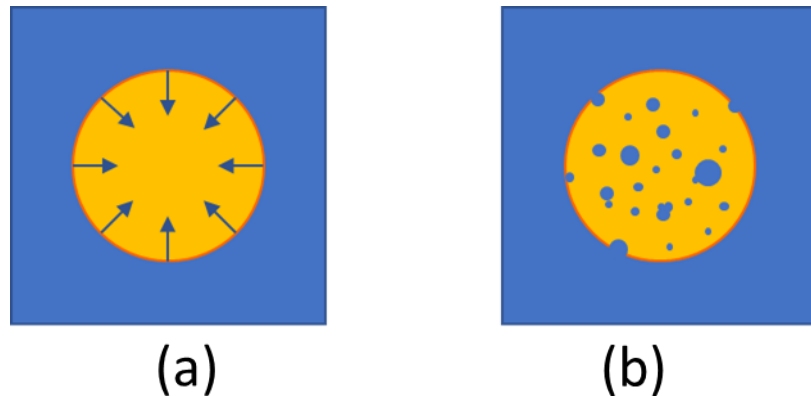
Figure I-32 : Schematic of crystallization process on a PCM surface. (a) interface grown process of the crystalline phase (blue toward the amorphous phase (yellow). (b) nucleation crystallization process from the inside of the amorphous spot.

In an interface grown process (Figure I-32a), the growth of the crystalline phase will start from the interface between the amorphous and the crystalline phase and grow toward the center of the amorphous spot. Whereas, if the crystallization starts from the center or different other areas in the amorphous phase under laser exposure, the process is called a nucleation process. It corresponds to the formation of crystalline nuclei in an amorphous matrix. On Figure I-33, we can observe the gradual crystallization process of a GeTe film with the increase of pulse number (fluence of 28 mJ/cm^2, with pulse duration of 8 ns at 800 nm) [71]. The film initially crystalline was beforehand partially amorphized using an optical pulse (78 mJ/cm^2, with pulse duration of 8 ns at 800 nm). After the application of 5 pulses, the recrystallization of the amorphous spot seems to be initiated from the crystalline amorphous interface toward the center of the spot which seems to indicate an interface controlled process (Figure I-33 b). However, for the application on the spot of additional pulses (Figure I-33 c-d) we can't see any progress of the interface-controlled process, instead the central area appears brighter than the initial state. It suggests that if the crystallization process is started by an interface-controlled process, after this the nucleation-controlled process is predominant. Even if the central area is completely crystallized, darker areas can be observed on the edge of the crystallized area. This can be due to the Gaussian profile of the laser beam for which most of the energy is concentrated in the center of the spot.
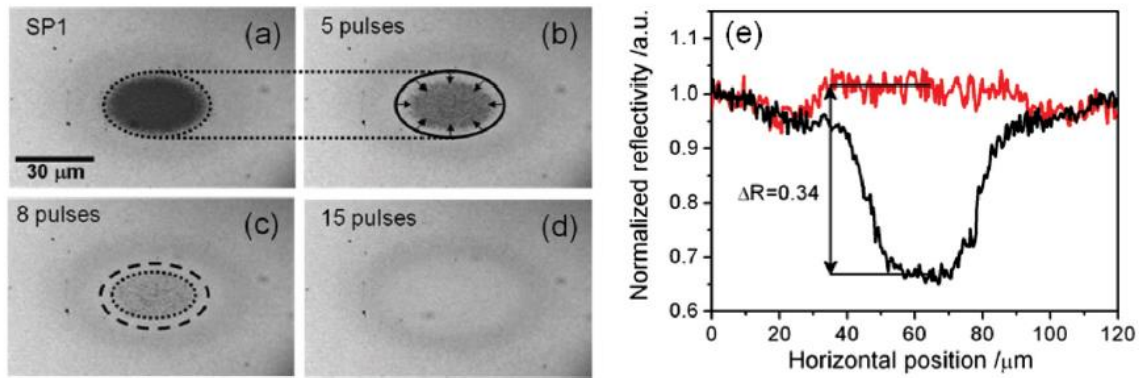
Figure I-33: Images of a 30 nm GeTe film expose to nanosecond pulses. (a) amorphous spot induced by a single high-fluence pulse at the center part of the laser focus. Subsequent low-fluence irradiation (28 mJ/cm²) with a total of (b) 5, (c) 8, and (d) 15 pulses shows the recrystallization process of the melt-quenched amorphous spot. (e) Spatial reflectivity profiles corresponding to the images shown in (a) and (d) [71].

The form of the laser beam is critical for the activation of the material because the phase change mainly depends on the temperature. To avoid incomplete crystallization on the edge of the laser beam due to the lack of energy, we can use a flat top laser beam which has an uniform power distribution [89]. On Figure I-34 the simulated temperature distribution in a GeTe film after a 20 ns single UV laser pulse with a fluence of 14 mJ/cm² and a flat-top intensity distribution is presented. We can see an uniform temperature distribution for a thickness of 60 nm.
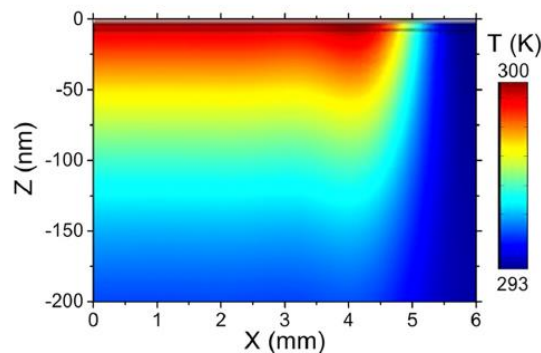
Figure I-34 : Simulation of 2D temperature distribution of a 60 nm GeTe film on Si substrate with a single laser pulse irradiation with a fluence of 14 mJ/cm² for 20 ns. z is the depth, x is the distance from the laser spot center [89].

Using nanosecond laser pulse (20 ns) at the wavelength of 248 nm Sun *et al.* studied the influence of the laser power for the crystallization and the amorphization processes of GeTe films [89]. For the crystallization, they realized exposures with a laser pulse number of 20 pulses with a fluence from 4 mJ/cm² to 160 mJ/cm². As it is presented on Figure I-35 a, we can observe an abrupt increase of the reflectivity for a fluence of 14 mJ/cm². After this value, the reflectivity increases only slowly when the fluence increases until a maximum value, where damages and ablation marks appear on the film surface. From these results we can conclude

that the threshold for crystallization of films irradiated with 20 pulses lies between 11 and 14 mJ/cm^2. This result is confirmed by the evolution of XRD patterns of the irradiated film (Figure I-35 b). The diffraction pattern of the as-deposited film shows only a broad bump located around 28°, characteristic of the amorphous phase. For fluence >11 mJ/cm^2, crystalline diffraction peaks appear at 26.1°, 30°, 42.3° and 43.6°. These peaks correspond to the lattice plane of the rhombohedral phase of the crystalline GeTe and their amplitudes slightly increase when continuously increasing the laser irradiation fluence from 14 to 36 mJ/cm^2.
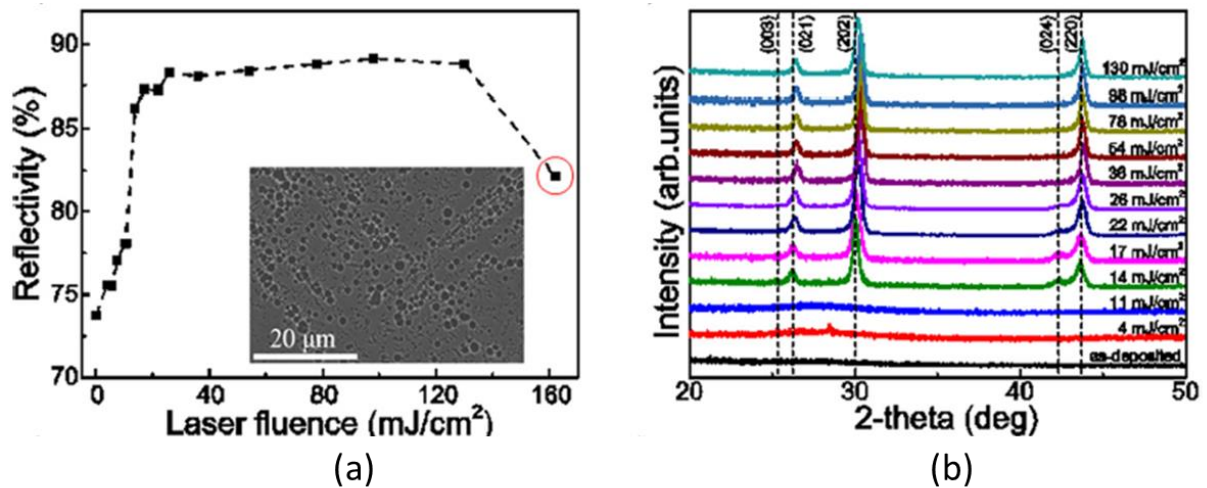
Figure I-35: (a) Optical reflectivity of GeTe-films at the wavelength of 650 nm after irradiation with 20 pulses depending on the laser fluence comprises between 4 and 162 mJ/cm^2. (b) Corresponding XRD patterns of GeTe-films after irradiation. The Miller indices correspond to the rhombohedral crystal structure of GeTe with the space group R3m [89].

In their study, Sun *et al.* used a single nanosecond laser pulse (20 ns) at the wavelength of 248 nm and at different laser fluences, up to 195 mJ/cm^2 [89]. As observed on Figure I-36, an increase of the laser fluence up to 160 mJ/cm^2 induce a gradual decrease of the reflectivity corresponding to formations of amorphous regions. For further increase of the fluence to 182 mJ/cm^2, a drastic decrease of the reflectivity can be observed. For higher fluences, significant ablation marks are visible (Figure I-36a). These results are confirmed by the XRD measurements where it can be observed a decrease of the crystalline diffraction peaks with the increase of the laser fluence.
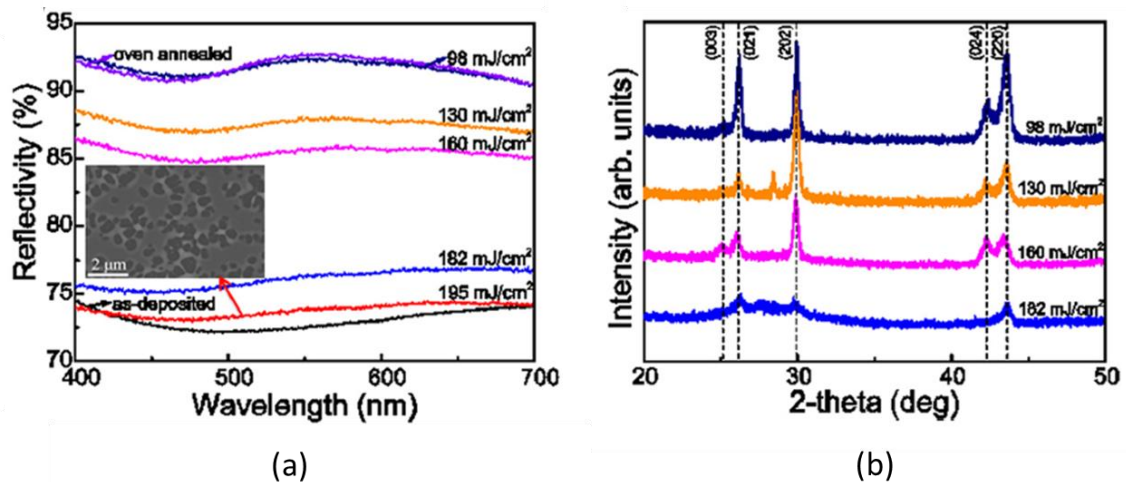
Figure I-36 : (a) Optical reflectivity of GeTe-films depending on the wavelength for different irradiation fluences of a single 20 ns pulse. (b) Corresponding XRD patterns of the GeTe films [89].

Unlike electrical based control [69, 74, 95, 96], fast optical activation of phase change materials using a laser pulses on nanoseconds or a femtosecond timescales allows an accurate thermal control during crystallization and amorphization mechanisms of the materials [72, 97, 98]. Additionally, using correct lenses or scanning system, optical activation allows large scale activation, and does not require additional metallic electrodes to control the specific states of the PCM, which may affect the overall response of the device. For these reasons, during my PhD, we focus our work on optical activation.

I.3.4. PCMs deposition

The properties of phase change materials are highly dependent on the deposition conditions. Depending on parameters during the deposition such as the pressure, the temperature, the target composition and the method used, the properties change and the temperature transition of the PCM will be different. Several deposition techniques have been reported to obtain PCM thin films such as magnetron sputtering,[96, 99, 100] enhanced atomic layer deposition [101] and pulsed laser deposition (PLD).[89, 102] In this part we will present several deposition examples of these different techniques.

1. Magnetron sputtering deposition

A DC sputtering system is composed of a vacuum chamber, a power supply, a sputter target and a substrate holder (Figure I-37). The vacuum chamber is pumped to a vacuum and then a sputter neutral gas (generally argon) is introduced in the chamber. By applying an electric field between the sputter target and the substrate holder, the ionized Ar atoms are accelerated towards a stochiometric target surface. The Ar ions hit the surface of the target and induce collision cascades at the target surface which provoke the ejection of target atoms.

Within this configuration the target atoms have no preferred sputtering direction and will cover all the surrounding surfaces including the substrate.

To be efficient, a sputtering process needs a sufficient number of argon ions, which are delivered by a plasma created by a steady state electric glow discharge inside the chamber. When an argon ion hits the target, electrons are additionally ejected from the target. These electrons accelerated away from the target surface by the electric field will ionize the argon atoms even more. When the argon ions bombard the target a part of the energy is converted to thermal energy and heat the target. To avoid the melting of the sputtering target a water-cooling system is placed beneath the target.
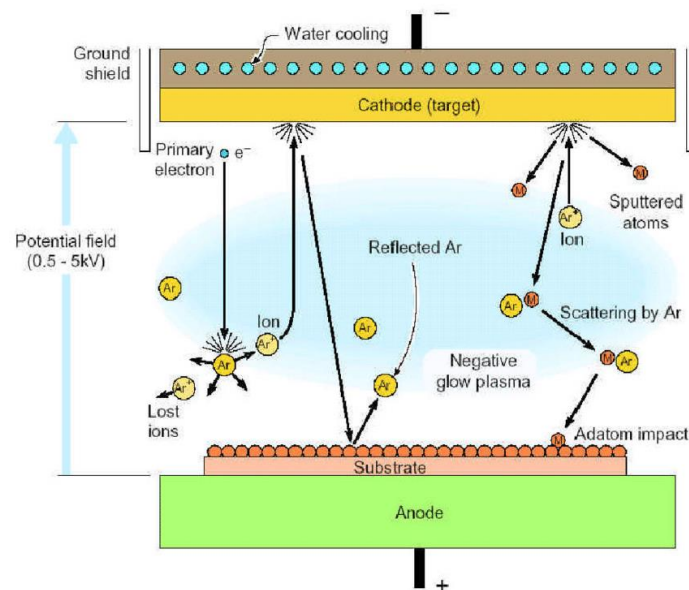
Figure I-37: Schematic of a DC sputtering system [103].

To enhance the deposition rate, it is possible to put magnets behind the negative cathode to trap electrons over the negatively charged target material so they are not free to bombard the substrate. This technique is called DC magnetron sputtering. Magnetron sputtering is widely used in industrial process because of the simplicity of the process and because it allows the deposition of thin film over a large area with good adherence. The grow rate of this technique is <1 nm/s [104]. Additional, it is possible to obtain films with the thicknesses within a large range, varying from a few nanometers to several micrometers.

2. Pulsed laser deposition

Pulsed laser deposition (PLD) or laser ablation, consists of a laser beam (generally a high-energy excimer laser operating in the UV -193 nm for the ArF or 248 nm for the KrF lasers) on a target placed in front of a heated substrate in a closed enclosure of controlled atmosphere. The interaction between the high energy laser pulse and the target leads to the evaporation of

the target material in the form of a plasma plume. The evaporated material is then deposited on a substrate placed in front of the target.

The schematic of a typical PLD system is presented on Figure I-38, the laser beam is sent toward the target through a quartz glass using a mirror system. The target holder is fixed on a rotation axis to renew the target surface between each laser pulse and avoid its prolonged erosion under the laser beam.
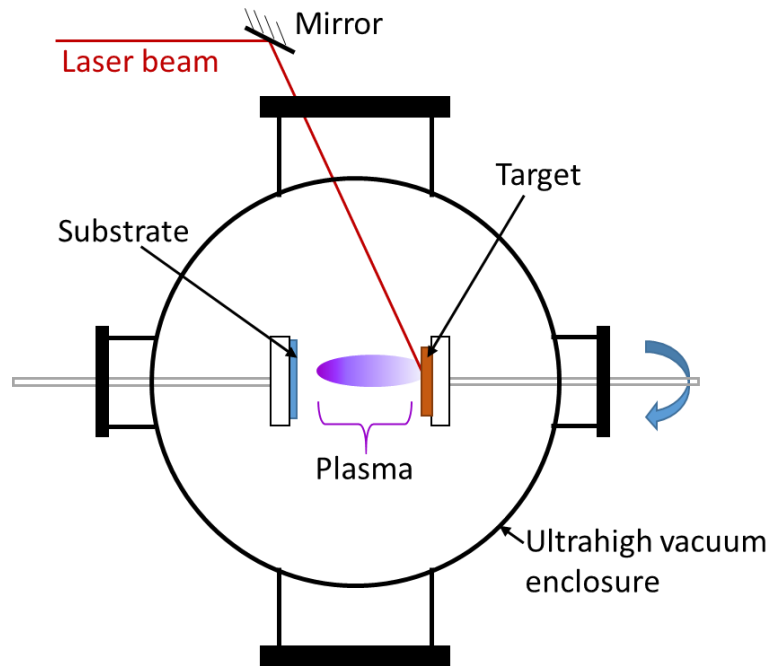
Figure I-38 : Schematic of a pulse laser deposition system for thin films deposition.

As in the case of magnetron sputtering, this method allows stochiometric transfer of target material.[105] With PLD it is possible to realize mono-oriented crystal deposition with growth rates of 10-24 nm/s [106]. However with this technique, it is difficult to obtain films with constant thickness and structural properties over a large area due to the small size of the plasma plume, the uniform surface of the films being usually limited to 1 cm^2.[105]

3. Enhanced atomic layer deposition (ALD)

Enhanced ALD method is a chemical vapor deposition method. Reactants are used to obtain the final compound. To grow a thin film the different gaseous species containing the atoms of the layer to be obtained are introduced in a vacuum chamber in a series of sequential, non-overlapping successive periods. First a precursor is introduced in the chamber in the gaseous phase and reacts with the heating substrate to form a solid monolayer. Secondly, the excess of precursor is purged out of the chamber. In a third step, the reactive gas is introduced in the chamber. This gas is used to activate the deposited layer by creation of nucleation sites thanks to new terminated surface. Finally, the chamber is purged before another introduction

of precursors and the start of a new cycle. On Figure I-39 the succession of the different step forming a complete cycle is presented.
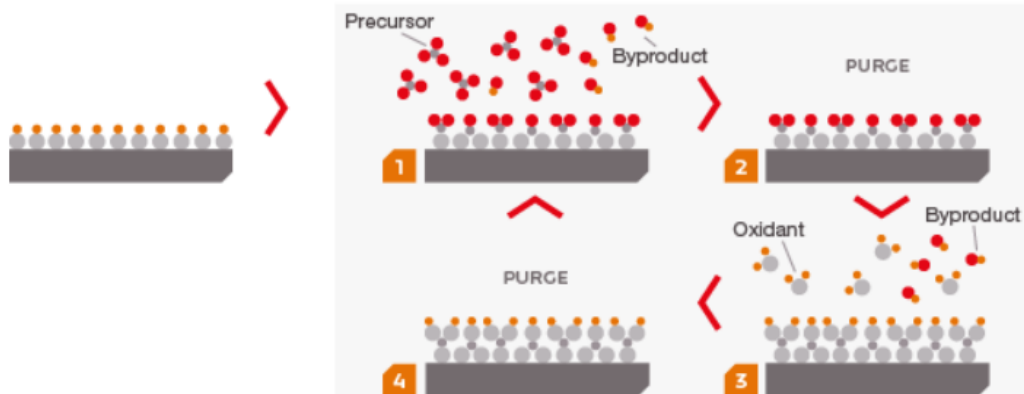
Figure I-39: Different steps of a typical atomic layer deposition cycle (source. asm.com).

Gwon *et al.* proposed to use the ALD method to realize GeTe films. They used $HGeCl_3$ and $\{(CH_3)_3Si\}_2Te$ as precursors for their deposition. This method offers good control of the film thickness (at the atomic level) and composition of the film and thus good reproducibility and very low impurity level [101]. This method also allows precise control for uniform and conformal film deposition [102, 107]. Uniform films have an equal composition and thickness at each position along a planar substrate. Conformal films have the same thickness even inside 3D features. However, it suffers from low deposition rate between 0.3 Å to 1.5 Å per cycle and a cycle lasts about 10 seconds to 1 minute [108].

4. Comparison of the different techniques

On

Table I-2, the different techniques of GeTe depositions are summarized.

Table I-3 : Comparison of different GeTe deposition techniques

	Magnetron sputtering [104]	PLD [105, 106]	ALD [101] [102, 107] [108]
Growth rate	0.65 - 1 nm/s	10-24 nm by pulse	0.3 Å to 1.5 Å/cycle
Thickness control	Precision at the nm	Difficult due to the high grow rate	Control at the atomic layer
Suitable for large deposition area	yes	No (limited to 1 cm^2)	yes

Thus, we can adopt one of the deposition techniques depending on the desired thickness, properties and structure. During my thesis we needed to test different PCM film with different precise thickness from 200 nm to 1 µm on substrate of 2.5 cmx2.5 cm, for these reasons we decide to use magnetron sputtering.

I.3.5. PCM applications

The high contrast between amorphous and crystalline phases of PCMs makes them highly desirable to realize many electronics functions based on non-volatile memory effect, over a large range of frequencies (DC, RF and optical).

1. Integration in rewritable optical memories

This type of technology is based on the variation of the optical reflectivity between amorphous and crystalline phases. CD-RW are multilayer devices (Figure I-40) where the PCM is sandwiched between two dielectric protective layers [109]. Using a laser pulse, it is possible to create amorphous regions in an initially crystalline PCM layer, regions which can be interpreted as a series of binary information (data) on the optical disc. Thus, two different areas on the disc are visible, some areas which are still in crystalline phase with high optical reflectivity, and other areas which have been exposed to the laser pulses which are amorphous with low reflectivity. This difference in reflectivity is used to code the information. The information on the CD-RW can then be erased using the reverse process of crystallization of the PCM layer. To read the data on the disc, a laser with low power is used to avoid state change and data modification on the PCM layer.
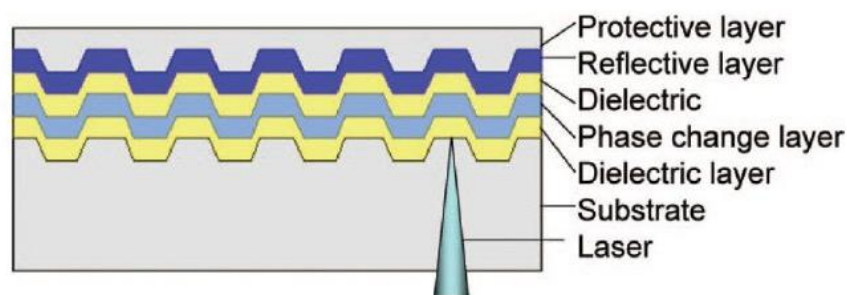
Figure I-40 : Schematic of a rewritable DVD structure based on a single PCMs layer

Over the years, optical activation with shorter wavelengths (from 750 nm to 405 nm) have been demonstrated to decrease the minimal beam size (and consequently increase the recording density) (Figure I-41) [110]. Germanium-antimony-telluride (GST) compounds are the most used materials for these applications because of their fast transition time [110].
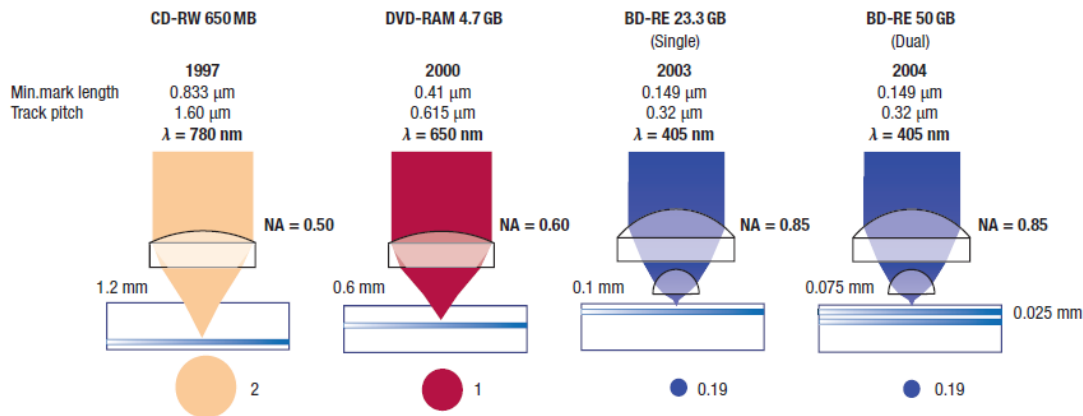
Figure I-41 : Comparison of the recording capacity for different rewritable CD-ROM technologies using different wavelengths [110].

Thus, optical activation of GST materials has been demonstrated with laser wavelengths from 405 nm to 780 nm.

The large development of phase change material for optical memories leads to the development of new technologies and notability random access memories.

2. Integration of PCMs in non-volatile random access memory (PCRAM)

PCRAM represents a promising new type of PCM-based memory technology having low costs, better lifetime and high contrast of resistivity than actual existing solutions around 3 orders of magnitude [111].PCRAM consists of a PCM layer deposited on a heater element and placed in between two electrodes (Figure I-42) [111]. To avoid thermal dissipation the heater is surrounded by insulator layers like SiO_2 or Si_3N_4. By applying an electrical pulse between the two electrodes, a current will go through the heater and the initially crystalline PCM film will undergo a phase change initiated by Joule effect. In this way, a specific memory state can be induced, by alternating the PCM region between a crystalline state, called SET state (state 1 with low resistivity) and an amorphous state, called RESET state (state 0 with high resistivity) [112].
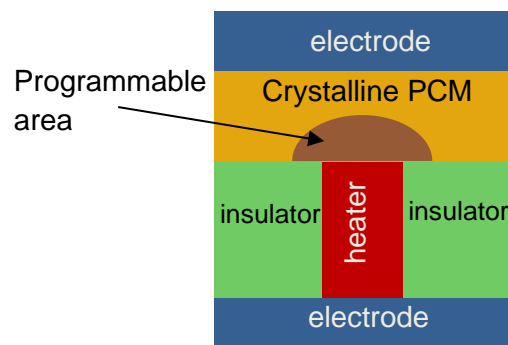
Figure I-42 : Conventional PCRAM design

As for the rewritable optical memories, ternary Ge-Sb-Te alloys are very good candidates for PC-RAM. $Ge_2Sb_2Te_5$ is the most used alloy in this group, it can achieve fast switching time (100 ns for the crystallization and 10 ns for the amorphization) with low voltage values (below 1.4 V), have data retention time over 10 years and a lifetime of at least 10^7 cycles [113, 114].

More recently, 3D PCM integration has been implemented with Intel's 3D XPoint (3D cross-point) memory technology. This type of memory can be used both as system memory (to replace a computer's RAM) and as non-volatile storage (to replace its SSD). These devices are up to 3 times faster (reading and writing) and more durable than NAND flash memory used in SSDs and have a higher storage capacity for the same volume, while remaining energy efficient. This technology uses the changes in the material resistance for storage in a volume, moving both in the x-y plane and in the z direction. The 3D XPoint structure is presented in Figure I-43. The structure is composed of conducting filaments, between each layer are vertical columns that contain "memory cells" (PCMs) and a "selector", which allows a specific memory cell to be read or rewritten. The access is controlled by varying the voltage receives via the filaments.
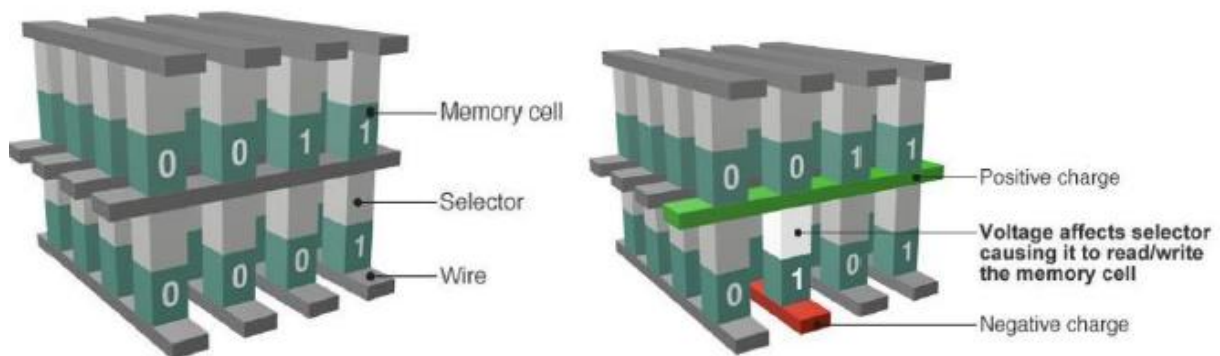
Figure I-43: Schematic diagram of the 3D XPoint memory (source. Intel)

Although PCMs have proven their reliability in data storage industrial technologies, they are not limited to these applications. In more prospective area, PCMs have been integrated as agile elements in reconfigurable devices for high-frequency electronics and optics.

3. Integration of PCMs in RF switches

The PCMs have been used to realize RF-switches since 2010 [115]. PCMs have been widely studied to realize bistable RF switches thanks to their high resistance variation between amorphous and crystalline phases (around 5 order of magnitude) and their low resistance value in the crystalline phase, which allows low insertion losses in ON state, below 0.3 dB. Additionally, the bistability of the phase change decreases the overall electrical consumption and open a new way for the realization of low consumption systems. Two different methods to control the phase change of RF switches based on PCMs have been developed.

The first one consists of an indirect heating control scheme, as indicated on Figure I-44 presenting the structure of a RF switch realized at Xlim [116]. The switch, integrated in a RF coplanar waveguide, is fabricated on a sapphire substrate, and is composed of a NiCr thin film resistor (TFR) separated by an AlN dielectric barrier from the GST patch. This barrier is used to electrically isolate the TFR from the RF circuit and to thermally couple the GST and the TFR. The RF switch is composed of a four terminal structure, two RF ports connected to the PCM patch and two orthogonal DC ports connected to the TFR. When an electric pulse is applied on the TFR, the generated heat is transmitted to the GST film through the dielectric layer. The material resistivity changes, allowing to modify (On/Off) the transmission of the RF signal propagating in the coplanar waveguide. In the ON state, the device presents insertion losses of about 1.4 dB from 100 MHz to 24 GHz with a R_{on} of 10 Ω. After transformation of the material to the amorphous state, the switch isolation is above 20 dB over the whole frequency band and its C_{off} capacitance is 30 fF.
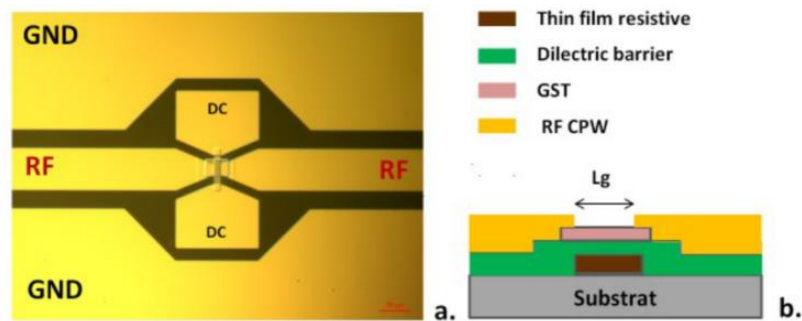
Figure I-44: Four terminal inline RF switch integrating a GST pattern of 3 µm separating the two segments of a coplanar RF transmission line : (a) Planar view of the device and (b) cross sectional view showing the stack of the structural layers [116].

The second solution consists in using a direct heating approach to heat the PCM. An example was proposed by Wang et al. [117]. Within this implementation, the heat created by Joule effect is directly transferred to the PCM layer which can change its state. This method decreases the necessary power to change the material phase. Figure I-45 shows the structure of the realized RF switch. As before, the structure is a four terminals structure with two RF ports and two DC ports. However, in this case the GeTe patch is connected horizontally to the RF electrodes and vertically to the DC electrodes (heating system). To change the phase of the PCM an electric pulse is applied on the DC ports, the OFF state is obtained by applying a current pulse with an amplitude of 5.5 mA, rise and fall time of 20 ns, and a pulse width of 0.5 µs and the ON state is obtained by applying heating current with an amplitude of 200 µA, rise time of 0.5 µs, duration of 200 µs, and a longer falling edge of 400 µs. In the ON state, insertion losses of less than 0.6 dB and a R_{on} of 5 Ω have been reported from 10 MHz to 20 GHz. In the OFF state, the switch isolation is around 20 dB over the whole frequency band and its C_{off} capacitance is 8.5 fF.
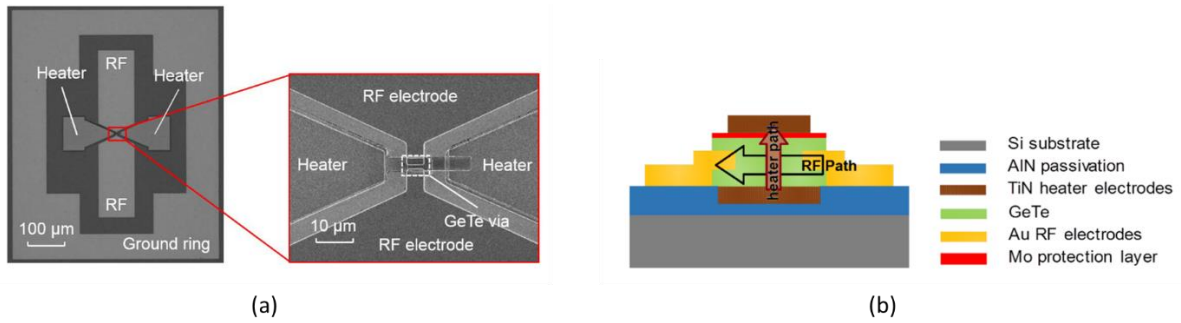
Figure I-45: (a) Top view SEM images of a fabricated phase change switch. (b) A cross-sectional view of the phase change switch

GeTe integration shows promising RF properties in terms of fast switching speed, isolation, linearity and much higher cut OFF frequency (define as $1/(R_{ON}xC_{OFF})$) than semiconductor switches over a wide frequency range, comparable to conventional MEMS switches.

4. PCM integration in optical devices

PCMs have also been used to realize reconfigurable devices in the optical domain. Gholipour *et al.* have demonstrated the possibility to realize an optical meta-switch in the infrared domain using GST (Figure I-46).[118]
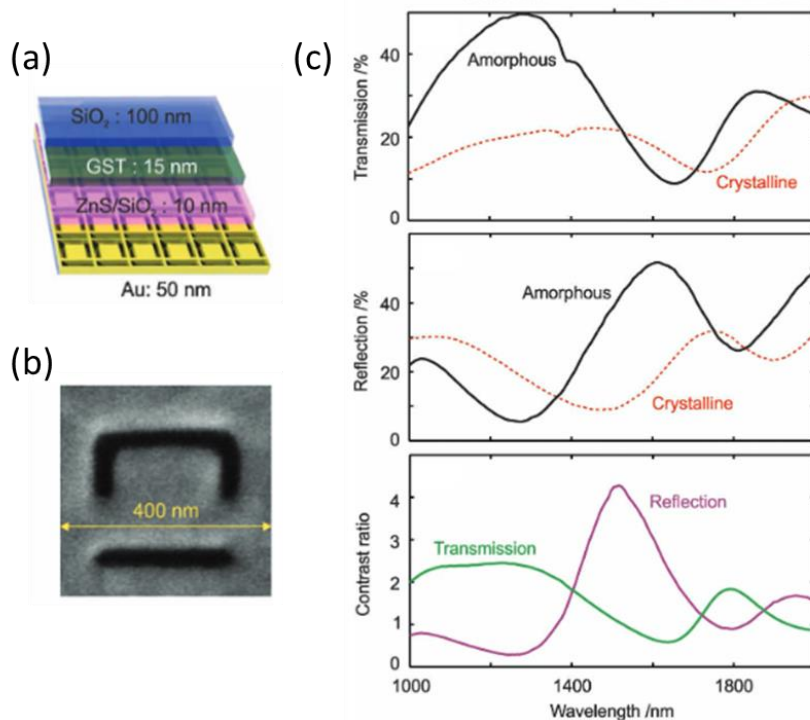
Figure I-46: (a) Structural details of a near-IR chalcogenide meta-switch layer thicknesses. (b) Scanning electron microscope image of a single 400 nm unit cell (c) optical transmission and reflection for the amorphous and crystalline phases of the GST layer of the meta-switch and corresponding contrast ratio associated with chalcogenide phase switching in the meta-device [118].

Using 660 nm laser pulses with duration of 50 ns, they demonstrate the possibility to achieve activation of GST film between amorphous and crystalline phases. By combining this GST film with a metasurface, they demonstrate the possibility to actively tune the metasurface response between an OFF state and an ON state. Between these two states, a large change of the transmission and reflection device can be observed with a contrast value approaching 4:1 whereas the meta-device thickness is only $\approx 1 / 27$ of the operating wavelength. (Figure I-46-c). More recently, Karvounis *et al.* demonstrated an all-dielectric optical device based on GST deposed on SIO_2 substrate in infrared domain [119]. The device consists of a GST grating. Using optically induced switching the authors demonstrate non-volatile modulation of the near infrared response of the device. The transition from amorphous to crystalline phase of GST provide a contrast ratio of 7 dB in reflection mode and 5 dB in transmission.

The group of Zheludev also demonstrated multifunctional and optically reconfigurable photonics devices based on phase change materials [120]. The proposed device consists of a GST film place between two protective layers of ZN-SIO_2 deposed on a glass substrate (Figure I-47). To inscribe metallic phase (device) in the initially amorphous film, they used a femtosecond laser pulse train (1 pulse lasts 85 fs). After inscription of the structure, the response of the device can be read and recorded with a camera coupled to a diode at 633 nm using a lens with NA = 0.7.
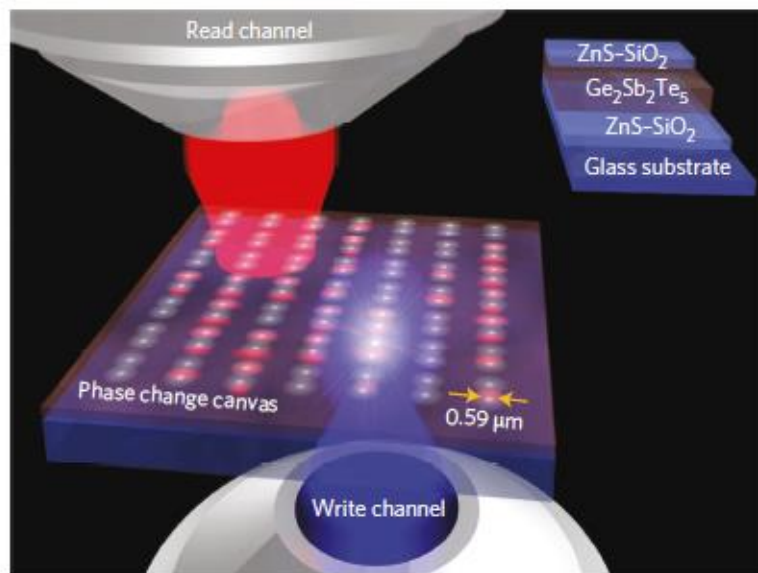
Figure I-47: Principle of writing of reconfigurable photonic devices in a phase-change material film [120].

Using this system, the authors demonstrated planar wavelength multiplexing focusing devices (Figure I-48).
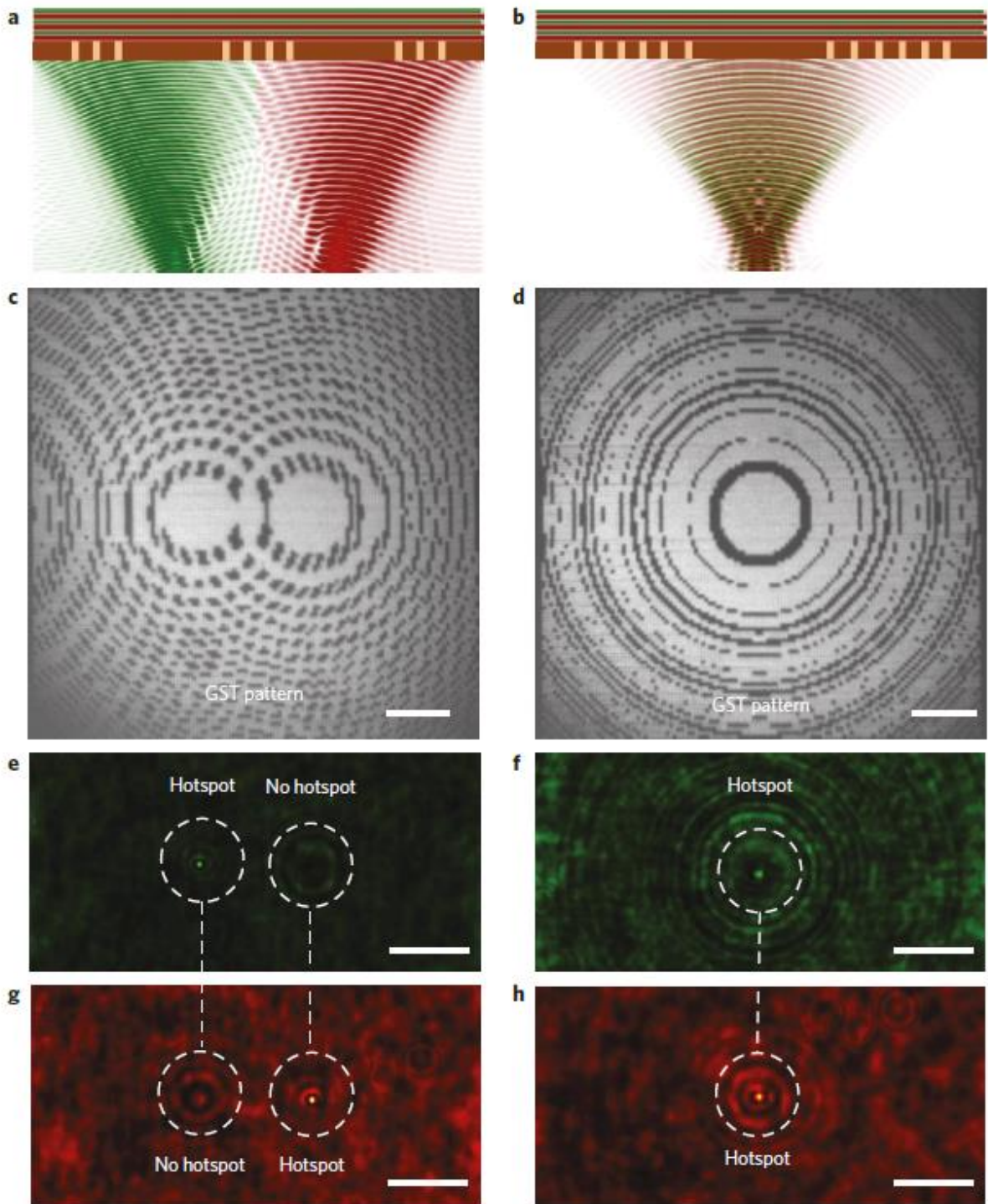
Figure I-48 : (a) GST Lens focusing two different wavelengths to spatially separated foci on the focal plane (deliberate transverse chromatic aberration)(b) Lens focusing two different optical wavelengths in the same focus (corrected chromatic aberration) (c-d), Optical images of the lens patterns in a GST film with deliberate transverse chromatic aberration (c) and corrected chromatic aberration (d).(e-f) Focal spots of lenses c and d at λ = 730 nm. (g-h) Focal spots of the same lenses at λ = 900 nm [120].

In the first lens, deliberate transverse chromatic aberration is created. Consequently, light with different wavelengths is focused in distinctly different focal spots (Figure I-48a), this type of lens can be used in signal multiplexing applications. The second lens presents correct

focusing which focuses the two different wavelengths on the same spot (Figure I-48b), this can be used for imaging application as an example.

In a second demonstration this study demonstrated the possibility to subsequently erase a previously write device to inscribe a new device on the film (Figure I-49). In this study, first a double Fresnel zone-plate pattern was written using 0.39 nJ pulses, which generate two different foci under optical illumination. In a second step, the partial erase (pixel by pixel with single pulse of 1.25 nJ) of the device is demonstrated by re-amorphization of the GST substrate to obtain a single Fresnel zone plate. Finally, the authors demonstrated that the first device can be restored by writing it again.
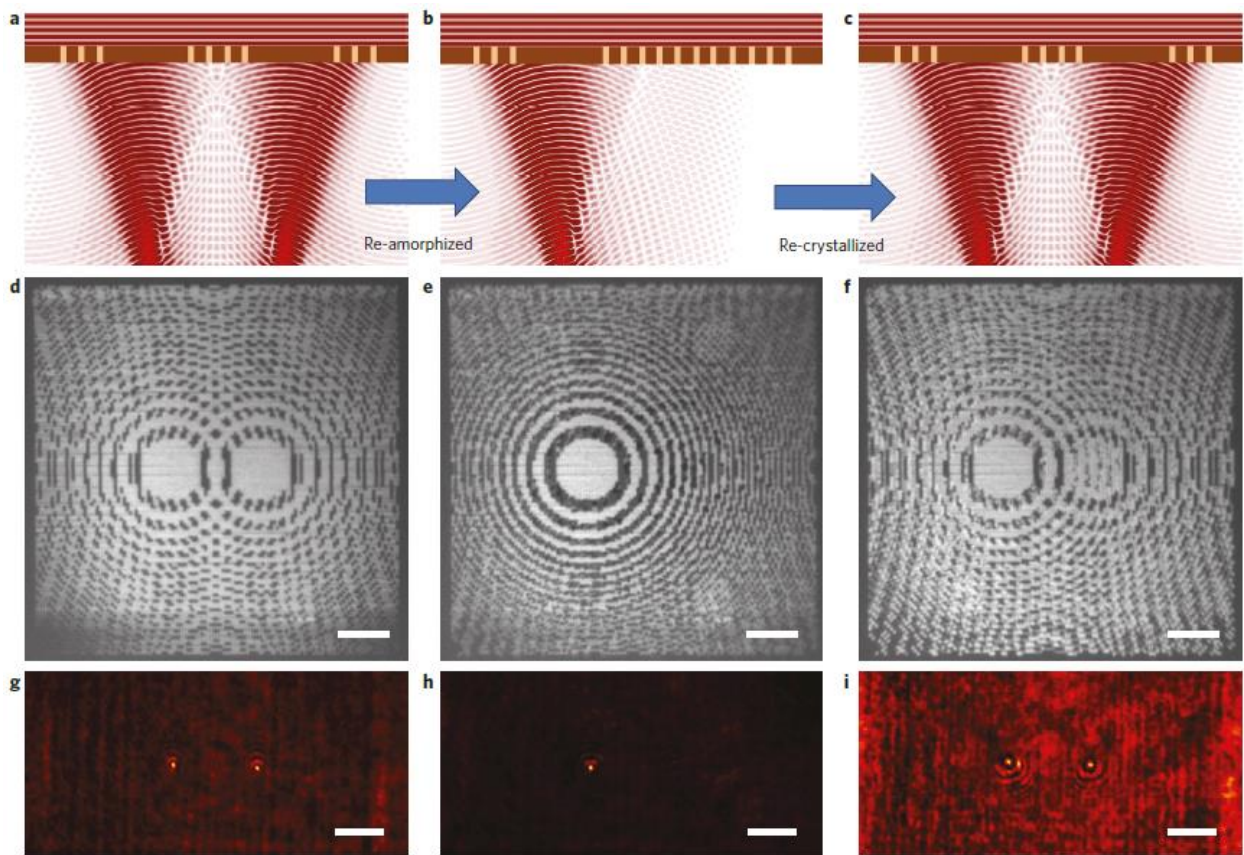
Figure I-49: (a) Two superimposed Fresnel zone patterns focusing a plane wave into two different foci. (b-c), One of the Fresnel zone patterns is erased (b) and then restored again (c). (d) Superimposed Fresnel zone patterns imaged at λ = 633 nm as they were first written. (e) The second Fresnel zone pattern is erased. (f), both patterns are restored. (g–i) Transmission focal spots as generated by patterns (d–f) [120].

In a final device, they finally demonstrate an all-dielectric metasurface which can actively modulate the transmission of the incident waves from 1,500 nm to 2,500 nm.

Through this study the group of Zheludev demonstrated the possibility to use PCM as a versatile platform for the realization of reconfigurable optical devices controlled by laser activation. This technology opens a new way for the realization of optical multifunctional

devices such as dynamic diffraction gratings for spectroscopy and wavelength division multiplexing; switchable frequency-selective surfaces, reflectors, light diffusers and scatters; non-volatile reconfigurable spatial light modulators and signal distributers both for on-chip applications and space division multiplexing in optical telecommunication networks.

Through these different applications, PCMs have attracted lots of interest and have demonstrated their high capabilities to actively control electromagnetic waves at the nanosecond time scale over a large range of frequencies (from electrical to optical domain) and for many different applications.

The main advantage of PCM (notably GeTe and GST) are numerous and summarized here:

- They are **bistable** material: they can retain their metallic or insulator state without external polarization bias (non-volatile memory effect), leading to low global energy consumption.

- Abrupt modification of their resistivity (5-6 order of magnitude) and very **broadband** (microwave, optical and millimetric waves)

- **Long-term stability** of their different phase they are placed (>10 years)

- **Fast** optical and/or electrical **switching time** at the nanosecond timescale and even ps second time scale for the optical activation

- RF **factors of merit** for simple microwave switches **superior to current solutions** based on semiconductors.

- **Ease of integration** (thin-film fabrication at room temperature or below 200°C or compatible with CMOS integration, on a wide variety of substrates)

These properties are a real technological breakthrough in the field of microwaves and THz, and open the way to numerous applications in the fields we are targeting.

I.3.6. PCM for terahertz applications

If the potential of PCMs has been extensively developed for electrical and optical applications, their employment is largely underexploited in the terahertz domain. Over last years, only few reports were related to THz properties of chalcogenide phase change materials or to their integration in THz devices.

The terahertz properties of PCM films have been investigated. Gwin *et al* have characterized a 100 nm GeTe film (Figure I-50) [121]. They have investigated the transmittance

modulation of GeTe films, defined as $M = \frac{T_a - T_c}{T_a}$ with T_a the transmission of the GeTe in amorphous phase and T_c the transmission of the GeTe in crystalline phase. They found values around 0.91 over a large range of frequencies between the two dissimilar states. They also demonstrated the possibility to actively modulate the response of the crystalline GeTe film. By modifying the temperature of a previously crystallized GeTe film it is possible to further decrease the crystalline GeTe transmission (and thus increase the transmittance modulation). When the crystalline GeTe temperature increases from room temperature to 250 °C the transmittance modulation goes from ≈0.9 to ≈0.95 at 2.4 THz (red curve in Figure I-50).
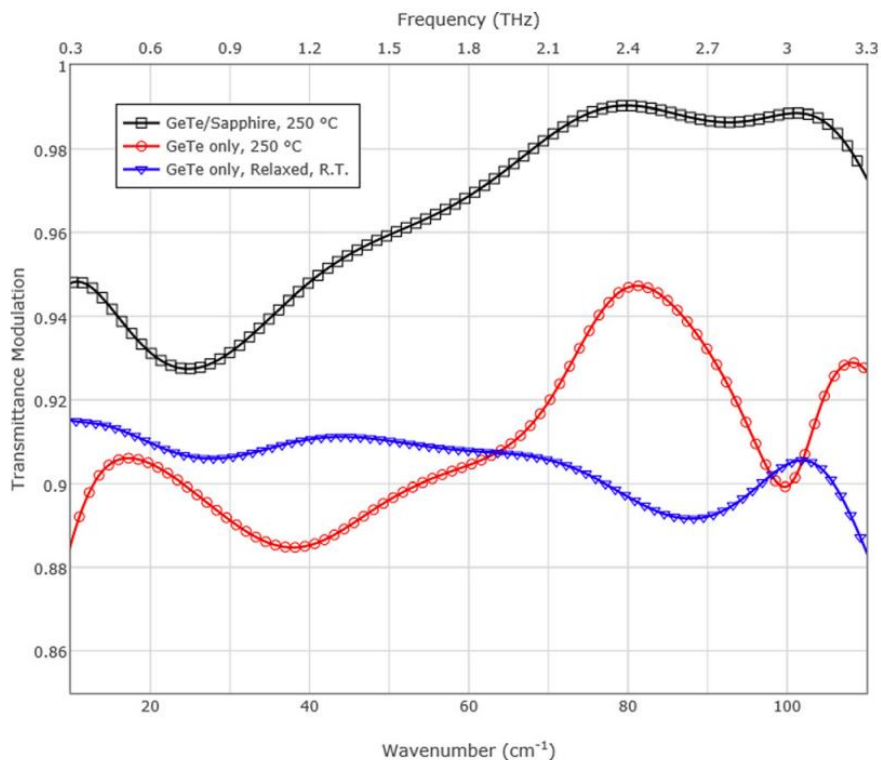
Figure I-50: Terahertz transmittance modulation of GeTe/ Sapphire and GeTe at 250 °C and GeTe at room temperature after cooling [121].

The performances of a 100-nm thick GST film follow the same behavior (Figure I-51) [122]. When the GST film goes from amorphous to crystalline phase, the transmittance decreases from 0.98 to 0.30 at 1 THz, which corresponds to a transmittance modulation around 0.69.
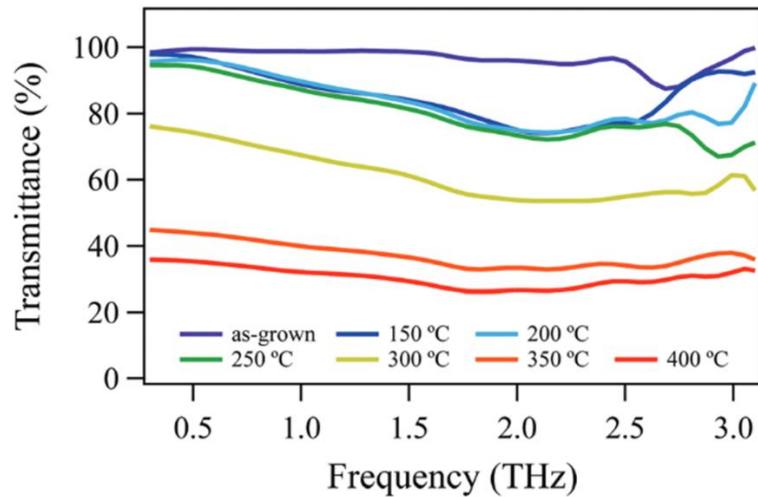
Figure I-51: THz transmittance of GST for various annealing temperatures [122].

Thus, PCMs can achieve strong modulations of terahertz waves and seems to be promising for the realization of reconfigurable terahertz devices. As expected from previous results in the other frequency domains, GeTe films have better THz transmission modulation than GST layers.

The first report on THz devices integrating phase change materials was reported for a metamaterial whose unit cell is a split ring resonator (SRR) [123]. Kodama et al. proposed two different designs, one design consisting of a SRR structure made only in GeTe and a second design consisting of a gold SRR integrating a GeTe patch in their gap (Figure I-52). In this study, direct thermal heating was used to crystallize the GeTe integrated in the metamaterial structure and investigate the modulation of the THz transmission during the heating process. For the SRR structures made only on GeTe, no resonance features specific to the SRR is observed, probably due to the losses of the realized GeTe film, except of a decrease of the transmission by ≈35% (Figure I-52.b). Nevertheless, with the second design based on a hybrid integration of metallic SRRs and GeTe material, they successfully demonstrated the possibility to modulate the resonance mode of the hybrid structure (Figure I-52.e). When the GeTe is amorphous it is transparent to the THz and the LC resonance characteristic to the SRR structure occurs at 0.8 THz. When the GeTe goes from amorphous to crystalline state, it forms a conducting path in the gap of the SRR which becomes a simple ring resonator and consequently the LC resonance disappears. The terahertz transmission after the crystallization of GeTe maintain their features during cooling, which confirms the nonvolatile phase change. The paper reports a modulation depth of 66% at 0.8 THz. However, even if the authors successfully demonstrated the possibility to realize bistable modification of the terahertz response, the reverse reconfiguration of the devices (when GeTe change from the crystalline to the amorphous state) was not completed.
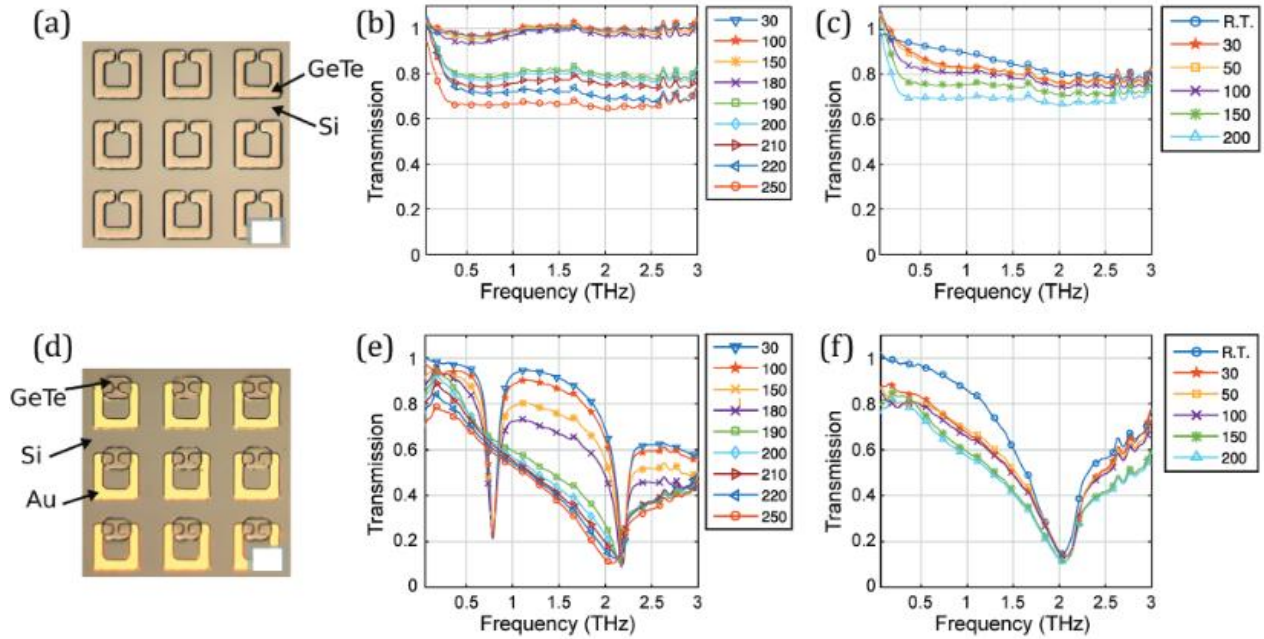
Figure I-52. (a) Array of all GeTe SRRs deposed on an intrinsic SI substrate (b) terahertz transmission of the GeTe SRRs evolution with the increase of the annealing temperature following by (c) the decrease of the temperatures. (d) Gold SRRs integrating GeTe patterns in their gap. (e) Terahertz transmission of the gold SRRs integrating GeTe patterns with the increase of the annealing temperature following by (f) the decrease of the temperatures [123].

More recently, Yasuyuki Sanari et al. [124] demonstrate the possibility to crystallize amorphous GST using ultrashort terahertz pulses (at the picosecond timescale) by combining it with plasmonic gold antennas (Figure I-53.a). They used an array of plasmonic gold antennas to enhance the THz electric field in the gap to few MV cm^{-1} to reach the crystallization threshold of the GeTe material. The high-energy terahertz field induce Zener tunneling in the gap of the antennas which leads to the expansion of the crystalline state in the direction of the electric field. The optical microscope pictures show the expansion of the crystalline phase depending on the number of terahertz pulses (Figure I-53.d-g). With this method the authors demonstrated the possibility to precisely control the crystallization process of GST to obtain very localized crystalline areas at the nanometer scale. However, with this structure no reconfigurability of the structure is presented.
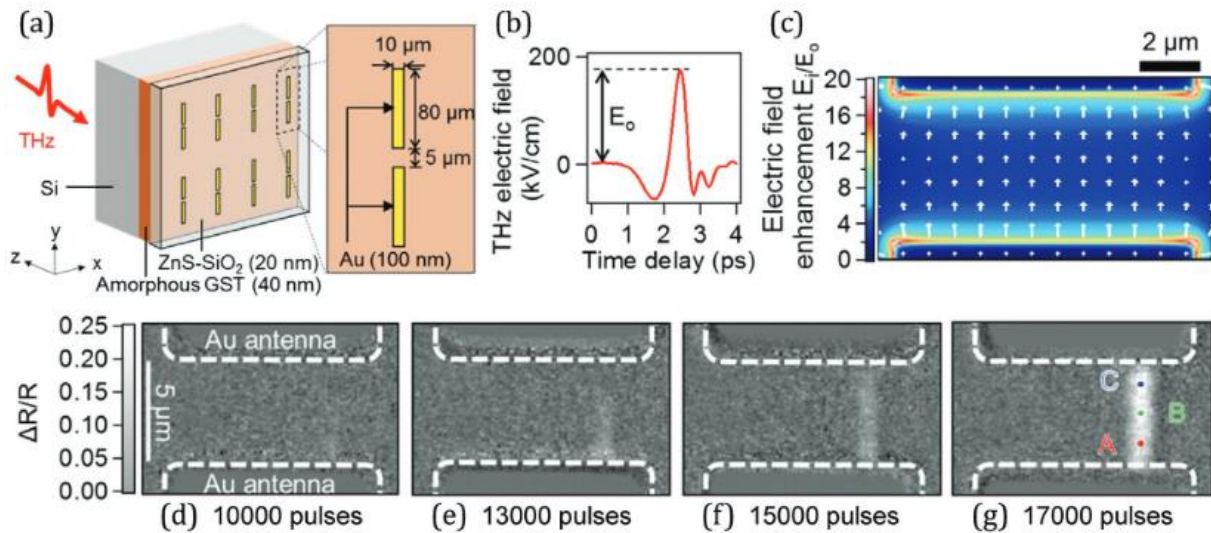
Figure I-53: (a) Schematic of the devices. (b) measured temporal profile of the terahertz pulse. (c) electric field enhancement. The white arrows indicate the electric field direction. (d-g) Microscopic images of an antenna gap for different number of terahertz pulses [124].

In a very recent report, Pitchappa *et al.* [125] demonstrate the possibility to tune the Fano resonance of aluminium-based asymmetric SRRs fabricated on a GST film (Figure I-54.a and b) . The frequency of the Fano resonance of the structure can then be shifted at different values in a non-volatile way, depending on the temperature and the heating time of the device (Figure I-54.b,c). Using a similar design and integrating control electrodes, the authors demonstrated the possibility to electrically crystallize the GST in the gap of the SRRs and realize a multicolor spatial light modulator (SLM) device for terahertz waves. (Figure I-54.d, e) They successfully demonstrated the possibility to tune the terahertz response of their devices using PCMs with a time transition of the device at the second timescale up to 60 min. However, they do not demonstrate the amorphization of the GST and demonstrate the possibility to reinitialize their SLM. To obtain faster modulation, they proposed to use the semiconducting nature of GST in the different crystallographic phases to achieve variable ultrafast switching under optical excitation. The bandgap of amorphous and crystalline GST is reported being ≈0.8 eV and 0.5 eV, respectively. When the GST film is optically pumped with photon energy of 1.55 eV, the photo-excited free carriers increase the film conductivity and decrease the terahertz transmission. Then, by varying the delay between an optical pump and the terahertz pulses, a modulation by 85% of the Fano resonance can be achieved in a time interval range of 15 ps (Figure I-54.f). Nevertheless, with this method the non-volatile characteristic of the PCM is not used.
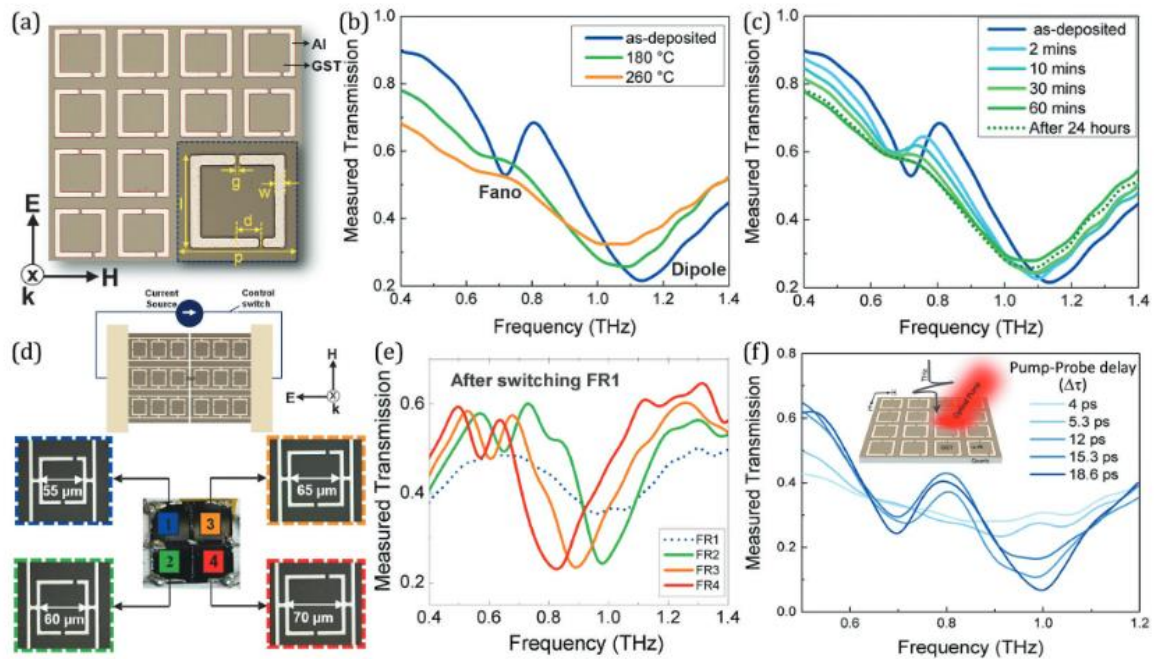
Figure I-54 : (a) Realized Fano SRR deposited on GST film with inset showing the geometrical parameters: p = 75 μm, l = 60 μm, w = 6 μm, g = 3 μm, and d = 15 μm, respectively. (b) Measured THz transmission of the metadevice for different annealed temperatures. (c) Multilevel Fano resonance modulation of the metadevice by controlling the annealing time at 180°C. (d) Schematics of electrically switched SRR with all unit cells electrically connected across two bond pads and the fabricated SLM sample with four electrically isolated quadrants (FR1, FR2, FR3, FR4) (e) Measured terahertz transmission responses of all FRs after the activation of FR1. (f) Ultrafast resonance recovery observed from the measured terahertz transmission responses of the as-deposited Fano SRR on GST film for various optical pump-THz probe delay times [125]

These examples, representing the state of the art of PCMs integration for THz domain, corroborate that PCMs may be good candidates for reconfigurable terahertz devices, their high contrast in the terahertz range (transmission modulation around 90%) and their bistable mode of operation. However, the study of PCMs for terahertz applications is very recent and the proposed studies require further research to demonstrate non-volatile reconfigurable THz devices with reversible functionalities. Indeed, if the previous studies demonstrate the possibility to tune the response of a terahertz device, they do not demonstrate the full reconfigurability of the device. They only demonstrate crystallization of the PCM and not the reverse amorphization process. Additionally, in the first study of Kodama *et al.* [123]*,* all dielectric SRR structure made of PCM only does not show the expected responses due to the important losses of the employed material.

The main objective of my thesis was to improve the existing state of the art in the domain by investigating GeTe films as an effective media to modulate the transmission of THz waves and to realize THz devices with non-volatile, reversible, reconfiguration capabilities. We investigated the possibility to use optical activation for modifying the GeTe states in a reversible way (both from amorphous to crystalline state and from crystalline to the amorphous one). We

designed and developed THz metamaterial devices integrating GeTe material and validated the optical activation approach by demonstrating a reconfigurable THz device which can be used as reconfigurable filters for future integration in THz telecommunication systems. Finally, we proposed a reconfigurable all dielectric THz polarizer made on GeTe-only which can achieve strong modulation of the THz waves.

Conclusion

In this chapter, we have presented the high potential of terahertz waves for telecommunications, security and medical imaging applications. We emphasize for these applications the need for reconfigurable terahertz devices such as filters, spatial light modulators, frequency selective surfaces, which allows controlling the properties of electromagnetic waves such as their amplitude, phase, polarization and/ or spatiotemporal distribution of their wave fronts. Reconfigurable devices may allow the optimization of terahertz systems by reducing the size, the energy consumption and the costs integration in smart systems to further development of Beyond 5G or imaging technologies …

We have identified several methods to realize reconfigurable devices using active components such as semiconductors, MEMs, liquid crystals, ferroelectric materials, graphene or phase transition materials. However, we noticed that semiconductors, MEMs and liquid crystal technologies suffered from a slow switching time, at µs timescale and have volatile-type responses requiring a permanent optical or electrical bias with complex integration technology when using large-area control schemes.

We have highlighted the interest of phase change materials such as GeTe (germanium telluride) or $Ge_2Sb_2Te_5$- GST (germanium antimony telluride). PCMs present a reversible, non-volatile phase transition on nanosecond timescales from an amorphous (insulating) state to a crystalline (metallic) state, triggered by different external stimuli (thermal, electrical, optical). The phase change is accompanied by a large variation of the materials' electromagnetic properties over a large range of frequencies (from dc and microwaves to optical domains). The simplicity of fabrication and their bistability (they maintain a specific state without additional external stimuli) make PCMs very promising materials for the realization of low consumption devices. Phase change materials have already proven their reliability in industrial applications such as rewritable optical memories or in NV-RAM-type resistive memories. Additional to these industrial applications, PCMs have attracted a real interest for the development of optical and electrical reconfigurable devices such as RF switches or variable optical lenses.

Among the existing PCM compositions we show that GeTe has a more stable amorphous phase than GST and the best resistivity in crystalline (metallic) phase, with a difference of 5 to 7 orders of magnitude of their resistivity between the amorphous and

crystalline phase. The optical-induced switching of GeTe between its two phases is abrupt and fast, at the nanosecond timescale, making the material a very promising candidate for the realization of reconfigurable terahertz devices compared to other PCM compounds.

In the terahertz domain, PCMs have demonstrated a high THz transmission modulation contrast. PCMs can be integrated in passive THz devices to modify their behavior/response in the THz domain. However, even if these studies successfully demonstrated the possibility to realize bistable modification of the terahertz response, the reverse reconfiguration of the devices was not completed. Therefore, there is a necessity to conduct works to improve the reliability and the quality of PCM based THz devices to demonstrate reconfigurability.

In my thesis we investigate GeTe as an effective media for the realization of non-volatile THz reconfigurable devices with fast switching time using optical activation of the material and develop specific devices which can be used to strongly modulate the transmission of terahertz waves. In the next chapter of this manuscript, I will present in a first step, the electrical and THz performances of GeTe thin films prepared in the microfabrication technological platform of the XLIM laboratory. In a second step, simulation and experimental optical activation of GeTe in both ways (amorphous to crystalline and crystalline to amorphous) for active modulation of THz waves will be presented.

References chapter I

1. Tonouchi, M., *Cutting-edge terahertz technology.* Nature Photonics, 2007. **1**(2): p. 97-105.
2. Khalid, N., N.A. Abbasi, and O.B. Akan. *300 GHz Broadband Transceiver Design for Low-THz Band Wireless Communications in Indoor Internet of Things.* in *2017 IEEE International Conference on Internet of Things (iThings) and IEEE Green Computing and Communications (GreenCom) and IEEE Cyber, Physical and Social Computing (CPSCom) and IEEE Smart Data (SmartData).* 2017.
3. Davies, A.G., E.H. Linfield, and M.B. Johnston, *The development of terahertz sources and their applications.* Phys Med Biol, 2002. **47**(21): p. 3679-89.
4. Fischer, B., et al., *Terahertz time-domain spectroscopy and imaging of artificial RNA.* Opt Express, 2005. **13**(14): p. 5205-15.
5. Woodward, R.M., et al., *Terahertz pulsed imaging of skin cancer in the time and frequency domain.* J Biol Phys, 2003. **29**(2-3): p. 257-9.
6. Gao, Z., et al., *MmWave massive-MIMO-based wireless backhaul for the 5G ultra-dense network.* IEEE Wireless Communications, 2015. **22**(5): p. 13-21.
7. Akyildiz, I.F., J.M. Jornet, and C. Han, *TeraNets: ultra-broadband communication networks in the terahertz band.* IEEE Wireless Communications, 2014. **21**(4): p. 130-135.
8. Elayan, H., et al. *Terahertz communication: The opportunities of wireless technology beyond 5G.* in *2018 International Conference on Advanced Communication Technologies and Networking (CommNet).* 2018.
9. Kürner, T., et al., *An Integrated Simulation Environment for the Investigation of Future THz Communication Systems: Extended Version.* Simulation, 2008. **84**(2-3): p. 123-130.
10. Davies, A.G., et al., *Where optics meets electronics: recent progress in decreasing the terahertz gap.* 2004. **362**(1815): p. 199-213.
11. Lewis, R.A., *A review of terahertz sources.* Journal of Physics D: Applied Physics, 2014. **47**(37): p. 11.
12. Nishida, Y., et al., *Terahertz coherent receiver using a single resonant tunnelling diode.* Scientific Reports, 2019. **9**(1): p. 18125.
13. Bhattacharjee, S., et al., *Folded Waveguide Traveling-Wave Tube Sources for Terahertz Radiation.* Plasma Science, IEEE Transactions on, 2004. **32**: p. 1002-1014.
14. Pérez, S., et al., *Terahertz Gunn-like oscillations in InGaAs/InAlAs planar diodes.* 2008. **103**(9): p. 094516.
15. Köhler, R., et al., *Terahertz semiconductor-heterostructure laser.* Nature, 2002. **417**(6885): p. 156-9.
16. Williams, B.S., *Terahertz quantum-cascade lasers.* Nature Photonics, 2007. **1**(9): p. 517-525.
17. Hübers, H.W., S.G. Pavlov, and V.N. Shastin, *Terahertz lasers based on germanium and silicon.* Semiconductor Science and Technology, 2005. **20**(7): p. S211-S221.
18. McIntosh, K.A., et al., *Terahertz photomixing with diode lasers in low-temperature-grown GaAs.* 1995. **67**(26): p. 3844-3846.
19. Tanoto, H., et al., *Nano-antenna in a photoconductive photomixer for highly efficient continuous wave terahertz emission.* Scientific Reports, 2013. **3**(1): p. 2824.
20. Withayachumnankul, W. and D. Abbott, *Metamaterials in the Terahertz Regime.* IEEE Photonics Journal, 2009. **1**(2): p. 99-118.
21. Padilla, W.J., et al., *Electrically resonant terahertz metamaterials: Theoretical and experimental investigations.* Physical Review B, 2007. **75**(4): p. 041102.
22. Uher, J. and W.J.R. Hoefer, *Tunable microwave and millimeter-wave band-pass filters.* IEEE Transactions on Microwave Theory and Techniques, 1991. **39**(4): p. 643-653.
23. Chen, H.T., et al., *Active terahertz metamaterial devices.* Nature, 2006. **444**(7119): p. 597-600.

24. Chen, H.T., et al., *Electronic control of extraordinary terahertz transmission through subwavelength metal hole arrays.* Opt Express, 2008. **16**(11): p. 7641-8.

25. Nouman, M.T., et al., *Terahertz Modulator based on Metamaterials integrated with Metal-Semiconductor-Metal Varactors.* Scientific Reports, 2016. **6**(1): p. 26452.

26. Pothier, A., et al. *Low Loss Ohmic Switches For RF Frequency Applications*. in *2002 32nd European Microwave Conference*. 2002.

27. Cheng, C.C., et al., *A very low loss 1.9–2.1 GHz RF MEMS phase shifter*. 2012. 1-3.

28. Malmqvist, R., et al., *RF MEMS Based Impedance Matching Networks for Tunable Multi-Band Microwave Low Noise Amplifiers*, in *International Semiconductor Conference 2009 - CAS 2009*. 2009, IEEE Institute of Electrical and Electronic Engineers. p. 303-306.

29. Stefanini, R., et al. *Compact 2-pole and 4-pole 2.4-2.8GHz dual-mode tunable filters*. in *2010 IEEE MTT-S International Microwave Symposium*. 2010.

30. Zhengli, H., et al., *Tunable Terahertz Filter and Modulator Based on Electrostatic MEMS Reconfigurable SRR Array.* IEEE Journal of Selected Topics in Quantum Electronics, 2015. **21**(4): p. 114-122.

31. Pappas, I., S. Siskos, and C. A, *Active-Matrix Liquid Crystal Displays - Operation, Electronics and Analog Circuits Design*, in *New Developments in Liquid Crystals*. 2009.

32. Singh, S., *Phase transitions in liquid crystals.* Physics Reports, 2000. **324**(2-4): p. 107-269.

33. Zografopoulos, D.C. and R. Beccherelli, *Tunable terahertz fishnet metamaterials based on thin nematic liquid crystal layers for fast switching.* Sci Rep, 2015. **5**: p. 13137.

34. Savo, S., D. Shrekenhamer, and W.J. Padilla, *Liquid Crystal Metamaterial Absorber Spatial Light Modulator for THz Applications.* Advanced Optical Materials, 2014. **2**(3): p. 275-279.

35. Shen, Z., et al., *Liquid-crystal-integrated metadevice: towards active multifunctional terahertz wave manipulations.* Opt Lett, 2018. **43**(19): p. 4695-4698.

36. Yang, J., et al., *Electrically tunable liquid crystal terahertz device based on double-layer plasmonic metamaterial.* Opt Express, 2019. **27**(19): p. 27039-27045.

37. Valasek, J., *Piezo-Electric and Allied Phenomena in Rochelle Salt.* Physical Review, 1921. **17**(4): p. 475-481.

38. Fiedziuszko, S.J., et al., *Dielectric materials, devices, and circuits.* IEEE Transactions on Microwave Theory and Techniques, 2002. **50**(3): p. 706-720.

39. Singh, R., et al., *Thermal tunability in terahertz metamaterials fabricated on strontium titanate single-crystal substrates.* Opt Lett, 2011. **36**(7): p. 1230-2.

40. Němec, H., et al., *Tunable terahertz metamaterials with negative permeability.* Physical Review B, 2009. **79**(24): p. 4.

41. Bian, Y., et al., *A tunable metamaterial dependent on electric field at terahertz with barium strontium titanate thin film.* Applied Physics Letters, 2014. **104**(4): p. 4.

42. Wu, L., et al., *A New Ba0.6 Sr0.4 TiO3 -Silicon Hybrid Metamaterial Device in Terahertz Regime.* Small, 2016. **12**(19): p. 2610-5.

43. Wu, L., et al., *Active KTaO3 hybrid terahertz metamaterial.* Sci Rep, 2017. **7**(1): p. 6072.

44. Novoselov, K.S., et al., *Electric field effect in atomically thin carbon films.* Science, 2004. **306**(5696): p. 666-9.

45. Castro Neto, A.H., et al., *The electronic properties of graphene.* Reviews of Modern Physics, 2009. **81**(1): p. 109-162.

46. Wang, F., et al., *Gate-variable optical transitions in graphene.* Science, 2008. **320**(5873): p. 206-9.

47. Lee, S.H., et al., *Switching terahertz waves with gate-controlled active graphene metamaterials.* Nat Mater, 2012. **11**(11): p. 936-41.

48. Liu, P.Q., et al., *Highly tunable hybrid metamaterials employing split-ring resonators strongly coupled to graphene surface plasmons.* Nat Commun, 2015. **6**: p. 8969.

49. Wen, Q.Y., et al., *Graphene based all-optical spatial terahertz modulator.* Sci Rep, 2014. **4**(1): p. 7409.

50. Liu, J., et al., *Graphene field effect transistor-based terahertz modulator with small operating voltage and low insertion loss.* Chinese Optics Letters, 2016. **14**(5): p. 052301.

51. Chhowalla, M., et al., *The chemistry of two-dimensional layered transition metal dichalcogenide nanosheets.* Nat Chem, 2013. **5**(4): p. 263-75.

52. Ganatra, R. and Q. Zhang, *Few-Layer MoS2: A Promising Layered Semiconductor.* ACS Nano, 2014. **8**(5): p. 4074-4099.

53. Yang, Z., C.Y. Ko, and S. Ramanathan, *Oxide Electronics Utilizing Ultrafast Metal-Insulator Transitions*, in *Annual Review of Materials Research, Vol 41*, D.R. Clarke and P. Fratzl, Editors. 2011, Annual Reviews: Palo Alto. p. 337-367.

54. Liu, K., et al., *Recent progresses on physics and applications of vanadium dioxide.* Materials Today, 2018. **21**(8): p. 875-896.

55. Morin, F.J., *Oxides Which Show a Metal-to-Insulator Transition at the Neel Temperature.* Physical Review Letters, 1959. **3**(1): p. 34-36.

56. Pergament, A., *Metal-insulator transition: the Mott criterion and coherence length.* Journal of Physics Condensed Matter, 2003. **15**: p. 3217-3224.

57. Stefanovich, G., A. Pergament, and D. Stefanovich, *Electrical switching and Mott transition in VO2.* Journal of Physics: Condensed Matter, 2000. **12**(41): p. 8837-8845.

58. Kim, H.-T., et al., *Switching of the Mott transition based on hole-driven MIT theory.* Physica B: Condensed Matter, 2008. **403**: p. 1434-1436.

59. Cavalleri, A., et al., *Evidence for a structurally-driven insulator-to-metal transition in ${\mathrm{VO}}_{2}$: A view from the ultrafast timescale.* Physical Review B, 2004. **70**(16): p. 161102.

60. Sakai, J. and M. Kurisu, *Effect of pressure on the electric-field-induced resistance switching of VO2 planar-type junctions.* Physical Review B - PHYS REV B, 2008. **78**.

61. Hilton, D.J., et al., *Enhanced photosusceptibility near Tc for the light-induced insulator-to-metal phase transition in vanadium dioxide.* Phys Rev Lett, 2007. **99**(22): p. 226401.

62. Jeong, Y.G., et al., *A Vanadium Dioxide Metamaterial Disengaged from Insulator-to-Metal Transition.* Nano Lett, 2015. **15**(10): p. 6318-23.

63. Wang, S., L. Kang, and D.H. Werner, *Active Terahertz Chiral Metamaterials Based on Phase Transition of Vanadium Dioxide (VO2).* Sci Rep, 2018. **8**(1): p. 189.

64. Shin, J.H., K.H. Park, and H.C. Ryu, *Electrically controllable terahertz square-loop metamaterial based on VO(2) thin film.* Nanotechnology, 2016. **27**(19): p. 195202.

65. Han, C., et al., *Broadband modulation of terahertz waves through electrically driven hybrid bowtie antenna-VO2 devices.* Sci Rep, 2017. **7**(1): p. 12725.

66. Zhang, Y., et al., *Photoinduced active terahertz metamaterials with nanostructured vanadium dioxide film deposited by sol-gel method.* Opt Express, 2014. **22**(9): p. 11070-8.

67. Choi, S.B., et al., *Nanopattern enabled terahertz all-optical switching on vanadium dioxide thin film.* Applied Physics Letters, 2011. **98**(7): p. 3.

68. Waterman, A.T., *XXI. On the positive ionization from certain hot salts, together with some observations on the electrical properties of molybdenite at high temperatures.* The London, Edinburgh, and Dublin Philosophical Magazine and Journal of Science, 2009. **33**(195): p. 225-247.

69. Ovshinsky, S.R., *Reversible Electrical Switching Phenomena in Disordered Structures.* Physical Review Letters, 1968. **21**(20): p. 1450-1453.

70. Ovshinsky, S.R. and H. Fritzsche, *Amorphous semiconductors for switching, memory, and imaging applications.* IEEE Transactions on Electron Devices, 1973. **20**(2): p. 91-105.

71. Gawelda, W., et al., *Dynamics of laser-induced phase switching in GeTe films.* Journal of Applied Physics, 2011. **109**(12): p. 123102.

72. Liu, Y., et al., *Crystallization of Ge2Sb2Te5 films by amplified femtosecond optical pulses.* Journal of Applied Physics, 2012. **112**(12).

73. Chen, M., K.A. Rubin, and R.W. Barton, *Compound materials for reversible, phase-change optical data storage.* Applied Physics Letters, 1986. **49**(9): p. 502-504.

74. Raoux, S., et al., *Phase change materials and phase change memory.* MRS Bulletin, 2014. **39**(8): p. 703-710.

75. Gourvest, E., et al., *Evidence of Germanium precipitation in phase-change Ge1–xTex thin films by Raman scattering.* Applied Physics Letters, 2009. **95**(3): p. 031908.

76. Lee, Y.M., et al., *Nitrogen contribution to N-doped GeTe (N: 8.4 at.%) in the structural phase transition.* Current Applied Physics, 2011. **11**(3): p. 710-713.

77. Shelby, R.M. and S. Raoux, *Crystallization dynamics of nitrogen-doped Ge2Sb2Te5.* Journal of Applied Physics, 2009. **105**(10): p. 104902.

78. Betti Beneventi, G., et al., *Carbon-doped GeTe: A promising material for Phase-Change Memories.* Solid-State Electronics, 2011. **65-66**: p. 197-204.

79. Matsuzaki, N., et al. *Oxygen-doped gesbte phase-change memory cells featuring 1.5 V/100-/spl mu/A standard 0.13/spl mu/m CMOS operations*. in *IEEE InternationalElectron Devices Meeting, 2005. IEDM Technical Digest.* 2005.

80. Jeong, S.-M., et al., *Influence of Silicon Doping on the Properties of Sputtered Ge2Sb2Te5Thin Film.* Japanese Journal of Applied Physics, 2009. **48**(4): p. 045503.

81. Singh, G., et al., *Theoretical and experimental investigations of the properties of Ge2Sb2Te5 and indium-doped Ge2Sb2Te5 phase change material.* Applied Physics A, 2014. **117**(3): p. 1307-1314.

82. Kim, I.S., et al. *High performance PRAM cell scalable to sub-20nm technology with below 4F2 cell size, extendable to DRAM applications*. in *2010 Symposium on VLSI Technology*. 2010.

83. Noé, P., et al., *Phase-change materials for non-volatile memory devices: from technological challenges to materials science issues.* Semiconductor Science and Technology, 2018. **33**(1): p. 013002.

84. Huang, H., et al., *Fast phase transition process of Ge2Sb2Te5 film induced by picosecond laser pulses with identical fluences.* Journal of Applied Physics, 2009. **106**(6): p. 5.

85. Mahanta, P., M. Munna, and R.A. Coutu, *Performance Comparison of Phase Change Materials and Metal-Insulator Transition Materials for Direct Current and Radio Frequency Switching Applications.* 2018. **6**(2): p. 48.

86. Navarro, G., et al., *Material engineering of GexTe100–x compounds to improve phase-change memory performances.* Solid-State Electronics, 2013. **89**: p. 93-100.

87. Raoux, S., et al., *Crystallization times of Ge–Te phase change materials as a function of composition.* Applied Physics Letters, 2009. **95**(7): p. 071910.

88. Bahl, S.K. and K.L. Chopra, *Electrical and Optical Properties of Amorphous vs Crystalline GeTe Films.* Journal of Vacuum Science and Technology, 1969. **6**(4): p. 561-565.

89. Sun, X., et al., *Nanosecond laser-induced phase transitions in pulsed laser deposition-deposited GeTe films.* Journal of Applied Physics, 2014. **116**(13): p. 133501.

90. Crunteanu, A., et al., *Optical Switching of GeTe Phase Change Materials for High-Frequency Applications*. 2017 Ieee Mtt-S International Microwave Workshop Series on Advanced Materials and Processes for Rf and Thz Applications. 2017, New York: Ieee.

91. Wuttig, M., H. Bhaskaran, and T. Taubner, *Phase-change materials for non-volatile photonic applications.* Nature Photonics, 2017. **11**(8): p. 465-476.

92. Lencer, D., M. Salinga, and M. Wuttig, *Design Rules for Phase-Change Materials in Data Storage Applications.* 2011. **23**(18): p. 2030-2058.

93. Xu, M., *Study of the Crystallization Dynamics and Threshold Voltage of Phase Change Materials for Use in Reconfigurable RF Switches and Nonvolatile Memories*. 2017.

94. Wiggins, S.M., et al., *The influence of wavelength on phase transformations induced by picosecond and femtosecond laser pulses in GeSb thin films.* Journal of Applied Physics, 2005. **98**(11): p. 113518.

95. El-Hinnawy, N., et al., *12.5 THz F-co GeTe Inline Phase-Change Switch Technology for Reconfigurable RF and Switching Applications*, in *2014 Ieee Compound Semiconductor Integrated Circuit Symposium*. 2014, Ieee: New York.

96. El-Hinnawy, N., et al., *A Four-Terminal, Inline, Chalcogenide Phase-Change RF Switch Using an Independent Resistive Heater for Thermal Actuation.* IEEE Electron Device Letters, 2013. **34**(10): p. 1313-1315.

97. Makino, K., J. Tominaga, and M. Hase, *Ultrafast optical manipulation of atomic arrangements in chalcogenide alloy memory materials.* Opt Express, 2011. **19**(2): p. 1260-70.

98. Lei, K., et al., *Refractive index modulation of Sb70Te30 phase-change thin films by multiple femtosecond laser pulses.* Journal of Applied Physics, 2016. **119**(17): p. 8.

99. Ryu, S.W., et al., *SiO[sub 2] Incorporation Effects in Ge[sub 2]Sb[sub 2]Te[sub 5] Films Prepared by Magnetron Sputtering for Phase Change Random Access Memory Devices.* Electrochemical and Solid-State Letters, 2006. **9**(8): p. G259-G261.

100. Rimini, E., et al., *Crystallization of sputtered-deposited and ion implanted amorphous Ge2Sb2Te5 thin films.* Journal of Applied Physics, 2009. **105**(12): p. 6.

101. Gwon, T., et al., *Atomic Layer Deposition of GeTe and Ge–Sb–Te Films Using HGeCl3, Sb(OC2H5)3, and {(CH3)3Si}2Te and Their Reaction Mechanisms.* Chemistry of Materials, 2017. **29**(19): p. 8065-8072.

102. Cheng, L., et al., *Conformal deposition of GeTe films with tunable Te composition by atomic layer deposition.* Journal of Vacuum Science & Technology A, 2019. **37**(2): p. 020907.

103. Martins, R.M.S., *In-situ X-Ray diffraction studies during growth of Ni-Ti Shape Memory Alloy films and their complementary ex-situ characterization*. 2008.

104. Orava, J., T. Kohoutek, and T. Wagner, *Deposition Techniques for Chalcogenide Thin Films*. 2014. p. 265–309.

105. Willmott, P.R. and J.R. Huber, *Pulsed laser vaporization and deposition.* Reviews of Modern Physics, 2000. **72**(1): p. 315-328.

106. Gamaly, E.G., et al., *Ablation of solids by femtosecond lasers: Ablation mechanism and ablation thresholds for metals and dielectrics.* 2002. **9**(3): p. 949-957.

107. Cremers, V., R. Puurunen, and J. Dendooven, *Conformality in atomic layer deposition: Current status overview of analysis and modelling.* Applied Physics Reviews, 2019. **6**: p. 021302.

108. Ritala, M., et al., *Atomic layer deposition of Ge2Sb2Te5 thin films.* Microelectronic Engineering, 2009. **86**(7): p. 1946-1949.

109. Raoux, S., W. Welnic, and D. Ielmini, *Phase change materials and their application to nonvolatile memories.* Chem Rev, 2010. **110**(1): p. 240-67.

110. Wuttig, M. and N. Yamada, *Phase-change materials for rewriteable data storage.* Nat Mater, 2007. **6**(11): p. 824-32.

111. Lacaita, A.L., D. Ielmini, and D. Mantegazza, *Status and challenges of phase change memory modeling.* Solid-State Electronics, 2008. **52**(9): p. 1443-1451.

112. Burr, G.W., et al., *Phase change memory technology.* Journal of Vacuum Science & Technology B, Nanotechnology and Microelectronics: Materials, Processing, Measurement, and Phenomena, 2010. **28**(2): p. 223-262.

113. Bruns, G., et al., *Nanosecond switching in GeTe phase change memory cells.* Applied Physics Letters, 2009. **95**(4): p. 3.

114. Lai, S. and T. Lowrey. *OUM - A 180 nm nonvolatile memory cell element technology for stand alone and embedded applications*. in *International Electron Devices Meeting. Technical Digest (Cat. No.01CH37224)*. 2001.

115. Lo, H., et al., *Three-Terminal Probe Reconfigurable Phase-Change Material Switches.* IEEE Transactions on Electron Devices, 2010. **57**(1): p. 312-320.

116. Mennai, A., et al., *Bistable RF Switches Using Ge2Sb2Te5 Phase Change Material*, in *2015 45th European Microwave Conference*. 2015, Ieee: New York. p. 945-947.

117. Wang, M., Y. Shim, and M. Rais-Zadeh, *A Low-Loss Directly Heated Two-Port RF Phase Change Switch.* IEEE Electron Device Letters, 2014. **35**(4): p. 491-493.

118. Gholipour, B., et al., *An all-optical, non-volatile, bidirectional, phase-change meta-switch.* Adv Mater, 2013. **25**(22): p. 3050-4.

119.   Karvounis, A., et al., *All-dielectric phase-change reconfigurable metasurface.* Applied Physics Letters, 2016. **109**(5): p. 051103.

120.   Wang, Q., et al., *Optically reconfigurable metasurfaces and photonic devices based on phase change materials.* Nature Photonics, 2015. **10**(1): p. 60-65.

121.   Gwin, A.H., et al., *Improved terahertz modulation using germanium telluride (GeTe) chalcogenide thin films.* Applied Physics Letters, 2015. **107**(3): p. 031904.

122.   Makino, K., et al., *Terahertz spectroscopic characterization of Ge2Sb2Te5 phase change materials for photonics applications.* Journal of Materials Chemistry C, 2019. **7**(27): p. 8209-8215.

123.   Kodama, C.H. and R.A. Coutu, *Tunable split-ring resonators using germanium telluride.* Applied Physics Letters, 2016. **108**(23): p. 231901.

124.   Sanari, Y., et al., *Zener Tunneling Breakdown in Phase-Change Materials Revealed by Intense Terahertz Pulses.* Phys Rev Lett, 2018. **121**(16): p. 165702.

125.   Pitchappa, P., et al., *Chalcogenide Phase Change Material for Active Terahertz Photonics.* 2019. **31**(12): p. 1808157.

Chapter II : Fabrication of PCM thin films and characterization in the THz domain

Chapter II.   Fabrication of PCM thin films and characterization in the THz domain

Introduction

We have presented in the first chapter the interest and several applications of the THz domain such as THz spectroscopy, THz imaging for biological, security and defense domain and also wireless telecommunications for the development of beyond 5G technologies. However, we highlighted that for most of these practical applications, reconfigurable terahertz devices such as filters, spatial light modulators, or frequency selective surfaces, which allow controlling the properties of electromagnetic waves, are essential. In this context, we have presented different active elements (such as semiconductor, MEMS, graphene…) which can be integrated in passive structures to realize reconfigurable THz devices. Among the proposed materials and devices, we notably focused on phase change materials. These materials present a non-volatile phase change from an amorphous/insulating state to a crystalline/conducting one. This phase change can be achieved in a repeatable way using external stimuli (thermal, optical, electrical) and occurs with a large change of the material properties (electric, optical…). These materials are extensively used in optical and electrical domain in numerous applications. However, in terahertz domain, only few studies have been realized to demonstrate the possibility to realize bistable modification of the response of devices and no reconfigurability of the realized devices have been demonstrated in the THz domain.

In this second chapter, we present a study on GeTe phase change material in the THz domain to better assess their properties variation during the phase change and their capabilities to control and modulate the amplitude and the phase of THz waves. The first objective of this chapter is to realize and study PCMs films which presented a high contrast of properties (in conductivity, transmission…) in the THz range when changing between their crystalline and amorphous phase for the realization of reconfigurable THz devices and future integration in THz system. For the realization of reconfigurable devices, a reliable and simple activation scheme is required. Thus, the second objective is to develop a method to actively control the PCM states. We will briefly present the realization of PCMs using the DC magnetron sputtering method. We will characterize the DC electrical and THz properties of PCMs films at each state and compare the performance of the two PCM compositions, GeTe and GST. Finally, we will focus on the GeTe material optical activation between amorphous and crystalline states in a repeatable way.

II.1. Realization of PCM films and their DC electrical properties

II.1.1. Deposition of thin PCM film by DC magnetron sputtering

Among the different possible techniques to obtain GeTe films, we choose to use the DC magnetron sputtering technique (presented in chapter I) because it allows us to realize uniform films over a large area in a reproducible manner. Different parameters such as the pressure of the vacuum chamber, the temperature of the substrate, the composition of the target and the magnetron power have to be considered to obtain GeTe films of good quality.

The pressure of the chamber during the deposition affects the film structural properties. During depositions collisions between occurs between the atoms of the target and the gas. Each time accelerated atoms of the target hit gas atoms, their speed, and consequently their kinetic energy, decreases. At low pressure, the collision between the sputtered atoms and the ambient Ar gas atoms are few in number. Consequently, the atoms kinetic energy when they arrive on the substrate is more important and thus the deposited film will be denser (better quality). Nevertheless, a high kinetic energy can lead to the sputtering of the growing film and create faults in the film and overall slower grow rates. On the contrary, when the pressure increases, the film morphology becomes porous due to the decrease of the kinetic energy of the atoms. Therefore, to obtain a good quality deposition, it is necessary to find a compromise between an Ar pressure low enough to obtain a high-density film but high enough to maintain the plasma discharge [1].

The second parameter to consider is the temperature of the substrate during the deposition. A high temperature increases the species mobility on the substrate surface and thus allows the diffusion of the atoms over it. It leads to the formation of equiaxial grains and denser films and thus increases the homogeneity of the film. The deposition temperature also affects the effective activation energy (temperature) required to crystallize the PCM films after the fabrication and consequently the crystallization temperature.
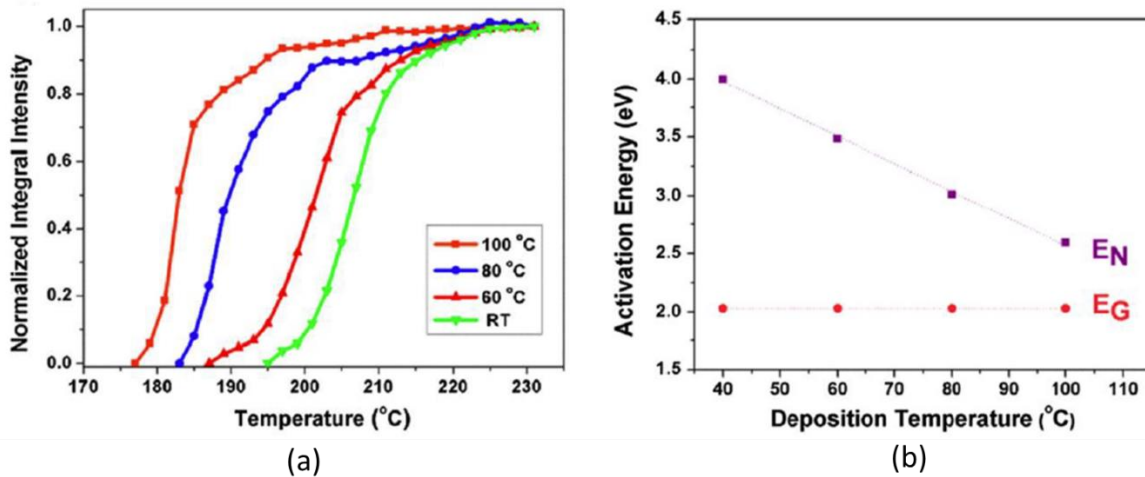
Figure II-1 : (a) GeTe crystallization trace for different deposition temperatures (RT: room Temperature, 60°C, 80°C and 100°C) obtained by direct heating until 230 °C. (b) activation energies for nucleation (EN) and growth (EG) as a function of the deposition temperature [2]

Indeed, in the literature, studies realized on GeTe films grown on silicon substrate have shown that the increase of the temperature deposition leads to a diminution of the activation energy of the crystallization process, and consequently, to a lower crystallization temperature and better crystallization of the film (Figure II-1) [2]. This decrease of the temperature can be explained by a linear decrease of the crystallization activation energy of nucleation process with the increase of the deposition temperature (Figure II-1b). Nevertheless, the activation energy of growth remains constant and starting from a certain deposition temperature no further decrease of the activation energy will be observed.

It has been proven that an increase in the growth rate of the films results in denser films with smaller roughness, lower crystallization temperature and lower electrical resistance of the crystalline phase (Figure II-2) [3]. The grow rate of GeTe film is directly proportional to the sputtering power and inversely proportional to the working pressure.
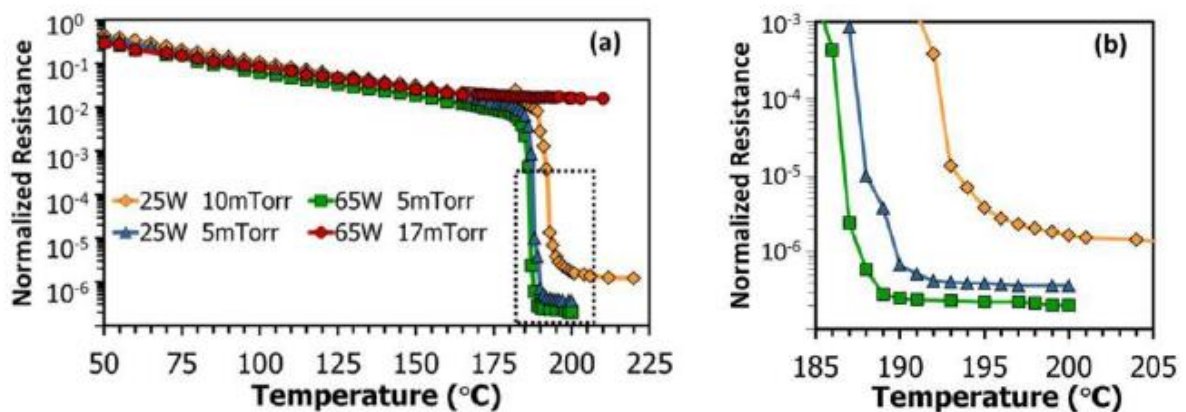
Figure II-2 : Normalized resistance variation of GeTe depending on the temperature with different deposition conditions. (b) Zoom in the dash line area [3].

High grow rates reduce the number of impurities in the film (notably residual oxygen) which can alter the resistivity of the crystalline films.

Considering these different parameters and previous work realized in Xlim laboratory by the MINT group [4], we optimized the different parameters of the magnetron sputtering system to obtain GeTe films having the best quality (film with no default, low rugosity and high contrast of resistivity between the two states). Table II-1 resumes the optimum conditions for GeTe film deposition to obtain the maximum amplitude variation between amorphous and crystalline phases.

Table II-1 : Optimized parameters for GeTe film deposition with DC magnetron sputtering

Target	Stoichiometric GeTe target (50:50)
Deposition temperature	250 °C
Ar pressure	5.10^{-3} mbar
Power	55 W

Before the fabrication of the GeTe film, the GeTe target is pre-sputtered with a power of 50 W during 10 min to remove surface contaminations and oxide layer. For the realization of GeTe films, we used two different types of substrates, c-cut sapphire and silica (SiO_2). Before deposition, all the substrates were ultrasonically cleaned in an acetone bath (5 min), then in an isopropanol one and deionized water. They were finally dried under a flow of dry, filtered air. This cleaning process ensures a good adhesion and quality of GeTe films.

After deposition, the GeTe film is obtained in an amorphous state. We heated the fabricated film at 300°C by using a heating plate during 30 min to ensure the complete crystallization of the GeTe. Figure II-3 presents typical images of a 250 nm GeTe film grown on a c-cut sapphire substrate in amorphous and in crystalline states.
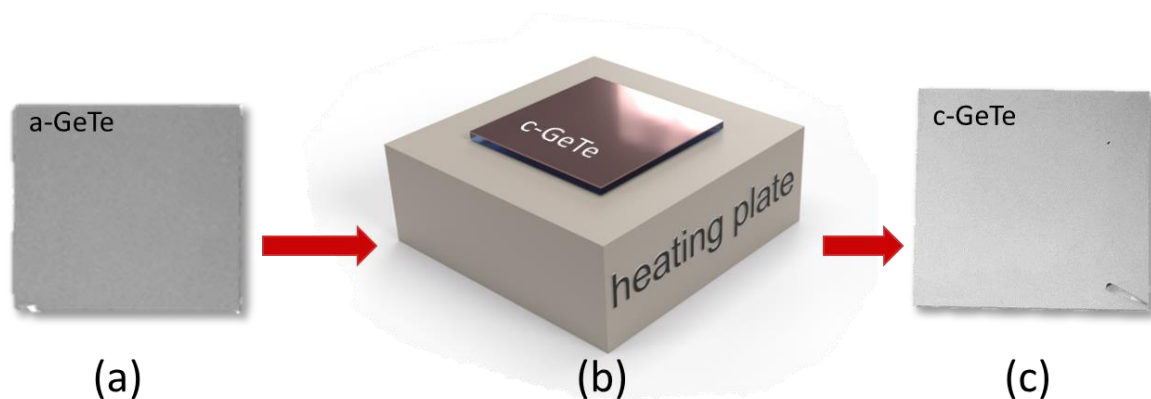
Figure II-3: Optical images of a 250 nm GeTe film grown on a 20x20 mm² sapphire c-cut substrate in the amorphous state (a) and in the crystalline state (c) prepared by thermal heating on a hot plate (b)

The modification of the film's optical properties can be easily observed, since the amorphous GeTe is darker than the crystalline film. This can be explained by a difference in reflectivity of each states, amorphous GeTe tends to absorb or transmit visible light (thus has a less reflective surface), whereas crystalline GeTe is more reflective to the visible light.

II.1.2. DC electrical characterization of PCM films

We measured the electric resistance variation depending on the temperature (during a crystallization process) of GeTe and GST films in real time using a two-port planar device consisting of two metallic probes (spaced by two millimeters and placed on the film surface) under ambient air. To crystallize the films, we used a heating stage underneath, using a heating rate of 10°C/min and a 10 minutes rest period at maximum temperature (300 °C), followed by cooling under ambient air to room temperature. Figure II-4 shows the resistance variation of the initially amorphous GeTe film (500 nm thick) obtained on sapphire (a) and silica (b) substrate during a heating cycle from 25 °C to 300 °C and a cooling cycle down to 25 °C (under ambient air).
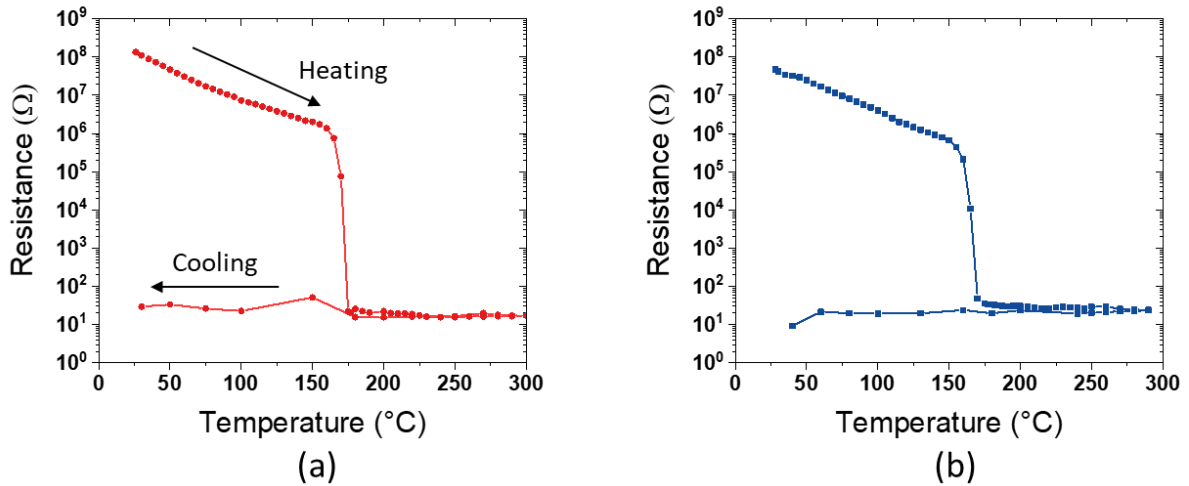
Figure II-4 : Resistance variation depending on the temperature of 500-nm thick GeTe film grown on (a) sapphire substrate and (b) silica substrate using DC magnetron sputtering.

On sapphire substrate (Figure II-4-a), the deposited GeTe (amorphous) has a high resistivity around 100 MΩ. During the heating cycle, its surface resistance gradually decreases until drastically dropping at 177 °C, a temperature corresponding to the crystallization temperature of the film. Above this temperature, its resistance of the GeTe does not change even during the cooling down to 25 °C with a value around 20 Ω. This confirms the non-volatile behavior on the GeTe phase change. We achieve a resistance variation of more than seven orders of magnitude between the amorphous and crystalline states with optimized deposition conditions, which is better than the previous reported values for stochiometric GeTe compounds [5, 6].

A similar 500 nm GeTe film was grown on a silica substrate (Figure II-4-b). We observed the same behavior, the transition occurs at 170 °C instead of 177 °C. This difference of temperature transition can be induced by the difference in thermal conductivity between the two substrates. The small difference in the minimal and maximal resistance value can be due to an error in the measure using the two-port planar device. The space between the two probes may be not exactly the same for the both measures which can modify the experimental value.

If we compare the transition temperature of the fabricated GeTe films with previous reports [5, 6], we found values very close to the transition temperature (180 °C) of stoichiometric GeTe films (50% Ge and 50% Te).

To compare the performances of GeTe films with GST films, we realized films of GeTe and GST on silica substrates using optimal deposition conditions, with a thickness of 250 nm. Figure II-5 shows the resistance variation of both films during a heating- cooling cycle up to 250°C.
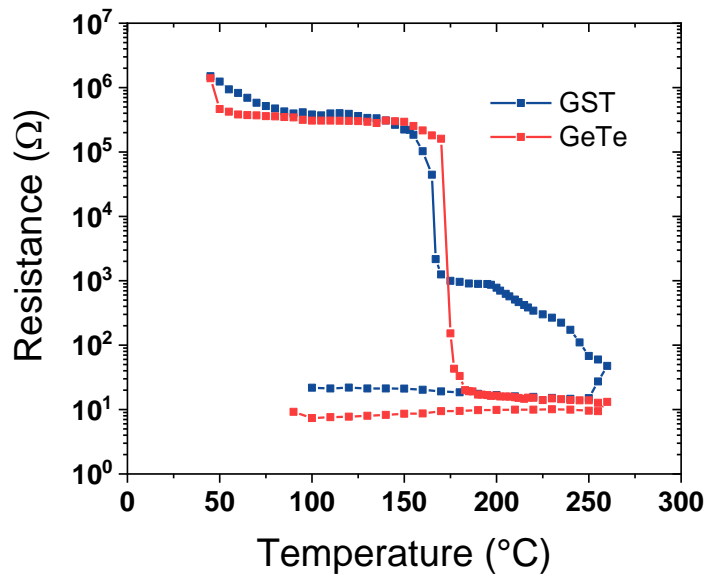
Figure II-5 : Resistance variation with the temperature of (a) 250-nm thick GeTe film and (b) a 250 nm thick GST film grown on silica substrates using DC magnetron sputtering

In the case of GeTe films (Figure 2.3, red plot), during the heating cycle we observe, as previously, a resistivity change toward the metallic phase at 175°C. For GST (Figure 2.3, blue plot) this is slightly different, the phase change occurs in two steps (corresponding to two different phase transitions). A first phase change from an amorphous to a metastable cubic crystalline phase occurs at 155°C. After this first phase change, the resistance continues to decrease. This corresponds to phase change from a metastable cubic crystalline phase to a stable hexagonal crystalline phase. As previously observed in chapter I with the work of Noé *et al.* [6], after cooling, the crystalline GST resistance is higher (≈22 Ω) than the crystalline GeTe resistance (≈7 Ω).

This two-point probe measure system allows us to evaluate the resistance evolution with the temperature and to extract the phase change temperature in real time. However, it does not give exact values of the electrical surface resistance of the films since these simple measurements are including the contact resistance between the probes and the films and the resistance of the measurement system. If this error can be neglected in the case of high resistances (>1 kΩ) as in the case of amorphous PCMs, it is not very appropriate to measure low resistance systems such as crystalline PCMs. To obtain precise values of PCM resistivity as deposited and after crystallization, we used a four-point probe system. The four-point probe method is based on four equidistant aligned probes. It allows to overcome the contact resistance between the probe and the sample because the current is applied by the two external probes and the voltage is measured almost without passing current through the two internal probes (Figure II-6).
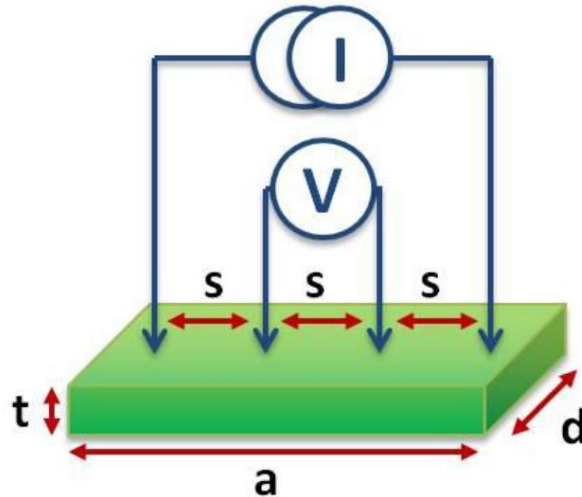
Figure II-6: Schematic of the four points system

This method avoids the Schottky diode effect which occurs with a two-point probe system (such as an ohmmeter).

To determine the film resistivity, it is necessary to consider parameters such as the thickness and the size of the film. The resistivity ρ of the sample can be expressed as:

$$\rho = \left(\frac{V}{I}\right) t CF_d CF_t \qquad (II.1)$$

With:

- $V(V)$: measured voltage

- $I(A)$: injected current

- $t(m)$: thickness of the film

- CF_d : correction coefficient depending on the film area

- CF_t: correction coefficient depending on the film thickness

The coefficients CF_d and CF_t are used because the measured film is not an infinite plane (film dimensions smaller than 40s). In this case, the possible current paths between the probes are limited by the proximity to the edges of the sample, resulting in an overestimation of the sheet resistance. Here, the distance "s" between each point of the four-point probe is equal to 1 mm. The thickness of the studied films is very low compared to the spacing between each probe. Consequently, the CF_t coefficient is considered equal to 1. The CF_d coefficient for the 20x20 mm² films is determined using a table of empirically-determined correction factors and considered to be 4.4364.

Using this method, we measured the resistivity of amorphous and crystalline GeTe films deposited on silica substrate with different thickness (250 nm, 500 nm and 1 µm). The

resistivity values for the different films are shown on Table II-2. We also added in the table the measured resistivity of a 500 nm GST film in the amorphous and crystalline states.

Table II-2 : Resistivity measurement of amorphous and crystalline phases of thin GeTe and GST and films with different thicknesses grown on silica substrate.

Material	Phase	Thickness (nm)	Resistivity (Ω.cm)
GeTe	amorphous	250	2.57×10^3
GeTe	amorphous	500	3.26×10^3
GeTe	amorphous	1000	3.33×10^3
GST	amorphous	250	6.65×10^3
GeTe	crystalline	250	3.43×10^{-4}
GeTe	crystalline	500	4.04×10^{-4}
GeTe	crystalline	1000	6.34×10^{-4}
GST	crystalline	250	1.1×10^{-3}

As observed from the resistivity values in Table II-2 : Resistivity measurement of amorphous and crystalline phases of thin GeTe and GST and films with different thicknesses grown on silica substrate., when the thickness of the GeTe film increases, its resistivity is also increasing. This difference in resistivity can be explained by a difference in the film quality, when we increase the thickness the density of faults and impurities in the film increase and thus the resistivity can increase. The value of the electrical resistivity of the crystalline GST film is higher than the GeTe resistivity in the crystalline state. These values agree very well with the literature values and the ones presented in Ch. I and confirm our choice to use GeTe for THz applications. To compare our work with the literature, Table II-3 resumes different values of GeTe resistivity in amorphous and crystalline phase presented in the literature. A good agreement to our obtained values was found.

Table II-3 : Different resistivity value for amorphous and crystalline GeTe reported in the literature.

Reference	Substrate	Thickness (nm)	Amorphous state resistivity (Ω.cm)	Crystalline state resistivity (Ω.cm)
Bahl *et al.* [7]	Glass	68	5×10^2	10^{-4}
Navarro *et al.* [5]	Si	100	10^3	1.5×10^{-3}
Noé *et al.* [6]	Si	100	$\approx 2 \times 10^2$	$\approx 8 \times 10^{-4}$
Sarnet *et al.* [8]	Glass	35	1.4×10^3	4×10^{-4}
Our work	Silica	250	2.57×10^3	3.43×10^{-4}

To conclude this part, through optimization of deposition conditions we have realized GeTe films with a resistivity contrast between amorphous and crystalline phase of more than 6 orders of magnitude, comparable to previous reports in the literature.

II.2. Characterization of PCMs properties at THz frequencies

In order to investigate the performances of PCMs at THz frequencies, we used a terahertz time domain spectroscopy (THz-TDS) system to characterize the THz properties (refractive index, conductivity, permittivity) of GeTe and GST films.

II.2.1. Presentation of the terahertz time-domain spectroscopy (THz-TDS)

The THz-TDS technique enables to characterize properties such as refractive index, absorption, permittivity and conductivity of a material by analyzing the transmission and/or the reflection of a THz pulse [9]. For our measurements we used a transmission configuration (Figure II-7).
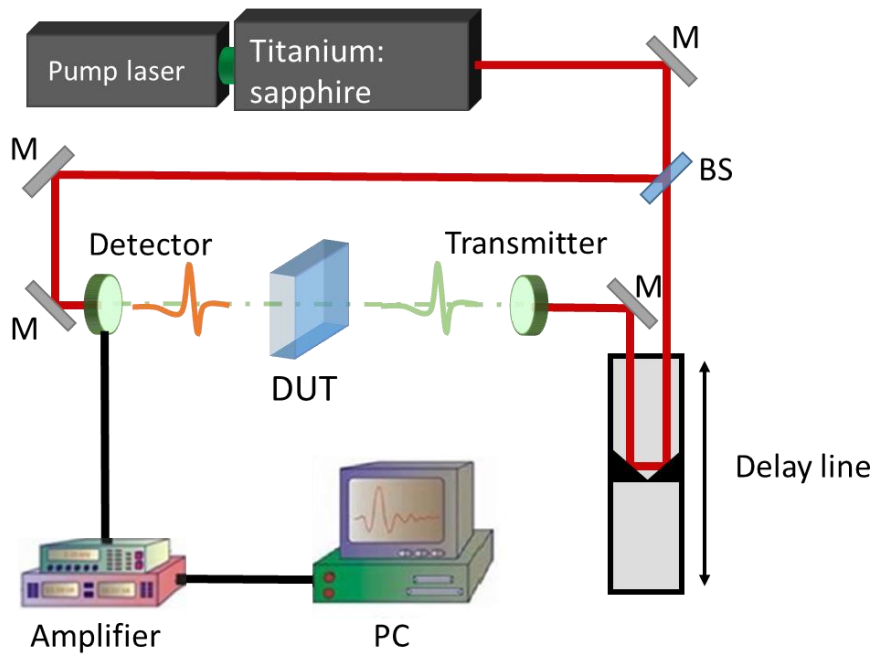
Figure II-7: Schematic of a THz TDS system. M, BS and DUT correspond to mirror, beamsplitter and dispositive under test respectively

The THz wave generation and detection technique used in a typical THz-TDS system is based on two photoconductive antennas. The excitation of the two photoconductive antennas (used for emission and detection of THz waves) is employing a femtosecond mode-locked Ti:sapphire laser (Tsunami-Spectra-Physics) with a central wavelength of 800 nm and a repetition rate of 80 MHz. In order to achieve synchronous detection, the laser beam is split into two beams: one for the emission of the THz radiation and the other one for its detection. The measurement of the THz field ($\approx$30 µW) at the detector is performed by a synchronous detection amplifier combined with a current amplifier, provided that the terahertz wave and the laser beam arrive at the detector at the same time. The temporal THz signal is obtained by temporal sampling thanks to the optical delay line allowing to modify the path followed by the laser beam illuminating the detector. Then by using a Fast Fourier Transform it is possible to transpose the temporal measure to the frequency domain. The main interest of the THz-TDS is the measure of both amplitude and phase of the THz transmission of a material over a large frequency band. From these THz measurements it is possible to extract THz properties of the material (refraction index, conductivity). The material characteristics are obtained by comparing the spectroscopic measurements of the material with a reference measure realized without the sample (Figure II-8).
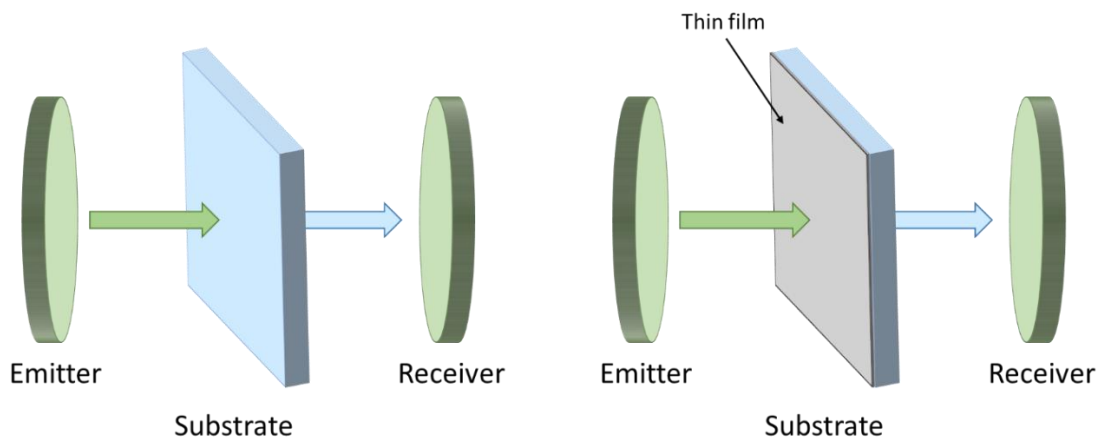
Figure II-8: Schematic of the reference measure (left) and sample measure (right) allowing to determine the material characteristics (here a thin PCM film).

II.2.1.1. Characterization in temporal domain

Before characterizing the fabricated PCM film, it is necessary to characterize the different substrates. The THz-TDS temporal responses of the reference (ambient air), of a sapphire substrate and of a silica substrate are shown on Figure II-9 a and b. On the temporal transmission of the sapphire substrate, after the first pulse T_1 (corresponding to the direct transmitted pulse by the substrate), several echoes are observed (T_2 and T_3) due to the Fabry-Perot effect resulting from multiple reflections of the primary pulse T_1 on the two substrate faces.
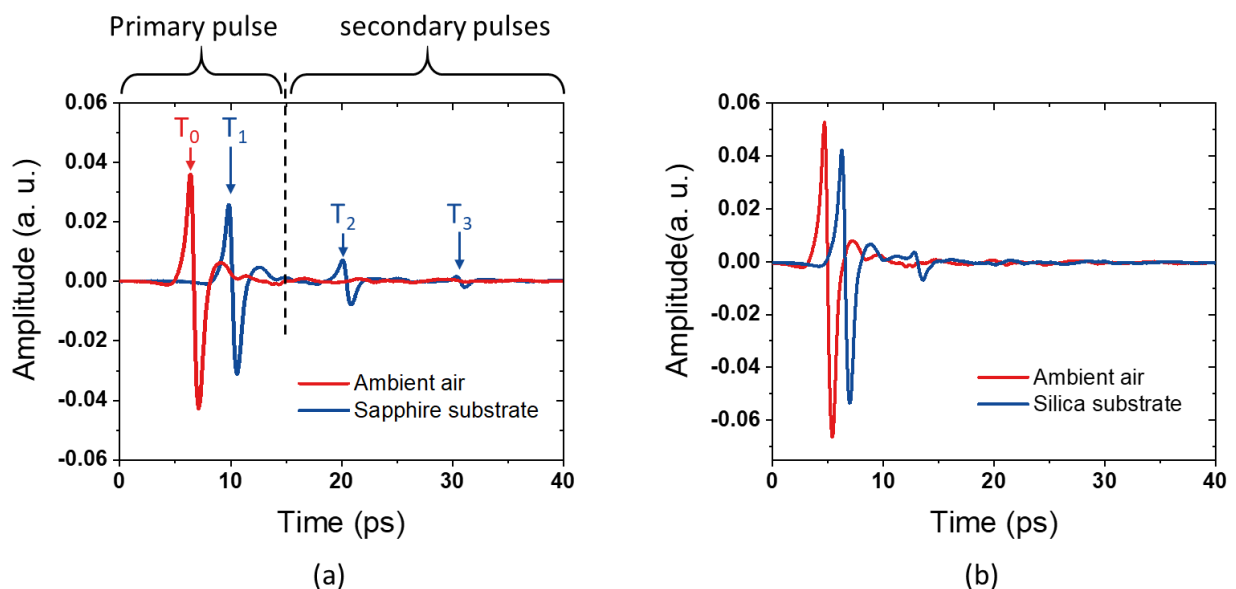
Figure II-9: (a) Temporal THz-TDS measure of a sapphire substrate and of the air reference. (b) Same measures realized with silica substrate

If we compare the measures of the air (reference) and the substrate, we can clearly see the effect of the substrate on the temporal trace of the THz transmission. First, we can

observe a temporal delay T_1-T_0 of the first pulse between the two measures due to the optical path difference introduced by the substrate. This delay can be expressed as:

$$T_1 - T_0 = \frac{(n_b - n_a)L_b}{c_0} \qquad (II.2.)$$

With:

- n_a : group index of air

- n_b, L_b : group index and thickness of sapphire substrate

- c_0 : light speed in vacuum

Secondly, we can clearly differentiate the primary pulse from the secondary pulse, in this case, the substrate is considered as an optically thick element and we can express:

$$T_2 - T_1 = \frac{2n_b L_b}{c_0} \qquad (II.3.)$$

From equation ($II.1.$) and equation ($II.2.$) we can determine the precise thickness of the substrate, expressed as:

$$L_b = \left(T_0 - \frac{3}{2}T_1 + \frac{1}{2}T_2\right)\frac{c_0}{n_a} \qquad (II.4.)$$

For the substrates we were using, we determined, using a stylus profilometer, a thickness of 483 µm for the sapphire substrate and 510 µm for the silica substrate. Knowing the precise thickness of the substrate, we can determine a first approximation of the group refractive index with equation ($II.2.$) or ($II.3.$). We find a group refractive index of 3.18 for the sapphire substrate and 1.92 for the silica substrate.

Finally, an amplitude decrease of the principal pulse is observed compared to the reference measure due to the absorption and the Fresnel reflection of the substrate (decrease by 25% of the temporal pulse amplitude in the case of sapphire substrate and 24% in the case of silica substrate), which is proportional to the substrate thickness. Under normal incidence, the Fresnel reflection can be expressed as:

$$R_{air-substrate}(\omega) = \frac{\tilde{n}_{air} - \tilde{n}_{substrate}}{\tilde{n}_{air} + \tilde{n}_{substrate}} \qquad (II.5.)$$

Considering the group index we can evaluate the reflection coefficient to -0.31 for the silica substrate and to -0.52 for the sapphire substrate.

II.2.1.2. Characterization in frequency domain

We can now transpose the temporal trace into the frequency domain using a Fourier transformation (FT) which can be expressed as:

$$E(\omega) = \frac{1}{2\pi} \int_{-\infty}^{+\infty} E(t)e^{-j\omega t}\, dt \qquad (II.6.)$$

The Figure II-10 shows the transmission amplitude and phase versus the frequency in the case of a ≈ 500 μm sapphire substrate (previously measured at 483 μm). The amplitude spectrum is composed of periodic oscillations. This phenomenon is due to the Fabry-Perot effect (echoes observed on the temporal measure). The frequency of theses oscillations depends on the time delay between the principal pulse and the first echo of the temporal measure and corresponds to the free spectral range (FSR) of the Fabry-Perot cavity. The FSR can be express as:

$$FSR = \frac{2\pi c_0}{n_b L_b} \qquad (II.7.)$$

The measured period of the oscillations is around 0.12 THz, leading to a group index n_b= 3.19 (with a thickness L_b=483 μm) as the previous estimate value from temporal pulse.
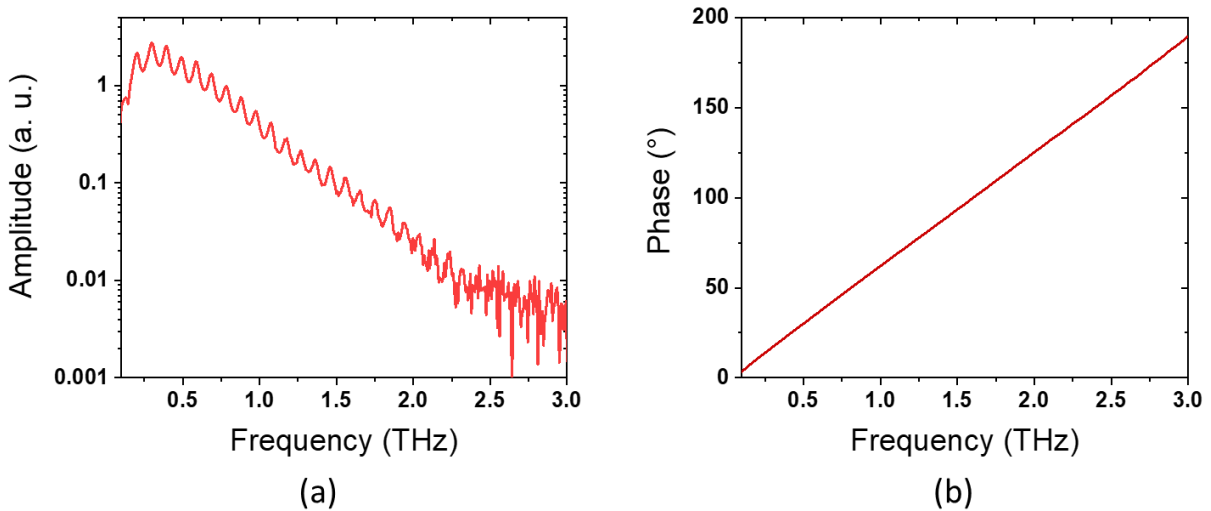
Figure II-10: (a) Amplitude and (b) phase of the transmitted THz signal through a 483 μm sapphire substrate calculated from the temporal measure using a fast Fourier transformation.

These oscillations are only due to the multiple reflections on the substrate faces. In theory, it is possible to define an analytic equation of the transmission from the first pulse without echoes in the temporal measure. To neglect the Fabry-Perot effect and only conserve the first pulse, we « we applied a rectangular window to the temporal signal after the primary pulse and used a method which consists of replacing the deleted data by artificial zeros (Figure II-11).
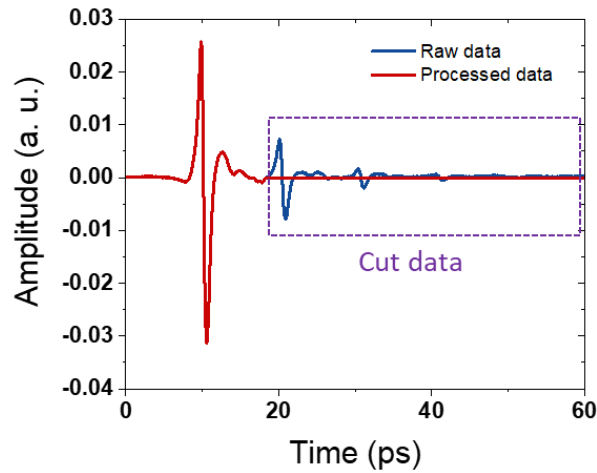
Figure II-11: Graphical explanation of the processing technique on the temporal THz measure

Nevertheless, this method effectively reduces the frequency resolution by smoothing the spectrum and removing very narrow peaks. In our case, no narrow peaks are observed and we can use this technique. On Figure II-12, we characterized the transmission of a 505 μm thick silica and of a 450-μm thick sapphire substrates (obtained by normalizing the measured substrate spectrum by the reference air spectrum).
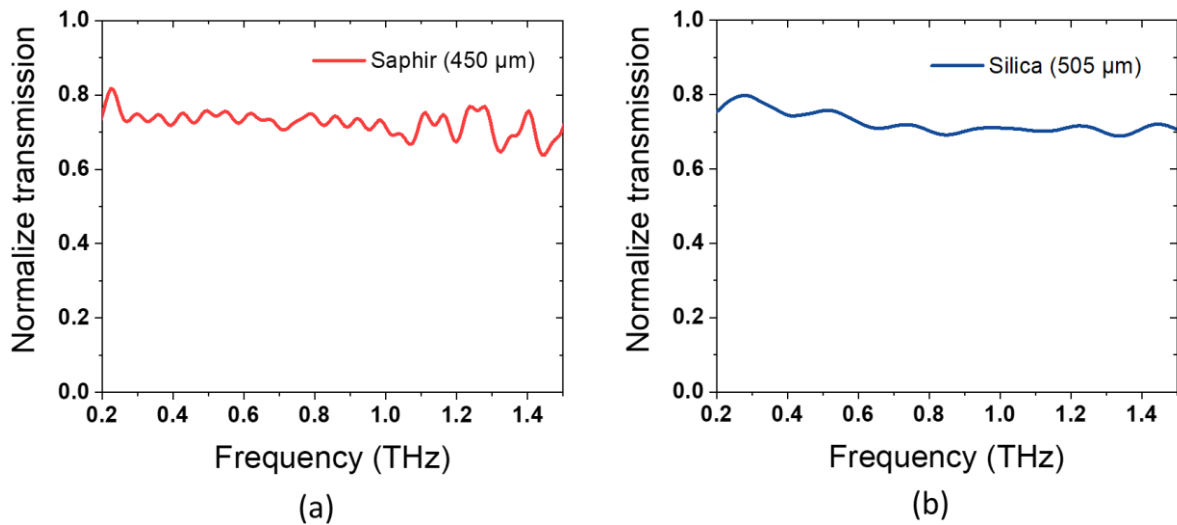
Figure II-12: THz transmission of a (a) sapphire and (b) silica substrate without Fabry-Perot echoes

From this measurement, we observe that both substrates have a flat normalize transmission on the range of frequencies from 0.2 THz to 1.5 THz with a THz transmission coefficient of 0.8.

II.2.1.3. Extraction of the substrate refractive index

From the measures obtained using THz-TDS, we can calculate the absorption coefficient and the complex refractive index of the silica and sapphire substrates. It is possible

to define an analytic expression of the material transmission, as developed in [10]. We are considering a THz pulse which goes through 3 mediums (A, B, C) defined by their complex refractive index (ñ$_a$, ñ$_b$, and ñ$_c$ with ñ$_b$> ñ$_a$ and ñ$_b$>ñ$_c$) and having thickness of L$_a$, L$_b$ and L$_c$, respectively, as shown on Figure II-13.
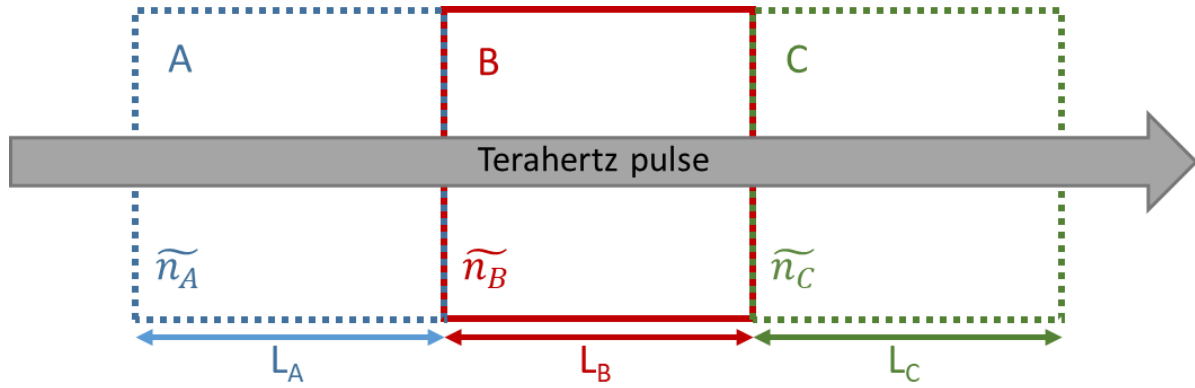
Figure II-13: Schematic showing the transmission of the terahertz pulse through 3 different mediums

The THz transmitted signal S can be expressed as:

$$S(\omega) = E_0(\omega)\,\eta(\omega)A_a(\omega,L_a)T_{ab}(\omega)A_b(\omega,L_b)T_{bc}(\omega)A_c(\omega,L_c)FP(\omega) \qquad (II.8.)$$

With:

- $E_0(\omega)$: the incident THz signal

- $\eta(\omega)$: the internal reflection of the material. If the material is homogenous, the reflection is equal to 1.

- $A_x(\omega,L_x)$: material absorption over the length L$_x$, if we define $\tilde{n}_x = n_x - j\kappa_x$ the absorption can be expressed as:

$$A_x(\omega,L_x) = e^{-\frac{j\tilde{n}_x\omega L_x}{c}} \qquad (II.9.)$$

- $T_{xy}(w)$: transmission at the interface between the material X and the material Y defined as:

$$T_{xy}(\omega) = \frac{2\tilde{n}_x\cos\theta_i}{\tilde{n}_x\cos\theta_i + \tilde{n}_y\cos\theta_t} \qquad (II.10.)$$

In the case of normal incidence, we have: $\cos\theta_i = \cos\theta_t = 1$ and we obtain:

$$T_{xy}(\omega) = \frac{2\tilde{n}_x}{\tilde{n}_x + \tilde{n}_y} \qquad (II.11.)$$

- $FP(\omega)$: Fabry-Perot reflections which can be expressed as:

$$FP(\omega) = \sum_{k=0}^{+\infty}\left\{R_{bc}(\omega)A_b^2(\omega,L_b)R_{ba}(\omega)\right\}^k \qquad (II.12.)$$

Where R_{xy} corresponds to the reflection at the interface between the material X and the material Y express as:

$$R_{xy}(\omega) = \frac{\tilde{n}_x \cos \theta_i - \tilde{n}_y \cos \theta_t}{\tilde{n}_x \cos \theta_i + \tilde{n}_y \cos \theta_t} \qquad (II.13.)$$

In the case of normal incidence, the relation $(II.13.)$ becomes:

$$R_{xy}(\omega) = \frac{\tilde{n}_x - \tilde{n}_y}{\tilde{n}_x + \tilde{n}_y} \qquad (II.14.)$$

Using the analytic values of the sample and reference signals $(II.8.)$ we can define the transmission of the material as expressed in equation $(II.15.)$:

$$T_{sample}(\omega) = \frac{S_{sample}(\omega)}{S_{ref}(\omega)} \qquad (II.15.)$$

If we consider the case of measures realized in the same environment with and without substrate ($\tilde{n}_a = \tilde{n}_c = \tilde{n}_0$) and if we assume that the substrate is optically thick, so echoes are not measured in the temporal window, we can remove the Fabry-Perot reflections ($FP(w)$). Equation $(II.8.)$ can be simplified and we have:

$$S_{ref}(\omega) = S_{air}(\omega) = \eta T_{ab} A_b T_{bc} E_0 = e^{-j\frac{\tilde{n}_0 \omega L_s}{c}} E_0 \qquad (II.16.)$$

$$S_{sample}(\omega) = S_{substrate}(\omega) = T_{ab} A_b T_{bc} \eta E_0 = \frac{4\tilde{n}_0 \tilde{n}_s(\omega)}{(\tilde{n}_0 + \tilde{n}_s(\omega))^2} e^{-j\frac{\tilde{n}_s(\omega) \omega L_s}{c}} \eta E_0 \qquad (II.17.)$$

With:

- $\tilde{n}_s = n_s - j\kappa_s$: complex refractive index of the substrate

- L_s : the thickness of the substrate

The transmission becomes:

$$\tilde{T}(\omega) = \frac{S_{sample}(\omega)}{S_{ref}(\omega)} = \frac{4\tilde{n}_0 \tilde{n}_s(\omega)}{\left(\tilde{n}_0 + \tilde{n}_s(\omega)\right)^2} e^{-j(\tilde{n}_s(\omega) - \tilde{n}_0)\frac{\omega L_s}{c}} \qquad (II.18.)$$

In our case the environment is air ($n_0=1$), leading to the equation:

$$\tilde{T}(\omega) = \frac{4\tilde{n}_s(\omega)}{\left(1 + \tilde{n}_s(\omega)\right)^2} e^{-j(\tilde{n}_s(\omega) - 1)\frac{\omega L_s}{c}} \qquad (II.19.)$$

As we have seen on the transmission spectrum the substrates can be considered as transparent, with $\kappa_s \ll n_s$, leading to this simplification:

$$\tilde{T}(\omega) = \frac{4n_s(\omega)}{\left(1 + n_s(\omega)\right)^2} e^{-\kappa_s \frac{\omega L_s}{c}} e^{-j(n_s(\omega)-1)\frac{\omega L_s}{c}} \qquad (\boldsymbol{II.20.})$$

By definition the transmission from experimental measures can be expressed as:

$$\tilde{T}'(\omega) = \left|\widetilde{T}'(\omega)\right| e^{-j\phi(\widetilde{T\prime}(\omega))} = \frac{E_{sample}(\omega)}{E_{ref}(\omega)} = \frac{\left|E_{sample}(\omega)\right|}{\left|E_{ref}(\omega)\right|} e^{j(\phi_s - \phi_r)} \qquad (\boldsymbol{II.21.})$$

With :

- $\left|\widetilde{T}'(\omega)\right|$: experimental measured amplitude of the sample transmission

- $\phi\left(\widetilde{T}'(\omega)\right)$: experimental measured phase of the sample transmission

By identification of each term, we have:

$$\phi\left(\widetilde{T}'(\omega)\right) = (n_s - 1)\frac{\omega L_s}{c} \qquad (\boldsymbol{II.22.})$$

$$\left|\widetilde{T}'(\omega)\right| = \frac{4n_s}{(1 + n_s)^2} e^{-\kappa_s \frac{\omega L_s}{c}} \qquad (\boldsymbol{II.23.})$$

Leading to:

$$n_s = 1 + \phi\left(\widetilde{T}'(\omega)\right)\frac{c}{\omega L_s} \qquad (\boldsymbol{II.24.})$$

$$k_s = -\frac{c}{\omega L_s} \ln\left(\left|\widetilde{T}'(\omega)\right| \frac{(1 + n_s)^2}{4n_s}\right) \qquad (\boldsymbol{II.25.})$$

And finally, we can determine the absorption coefficient α_s of the substrate:

$$\alpha_s = \frac{2\omega}{c} \kappa_s = \frac{2}{L_s} \ln\left(\left|\widetilde{T}'(\omega)\right| \frac{(1 + n_s)^2}{4n_s}\right) \qquad (\boldsymbol{II.26.})$$

On Figure II-14 we present the extraction of the real part and of the imaginary part of the refractive index of a 450 µm c-cut sapphire substrate and of a 505 µm silica substrate. These calculations are obtained by considering the measures without echoes. For the low frequency domain, in the case of sapphire substrate, k is inferior to 0, due to the noise errors in the k calculation. In the same manner, for the case of silica substrate, we observe an increase of k when the frequency decrease. This increase is an artefact due to the noise of the measure.
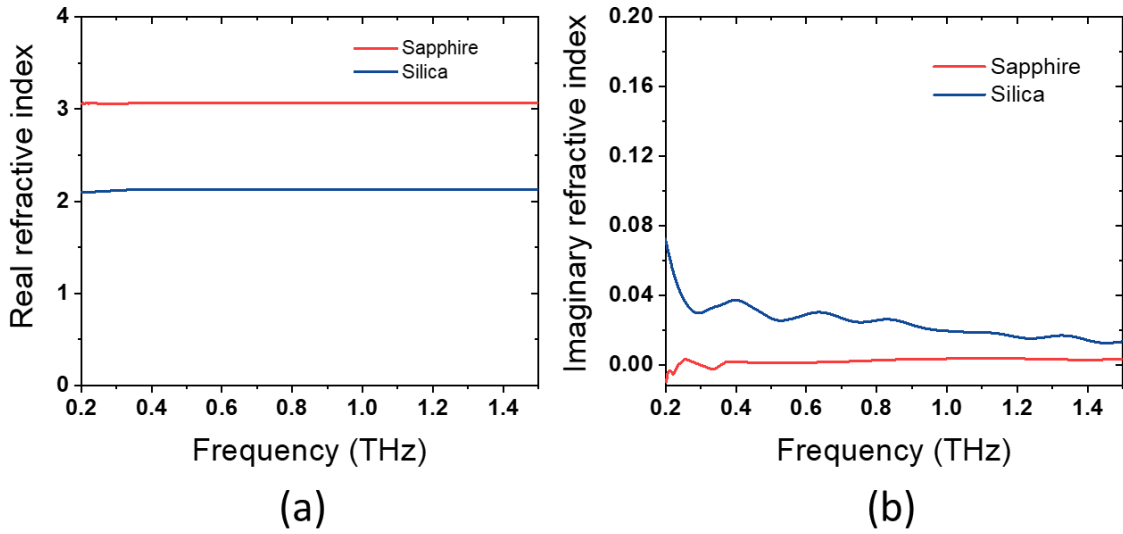
Figure II-14: (a) Real and (b) imaginary part of refractive index of a 450 µm sapphire and a 505 µm silica substrate

We found values in accordance with the silica refractive index measured by M. Naftalya and R. E. Miles (1.96) [11] and the sapphire refractive index found by Youngchan Kim *et al.* (3.19) [12].

The previous results were obtained by suppressing the Fabry-Perot effect. However, using this method we lose information contained in the echoes which may lead to errors in the extracted value of the complex refractive index. To obtain more precise results and quantify this error we tried to extract the refractive index from the same previous THz measurement but by considering the Fabry-Perot effect in the calculation.

In the case the Fabry-Perot effect are taken into account, the theoretical transmission can be expressed as:

$$\tilde{T}(\omega) = \frac{S_{sample}(\omega)}{S_{ref}(\omega)} = \frac{4\tilde{n}_s(\omega)}{\left(1 + \tilde{n}_s(\omega)\right)^2} e^{-j(\tilde{n}_s(\omega)-1)\frac{\omega L_s}{c}} FP(\omega) \qquad (II.27.)$$

With:

$$FP(\omega) = \sum_{k=0}^{M} \left\{ R_{air-substrate}(\omega) A_{substrate}^2(\omega, L_{substrate}) R_{substrate-air}(\omega) \right\}^k \qquad (II.28.)$$

Given:

$$FP(\omega) = \sum_{k=0}^{M} \left\{ \left(\frac{\tilde{n}_s(\omega) - 1}{1 + \tilde{n}_s(\omega)} \right)^2 e^{-2\omega j \frac{\tilde{n}_s(\omega) L_s}{c}} \right\}^k \qquad (II.29.)$$

With M the number of echo pulses included in limited length of the measurement time window. From equation $(II.27.)$, the complex refractive index and the thickness of the sample can be calculated with a numerical optimization algorithm that consists of minimizing the difference between the measured and the theoretical transmission $\tilde{T}'(\omega) - \tilde{T}(\omega)$, such as the Nelder-Mead simplex algorithm as described by Lagarias et al. in [13]. As previously explained, the multiple reflections on the substrate faces cause an oscillation of the transmission in the frequency domain. A closer look at equation $(II.27.)$ reveals that this oscillation depends on the sample thickness L_s and the complex refractive index $\tilde{n}_s(\omega)$. Additional, L_s and $\tilde{n}_s(\omega)$ are linearly independent. This implies that an incorrect L_s value during the calculation of $\tilde{n}_s(\omega)$ will induce oscillations in the calculated refractive index. Only if a correct thickness is chosen, the oscillations are supposed to disappear [14]. For analyzing the FP-oscillations the quasi-space (QS) method is used [14]. As the FP oscillations are periodic in the frequency domain, by applying a Fourier transform to the found material refractive index, we obtain a discrete peak. This Fourier transform is then introduced in the QS. The QS discrete values QS_k can be determined by [14]:

$$QS_k = \sum_{n=0}^{N-1}\left[y(\omega_n)e^{-i\frac{2\pi}{N}kn}\right], k = 0, \ldots, N-1 \qquad (II.30)$$

where $y(\omega_n)$ represents one spectral material parameter (refractive index in our case) and N is the amount of sampling points.

By minimizing the QS value, the correct thickness is determined, and the correct complex refractive index of the sample is obtained. On Figure II-3 the corresponding extracted value of complex refractive index of a sapphire and a silica substrate are presented in solid lines. For comparison the previous values calculated without Fabry-Perot effect are plotted in dashed lines.
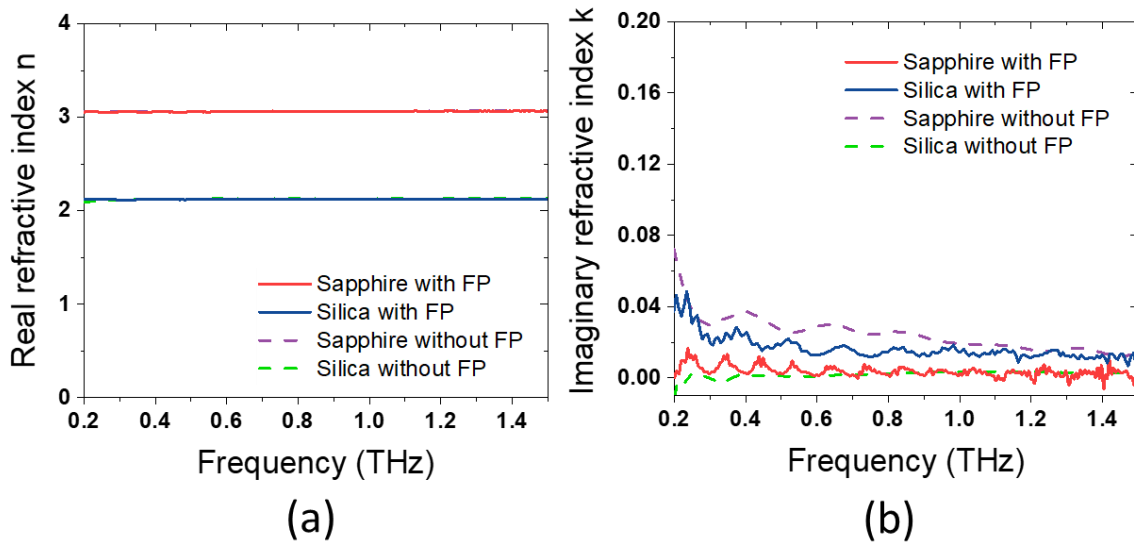
Figure II-15 : (a) Real part of refractive index and (b) Imaginary parts of refractive index of a 450 µm c-cut sapphire and a 505 µm silica substrate when the Fabry-Perot (FP) are considered in the calculation (plain line) and when the FP are removed for the calculation (dash lines).

The found complex refractive index values are similar to the previous measure without FP echoes and we can validate the approximations realized to calculate the refractive index without echoes.

Thus, in this part, we have characterized and calculated the refractive index values of sapphire and silica substrates which present a good agreement with the work realized by M. Naftalya and R. E. Miles and by Youngchan Kim *et al.* [11, 12]. In the next part we will use these values to extract the THz properties of the GeTe film.

II.2.2. Characterization of the THz properties of GeTe thin films

II.2.2.1. Measurements of the THz transmission of GeTe thin films

The temporal measure and the corresponding frequency spectrum of the normalized transmission (corresponding to the transmission of the GeTe film grown on the silica substrate divide by the transmission of the bare substrate) are shown on Figure II-16 for a 250-nm thick GeTe film grown on a silica substrate in both states, amorphous and crystalline (obtained using thermal heating).
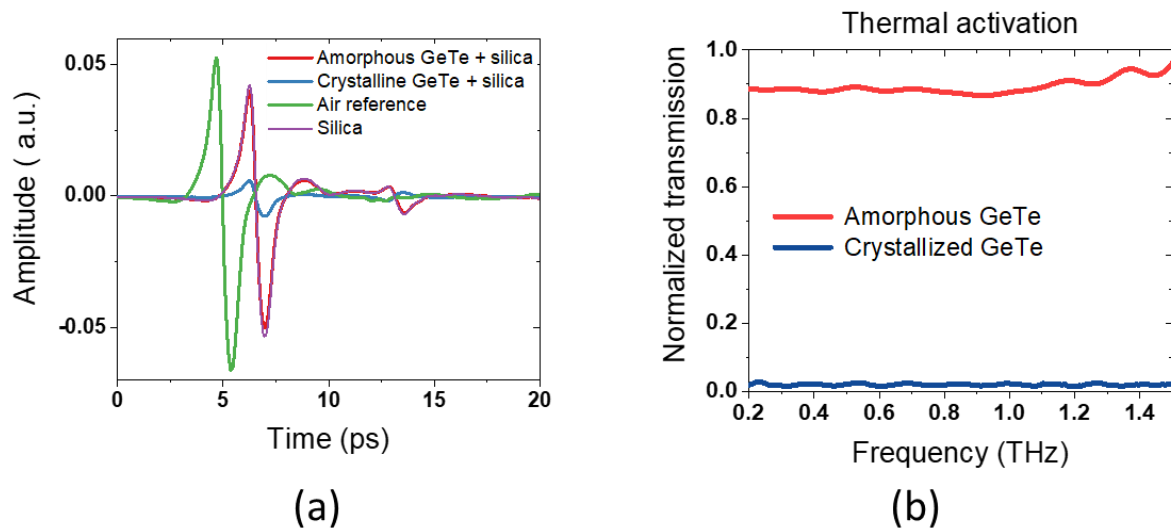
Figure II-16: (a) Temporal THz-TDS measurements for amorphous and crystalline 250 nm GeTe on a silica substrate. (b) Corresponding normalized THz transmission

On the THz temporal spectrum, we observe echoes due to the silica substrate. However, the GeTe film (in amorphous and crystalline phase) does not introduce visible supplementary Fabry-Perot echoes. This is because the GeTe is optically thin, the film optical path (n_{film} x 250 nm) is very small in comparison to the wavelength at 1 THz (300 μm). The GeTe film in the amorphous state has a very low impact on the THz signal transmission, only a decrease by 4.5% of the first pulse amplitude is observed. On the contrary, when the GeTe is crystalline, we observe an important decrease of the first pulse amplitude by 85 %.

This phenomenon implies a decrease of the transmission (Figure II-16b). The transmission at 1 THz decreases by 97% from 0.89 in amorphous phase to 0.02 in crystalline phase. Thus, the amorphous GeTe is almost transparent to the THz waves whereas the crystalline GeTe is absorbent/reflective to the THz waves. GeTe film also presents broadband characteristic with a flat transmission over the studied frequency range.

The transmission of a 250 nm GST film on a silica substrate has also been measured (Figure II-17). As expected, the GST has a similar behavior as the GeTe. However, in crystalline state the GST is more transparent than GeTe (0.6).
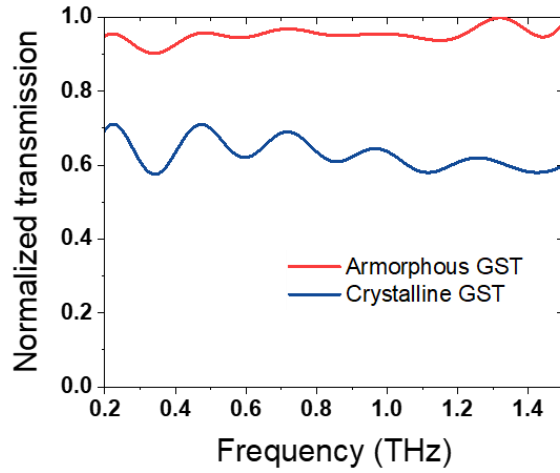
Figure II-17: Normalized THz transmission of a 250 nm GST film obtained on a silica substrate in amorphous and crystalline states without echoes.

This confirms our choice to use GeTe. If we define the modulation as $M = \frac{T_a - T_c}{T_a}$ with T_a, T_c being the transmission of the amorphous phase and the crystalline phase, respectively. For the same thickness (250 nm), the GeTe presents a modulation of 97.7 % instead of 30% for GST. From these results we can conclude that GeTe presents more potential for THz applications.

II.2.2.2. Extraction of the THz properties of amorphous GeTe films

We have shown in the previous section that THz-TDS measurements allows the determination of the THz properties of a sample. For the determination of the complex refractive index ($\tilde{n}_f$) of the GeTe film as previously explained for the substrate case, the basic method consists of numerically solving the equation:

$$T_{sample}(\omega) - T'_{sample}(\omega) = 0 \qquad (II.31.)$$

with $T'_{sample}(\omega) = |T'_{sample}(\omega)| e^{-j\Phi(T'_{sample}(\omega))}$ being the measured normalized transmission and $T_{sample}(\omega)$ the theoretical transfer function. To calculate T_{sample} of the film, we first determine the theoretical transmitted signal of the substrate (considered homogenous) without the film and then determine the signal with the GeTe. Thereafter, the complex conductivity $\tilde{\sigma}(\omega)$ of the film can be extracted using [15]:

$$\tilde{\sigma}(\omega) = j\omega\varepsilon_0(1 - \tilde{n}^2) \qquad (II.32.)$$

Where ε_0 is the permittivity of free space.

Using this method, Kadlec *et al.* proposed to extract THz properties of a 1.12 µm GeTe film deposed on an undoped 500 µm Si substrate [16]. The value they found for the real permittivity and real conductivity extracted for different PCMs are shown on Figure II-18.

Figure II-18: Real permittivity (a) and conductivity (b) spectra of amorphous thin PCM films calculated by Kadlec et al. The symbol corresponds to the experimental data and the lines to fits of the data by a model containing a harmonic oscillator and an additional Drude term [16].

They found a real permittivity around 18 for amorphous GeTe. Considering n²=ε and that amorphous GeTe is very transparent to THz radiation, it corresponds to a refractive index around 4.25. As see on the results proposed by Kadlec *et al.,* the extraction of thin film terahertz properties is very sensitive to the measurement noise of the THz-TDS system and the film must be thick enough to ensure precise measure of the film and reduce the impact of the phase noise on the measure which will introduce an error on the optical path [17]. In consequence, we realized 10 measures of a 500 µm sapphire substrate and a 1 µm GeTe film on the 500 µm sapphire substrate and calculate the average value to reduce errors in the measurement as shown on Figure II-19.

Figure II-19 : Schematic showing the transmission of the terahertz pulse through the substrate and through an amorphous GeTe thin film deposed on a substrate.

In the previous part, we have seen that the theoretical signal of the substrate (considered homogenous) without the film can be expressed as:

$$S_{substrate}(\omega) = E_0(\omega)A_{air}(\omega, L_a)t_{air-substrate}(\omega)A_{substrate}(\omega, L_s)$$
$$\times t_{substrate-air}(\omega)A_{air}(\omega, L_c)FP_{substrate}(\omega) \qquad (II.33.)$$

With:

- $E_0(\omega)$: the incident THz signal

- $A_{air}(\omega, L_a)$: air absorption over the length L_a

- $t_{air-substrate}(\omega)$: transmission at the interface between the air and the substrate

- $A_{substrate}(\omega, L_{substrate})$: substrate absorption over the length L_s

- $t_{substrate-air}(\omega)$: transmission at the interface between the substrate and the air

- $FP(w)$: Fabry-Perot reflections

In the case of a GeTe thin film deposited on a substrate, the theoretical signal of the grown on the substrate can be written as:

$$S_{film}(\omega) = E_0(\omega)A_{air}(\omega, L_a)t_{air-film}(\omega)A_{film}(\omega, L_{film})t_{film-substrate}(\omega)$$
$$\times A_{substrate}(\omega, L_{substrate})t_{substrate-air}(\omega)A_{air}(\omega, L_c)FP_{film+substrate}(\omega) \qquad (II.34.)$$

The transmission of the film can then be determined by:

$$T'_{film}(\omega) = \frac{S_{film}(\omega)}{S_{substrate}(\omega)} = \frac{t_{air-film}(\omega)A_{film}(\omega, L_{film})t_{film-substrate}(\omega)FP(\omega)}{t_{air-substrate}(\omega)} \qquad (\boldsymbol{II.35.})$$

With:

$$FP(\omega) = \frac{FP_{film+substrate}(\omega)}{FP_{substrate}(\omega)} \qquad (\boldsymbol{II.36.})$$

In the case of normal incidence, we obtain:

$$T'_{film}(\omega) = \frac{2\tilde{n}_{film}(\omega)\big(\tilde{n}_{air}(\omega) + \tilde{n}_{substrate}(\omega)\big)e^{-j\frac{\omega L_{film}\big(\tilde{n}_{film}(\omega)-\tilde{n}_{air}(\omega)\big)}{c}}}{\big(\tilde{n}_{air}(\omega) + \tilde{n}_{film}(\omega)\big)\big(\tilde{n}_{film}(\omega) + \tilde{n}_{substrate}(\omega)\big)}FP(\omega) \qquad (\boldsymbol{II.37.})$$

With:

$\tilde{n}_x = n_x - jk_x$: refractive index of the material x

L_{film} : film thickness

To neglect the Fabry-Perot echoes in the measure, the Fabry-Perot cavity must be optically thick, so echoes are not measured in the temporal window. Fabry-Perot echoes are observed in the film if the thickness of the film L is larger than $\frac{\lambda}{2n}$. If we consider a refractive index of 4.25, the thickness of the film must be bigger than 37.5 µm which is not the case. Consequently, no Fabry-Perot resonance occurs in the film but the cavity must be composed of the film and the substrate as shown in Figure II.3-13. To confirm this, we plot the temporal measures on Figure II-20. If the GeTe film is included in the Fabry-Perot cavity, when we compare the temporal trace of the substrate with the one with GeTe film deposited over the substrate, the delay between the first pulse and the first echo should increase in the second case. Indeed, with GeTe film, the first echo passes three times through the film and we have:

$$\Delta T_{2:film,substrate} = 3\Delta T_{1:film,substrate} \qquad (\boldsymbol{II.38.})$$
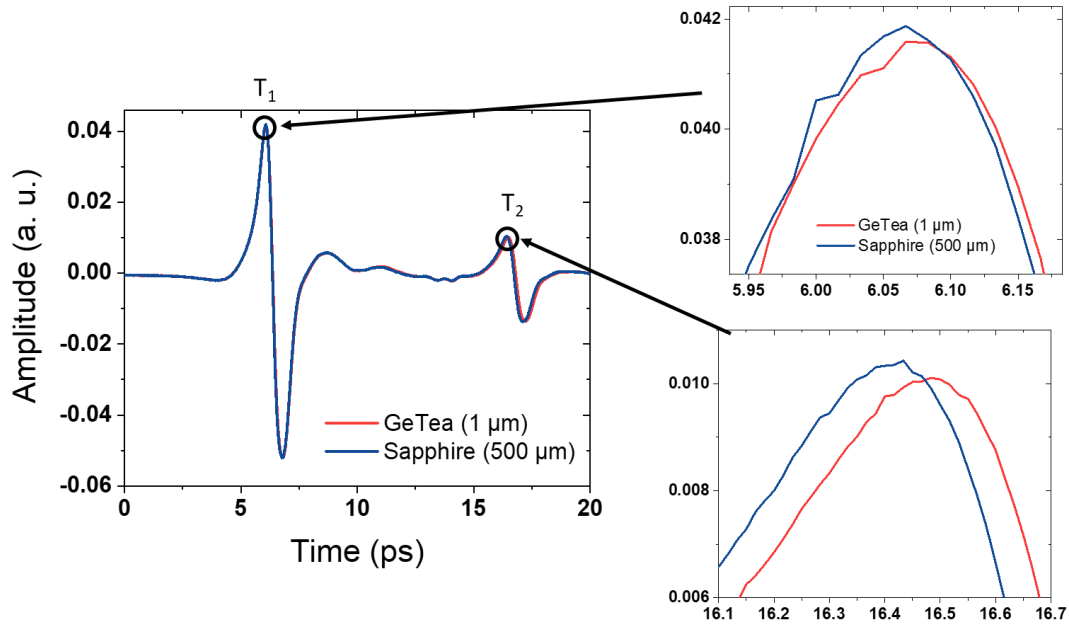
Figure II-20 : Temporal THz-TDS measure of a 1 μm amorphous GeTe film on a sapphire-c substrate and of the sapphire reference with zoom in on the two different pulses

Between the temporal trace of the substrate and the film deposited over the substrate we found a delay ΔT_1 of 17 fs. Considering equation (***II.2***), it corresponds to a group index of 6.1 If we look at the first echoes, we can see an increase of the delay between the two measures to 60 fs corresponding to a group index of 7. This value is closed to $3\Delta T_{1:film,substrate}$ = 51 fs and it confirms a group index value around 6.1 and 7. The difference can be explained by the very small measured delay close to the resolution of the experiment system and the difficulty to extract precise delay time from noise of the measure. To improve the precision of the measure we realized the same measures with 4 μm GeTe film deposited on sapphire substrate (Figure II-21).
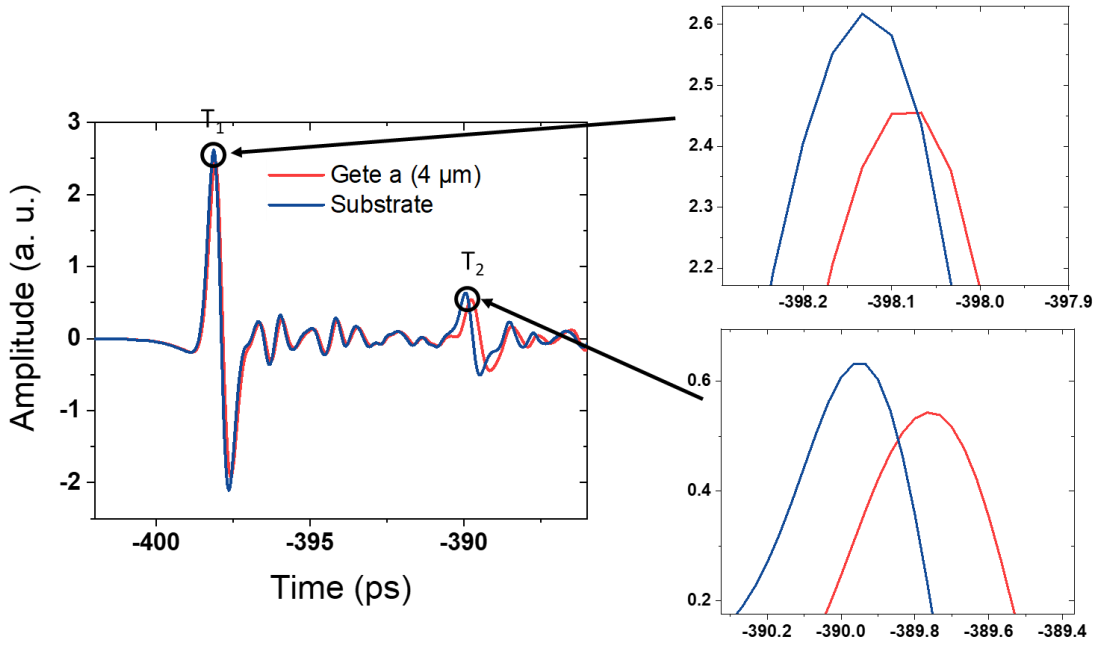
Figure II-21 : Temporal THz-TDS measure of a 4 µm amorphous GeTe film on a sapphire-c substrate and of the sapphire reference with zoom in on the two different pulses

As expected the delay between the two pulses increases and we confirm our previous observations, the delay ΔT_2 (194 fs) is equal to $3\Delta T_1$ corresponding to a group index of 5.8. Therefore, from these results, we can conclude that no Fabry-Perot echoes are presented in the film alone. Additionally, the Fabry-Perot cavity is composed of the film and the substrate and is optically thick.

In this case we can neglect the Fabry-Perot resonances and the transmission of the film can be determined by:

$$T'_{film}(\omega) = \frac{S_{film}(\omega)}{S_{substrate}(\omega)} = \frac{t_{air-film}(\omega)A_{film}(\omega, L_{film})t_{film-substrate}(\omega)}{t_{air-substrate}(\omega)} \qquad (II.39.)$$

Leading in the case of normal incidence to:

$$T'_{film}(\omega) = \frac{2\tilde{n}_{film}(\omega)(\tilde{n}_{air}(\omega) + \tilde{n}_{substrate}(\omega))e^{-j\frac{\omega L_{film}(\tilde{n}_{film}(\omega) - \tilde{n}_{air}(\omega))}{c}}}{(\tilde{n}_{air}(\omega) + \tilde{n}_{film}(\omega))(\tilde{n}_{film}(\omega) + \tilde{n}_{substrate}(\omega))} \qquad (II.40.)$$

Additionally, with $\tilde{n}_{air}(\omega)=1$ and the substrate is considered to be transparent with $\kappa_s \ll n_s$, the equation can be written as:

$$T'_{film}(\omega) = |T'^{(w)}|e^{-j\phi(T'^{(\omega)})} \approx \frac{2\tilde{n}_{film}(\omega)(1 + n_{substrate}(\omega))e^{-j\frac{\omega L_{film}(\tilde{n}_{film}(\omega) - 1)}{c}}}{(1 + \tilde{n}_{film}(\omega))(\tilde{n}_{film}(\omega) + n_{substrate}(\omega))} \qquad (II.41.)$$

We numerically solved equation $(II.30.)$ with MATLAB using the theoretical expression of the transmission (equation $(II.40.)$) and the measured value. The minimum analyzable thickness of the previous algorithm and QS method used for the determination of the substrate refractive index is limited to [14]:

$$L_{film,min} = \frac{c_0}{2n_{film}\Delta f} \qquad (II.42.)$$

With Δf the spectral range of the measurement bench. Consequently, to measure a 1 µm amorphous GeTe film with this method, if we consider $n_{film} = 5.8$ we need a THz-TDS system with a spectral range of 26 THz. Whereas, to a measure a 4 µm film a spectral range of 6.4 THz is required. Our system only has a bandwidth of 1.5 THz, thus it is not possible to use the QS method used in the previous part. To solve the equation, the n and k values are initially fixed arbitrarily near the value reported by previous works on PCM [16, 18]. Increasing step by step the values of n and k we search the minimum of equation $(II.31.)$. Once a minimum is found, we repeat the procedure with a smaller step between each value. The obtained refractive index for amorphous phase is shown on Figure II-22. Due to the difficulty to extract precise and relevant value because of the phase noise of the system we choose to focus on the case of a 4 µm GeTe film.
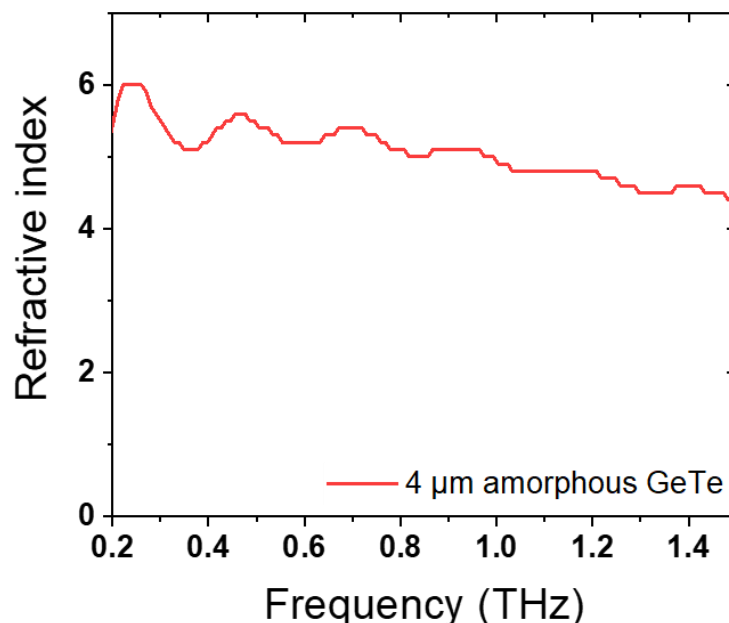
Figure II-22 : Calculated refractive index for 4 µm amorphous GeTe deposed on sapphire substrate.

To validate these experimental results, we tried another approach proposed by J.L Coutaz *et al.* to precisely determine the refractive index of amorphous GeTe [15]. If we consider a THz wave propagate through a multilayer structure (Figure II-23).
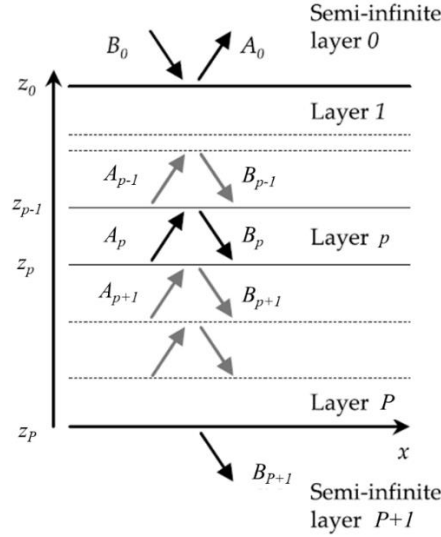
Figure II-23: Reflection and transmission by a multilayer structure [15]

The transfer function $M_{p,p+1}$ between the layer p+1 and layer p can be express as:

$$M_{p,p+1} = \frac{1}{t_{p,p+1}} \begin{pmatrix} e^{j\frac{\omega}{c}(\tilde{n}_p - \tilde{n}_{p+1})z_p} & r_{p,p+1}e^{j\frac{\omega}{c}(\tilde{n}_p - \tilde{n}_{p+1})z_p} \\ r_{p,p+1}e^{-j\frac{\omega}{c}(\tilde{n}_p - \tilde{n}_{p+1})z_p} & e^{-j\frac{\omega}{c}(\tilde{n}_p - \tilde{n}_{p+1})z_p} \end{pmatrix} \qquad (\boldsymbol{II.43.})$$

Where $t_{p,p+1}$ and $r_{p,p+1}$ are the transmission and the reflection coefficients from layer p to layer p+1, respectively.

Consequently, in the case of a substrate covered by a film (two layers) at normal incidence the transmission can be written as:

$$\tilde{T}(n,\kappa,\omega) = \frac{1}{M_T(2,2)} = \frac{1}{\left(\prod_{p=0}^{2} M_{p,p+1}\right)(2,2)} \qquad (\boldsymbol{II.44.})$$

In general case the resolution of this equation is very difficult because the signature of the film is strongly perturbed by the Fabry–Perot resonances in the substrate. However, in our case we can make some hypothesis to simplify the problem. The substrate is supposed to be transparent ($\tilde{n}_s = n_s$) and thick enough to permit a time-windowing of only the first transmitted pulse. Finally, the film is supposed to be thin, meaning that:

$$\frac{nd\omega}{c} \ll 1 \qquad (\boldsymbol{II.45})$$

For a 4 μm GeTe film, at 0.3 THz, we found a value of 0.1. Therefore, we can consider the film optically thin. In this case the relative change of the THz field transmitted by the covered substrate in regard to the bare substrate can be expressed:

$$\Delta\tilde{T}(n_f,\kappa_f,\omega) = \frac{\tilde{T}_{covered}(n_f,\kappa_f,\omega) - \tilde{T}_{bare}(n_s,\omega)}{\tilde{T}_{bare}(n_s,\omega)} \qquad (\boldsymbol{II.46.})$$

If subscripts f, s and a refer to the film, the substrate and the ambient air, respectively, we have:

$$\tilde{T}_{covered}(n_f, \kappa_f, \omega) = t_{as}t_{fa}t_{sf}\frac{e^{-j\frac{\omega}{c}(L_f - L_s)}e^{-j\frac{\omega}{c}L_f\tilde{n}_f}}{1 + r_{fa}r_{sf}e^{-2j\frac{\omega}{c}L_f\tilde{n}_f}} \qquad (II.47.)$$

$$\tilde{T}_{bare}(n_s, \omega) = t_{as}t_{sa}e^{-j\frac{\omega}{c}(L_f - L_s)}e^{-j\frac{\omega}{c}L_f} \qquad (II.48.)$$

Given:

$$\Delta\tilde{T}(n_f, \kappa_f, \omega) = \frac{t_{fa}t_{sf}}{t_{sa}}\frac{e^{-j\frac{\omega}{c}(\tilde{n}_f - 1)L_f}}{1 + r_{fa}r_{sf}e^{-2j\frac{\omega}{c}L_f\tilde{n}_f}} - 1 \qquad (II.49.)$$

Considering we have a thin film, we can realize a development in series of the exponential terms and we obtain:

$$\Delta\tilde{T}(n_f, \kappa_f, \omega) \approx -j\frac{\omega}{c}L_f\frac{\tilde{n}_f^2 - 1}{n_s + 1} \qquad (II.50.)$$

From equation $(II.49)$ we can deduce:

$$n_f^2 \approx 1 - \frac{(n_s + 1)c}{L_f\omega}Im\Delta\tilde{T}(\omega), \qquad \kappa_f \approx \frac{-(n_s + 1)c}{2L_f\omega n_f}Re\Delta\tilde{T}(\omega) \qquad (II.51.)$$

Using equation $(II.51.)$ we calculated the complex refractive index 4 µm thick GeTe film grown on sapphire substrate (500 µm) (Figure I-24).
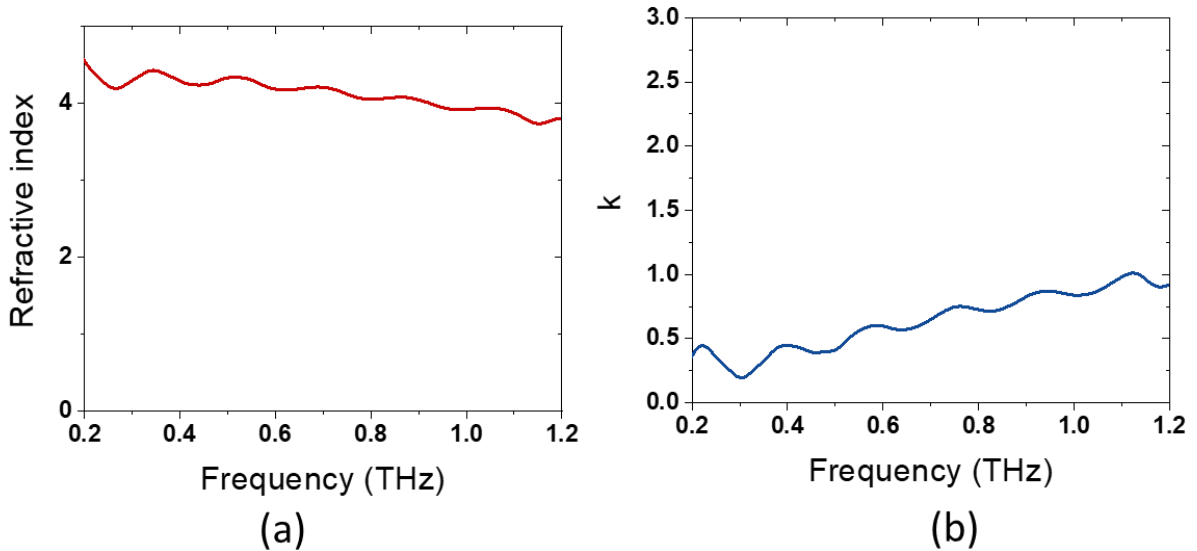
Figure II-24 : Measured (a) real part and (b) imaginary part of the refractive index of a 4 µm amorphous GeTe film deposited on a 500 µm sapphire substrate.

For a 4 µm GeTe film we found a permittivity value of 15.75 ($\varepsilon_f = \tilde{n}_f^2$). As explained, from the refractive index values, it is possible to extract the conductivity using equation ($II.32.$) (Figure II-25).
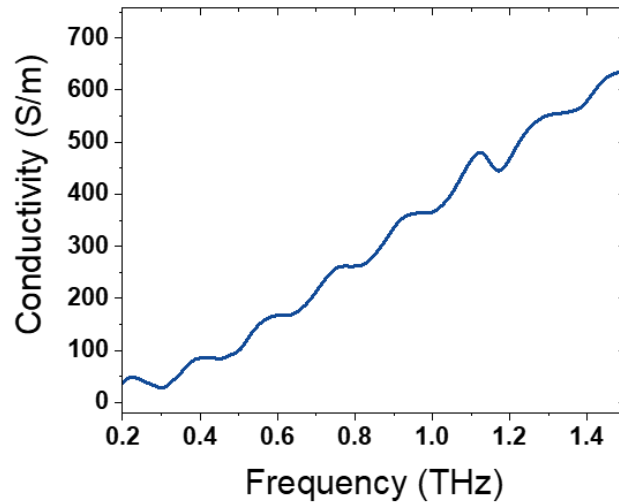
Figure II-25 : THz conductivity values of a 4 µm GeTe film deposed on a 500 µm sapphire substrate.

We found low conductivity values in accordance with the high resistivity state of the amorphous GeTe film. In the case of a 4 µm film we found a conductivity value in accordance with previous works [16]. The increase of the conductivity with the frequency is mainly due to a Drude conductivity behavior [16].

II.2.2.3. Extraction of the THz properties of crystalline GeTe films

In the case of crystalline GeTe the same method can be applied to extract THz properties using equation ($II.31.$). From this method Kadlec *et al.* calculated the real permittivity and conductivity of different crystalline PCM films (Figure II-26).
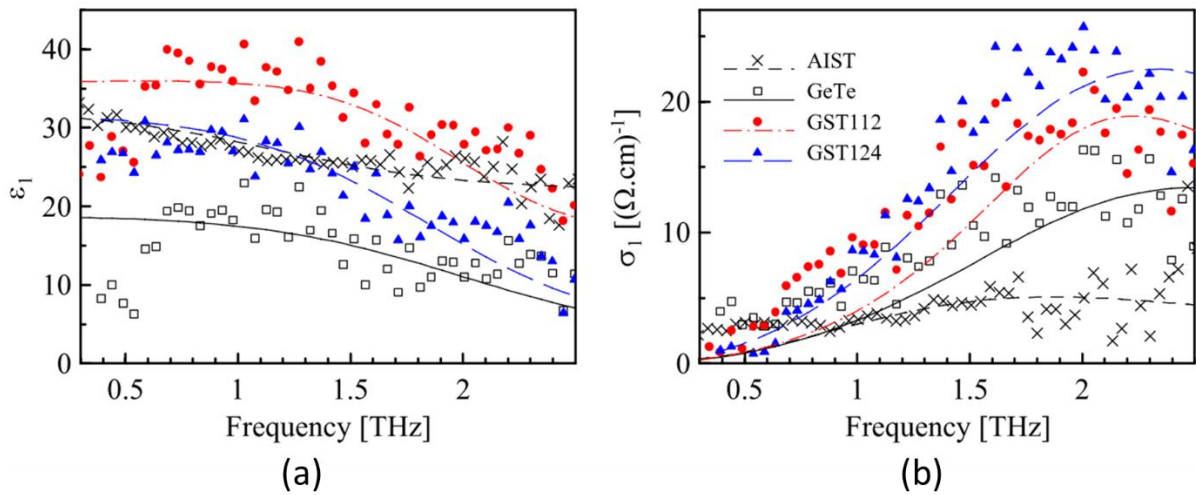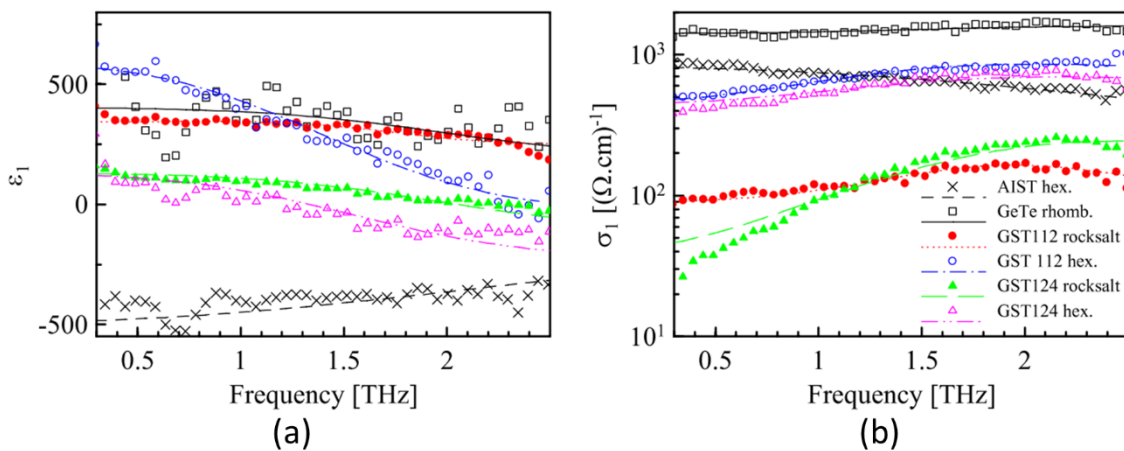

Figure II-26 : Real permittivity (a) and conductivity (b) spectra of crystalline thin PCM films calculated by Kadlec et al. The symbol corresponds to the experimental data and the line to fit of the data [16].

As expected from the metallic behavior of the crystalline phase, they found a high conductivity around 140 kS/m and a permittivity around 400 corresponding to a refractive index around 20.

To obtain crystalline GeTe we heat the previous amorphous films at 300°C using a heating plate until complete crystallization. As before, we then realized 10 measures of a 500 µm sapphire substrate and a 1 µm and a 4 µm GeTe film on the 500 µm sapphire substrate and calculate the average value to reduce errors in the measurement. Figure II-27 show the temporal trace of a 4 µm crystalline GeTe film.
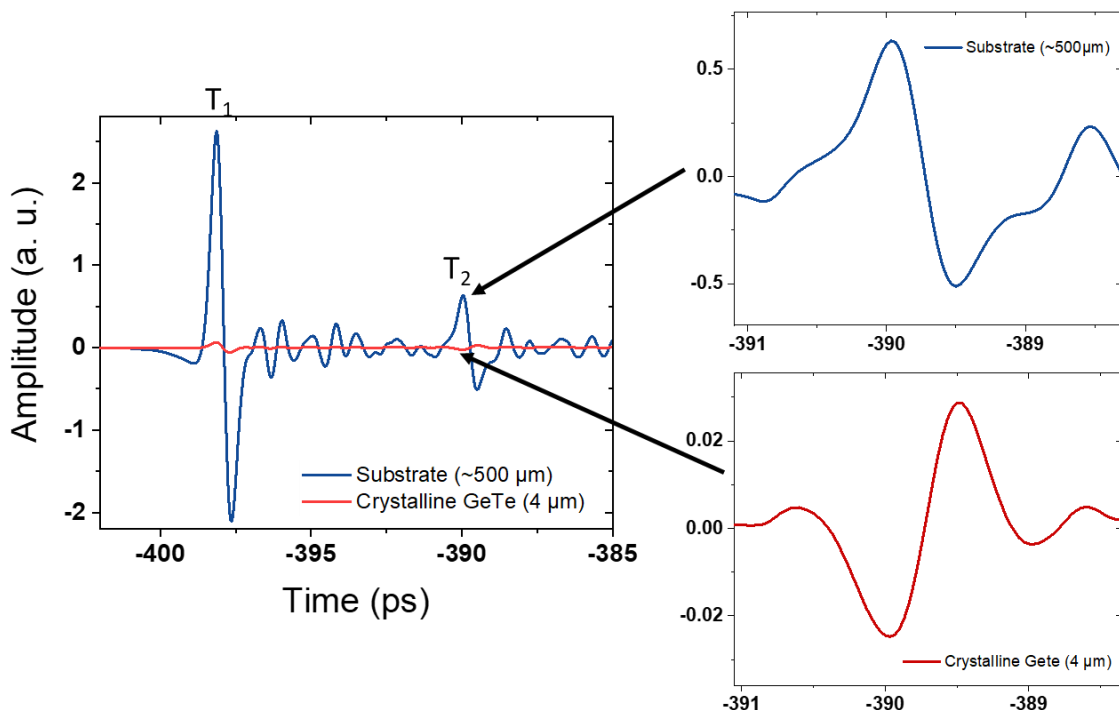
Figure II-27 : Temporal THz-TDS measure of a 4 µm crystalline GeTe film on a sapphire-c substrate and of the sapphire reference with zoom in on first Fabry-Perot echo of the substrate and of the film.

The first observation is that the crystalline GeTe film induces a change of sign (delay by π) of the first echo characteristic to a metallic film. Secondly, if we look at the delay ΔT_2 between the GeTe film and the substrate, no increase of the value is observed compared to the delay ΔT_1 between the direct transmitted pulses. This suggests that the film is highly reflective and the Fabry-Perot resonance occurs only in the substrate (Figure II-28).
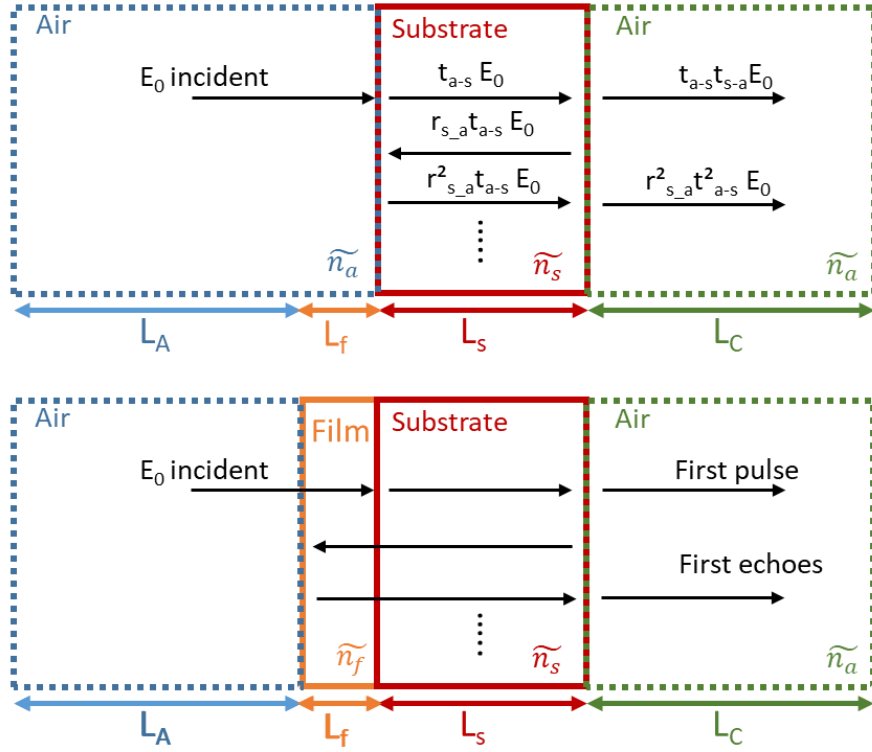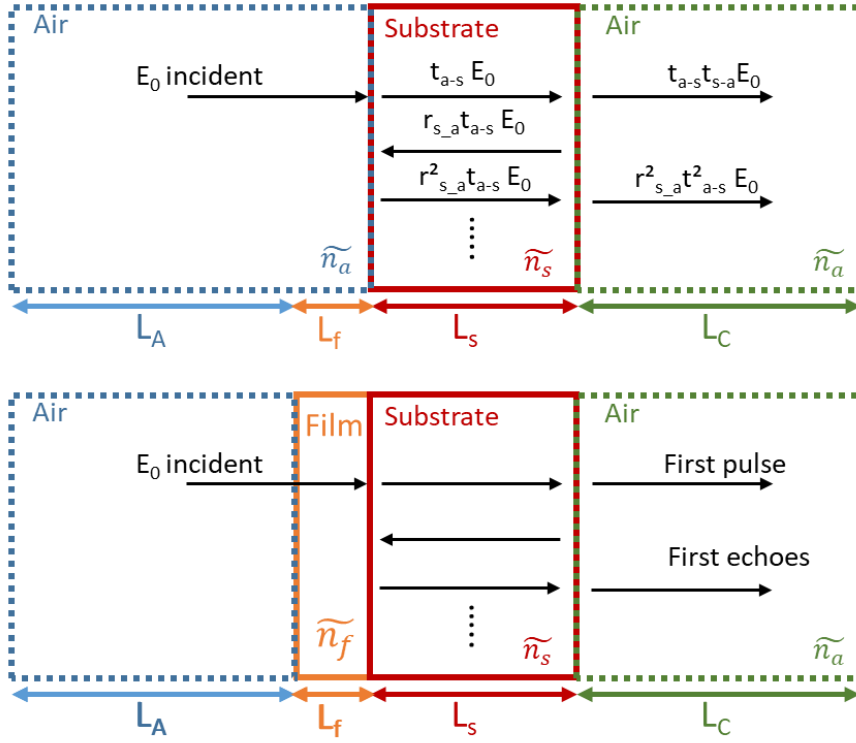
Figure II-28 : Schematic showing the transmission of the terahertz pulse through the substrate and through a crystalline GeTe thin film deposed on a substrate.

In this case, the transmitted signal within the thin film can be expressed as:

$$S_{film}(\omega) = E_0(\omega)A_{air}(\omega, L_a)t_{air-film}(\omega)A_{film}(\omega, L_{film})t_{film-substrate}(\omega)$$
$$\times A_{substrate}(\omega, L_{substrate})t_{substrate-air}(\omega)A_{air}(\omega, L_c)FP_{substrate}(\omega) \qquad (II.52.)$$

In the case of normal incidence, the transmission of the film can be expressed as:

$$T'_{film}(\omega) = \frac{S_{film}(\omega)}{S_{substrate}(\omega)} = \frac{t_{air-film}(\omega)A_{film}(\omega, L_{film})t_{film-substrate}(\omega)}{t_{air-substrate}(\omega)} \qquad (II.53.)$$

Leading to:

$$T'_{film}(\omega) = |T'^{(w)}|e^{-j\phi(T'^{(\omega)})} \approx \frac{2\tilde{n}_{film}(\omega)\left(1 + n_{substrate}(\omega)\right)e^{-j\frac{\omega L_{film}(\tilde{n}_{film}(\omega)-1)}{c}}}{\left(1 + \tilde{n}_{film}(\omega)\right)\left(\tilde{n}_{film}(\omega) + n_{substrate}(\omega)\right)} \qquad (II.54.)$$

Using the same method as for the amorphous film, we extracted the refractive index of 1 μm and 4 μm crystalline GeTe deposited on a sapphire substrate using Mathlab software. However, due to the low amplitude of the measured signal in crystalline phase the noise on the measure is important and the numerical simulation does not converge.

To overcome this difficulty we tried another method based on approximation which can be used to calculate analytic value of the conductivity.

In the crystalline state, the GeTe film is metallic. We can determine the conductivity of the film $\sigma_f(\omega)$ using the transmission equation used to determine the THz conductivity of metallic films [19, 20]. This method has notably been used for the determination of the conductivity of thin phase transition material films such as VO₂ [21, 22]. In the case of a thin film deposed over a substrate, the transmission can then be express as [23]:

$$T'_{film} = \frac{2\tilde{n}_f(\tilde{n}_a + \tilde{n}_s)e^{-j\frac{\omega L_f(\tilde{n}_f - \tilde{n}_a)}{c}}}{(\tilde{n}_a + \tilde{n}_f)(\tilde{n}_f + \tilde{n}_s) + (\tilde{n}_f - \tilde{n}_s)(\tilde{n}_f - \tilde{n}_a)e^{-j\frac{2\omega\tilde{n}_f L_f}{c}}} \qquad (II.55.)$$

With:

- $\tilde{n}_a$: air refractive index

- $\tilde{n}_s = n_s - jk_s$: substrate refractive index

- $\tilde{n}_f = n_f - jk_f$: thin film refractive index

- L_f : film thickness

Considering $\tilde{n}_{air}(\omega)=1$ we obtain:

$$T'_{film} = \frac{2\tilde{n}_f(1 + \tilde{n}_s)e^{-j\frac{\omega L_f(\tilde{n}_f - 1)}{c}}}{(1 + \tilde{n}_f)(\tilde{n}_f + \tilde{n}_s) + (\tilde{n}_f - \tilde{n}_s)(\tilde{n}_f - 1)e^{-j\frac{2\omega\tilde{n}_f L_f}{c}}} \qquad (II.56.)$$

For optically thin films, the transmission can be developed as:

$$T'_{film}(\omega) = \frac{\tilde{n}_a(\omega) + \tilde{n}_s(\omega)}{B(\omega)}\left(1 - j\frac{\left(\tilde{n}_f(\omega) - \tilde{n}_a(\omega)\right)\omega L_f}{c}\right) \qquad (II.57.)$$

With:

$$B(\omega) = \tilde{n}_a(\omega) + \tilde{n}_s(\omega) + j\frac{\left(\tilde{n}_f^2(\omega) - \tilde{n}_f(\omega)\tilde{n}_a(\omega) - \tilde{n}_s(\omega)\tilde{n}_f(\omega) + \tilde{n}_a(\omega)\tilde{n}_s(\omega)\right)\omega L_f}{c} \qquad (II.58.)$$

In the case of metallic film, we have:

$$\varepsilon_f(\omega) = 1 - j\frac{\tilde{\sigma}_f(\omega)}{\omega\varepsilon_0} \qquad (II.59.)$$

with:

- $\varepsilon_f(\omega) = \varepsilon_f'^{(\omega)} - j\varepsilon_f''(\omega)$ complex permittivity of the film

- $\tilde{\sigma}_f(\omega) = \sigma_f'^{(\omega)} - j\sigma_f''(\omega)$ complex conductivity of the film

Moreover, considering the film does not have a magnetic response (μ_f = 1), we have:

$$\varepsilon_f(\omega) = \tilde{n}_f^2(\omega) = (n_f - jk_f)^2 \qquad (II.60.)$$

Thus, we can write the following equation:

$$B(\omega) = \tilde{n}_a(\omega) + \tilde{n}_s(\omega) + j\frac{\left(1 + j\dfrac{\sigma_f(\omega)}{\omega\varepsilon_0} - \tilde{n}_f(\omega)\tilde{n}_a(\omega) - \tilde{n}_s(\omega)\tilde{n}_f(\omega) + \tilde{n}_a(\omega)\tilde{n}_s(\omega)\right)\omega L_f}{c} \qquad (II.61.)$$

Leading to:

$$B(\omega) = \tilde{n}_a(\omega) + \tilde{n}_s(\omega) + \sigma_f(\omega)L_f Z_0$$
$$+j\frac{\left(\varepsilon_\infty - \tilde{n}_f(\omega)\tilde{n}_a(\omega) - \tilde{n}_s(\omega)\tilde{n}_f(\omega) + \tilde{n}_a(\omega)\tilde{n}_s(\omega)\right)\omega L_f}{c} \qquad (II.62.)$$

Finally, considering that we have a thin film ($L_f \ll \lambda$) and $\omega = \frac{2\pi c}{\lambda}$, the transmission can be written as [20]:

$$T_f(\omega) = \frac{\tilde{n}_a(\omega) + \tilde{n}_s(\omega)}{\tilde{n}_a(\omega) + \tilde{n}_s(\omega) + \sigma_f(\omega)L_f Z_0} \qquad (II.63.)$$

With:

- $Z_0 = \frac{1}{\varepsilon_0 c}$: vacuum impedance (= 376.7 Ω)

- $T_f(\omega) = |T_f(\omega)|e^{-j\Phi(T_f(\omega))}$: experimentally recorded THz transmission of the GeTe film in the two states

Namely:

$$\sigma_f(\omega) = \frac{\tilde{n}_a(\omega) + \tilde{n}_s(\omega)}{T_f(\omega)L_f Z_0} - \frac{\tilde{n}_a(\omega) + \tilde{n}_s(\omega)}{L_f Z_0} \qquad (II.64.)$$

Knowing the refractive index of the substrate, we can determine the conductivity of the GeTe film depending on the frequency. The THz conductivity value for a 1 µm and 4 µm GeTe film (on sapphire substrate) in crystalline phase is presented (Figure II-29).
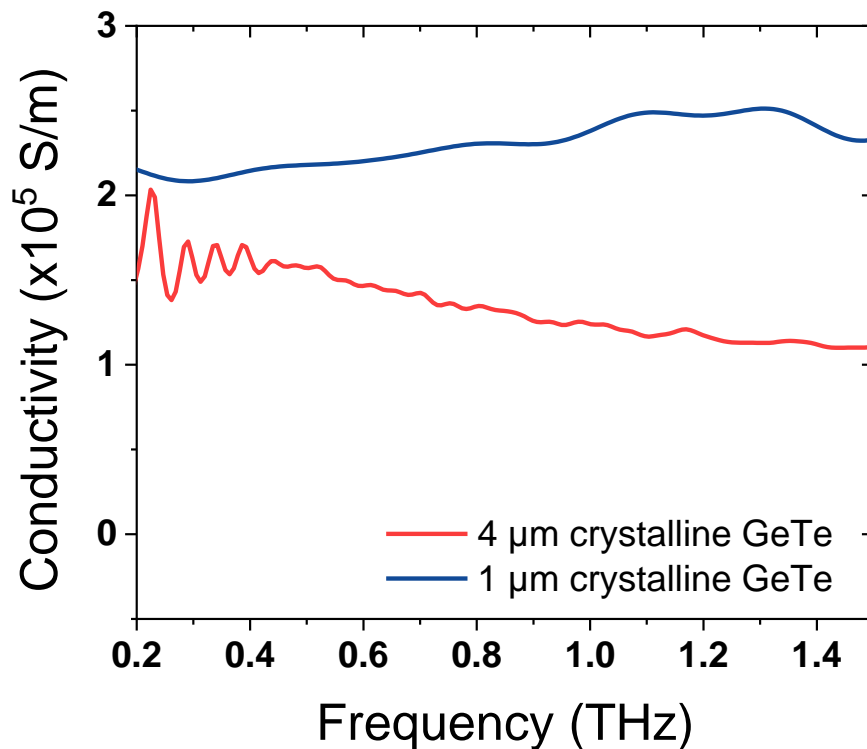
Figure II-29: Extracted conductivity of a 1 µm (blue) and 4 µm (red) crystalline GeTe deposited on a sapphire substrate.

For a 4 µm thick GeTe film on a sapphire substrate we found a conductivity value around 150 kS.m^{-1} that is slightly lower than the 220 kS.m^{-1} measured for the 1 µm GeTe film. This difference can be explained by the lower quality of the film due to the large thickness. Indeed, as previously seen during the measures of DC conductivity of the film, when the thickness of the film increases the resistivity tends to increase (namely the conductivity decrease) due to the increase of impurities and faults in the film. If we compare the value with the report of Kadlec *et al.* we found the same order of magnitude.

In conclusion, in this section, we have highlighted the non-volatile phase change phenomenon in the THz domain. This phenomenon induces significant variations of the transmission amplitude of an incident THz signal on the material. More precisely, the transformation from amorphous to crystalline phase of the GeTe film is accompanied by a significant decrease of the THz transmission, which changes from a quasi-perfect transmission to a transmission in the order of 2% in a broad frequency domain. THz-TDS allows the recording of the amplitude and phase of a THz signal transmitted through the sample and, thus, determine the conductivity of the thin films. Even if the extracted conductivity values are approximated, they confirm that the variation of the THz transmission is a consequence of the GeTe conductivity change in the THz range. Thus, bare GeTe films can be used for the realization of switches or attenuators in the THz domain. However, we can envisage integrating

GeTe in more complex structures for the realization of complex THz devices such as filters, polarizers, flat lenses, etc.

II.3. Optical switching of GeTe states using laser pulses

Compared to the PCM crystallization induced by direct heating presented previously, the crystallization induced by laser pulses is characterized by faster heating and cooling times (>10^9 K/s) [24]. In the direct heating case, the heating and cooling speed are too slow to allow the phase change of the material from the crystalline to the amorphous phase. Compared to the electrical activation of PCMs, optical activation does not require supplementary fabrication steps for the polarization lines of the localized heating elements which can perturb the response of the device in which the GeTe material would be integrated.

II.3.1. COMSOL Multiphysics simulation of GeTe optical activation using UV pulses from an excimer laser.

As presented in Chapter I, optically induced phase change of GeTe material requires a good control of the laser parameters (pulse duration, fluence…) which are essential to ensure a correct crystallization or amorphization of the GeTe film.

In our experiments we used a KrF* excimer laser with a wavelength of 248 nm, a repetition rate from 1 Hz to 20 Hz and a fixed super Gaussian pulse duration of 35 ns (Figure II-30). The laser is directed towards the film surface at normal incidence using a mirror. The incident energy of the laser pulse can be modified between 30 mJ and 200 mJ. A cylindric focus lens (with a focal length of 50 mm) is added to modify the focalization of the system and thus, modify the diameter of the laser beam and further control the incident fluence (corresponding to the energy of a laser pulse divided by the area it is illuminating) on the film surface. To ensure an equal distribution of the laser energy and thus equal heating over the whole illuminated film area, the energy distribution of the laser beam has a 5 mm x 15 mm "flat-top" profile (uniform on the whole surface).
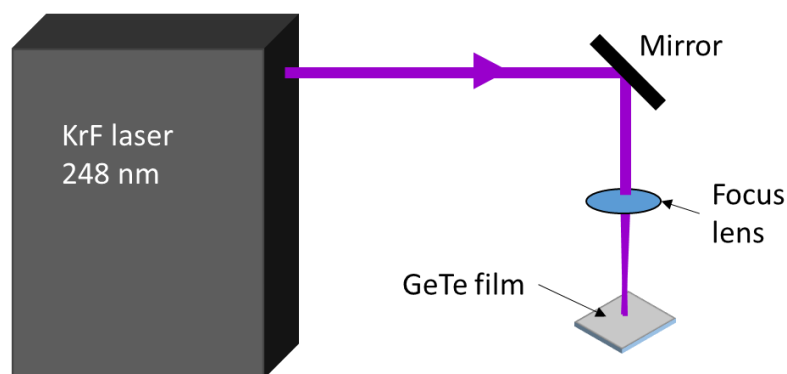
Figure II-30: Schematic of the UV laser exposure bench

To better understand the interaction of the laser beam with the material in order to precisely control the optical activation of GeTe films, we studied the thermal evolution of a GeTe film under different irradiation conditions using finite element method (FEM) with COMSOL Multiphysics software.

II.3.1.1. Model definition of the GeTe film and of the laser beam

When a laser beam hits a material, a part of the energy is absorbed, and localized heating of the material occurs. Consequently, if the laser energy is high enough, it is possible to heat an amorphous GeTe film beyond its crystallization temperature over the film thickness leading to crystalline GeTe. Based on the same principle it is possible to heat a crystalline film above its melting temperature to amorphize a crystalline GeTe film. To simulate this interaction for finding optimal laser energy values, it is necessary to define a model. Depending on the wavelength of the beam and of the material properties (absorption, reflectivity, heat capacity), different approaches for modeling the material heat induced by the laser source can be used.

In our case we used a UV laser beam emitting at 248 nm to activate the GeTe films. At this spectral range, GeTe can be considered as an opaque material [25]. Thus, we can consider that the energy of the beam is absorbed over a small distance into the material and the laser beam can be treated as an uniform surface heat source. In this case, the laser beam is considered as a surface heat load and the spatial distribution of the temperature within the film thickness can be determined using FEM depending on the laser power by resolving the two dimensional heat flow equation [26]:

$$\rho C_p \frac{\partial T}{\partial t} - \nabla(k \nabla T) = Q \qquad (II.65.)$$

With:

- ρ : the density

- C_p : the specific heat

- k : the thermal conductivity

- Q : the heat source term

In the case of volumetric heating with a flat-top laser beam the heat term can be express as:

$$Q(x, y, z) = Q_0(1 - R_c) \frac{A_c}{4 L_x L_y} S(x, y) e^{-A_c z} \qquad (II.66.)$$

With:

- $Q(x, y, z)$: the thermal energy delivered by the laser at one point of the film,

- Q_0 : laser power incident to the surface,

- R_c : the reflection coefficient of the film at the laser wavelength,

- A_c : the absorption coefficient of the film at the laser wavelength,

- L_x and L_y : the length and the width of the incident laser beam area on the film,

- $S(x, y)$: the 2D rectangular distribution of the laser energy in the xy plane on the film,

- $e^{-A_c z}$: the exponential power decay due to the absorption of the film,

II.3.1.2. Definition of the geometry and the meshing parameters

For the simulation under COMSOL, we simulated two different GeTe films with a thickness of 250 nm and 500 nm deposited on a 200 µm sapphire c-cut or silica substrate (Figure II-31). The laser beam is modelled by a rectangular surface (5 mm x 15 mm).
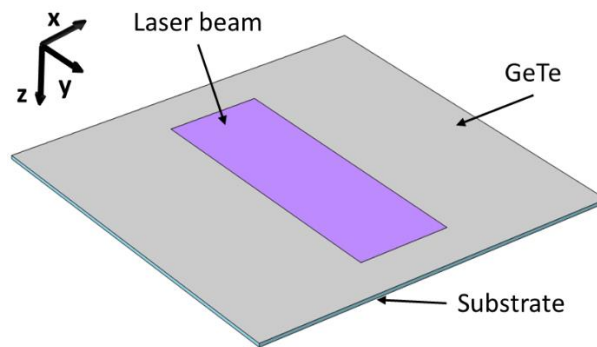
Figure II-31: Schematic of the simulated structure

The mesh discretizes the structure in finite elements to solve the main equation and it is a critical parameter to obtain a correct solution. If the mesh dimensions are too large compared to the structure dimension, we will obtain an incorrect solution. However, decreasing the meshing dimensions will increase the number of sequential calculations and thus the calculation time. We used a mesh with a distance between two nodes limited between 400 nm and 500 nm on the laser beam area to avoid errors. For the mesh distribution along the z axis, to limit the calculation time, we chose to use an asymmetric distribution with an adaptive meshing limited between 10 nm and 35 nm in the GeTe film to obtain precise temperature values. Then the meshing increases proportionally to |z| in the substrate, where the temperature value is less important for the simulation (Figure II-32b). On the areas not exposed to the laser beam, we used a coarse mesh (between 0.18 mm and 1 mm) to reduce the calculation time (Figure II-32).
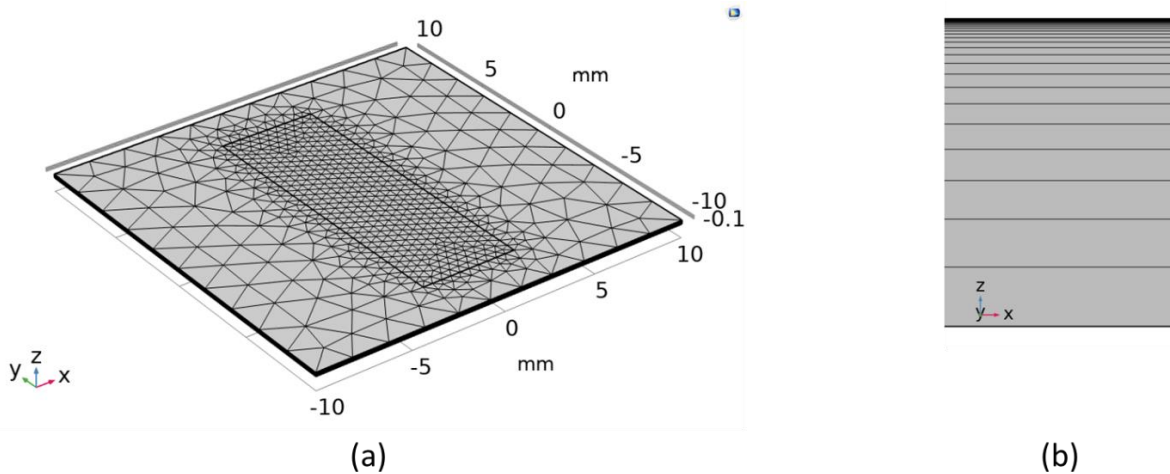
Figure II-32: Meshing of the simulated structure

II.3.1.3. Simulations results

Previous experimental works on GeTe optical activation at Xlim laboratory [4] have defined the optimal fluence for crystallization of GeTe between 85mJ/cm^2 and 90 mJ/cm^2, depending on the film thickness. For the amorphization, it was found that an optimal fluence around occurs at 190mJ/cm^2. Therefore, the corresponding pulse peak power introduced in the COMSOL simulations are 1.1 MW (blue curve Figure II-33) for the GeTe crystallization, and 2.25 MW for the amorphization process (red curve Figure II-33).
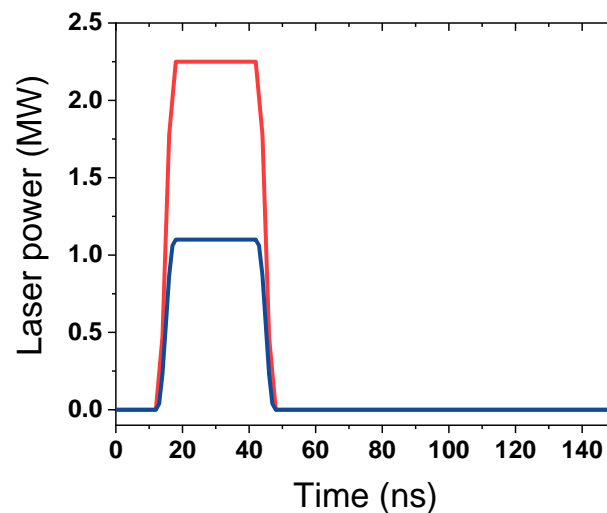
Figure II-33 : Temporal shape of the simulated laser pulse for GeTe amorphization (in red) and for crystallization (blue curve)

As mentioned in chapter I the temperature is a critical parameter to ensure a complete crystallization of the film, since the temperature of the film must be higher than its crystallization temperature through the whole thickness of the film. Figure II-34**a** shows the temperature

distribution depending on the thickness of a 500 nm GeTe film exposed to a KrF* laser pulse (30 ns) for the crystallization case. If the temperature at the surface (908 K) is above the crystallization temperature (T_c), the temperature is below T_c starting from a depth of 375 nm. Thus, the laser energy is not high enough to crystallize all the material along its thickness. A solution could be to use several laser pulses instead of one or to use thinner GeTe films. Figure II-34**b.** shows the simulations of a thinner 250 nm GeTe film on sapphire substrate. When we reduce the thickness of the GeTe film the cooling time (time necessary for the film to return to the ambient temperature after heating) of the film decreases and the maximum surface temperature value decreases. This is due to a better thermal dissipation along the film thickness. Consequently, except near the interface between the film and the substrate, the film temperature is above T_c and we can expect a good crystallization of the GeTe film within all its thickness.
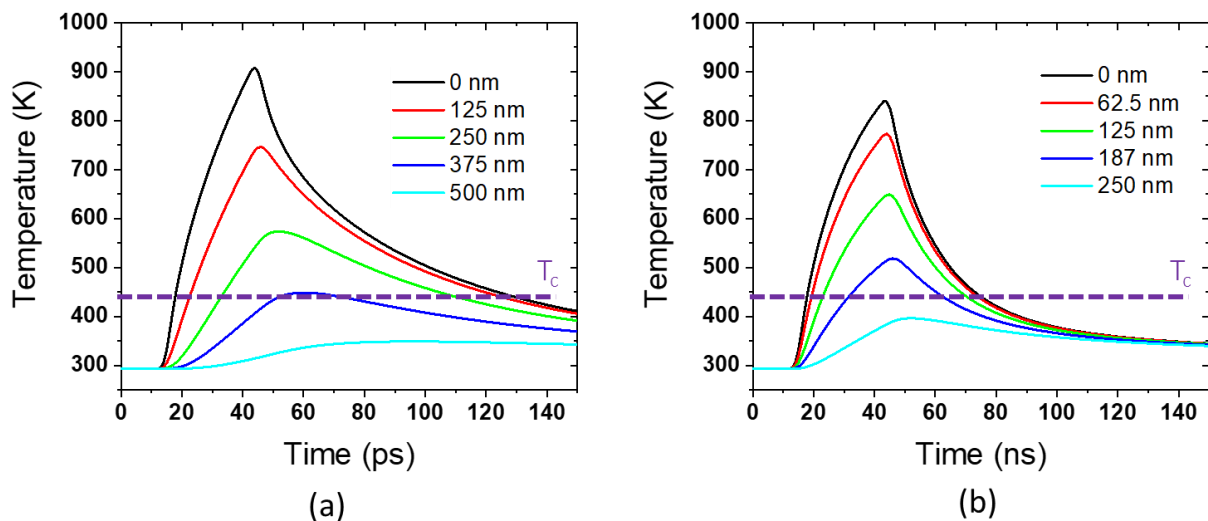
Figure II-34: Temperature evolution with time of a GeTe film at different depths during crystallization process for (a) 500 nm GeTe on a sapphire substrate and (b) a 250 nm GeTe on a sapphire substrate (T_c corresponding to the crystallization temperature).

During the amorphization of a 250 nm crystalline GeTe film (Figure II-35), we can observe the fast heating-cooling cycle of the film, after 100 ns the GeTe temperature is below the crystallization temperature. This fast cooling is compatible with the melt-quenching dynamics of the crystalline-to-amorphous process in the GeTe film. Secondly, the maximum temperature at the surface is above the melting temperature (T_m) and reaches 1500 K. Nevertheless, when we go deeper in the film, the temperature decreases rapidly and at 200 nm the maximum temperature is below the melting temperature. Thus, the film will not completely transform to the amorphous state.
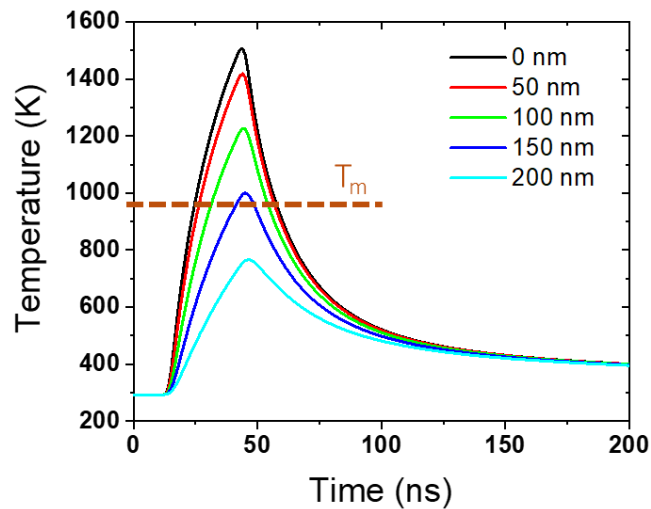
Figure II-35: Temperature evolution with time at different GeTe film depths during amorphization process, for a 250 nm GeTe on a sapphire substrate using an incident laser fluence of 185 mJ/cm² (T_m corresponding to the crystallization temperature)

To completely transform the film to the amorphous state, the laser power can be increased for obtaining a fluence of 200 mJ/cm². In this case the time-dependent temperature variation at different film depths is shown on Figure II-36.
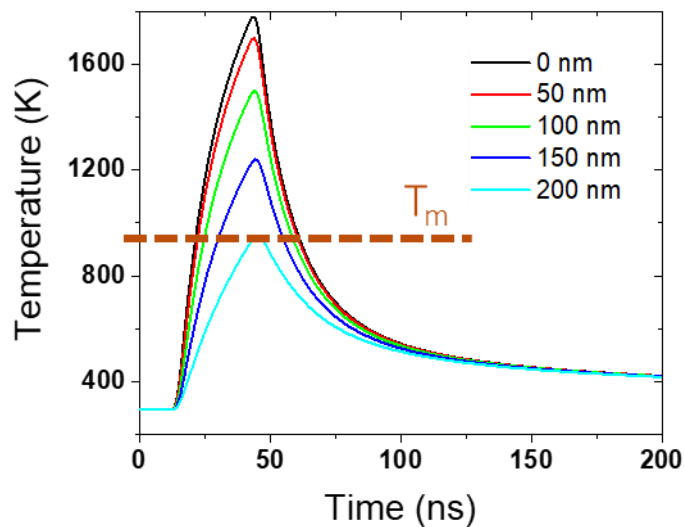
Figure II-36 : Temperature evolution with time for different film depths during amorphization process for a 250 nm GeTe on a sapphire substrate when using a fluence of 200 mJ/cm²

Thus, the global temperature of the film increases, and we obtain a complete amorphization of the film within its entire depth, for melt-quenching times below 110 ns. However, the higher temperature at the film surface (≈1700 K) may damage the GeTe film surface. A solution could be to use a protective and anti-reflective layer. By reducing the reflected power, more laser power will interact with the film and consequently lower energy laser pulse are required to heat the material above its melting temperature. Secondly, during

laser activation, the high temperature observed at the surface will be applied on the anti-reflective coating layer instead of the GeTe film. Finally, by choosing a correct anti-reflective layer, we may improve the thermal diffusion over the film thickness.

To characterize the influence of the substrate on the GeTe phase changes, we performed simulations using similar laser pulse simulations for a 250 nm GeTe film deposited on a silica substrate (instead of sapphire). In this case, the time-dependent temperature variation at different film depths for crystallization is shown on Figure II-37.
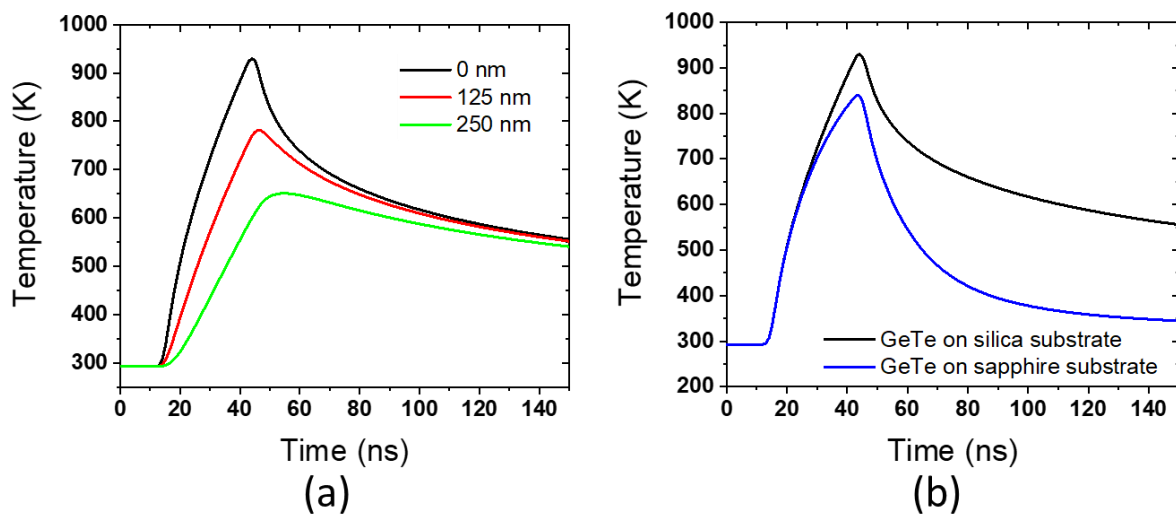
Figure II-37: (a) Temperature evolution with time for different depths during crystallization process of a 250 nm GeTe on a silica substrate. (b) Temperature evolution with time at the surface of a 250 nm GeTe on a silica (black) and sapphire (blue) substrate.

If we compare the results with the ones for a sapphire substrate (Figure II-37), the maximum reached temperature is higher (925 K Instead of 850 K) and the cooling time is much longer for silica substrate. After 150 ns the temperature is still above the crystallization temperature at 550 K, whereas for the sapphire case, the temperature is equal to 350 K after 105 ns. This difference is mainly due to the difference of thermal conductivity of the substrate. Silica has a thermal conductivity of 1.38 $Wm^{-1}K^{-1}$ at 298 K whereas it's 40 W $m^{-1}K^{-1}$ for the sapphire c substrate. The thermal conductivity corresponds to the ability of a material to transfer or conduct heat. Thus, the sapphire substrate can more rapidly dissipate the heat load and cool the GeTe film. If a slow cooling time allows a good crystallization of GeTe, it is not suitable for amorphization of the film which requires fast cooling time to melt-quench the material ($>10^9$ K/s). Considering the slow cooling time of silica, the amorphization of a GeTe film seems to be difficult on a silica substrate. Thus, for the optical activation of GeTe film we prefer to use sapphire c substrate.

We also simulated the heating effect of the laser beam on a 500 nm amorphous GeTe film grown on sapphire substrate. Figure II-38 shows the temperature distribution on the GeTe

film surface at t = 40 ns (when the temperature value of the film is maximal) for the low-energy laser pulse (85 mJ/cm^2) applied on an amorphous GeTe film (Figure II-38a) and for the high-energy laser pulse (185 mJ/cm^2) applied on a crystalline GeTe film (Figure II-38b). As expected, the thermal distribution is similar for both cases. The surface temperature distribution is around 908 K for the crystallization case and around 1500 K for the crystalline-to amorphous transition.
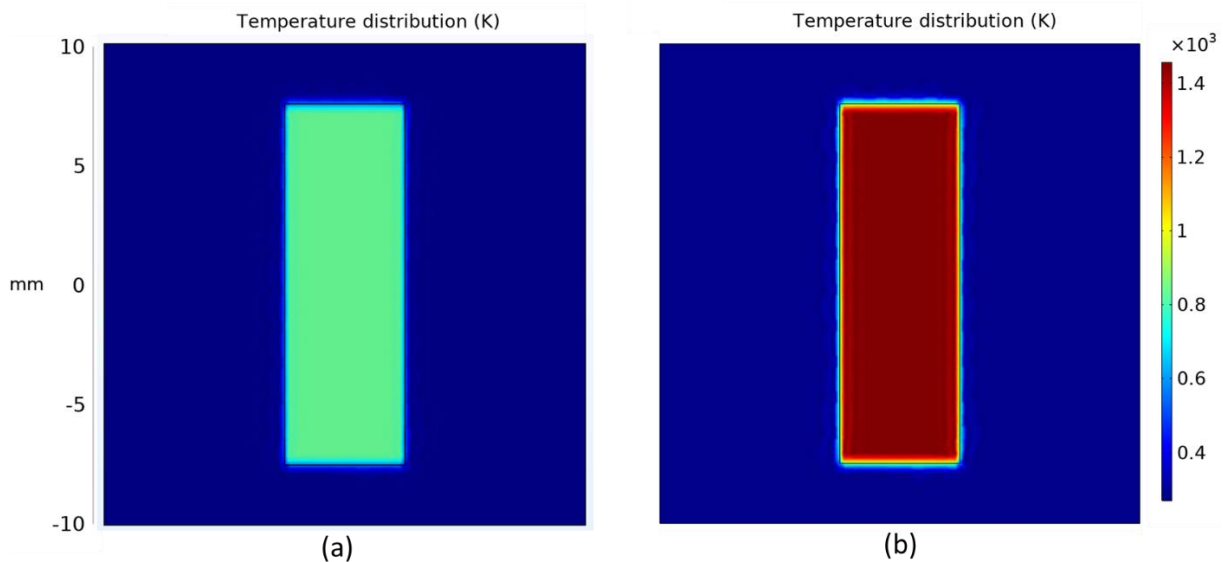
Figure II-38 : Temperature surface distribution at 40 ns for (a) crystallization process and (b) amorphization process.

II.3.2. Experimental results of GeTe films optical phase change using an excimer laser

Based on the presented simulation we used a Compex Pro110 excimer KrF* laser (wavelength of 248 nm, a repetition rate from 1 Hz to 20 Hz and a pulse duration of 30 ns) to investigate the laser activation of GeTe films. The incident laser energy to the surface can be changed from 30 to 200 mJ. The laser fluence (expressed in mJ/cm^2) can be further modified using a focus lens with a focal length f = 50 mm. The laser spot has an energy distribution with a flat-top profile (uniform energy distribution over the surface). To ensure a complete crystallization and amorphization of the GeTe film over the whole thickness during optical activation, we choose to use a 250-nm thick GeTe films grown on a sapphire substrate (Figure II-39).
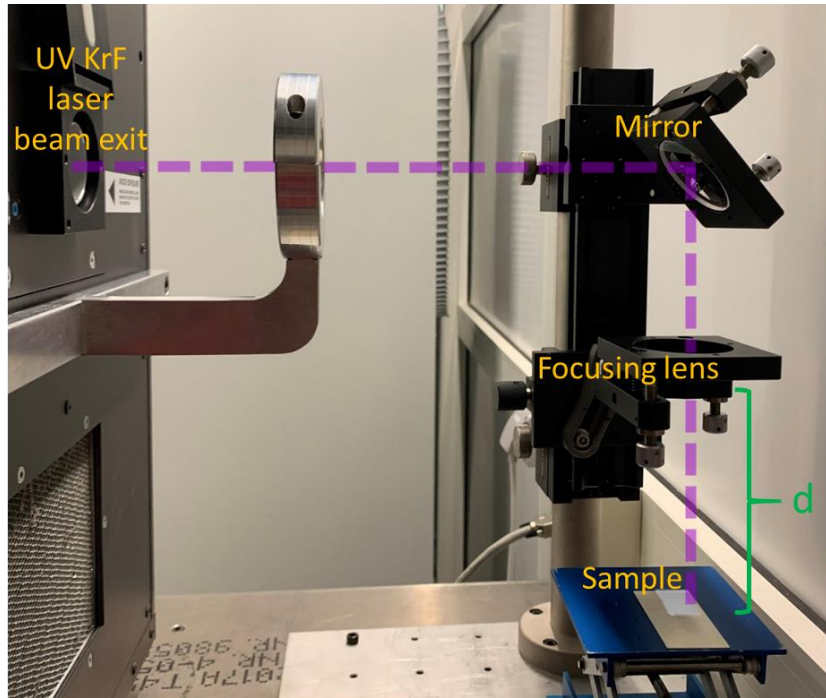
Figure II-39 : Experimental system for laser exposure of GeTe films

As fabricated, the GeTe is amorphous with a measured surface resistivity of 350.10^5 $\Omega\square$. We realized multiple tests with different laser fluences to crystallize the amorphous GeTe film. In parallel, we crystallized a GeTe films using thermal heating and tried to amorphized them using different laser fluences. For each test we measured the resistivity (using the four points system) after laser exposure**.**

For GeTe crystallization, when the incident laser fluence is increased we observe a decrease of the film resistivity for laser fluences up to 90 mJ/cm^2 **(**Table II-4**)**, after this fluence the surface resistance value is constant around 4.63 $\Omega\square$.

Table II-4 : GeTe films resistivity measured before and after laser exposure of an amorphous GeTe films for different fluences values

Surface resistance before laser exposure ($\Omega\square$)	Laser fluence (mJ/cm^2)	Surface resistance after laser exposure ($\Omega\square$)
350.10^5	70	16
350.10^5	91	4.63
350.10^5	112	4.72

To transform crystalline GeTe film to an amorphous state, no variation of the resistivity is observed for laser fluences below 180 mJ/cm^2 (Table II-5). When the applied laser fluence

is 185 mJ/ cm^2 the resistivity increases to 300.10^5 $\Omega_\square$, almost 7 orders of magnitude higher than that of the initially crystalline state.

Table II-5 : GeTe films resistivity measured before and after laser exposure of a crystalline GeTe films for different fluences values

Surface resistance before laser exposure (Ω□)	Laser fluence (mJ/cm²)	Surface resistance after laser exposure (Ω□)
4.3	130	4.4
4.3	185	300.10^5
4.3	200	Damages on the film

Then, with further increase of the laser fluence (at 200mJ/cm^2) we notice damages on the film surface (Figure II-40).

(a) (b)
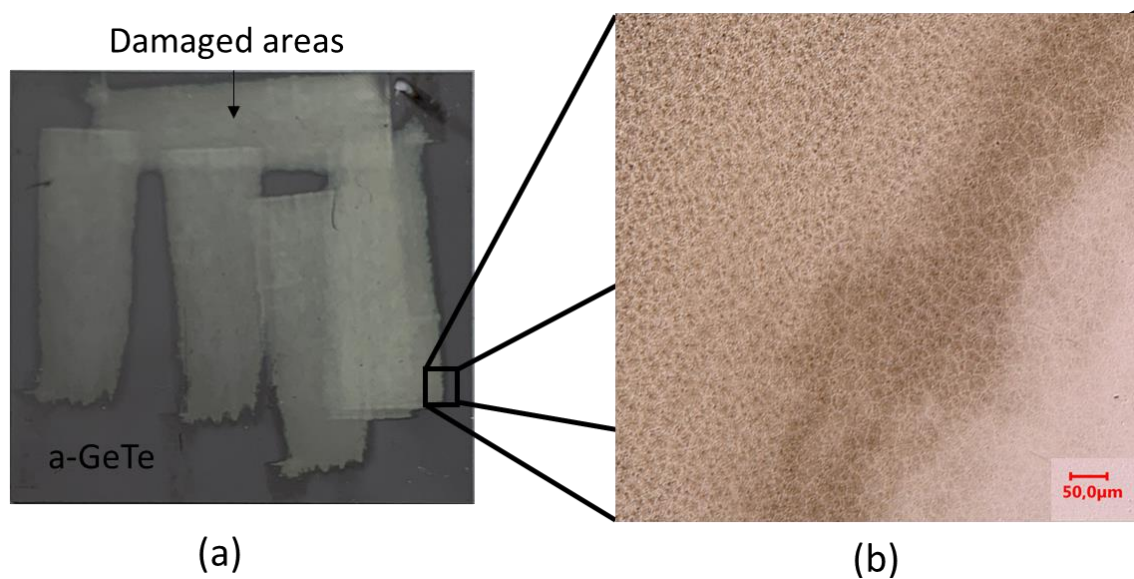
Figure II-40 : (a) Optical image of a damaged 250 crystalline GeTe film on sapphire c substrate after exposure to a 200 mJ/cm^2 UV laser pulse and (b) zoomed view of the damaged area

These experimental results are in good agreement with the simulations. We found a fluence around 90 mJ/cm^2 for complete crystallization and a fluence around 185 mJ/cm^2 for complete amorphization of a 250 nm GeTe film. The resistivity measurements of a 250 nm GeTe film grown on sapphire substrate, transformed to the crystalline state using optical activation are comparable with the resistivity values obtained when transformed to the same state by direct thermal heating (Table II-6).

Table II-6 : Comparison of 250 nm crystalline GeTe film resistivity obtained from an amorphous film by thermal activation and optical activation. In the case of optical activation, the amorphous resistivity value corresponds to an amorphization of crystalline GeTe film (obtained by thermal heating).

	Thermal activation	**Optical activation**
Amorphous GeTe (Ω.cm)	3881 (as fabricated)	3327.15 (from crystalline state)
Crystalline GeTe (Ω.cm)	3.43×10^{-4}	4.88×10^{-4}

An important parameter for the integration of GeTe in reconfigurable THz devices is the capacity to realize a large number of switching cycles between amorphous and crystalline phase. Thus, it is necessary to test the reliability and repeatability of the optical activation of GeTe films.

The crystallization of a deposited 250-nm thick amorphous GeTe film is obtained by irradiating the film's surface with consecutive sets of single 90 mJ/cm^2 laser pulse heat the material above its T_c (Figure II-41a). The amorphization, after complete crystallization of the GeTe film, was realized by scanning the surface using consecutive single 185 mJ/cm^2 pulses to heat the material above its melting temperature on a short delay time. Thus, the GeTe film underwent a melt-quenching phenomenon and returned to its amorphous phase (Figure II-41b). The process is then repeated during several cycles (Figure II-41c).
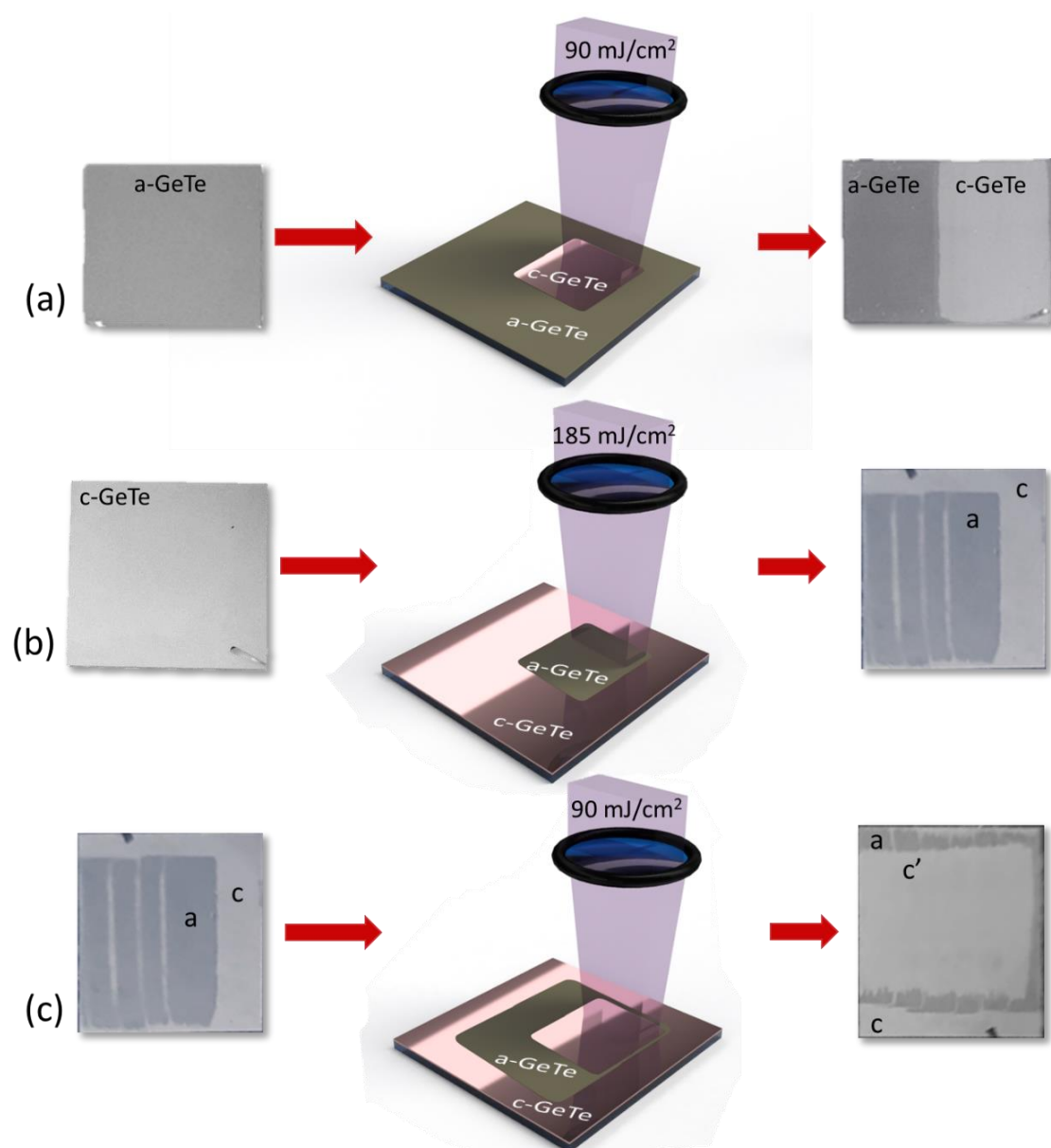
*Figure II-41 : Optical activation of a 250 nm GeTe film on a sapphire c substrate. (a) Phase change from amorphous to crystalline phase of GeTe film using a 35 ns UV laser pulse with a fluence of 90 mJ/cm² . (b) Phase change from crystalline to amorphous phase of GeTe film. using a 35 ns UV laser pulse with a fluence of 185 mJ/cm² (c) recrystallization of GeTe film after a first amorphization procedure (**c** corresponds to crystalline phase and **a** to amorphous phase)*

The surface resistance variation of a GeTe film grown on a sapphire substrate during several activation cycles as presented in Figure II-41 is shown on Figure II-42.
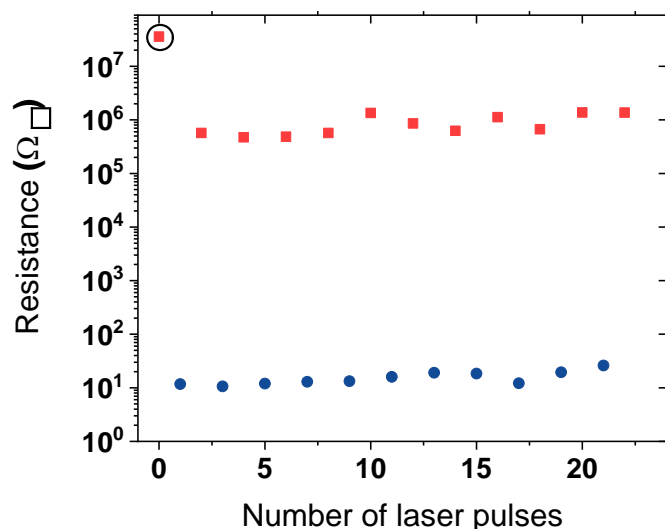
Figure II-42: Evolution of the surface resistance of a GeTe film depending on the number of laser pulses with a fluence of 90 mJ/cm² for crystallization and 185 mJ/cm² for amorphization.

After one crystallization when the GeTe returned to amorphous phase the resistivity is not as good as initial amorphous phase. This is probably due to the film composition which still presents some crystalline bond structures. However, after this first amorphization, we observe a constant variation of the resistance even after 22 dissimilar and consecutive laser pulses, with a contrast of 5 orders of magnitudes between amorphous and crystalline phases. We limit the repeatability measurements to 22 laser pulse because of the manual control of the measure (laser activation and then four-point measure). The number of cycles is far from the values reported in the literature where phase changes over 10^8 cycles have been reported for the test of memory cell prototypes [27, 28]. However, the dimensions of the used GeTe films are far below 250 nm (around 10 nm). Furthermore, they used electrical control with electrodes diameter around 10 nm with protective layer to avoid exposition to the atmosphere. In our test, we used a bare GeTe film with dimensions of 250 nm without a protective layer which would avoid exposition to the atmosphere and direct laser beam. Consequently, the require energy to completely crystallize the GeTe film is higher than the devices reported in the literature and the high temperature at the surface of the film can lead to progressive degradation of the film with the increase of optical cycles. Nevertheless, by developing correct protective layers we can decrease the deterioration of the film and expect repeatability over a large number of optical cycles.

The accumulation of activation cycles can lead to the appearance of fissures in the layer or even local changes in the stoichiometry of the material due to segregation or selective interdiffusion of the atoms constituting the material [29]. Indeed during the transformation to the amorphous state, the PCM film reaches temperatures beyond the melting temperature which means the film's stoichiometry is modified at each pulse and the film can interact with

the oxygen of the atmosphere. The addition of a protective layer can avoid this degradation and would increase the lifetime of the film. Another solution to improve it could be the modification of the film composition by tellurium enrichment, which could reduce the Ge segregation. The higher the Ge concentration, the higher is the formation probability of a stable cubic Ge during cycling, which leads to the formation of conductive paths and block the film in conducting state [30].

We can observe that the resistance of the amorphous states of the films after optical activation is not as high as the as-fabricated amorphous GeTe film resistance (first measure in Figure 4-13). This can be explained by the presence in the film of small crystalline area. As see in the previous simulations, with the fluence of 185 mJ/cm², the temperature of the film is not above the melting temperature over the whole thickness of the film and a part of the film is probably still crystalline. Nevertheless, we measured a contrast between amorphous and crystalline phase of 5 orders of magnitude which seems enough to envisage the use of this activation scheme for the realization of reconfigurable THz devices.

Although the measurements of the surface resistance of the film gives a good idea on the film evolution during optical activation, THz properties measurements are required to validate the reconfigurability of the films in the THz domain. Figure II-43a shows the modification of the THz transmission of a 250 nm GeTe film grown on sapphire substrate for a whole optical cycle (amorphous to crystalline following by crystalline to amorphous states modifications).
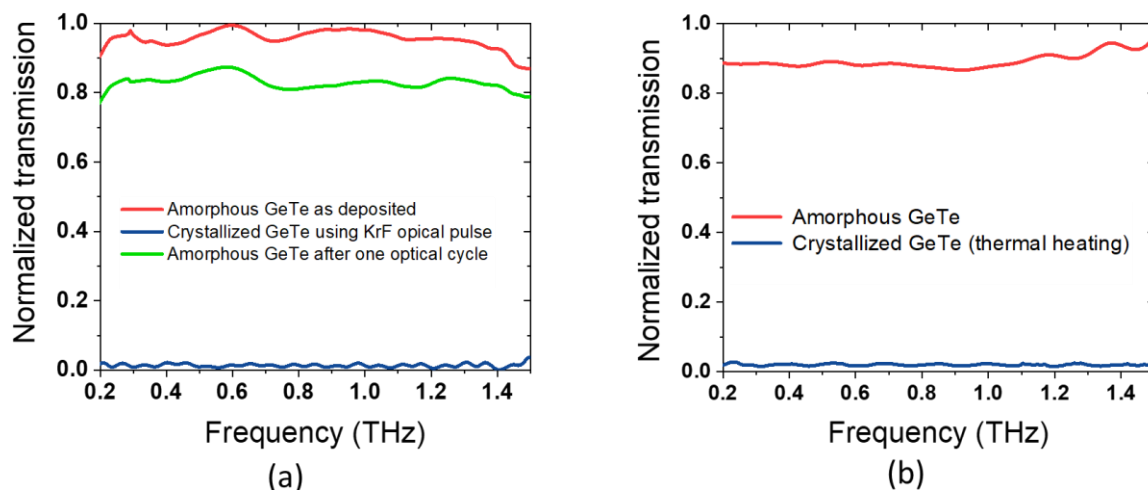
Figure II-43: THz normalized transmission of an as-fabricated 250-nm thick GeTe film (red curve) on a sapphire substrate, after crystallization of the film using a low energy (90mJ/cm²) KrF laser pulse (blue curve) and after its transformation to the amorphous phase using a high energy (185 mJ/cm²) pulse (green curve)

The application of a pulse with 90 mJ/cm^2 on the initially 250-nm thick amorphous GeTe film (red curve) allows to change the PCM in its crystalline phase (blue curve) with a decrease of the THz transmission from 0.95 to 0.01 at 0.5 THz. Optical activation is a reliable method to crystallize GeTe, we found a transmission contrast between amorphous and crystalline GeTe as good as thermal activation (Figure II-43b), Reversely, the application of a laser pulse with 185 mJ/cm^2 on the optically-transformed crystalline GeTe film allows to change the PCM in its amorphous phase (green curve), however the THz transmission is inferior compared to the initial THz transmission of the as-fabricated amorphous film. This confirms the resistivity measurement variations noticed during the electrical resistance repeatability test.

In conclusion, we have demonstrated for the first the time in the THz domain, the possibility to activate GeTe in a repeatable way from amorphous to crystalline phases using large-area optical activation. The possibility to activate GeTe over a large number of optical cycles with a strong modulation of the THz transmission (~98%) makes GeTe a very promising candidate for the realization of reconfigurable THz devices.

The use of a rather massive KrF laser complicates the integration of this optical activation schemes in practical applications which require compact reconfigurable THz devices. Indeed, to operate in real time, precise alignment of the laser beam with the GeTe area to optically modify is required, and the irradiating system must be implemented near or in the GeTe device which would be integrated in a complete and complex THz system. To reduce the size of the irradiation system we proposed to use a more compact system to realize laser activation. We used a Q-smart 450 commercial laser from Quantel with a Gaussian spatial pulse profile distribution (Figure II-44 Image of the Nd:YAG laser with frequency doubling crystal and corresponding schematic of the laser exposition setup.
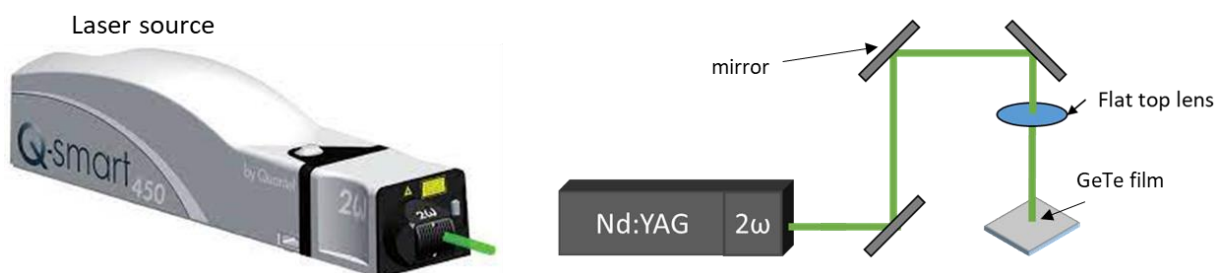
Figure II-44 Image of the Nd:YAG laser with frequency doubling crystal and corresponding schematic of the laser exposition setup

The system is composed of a pulsed Nd:YAG laser (6 ns pulse duration and 1064 nm wavelength) and a 2ω conversion module allowing to convert the wavelength from 1064 nm to 532 nm. The repetition rate of the laser can be modified from 1 Hz to 20 Hz. A flat-top lens was used to convert the gaussian profile of the pulse to a square flat top profile (uniform repartition of the power). This laser allows us to fully control the different irradiation parameters such as

the wavelength, the number of pulses, the repetition rate or the spatial profile of the laser beam and study their effect on the laser activation of PCM.

II.3.3. GeTe optical activation between the two states using a laser operating at 532 nm

We have investigated the GeTe crystallization using the Gaussian profile of the laser beam (without the flat-top lens) to observe the effect of the beam shape on the GeTe film. As presented in Chapter I, to obtain a complete crystallization of the film with a single pulse, the pulse duration needs to be at least higher than 30 ns. Thus, it is necessary to use several consecutive pulses to achieve complete crystallization of the film with 6-ns long laser pulses. The superposition of laser pulses leads to thermal energy accumulation on the film surface and an increase of the crystallized volume until complete crystallization of the film is achieved.

A second parameter which can affect the optical activation of GeTe is the laser repetition rate (not studied during my thesis). Several studies show that for time period between two pulses superior to 35 ns, the crystallization is independent from the repetition rate [31]. For our laser activation, we fixed the repetition rate to 20 Hz (period of 50 ms).

To optimize the crystallization process, we tried different laser fluence values and numbers of optical pulses with a beam diameter of 5 mm on as deposed 250 nm amorphous GeTe films deposited on sapphire c substrate as indicated in Figure II-45.

Name of the laser mark	Number of pulses	Fluence (mJ/cm^2)	Resistance ($\Omega\square$)
a	2	101	1002
b	2	71	$11,1 \cdot 10^5$
c	2	48	847,6
d	3	48	5,2

Figure II-45 : Optical irradiation conditions with a gaussian laser beam of an initially amorphous 250 nm GeTe film grown on a sapphire c substrate and the corresponding optical image of the laser marks.

We obtained a complete crystallization of the film (pattern having a surface resistance value of 5.2 $\Omega\square$) for a laser fluence of 48 mJ/cm^2 and a series of 3 consecutive pulses. For the other values we observed only a partial crystallization of the film. Regarding the irradiated patterns after crystallization when using 48 mJ/cm^2 laser pulses (Figure II-46), a crystalline

phase (c) is visible and around this area we can observe a darker region which corresponds to GeTe areas that are not completely crystallized. This structure is due to the gaussian energy profile of the laser pulse which concentrates the energy in the middle of the laser beam (the edge of the beam has low energy, insufficient to completely heat the GeTe above its crystallization temperature).
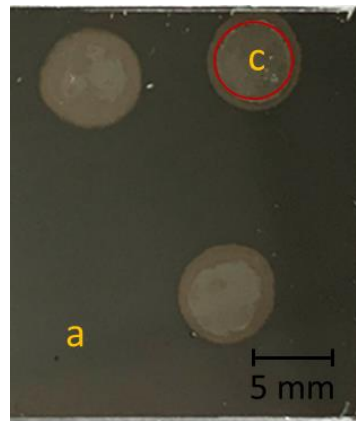
Figure II-46: Optical image of an amorphous GeTe film exposed to a gaussian laser beam (48 mJ/cm^2). "a" letter corresponds to the amorphous phase areas and"(c)" to the crystalline GeTe areas.

We integrated a flat-top lens to obtain a uniform distribution of the laser pulse energy. In the case of a uniform energy repartition (flat-top lens), the crystallization of the GeTe film is rather uniform. In this case, the optimum crystallization conditions of the irradiated GeTe areas were obtained for a laser fluence of 56 mJ/cm^2 and with 2 consecutive pulses (Figure II-47). We did not notice a major difference in the electrical resistance variation when the number of laser pulses was further increased, its value remains around 4 Ω□.

Name of the laser mark	Number of pulses	Fluence (mJ/cm^2)	Resistance (Ω□)
a	3	22	6,36
b	2	56	4,62
c	3	56	4,83
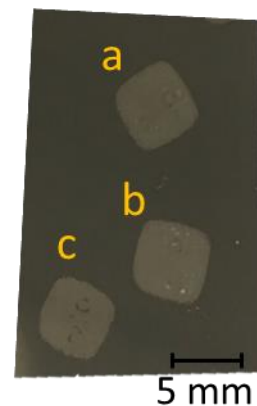
Figure II-47 : Optical irradiation conditions with flat-top laser beam (at 532 nm) of an amorphous 250 nm GeTe film grown on sapphire-c substrate and the corresponding optical image of the GeTe film

For achieving the amorphization of the GeTe crystalline areas, we used single laser pulse irradiation with a fluence between 100 mJ/cm^2 and 176 mJ/cm^2. However, we did not achieve a complete transformation to the amorphous state of the film and in some cases, the irradiated areas are damaged (Figure II-48).
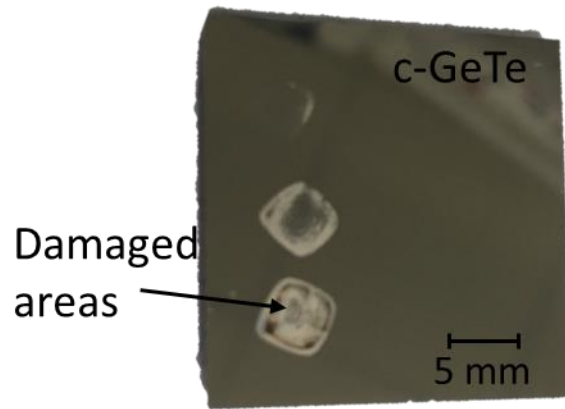
Figure II-48: Optical image of a 250 nm crystalline GeTe film deposed on a sapphire c substrate after exposition to a flat-top laser beam (532 nm) with a fluence varying from 100 mJ/cm^2 and 176 mJ/cm^2. No amorphization is observed, however, for high fluence (176 mJ/cm^2) damages are observed on the film.

The laser fluence and the pulse duration are very critical parameters, and, as explained in chapter I, the transformation of GeTe to the amorphous phase requires a very precise control of their values.

Even if this irradiation system employing a laser operating at 532 nm is not fully optimized, we demonstrated that optical activation of GeTe films is achievable using a more compact system. As we have seen the change of the wavelength from 248 nm to 532 nm modify the require fluence for laser activation. As it is shown on Figure II-49, GeTe absorption change depending on the wavelength [32]. Additionally, the energy of the laser beam depends on the wavelength.
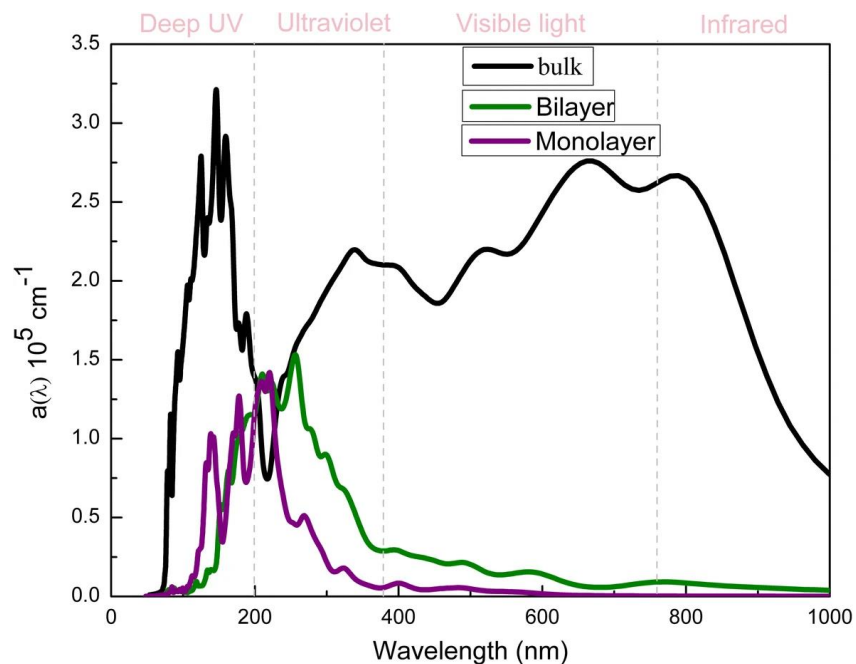
Figure II-49 : Absorption coefficient of monolayer, bilayer and bulk α-GeTe [32].

Because of the small size of the laser beam and of the possibility to use different laser wavelengths, this system allows versatile and localized activation of a GeTe film which can be very interesting for THz devices with multilevel activation areas, based on localized activation of a specific GeTe pattern integrating the device, instead of the whole device structure like in the irradiations using the KrF excimer laser.

Conclusion

In this chapter, we have studied the electrical and THz properties of PCM films in the perspective to realize reconfigurable devices. We show that GeTe films realized using the DC magnetron sputtering technique present a non-volatile variation of resistivity of more than 6 orders of magnitude (from 2573 Ω.cm to 3.43 x 10^{-4} Ω.cm for 250-nm thick films). Using the THz-TDS system, we successfully demonstrated the broadband variation of GeTe THz properties. THz normalized transmission of a GeTe film can decrease by 97 % between the amorphous and the crystalline state. We have also compared the GST and GeTe films properties in the THz domain and demonstrated that GST has higher resistance and THz transmission (60%) in crystalline phase than GeTe (2%) which confirms our choice to use GeTe for the realization of reconfigurable THz devices.

If thermal activation allowed us to demonstrate the high capacity of GeTe to control THz, the impossibility to reverse the crystallization with direct heating led us to investigate the optical activation of GeTe films on large areas using fast laser pulses. The use of laser pulses enables us to reduce the switching time (heating and cooling speed above 10^9 K/s) and simplify the realization of THz devices. For the first time, we have simulated and realized optical activation over large areas (15 mm x 5 mm) of GeTe films using a KrF laser with a pulse duration of 30 ns and a wavelength of 248 nm. Through the simulations we have demonstrated the effect of the different irradiation parameters (type of substrate, thickness of the film) on the electrical and THz properties of the films. We have demonstrated for the first time to the best of our knowledge in the THz domain, the possibility to successively switch GeTe films grown on a sapphire substrate between their amorphous and crystalline phases on large areas. Using a 90 mJ/cm^2 laser pulse, we achieved crystallization of a 250-nm thick GeTe film showing a decrease of the THz transmission by 98% compared to its amorphous state. The reversible transition was achieved using a single laser pulse with a fluence of 185 mJ/cm^2.

Therefore, GeTe material and the associated optical activation scheme can achieve strong non-volatile switching of THz waves in repeatedly way and can be further integrated in THz structures for the realization of reconfigurable THz devices. KrF laser sources are rather bulky systems and are difficult to implement in practical THz applications. In a second try, we studied the possibility to use a more compact laser source to realize localized activation of

GeTe films. Using a laser beam with a wavelength of 532 nm and a pulse duration of 6 ns, we studied the effect of different parameters such as the number of pulses, the fluence and the beam shape on the optical activation. Even if the realized experiments need further optimizations, we demonstrate the possibility to realize versatile and localized activation of a GeTe film for the development of THz devices with multilevel activation areas.

In the next chapter of the manuscript, we will exploit the large change of the THz properties occurring during the phase change of GeTe to investigate the realization of reconfigurable THz devices.

References chapter II

1. Chu, J.P., et al., *Deposition and characterization of TiNi-base thin films by sputtering.* Materials Science and Engineering: A, 2000. **277**(1-2): p. 11-17.
2. Khoo, C.Y., et al., *Impact of deposition conditions on the crystallization kinetics of amorphous GeTe films.* Journal of Materials Science, 2015. **51**(4): p. 1864-1872.
3. King, M.R., et al., *Development of cap-free sputtered GeTe films for inline phase change switch based RF circuits.* Journal of Vacuum Science & Technology B, Nanotechnology and Microelectronics: Materials, Processing, Measurement, and Phenomena, 2014. **32**(4): p. 041204.
4. Ghalem, A., et al. *Reversible, Fast Optical Switching of Phase Change Materials for Active Control of High-Frequency Functions*. in *2018 IEEE/MTT-S International Microwave Symposium - IMS*. 2018.
5. Navarro, G., et al., *Material engineering of GexTe100–x compounds to improve phase-change memory performances.* Solid-State Electronics, 2013. **89**: p. 93-100.
6. Noé, P., et al., *Phase-change materials for non-volatile memory devices: from technological challenges to materials science issues.* Semiconductor Science and Technology, 2018. **33**(1): p. 013002.
7. Bahl, S.K. and K.L. Chopra, *Electrical and Optical Properties of Amorphous vs Crystalline GeTe Films.* Journal of Vacuum Science and Technology, 1969. **6**(4): p. 561-565.
8. Sarnet, T., et al., *Atomic Layer Deposition and Characterization of GeTe Thin Films.* Journal of the Electrochemical Society, 2011. **158**(12): p. D694-D697.
9. Chen, L., et al., *Terahertz time-domain spectroscopy and micro-cavity components for probing samples: a review.* Frontiers of Information Technology & Electronic Engineering, 2019. **20**(5): p. 591-607.
10. Han, J., *Probing negative refractive index of metamaterials by terahertz time-domain spectroscopy.* Opt Express, 2008. **16**(2): p. 1354-64.
11. Kim, Y., et al., *Investigation of THz birefringence measurement and calculation in Al(2)O(3) and LiNbO(3).* Appl Opt, 2011. **50**(18): p. 2906-10.
12. Naftaly, M. and R.E. Miles, *Terahertz time-domain spectroscopy of silicate glasses and the relationship to material properties.* Journal of Applied Physics, 2007. **102**(4): p. 6.
13. Lagarias, J.C., et al., *Convergence Properties of the Nelder--Mead Simplex Method in Low Dimensions.* 1998. **9**(1): p. 112-147.
14. Scheller, M., C. Jansen, and M. Koch, *Analyzing sub-100-µm samples with transmission terahertz time domain spectroscopy.* Optics Communications, 2009. **282**(7): p. 1304-1306.
15. Coutaz, J.-L., F. Garet, and V. Wallace, *Principles of Terahertz Time-Domain Spectroscopy*. 2018.
16. Kadlec, F., C. Kadlec, and P. Kuzel, *Contrast in terahertz conductivity of phase-change materials.* Solid State Communications, 2012. **152**(10): p. 852-855.
17. Withayachumnankul, W., et al., *Limitation in thin-film sensing with transmission-mode terahertz time-domain spectroscopy.* Optics express, 2014. **22**: p. 972-86.
18. Makino, K., et al., *Terahertz spectroscopic characterization of Ge2Sb2Te5 phase change materials for photonics applications.* Journal of Materials Chemistry C, 2019. **7**(27): p. 8209-8215.
19. Laman, N. and D. Grischkowsky, *Terahertz conductivity of thin metal films.* Applied Physics Letters, 2008. **93**(5): p. 3.
20. Walther, M., et al., *Terahertz conductivity of thin gold films at the metal-insulator percolation transition.* Physical Review B, 2007. **76**(12): p. 9.

21.   Zhu, Y.H., et al., *Effect of substrate orientation on terahertz optical transmission through VO2 thin films and application to functional antireflection coatings.* Journal of the Optical Society of America B-Optical Physics, 2012. **29**(9): p. 2373-2378.

22.   Cocker, T.L., et al., *Terahertz conductivity of the metal-insulator transition in a nanogranular VO2 film.* Applied Physics Letters, 2010. **97**(22): p. 3.

23.   Zhou, D.-x., et al., *Determination of complex refractive index of thin metal films from terahertz time-domain spectroscopy.* Journal of Applied Physics, 2008. **104**: p. 053110-053110.

24.   Lu, H., et al., *Single Pulse Laser-Induced Phase Transitions of PLD-Deposited Ge2Sb2Te5 Films.* 2013. **23**(29): p. 3621-3627.

25.   Sun, X., et al., *Nanosecond laser-induced phase transitions in pulsed laser deposition-deposited GeTe films.* Journal of Applied Physics, 2014. **116**(13): p. 133501.

26.   Yang, S.T., et al., *Comparing the use of mid-infrared versus far-infrared lasers for mitigating damage growth on fused silica.* Applied Optics, 2010. **49**(14): p. 2606-2616.

27.   Kim, I.S., et al. *High performance PRAM cell scalable to sub-20nm technology with below 4F2 cell size, extendable to DRAM applications*. in *2010 Symposium on VLSI Technology*. 2010.

28.   Burr, G.W., et al., *Overview of candidate device technologies for storage-class memory.* IBM Journal of Research and Development, 2008. **52**(4.5): p. 449-464.

29.   Hong, S.-H. and H. Lee, *Failure Analysis of Ge 2 Sb 2 Te 5 Based Phase Change Memory.* Japanese Journal of Applied Physics, 2008. **47**: p. 3372-3375.

30.   Navarro, G., *Reliability analysis of embedded Phase-Change Memories based on innovative materials*. 2013, Université de Grenoble.

31.   Coombs, J.H., et al., *Laser-induced crystallization phenomena in GeTe-based alloys. I. Characterization of nucleation and growth.* Journal of Applied Physics, 1995. **78**(8): p. 4906-4917.

32.   Zhang, D., et al., *Tunable Electric Properties of Bilayer α-GeTe with Different Interlayer Distances and External Electric Fields.* Nanoscale Research Letters, 2018. **13**(1): p. 400.

Chapter III : Design and realization of GeTe- based reconfigurable THz device

Chapter III. Design and realization of GeTe- based reconfigurable THz devices

Introduction

In the previous chapter, we have presented the characteristics of GeTe in the THz domain. We have shown that the material has a non-volatile phase transition at the nanosecond time scale from an amorphous (insulating) state to a crystalline one (metallic). This transition occurs with a high contrast in their DC and THz properties (conductivity, transmission). These characteristics are adapted for the use of GeTe material as an active media for the realization of reconfigurable THz devices for high frequency telecommunications. It suggests that GeTe material can be integrated in fixed THz devices to actively tune their THz response. Additionally, the high contrast in the THz properties suggests that GeTe can also be used alone for the realization of all-dielectric devices.

We will first introduce the concept of metamaterials and their interest for the realization of THz devices. We will notably focus our study on a particular version of planar metamaterials integrating split ring resonators (SRR).

We will design, fabricate and evaluate the performances of a SRR-based metamaterial integrating GeTe patterns which can achieve strong modulations of the THz waves when the PCM material integrating the SRRs will change its state using laser irradiation. The significant differential amplitude response of the GeTe film's transmission at THz frequencies when optically switched between the amorphous and the crystalline states will be used to present for the first time to the best of our knowledge an all-dielectric THz device realized using solely GeTe. device which can actively control the polarization state of the incident THz waves. Finally, we will explore the possibility to directly write a functional metal-like device within a bare amorphous (insulator) GeTe film using laser activation and contact masks. This is a first step to realize on-demand, multifunctional THz devices without any lithographic process on the GeTe film.

3.1. Metamaterials for the Terahertz domain

Among the solutions considered by the scientific community in terms of materials compatible with THz technologies and applications, metamaterials (artificially structured materials) attracted a large interest.

3.1.1. Definition and properties

We can theoretically classify materials according to the sign of their permeability and permittivity values [1]. One can define four categories, as indicated in Figure III-1:
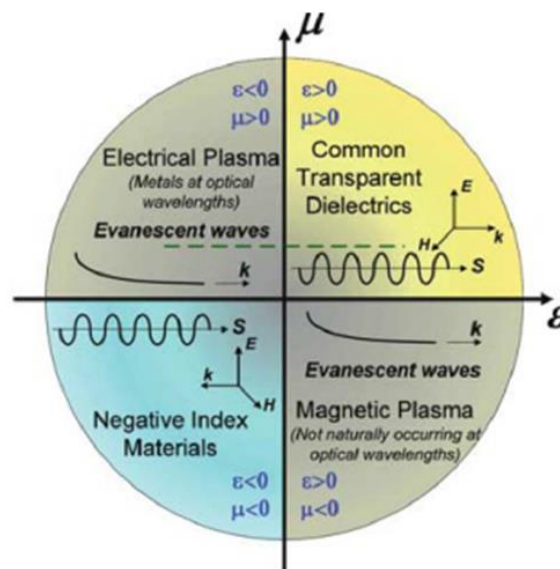
Figure III-1. Theoretical material classification depending on their permittivity and their permeability[1]

Among these categories, the most often materials encountered in the nature are regrouped only in two categories. First, the materials with positive permeability and positive permittivity are corresponding to dielectric materials (commonly transparent to the optical wavelength). Secondly, the metal electrical plasma which has negative permittivity and positive permeability at optical wavelengths.

In this context, artificially structured electromagnetic materials called metamaterials have been introduced in order to fill the two other remaining categories (negative permeability and positive or negative permittivity). Generally, a metamaterial is composed by arrays of subwavelength periodic inclusions (meta-atoms) in a host material. The material is considered as homogenous for an incident wave (with wavelength λ) when the period of the array is inferior to λ/4. Under this condition, the metamaterial can be seen as a single homogeneous material and we can define its refractive index n, which is as a function of the effective permittivity ε and permeability μ:

$$n = \sqrt{\varepsilon\mu} \qquad\qquad (\textbf{III.1.})$$

Metamaterials can have negative permeability and/or negative permittivity. If both are observed ($\varepsilon<0$, $\mu<0$), the metamaterial has a negative refractive index and it is called a left-hand material. This expresses the fact that the material allows the propagation of electromagnetic waves with the electric field, magnetic field and propagation vectors building a left-handed triad while for the conventional materials this triad is right handed. Concretely, negative refractive index reverses the Sneel-Descartes law and when an electromagnetic wave goes from a right-hand material (n>0) to a left-hand material (n<0), the refracted wave will be transmitted on the same normal side as the incident wave (Figure III-2a) [2]. It also implies that the phase speed and group speed of the wave are in opposite directions (Figure III-2b).
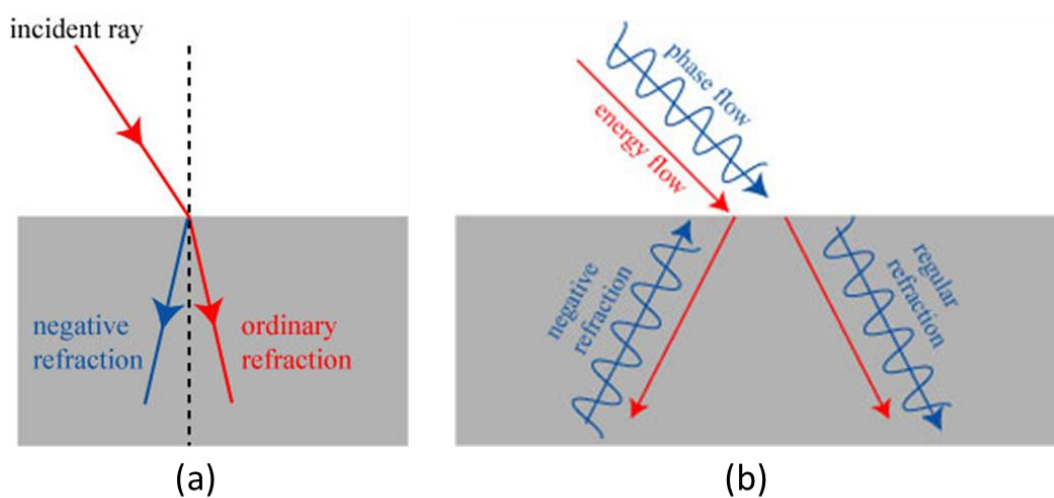
Figure III-2: (a) Schematic of an ordinary refraction with n > 0 (red) and a negative refraction with n < 0 (blue). (b)

As a consequence of these properties, metamaterials are inducing exotic phenomena such as perfect lensing or cloaking, but also allows more common functions like modulators and switches. These unique properties can be used over a large range of frequencies, metamaterials can be used in optics and acoustic domain [3] but also in frequency domains where other technologies are not adapted and cannot perform these functions, notably in the THz domain.

3.1.2. Metallic inclusion metamaterials

Metamaterials can be classified in three categories. First one groups metamaterials based on metallic inclusions in a dielectric matrix [4]. A second group assembles all dielectric metamaterials based on the use of high-permittivity inclusions in a dielectric matrix [5, 6], and finally, a third class is based on periodic transmission lines [7].
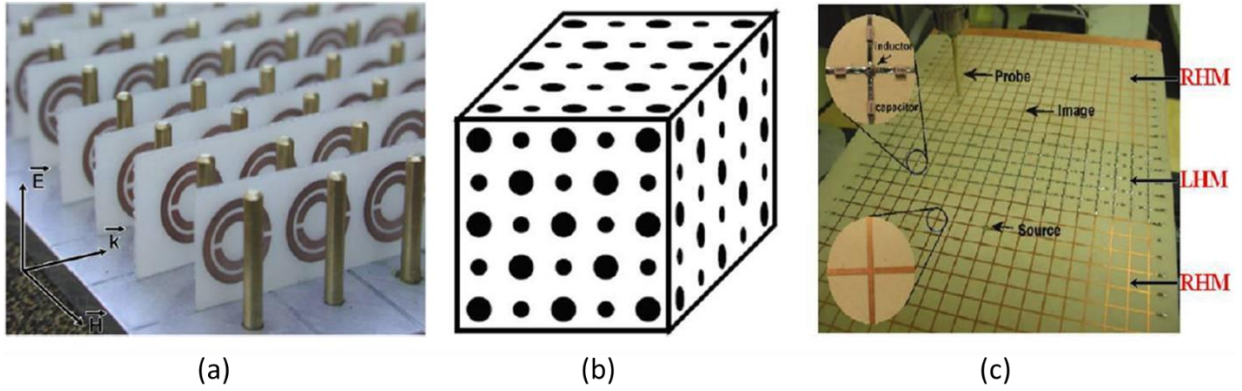
Figure III-3: Example of (a) metallic inclusion metamaterial, (b) all dielectric metamaterial and (c) transmission line type metamaterials [6, 7].

Among the different categories, we will focus our work on metallic inclusion metamaterials because of their simplicity of integration and their compatibility with relatively simple microfabrication technologies.

3.1.2.1. Metal wire arrays

Historically, the concept of metamaterials was introduced in 1996, when Pendry *et al.* demonstrated the possibility to realize a material with negative permittivity using a periodic lattice of metallic wires, which presented characteristics similar to a diluted plasma in the hyper frequency domain (Figure III-4.a) [8].

Plasmas are very interesting because they have naturally a negative permittivity. This phenomenon is notably found in metals, at optical frequencies, where their permittivity evolution with the frequency can be described using the Drude equation [1]:

$$\varepsilon(\omega) = 1 - \frac{\omega_p{}^2}{\omega(\omega + j\gamma)} \qquad (III.2.)$$

With:

- ω_p : plasma frequency

- γ : damping term representing the dissipation of the plasma's energy in the system

  ω_p and γ can be expressed as:

$$\omega_p = \sqrt{\frac{ne^2}{\varepsilon_0 m}} \qquad (III.3.)$$

$$\gamma = \frac{ne^2}{m\sigma} \qquad (III.4.)$$

with:

- n : electronic density

-   m : electron mass

-   e : elementary charge of one electron

-   ε_0 : vacuum permittivity

-   σ : metal conductivity

From equation (*III.2.*) we can conclude that it is possible to obtain Re(ε)<0 for $\omega^2 < \omega_p^2$-γ. If the damping factor can be neglected, we have $\gamma \approx 0$ and the real part of the permittivity is negative for $\omega<\omega_p$ as shown on Figure III-4.b for metallic gold.

If we look at the variation of the permittivity of gold with the frequency (Figure III-4.b), for a frequency band below the plasma resonance (2175 THz) we observe a negative permittivity. However, at low frequencies (THz and Hyper Frequencies) we have an increase of the imaginary part of the permittivity which corresponds to the appearance of metallic losses due to the increase of the conductivity. In this case, the metallic losses compensate the real part of the permittivity and it becomes impossible to observe negative permittivity.
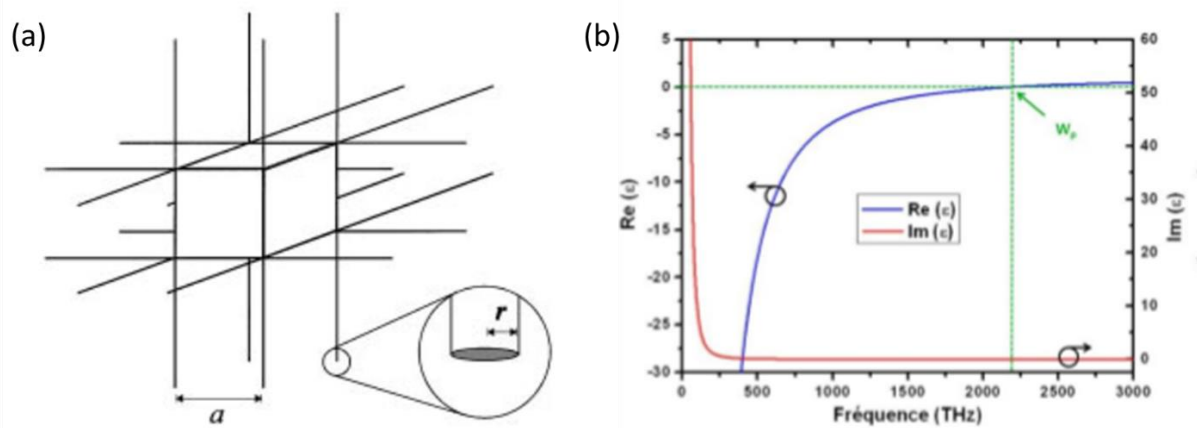
Figure III-4 : (a) Metallic wire periodic lattice proposed by Pendry et al.[8] (b) real and imaginary part of gold permittivity depending on the frequency

By using a periodic array of metallic wires instead of bulk metal (Figure III-4a) , one can achieve a variation of the electronic density and of the electrons effective mass which causes a large decrease of the plasmonic resonance ω_p of the structure [8]. In the example proposed by Pendry *et al.* based on an aluminum wire 3D periodic lattice consisting of cubic unit cells (Figure III-4a), it is possible to obtain an effective plasma frequency around 8.2 THz expressed as (from equation *III.2. - III.4.*):

$$\omega_p = \frac{2\pi c_0}{a^2 \ln\left(\frac{a}{r}\right)} \qquad (\textit{III.5.})$$

$$\gamma = \frac{\varepsilon_0 a^2 \omega_p^2}{\pi r^2 \sigma} \qquad (III.6.)$$

With:

- c_0: speed of light

- a: distance between each wires

- r : wire radius

Several years later, Pendry *et al.* experimentally demonstrated a 3D structure composed of thin wires presenting plasma characteristics in the micro-wave domain [9].

3.1.2.2. Split ring resonators (SSR) structures

In continuity with these incipient researches, Pendry's team has demonstrated the possibility to realize structures with negative permeability and positive permittivity. They proposed a material composed of a periodic 3D network of split ring resonators (SRR) which presents a LC type resonance (Figure III-5) [10].
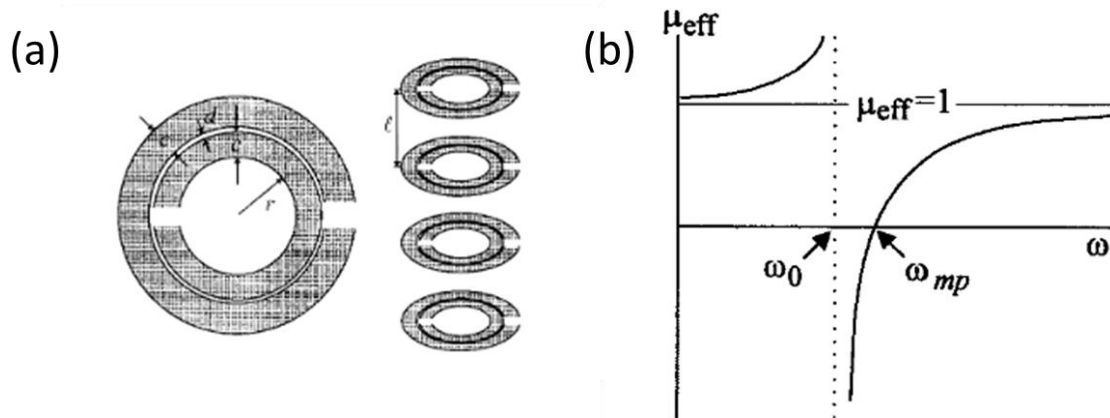
Figure III-5: (a) Double split ring resonator structure (SRR) (b) effective permeability of the double SRR structure [10]

This type of structure can achieve strong modulations of the electromagnetic field. If the magnetic field of the incident wave is perpendicular to the plane of the SRR, a current is induced in the ring and generates equivalent magnetic dipole moments. The frequency evolution of the permeability can be described using the Lorentz model:

$$\mu(\omega) = 1 - \frac{F\omega^2}{\omega(\omega + j\gamma) - {\omega_0}^2} \qquad (III.7.)$$

with: F - the fraction of the cell occupied by the SRR and ω_0 the LC resonance frequency

We can then determine the frequency range for Re(μ)<0 given by the condition γ≠0 (Figure III-5b) as:

$$\omega_0 < \omega < \frac{\omega_0}{\sqrt{1-F}} = \omega_{pm} \qquad (\boldsymbol{III.8.})$$

With: ω_{pm} - the magnetic plasma resonance which corresponds to the frequency where Re(μ)=0.

In the example Figure III-5, ω_{pm} and F can be express as:

$$\omega_{pm} = c_0 \sqrt{\frac{3p}{\pi \ln\left(2wa^3/t\right)}} \qquad (\boldsymbol{III.9.})$$

$$F = \pi \left(\frac{a}{p}\right)^2 \qquad (\boldsymbol{III.10.})$$

with:

- a : outer diameter of the SRR

- p : SRR period

- w : wire width of the SRR

- t : SRR thickness

Thus, by choosing the correct dimensions of the SRR it is possible to obtain a negative permeability over a large range of frequencies (from micro-waves to optical waves, passing through the THz waves).

3.1.2.3. Planar THz metamaterial

A particular type of the previously presented metamaterial are the planar ones (2D metamaterial), based on subwavelength resonators array which can be wire-grid or SRR obtained on a planar substrate [11, 12]. Some examples are shown on Figure III-6.
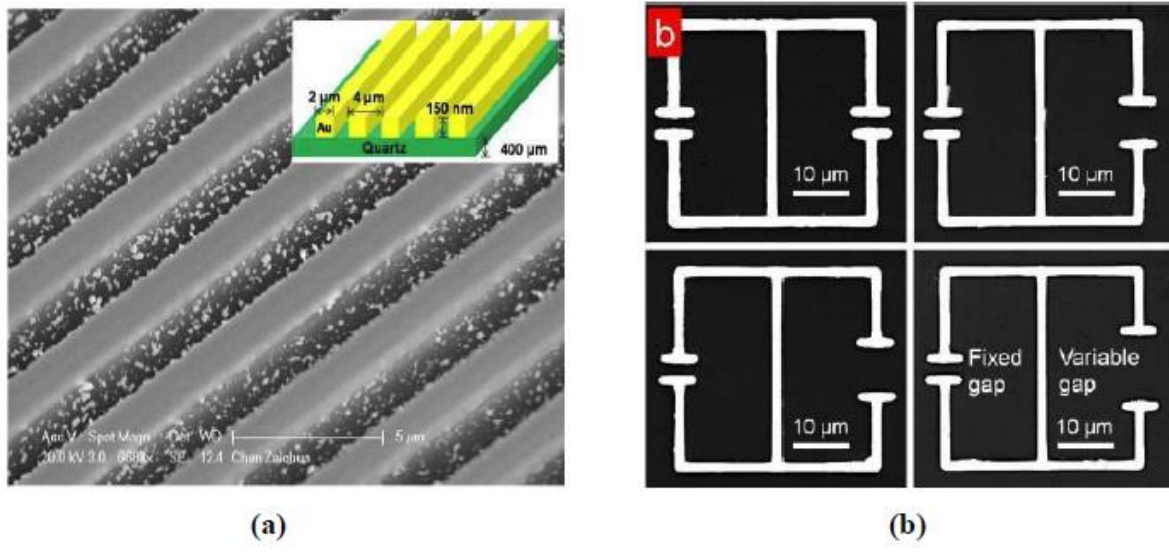
Figure III-6: Example of 2D metamaterial with (a) a wire-grid type structure and (b) a SRR type structure [12].

In our research we choose to focus on these 2D metamaterial because of their compatibility with micro-fabrication processes available in our technological platform. Among the possible approaches for the realization of THz metamaterials, we choose planar split ring resonator arrays in particular. A single SRR can be seen as a meta-atom within the metamaterial array and, depending on the shape of the SRR, the response of the whole structure will be different. Examples of reported planar SRR are shown in Figure III-7 [13].
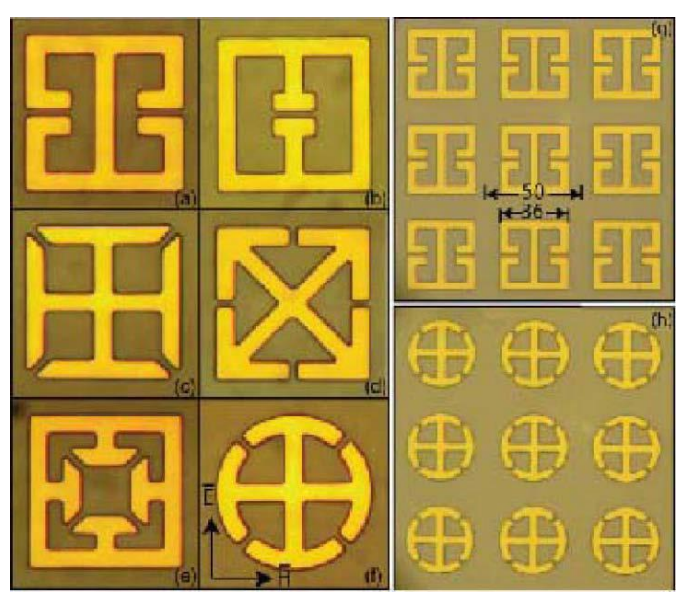
Figure III-7 : Example of single 2D SRR structures and SRR array [13]

A single SRR can be seen as an LC oscillator composed of a magnetic coil of inductance L and a capacitor C (Figure III-8). Consequently, we can define the fundamental resonance frequency of a SRR as a LC resonance frequency given by the equation (if the losses are neglected):

$$\omega_r = \frac{1}{\sqrt{LC}} \qquad\qquad (III.11.)$$
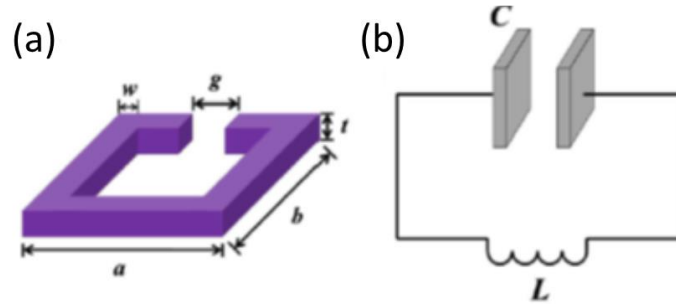
*Figure III-8: **(a)** Schematic of a split ring resonator **(b)** equivalent electrical circuit [12]*

The value of the capacity C depends on the gap size g, the cross-section area S and the effective permittivity of the surrounding environment ε_{eff}.

$$C = \frac{\varepsilon_{eff}S}{4\pi kg} = \frac{\varepsilon_{eff}wt}{4\pi kg} \qquad\qquad (III.12.)$$

With: k - Boltzmann constant and w- width of the SRR line and t- thickness of the SRR pattern

The inductance L is defined by the area of the SRR, a x b, the thickness t and the permeability of the surrounding environment μ_0 and is given by:

$$L = \mu_0 \frac{ab}{t} \qquad\qquad (III.13.)$$

Finally, the equation ($III.11.$) gives:

$$\omega_r = \frac{1}{\sqrt{\dfrac{\varepsilon_{eff}\mu_0}{4\pi k}\dfrac{abw}{g}}} \qquad\qquad (III.14.)$$

Therefore, by changing the gap size or by scaling up or down the outer dimensions of the SRR, we can tune the resonance frequency and it is possible to obtain a device operating from microwaves to optical frequency domain. However, beyond 100 THz the relation between resonance frequencies (ω_r) and the size of the SRR ($\sqrt{ab}$) is no longer valid. This is because the electrons inside the SRR cannot respond to the phase change of the incident terahertz wave [14]. As an example, in Figure III-9 the THz response of a SRR unit cell for different lengths "a" while the other parameters are fixed is presented [12].
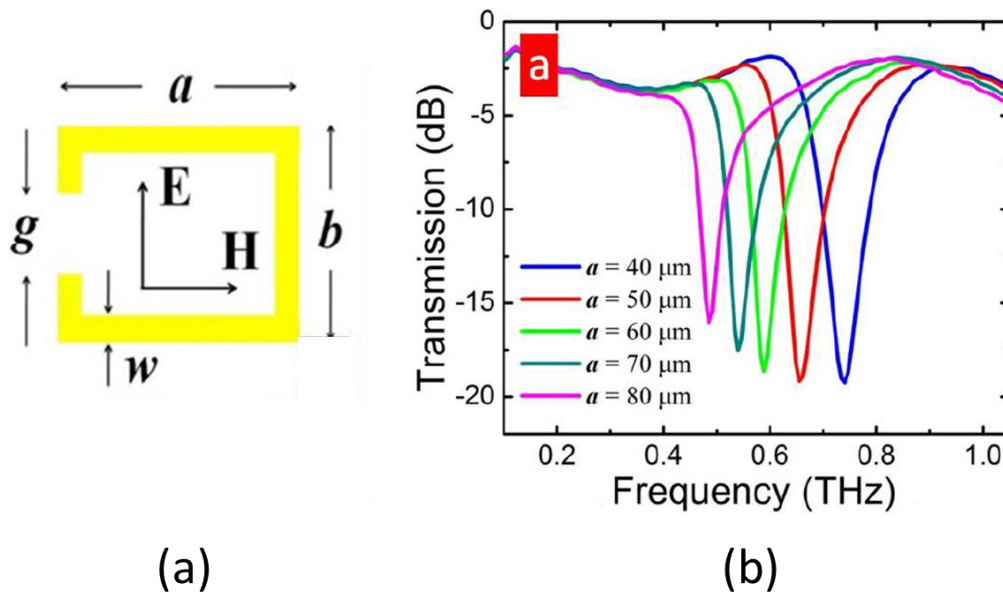
Figure III-9 : (a) Structural parameters of the SRR unit cell and (b) simulated transmission for different values of "a" parameter [12]

As can be noticed for the variation of the THz response of the SRR structure shown in Figure III.2-9, its resonant frequency increases when the length "a" decreases.

In the previous case we consider an individual resonator. In the real case, we need to consider additional losses due to the ohmic resistance of the metal which can affect the response of the resonator leading to a shift of the resonance frequency. Furthermore, if the unit cell is small enough (the period p<2a), mutual coupling between the different SRRs of the structure will modify the response of the array [12, 15]. The coupling between the different SRRs can be express in terms of coupling capacitance C_Σ and coupling inductance L_Σ which cause a shift of the resonance frequency.

3.1.2.4. Metamaterials applications

Metamaterials have shown high potential for numerous applications in a large domain of frequencies. One of the first application is the perfect lensing [16]. The principle is based on the use of the negative refractive index of a metamaterial as well as its possibility to amplify the evanescent waves. The combination of these two properties will allow the realization of a perfectly flat lens with the unique property of focusing all the components of the source object in a single image plane and thus obtain a perfect image, the first demonstration were realized at UV frequencies using Ag slabs as perfect lenses (Figure III-10) [17].
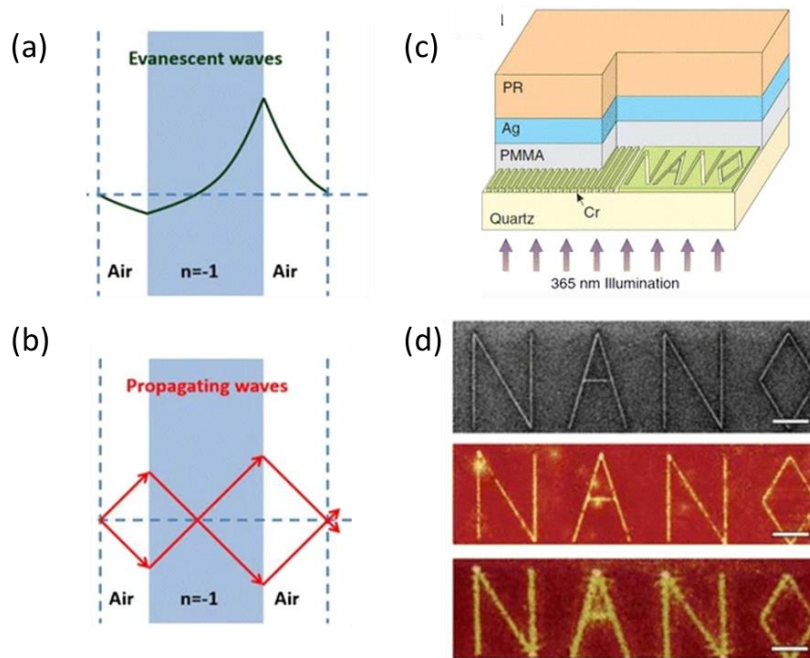
Figure III-10 : a) Evanescent wave amplification principle and b) focalization principle by a metamaterial with negative refractive index. c) Schematic of a perfect lens experiment made of a 35 nm Ag slab, the object for the experimental setup is a Cr film with the letters 'NANO' inscribe on it (linewidth of 40 nm). The image is recorded by a photoresist (PR) d) From top to bottom: comparison between a source object, the image obtained with a flat convergent lens made with a metamaterial with a negative refractive index and with a conventional convergent lens [17].

This type of flat convergent lenses have a better resolution because they are not limited by the diffraction phenomenon, contrary to classical lenses [17]. More recently, this technology has been implemented in industry by the start-up Metalenz with flat-lens based on the work of Capasso's group [18]. They commercialize precise meta-lenses which can replace several optics and thus reduce the cost and the size of different systems in many applications such as compact smartphone cameras, for the realization of virtual and augmented reality systems but also for sensors for self-driving cars.

Another application is the control of wave front propagation. Pendry and Smith proposed a 3D metamaterial design with a gradual permeability along the diameter of the structure and based on layers of SRR with cylindrical shapes (Figure III-11) [19]. To progressively modify the permeability, they gradually modified the dimension of the SRR central arms depending on the layer from 1.65 mm for the first layer (in the center) to 2.199 mm for the last layer (Figure III-11a). With this structure, they showed for an operating frequency of 8.5 GHz that the incident electromagnetic waves on the global structure bypass the empty zone located in the center of this structure (Figure III-11b-c). Thus, they gave birth to the concept of the electromagnetic invisibility cloak. In theory, the proposed structure allows to make a cylindrical zone of 2.7 cm radius invisible. In reality, the effect of invisibility is limited

by the losses of the structure and by its sensitivity to the different polarizations of the incident waves (at 8.5 GHz).
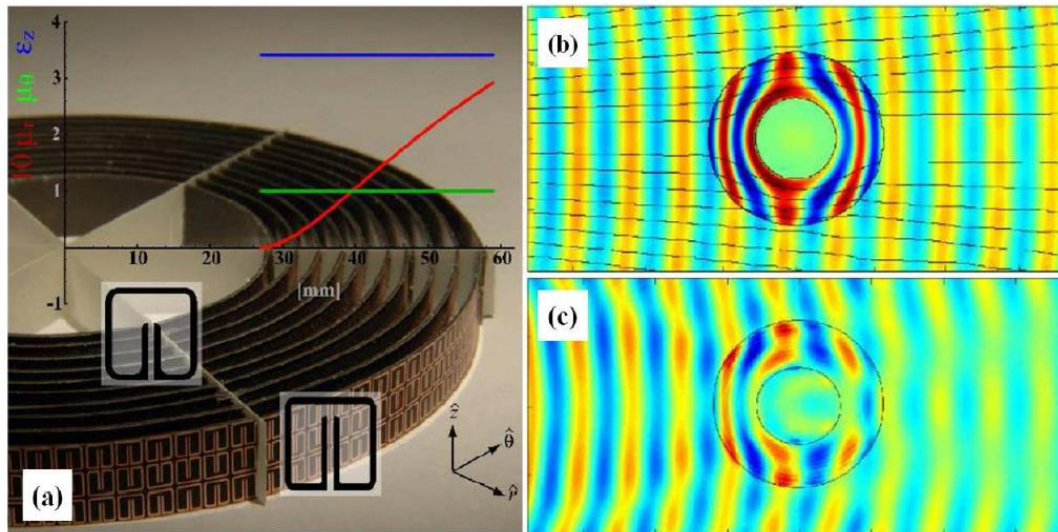
Figure III-11 : Example of a cylindrical metamaterial multi structure of with gradual permeability along the diameter of the device presenting, according to electromagnetic simulations, a zone of electromagnetic invisibility at a frequency of 8.5 GHz as shown in (b) but which remains imperfect in practice (c) [19].

More recently, Tie Jun Cui *et al.* proposed a coding/digital metamaterial [20]. By coding different unit cells with different phase responses, they demonstrated the possibility to control electromagnetic waves and realized different functionalities on a frequency band from 7 GHz to 16 GHz. As example, on Figure III-12 a 2-bit coding metasurface is presented. The 2-bit coding reposed on four different unit cells with phase responses of 0, π/2, π and 3π/2, corresponding to the '00', '01', '10' and '11' elements, respectively.
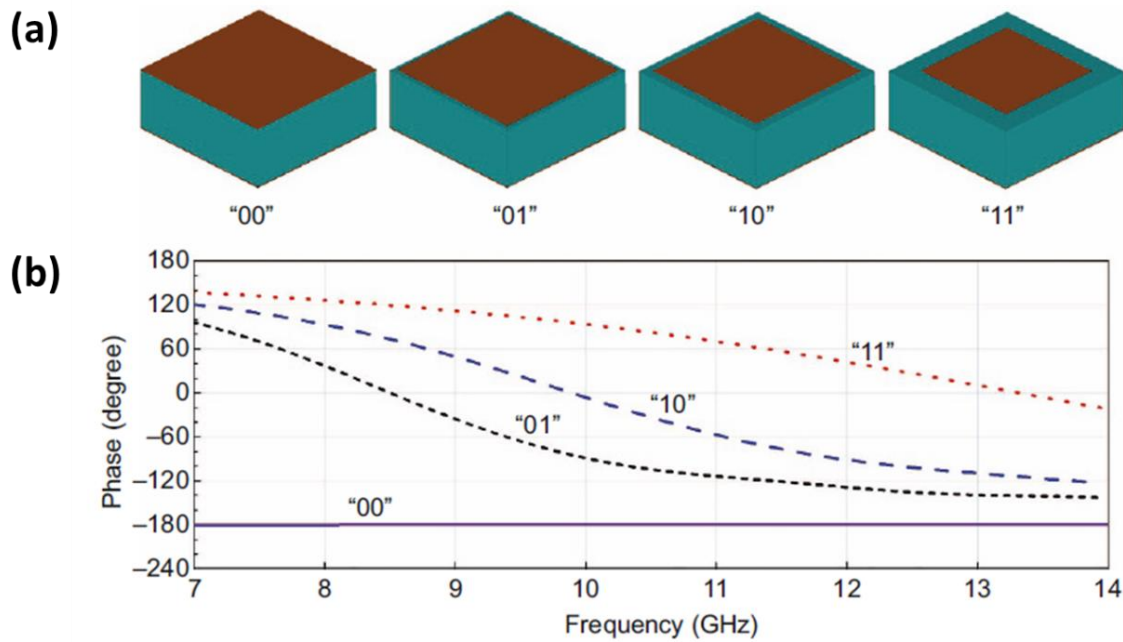
Figure III-12: 2-bit coding metasurface elements and their corresponding phase responses. (a) The '00', '01', '10' and '11' elements (from left to right) realized by square metallic patches with different sizes. (b) The phase responses of the '00', '01', '10' and '11' elements [20].

By coding sequences of different unit cells on a substrate, it is possible to obtain different responses of the metamaterial. As example, by coding the sequence 0001101100011011... (Figure III-13a), because of the created gradient phase change, the normally incident waves will be reflected at oblique angle (Figure III-13b). By changing the code sequence (Figure III-13c), it is possible to obtain a new response. In this example the structure is optimized to reduce the radar cross-section (RCS) for cloaking applications (Figure III-13d). The RCS corresponds to the target's ability to reflect radar signals in the direction of the radar receiver. They demonstrated a RCS reduction below -10 dB over a much wider frequency band from 7.5 to 15 GHz.
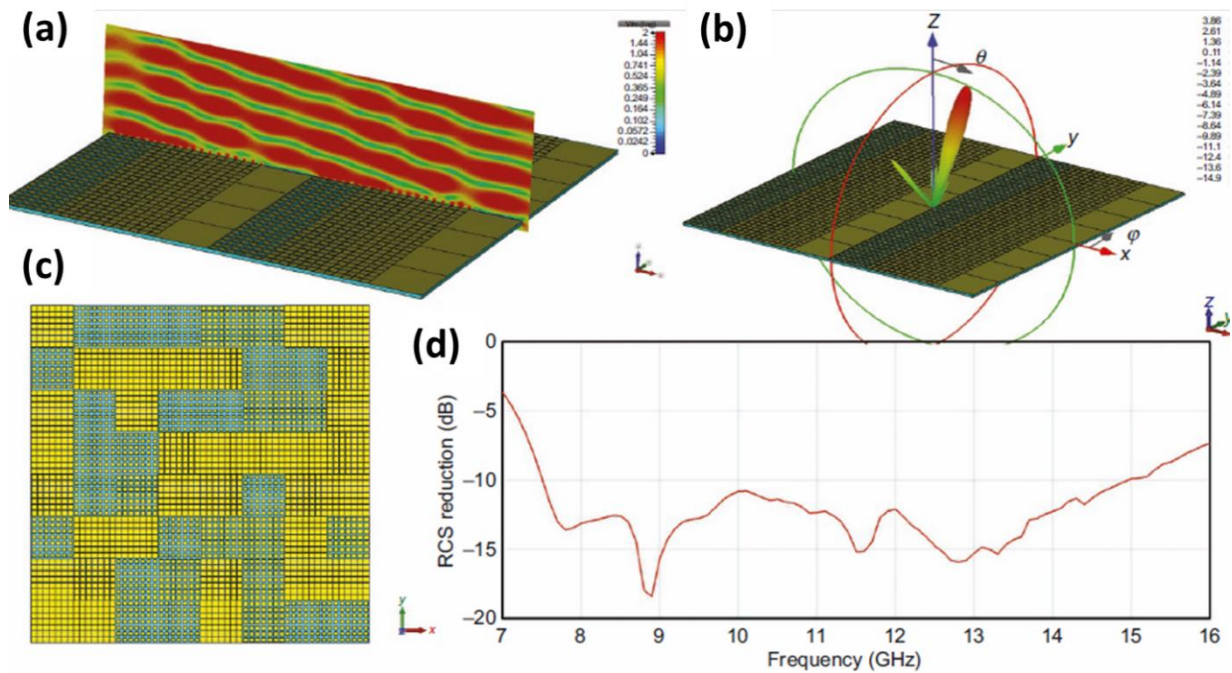
*Figure III-13: (a) A periodic 2-bit coding metasurface with the coding sequence 0001101100011011…
and the near-field distribution on an observation plane vertical to the metasurface. (b) Corresponding
3D far-field scattering pattern of the periodic 2-bit coding metasurface. (c) Non-periodic metasurface
constructed using an optimized 2-bit coding sequence and (d) corresponding simulation results of
monostatic RCS reductions over a wide frequency range from 7 to 16 GHz [20].*

Based on the previous coding metasurface, Tie Jun Cui *et al.* demonstrated the possibility to use biased diode to actively modify the element sequence by modifying the state of the unit cell. This type of metasurfaces is very attractive for many applications such as reducing the scattering features of targets, controlling the radiation beams of antennas similarly to phase-array antennas but using a different principle with a considerably less expensive approach. Additional this application can be extended to the millimeter wave and terahertz frequencies by simply changing the dimension of the unit cell.

The metamaterials represent a new alternative for numerous applications which can be easily transposed in different domains of the electromagnetic spectrum (optics, THz and micro-waves). They have been used in the terahertz range for numerous applications such as filters, polarizers, absorbers, antenna… [12, 21-23] in different domains such as defence, biomedical imaging systems or spatial telecommunication. However, metamaterials are fixed structures, after the fabrication process the dimension and thus the response of the metamaterial cannot be modified. However, as seen before, the response of the metamaterial, notably SRR depends on their dielectric environment. Thus, one can easily integrate an active material to actively tune the response of the metamaterial. For the realization of reconfigurable THz devices, in the next part, we choose to use GeTe as an active media because of its large THz properties variations emphasized in chapter II (conductivity, transmission…) but also due to

the facility to integrate and fabricate GeTe patterns using photolithographic process when integrated in a SRR structure.

3.2. Integration of GeTe in gold SRR metamaterials

3.2.1. Simulation of the SRR structure

Before integration of the GeTe, we propose to study the response of a metamaterial integrating a simple metallic SRR. The unit cell of the SRR structure is shown on Figure III-14.a The dimensions of the SRR have been chosen to have response around 0.3 THz, in the detection band of our THz TDS system (0.1-1.5 THz). For this frequency, the dimension of the unit cell has been fixed to 100x100 µm², the width of the SRR line to 10 µm, the ring size to 80 µm and the gap to 60 µm. The response of the device was evaluated using full wave electromagnetic simulations using the commercial software HFSS from Ansys.
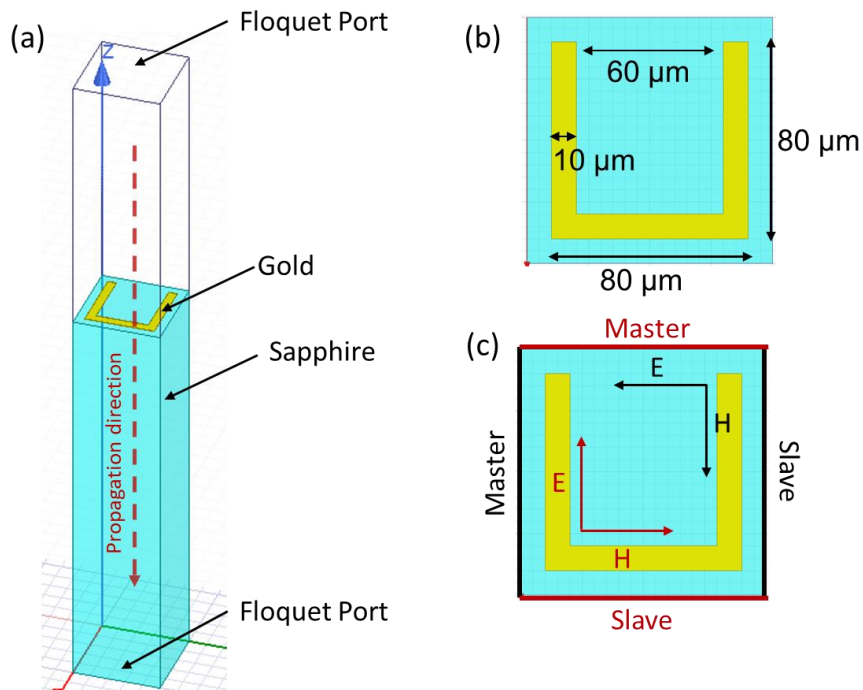
Figure III-14: (a) Schematic of the unit cell of the SRR with a large gap. (b) Dimensions of the unit cell of the SRR structure. (c) Boundary conditions with the two studied direction of the electric field.

HFSS is a software which used the finite element method (FEM) to simulate the response of a periodic structure. In our simulation the structure periodicity is defined by master/slave type boundaries. With this type of boundaries, the fields on the slave surface are constrained to be identical to those on the master surface. Contrary to other boundary conditions such as perfect magnetic conductors and perfect electric conductor boundaries, master/slave boundaries take into account the edge effects on the unit cell which can create artefacts in the simulation. On the other hand, this method generates calculations that are much more demanding in terms of volume and time, which limits their use, especially when

working with large structures at frequencies that are too high. The orientation of the electric field can be defined using Floquet ports, we simulated two orientations of the electric field, one parallel to the gap and one perpendicular to the gap (Figure III-14c). The simulated THz transmission of the SRR structure is shown on Figure III-15.
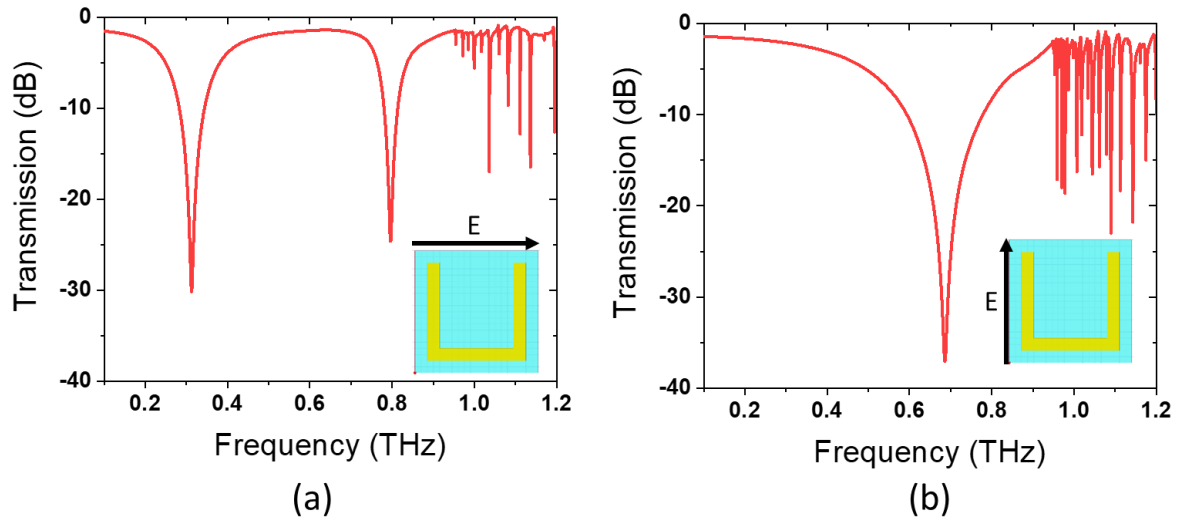
Figure III-15 : THz transmission responses of the simulation of the SRR structures for a polarization of the electric field parallel (a) and perpendicular (b) to the SRR gap

The incident THz wave is considered linearly polarized (the incident electric field is oriented in a unique direction). When the electric field is parallel to the SRR gap, a first resonance is observed at 0.3 THz which corresponds to the LC resonance of the structure. A second resonance can be observed at 0.8 THz which corresponds to a higher mode resonance of the SRR structure. In the case of the electric field is perpendicular to the gap (Figure III-15b), we observe a unique resonance at 0.69 THz which corresponds to the mutual coupling between each SRR structure. Finally, after 0.9 THz we can observe the appearance of resonance lobes for both polarizations, which should correspond to artifacts of the simulation.

In a similar way we simulated the effect of introducing the GeTe material within the SRR structure. The simulated structure is shown on Figure III-16, to limit the possible loses introduce by GeTe, we choose to reduce the gap size to 10 µm and fill it with a GeTe pattern.
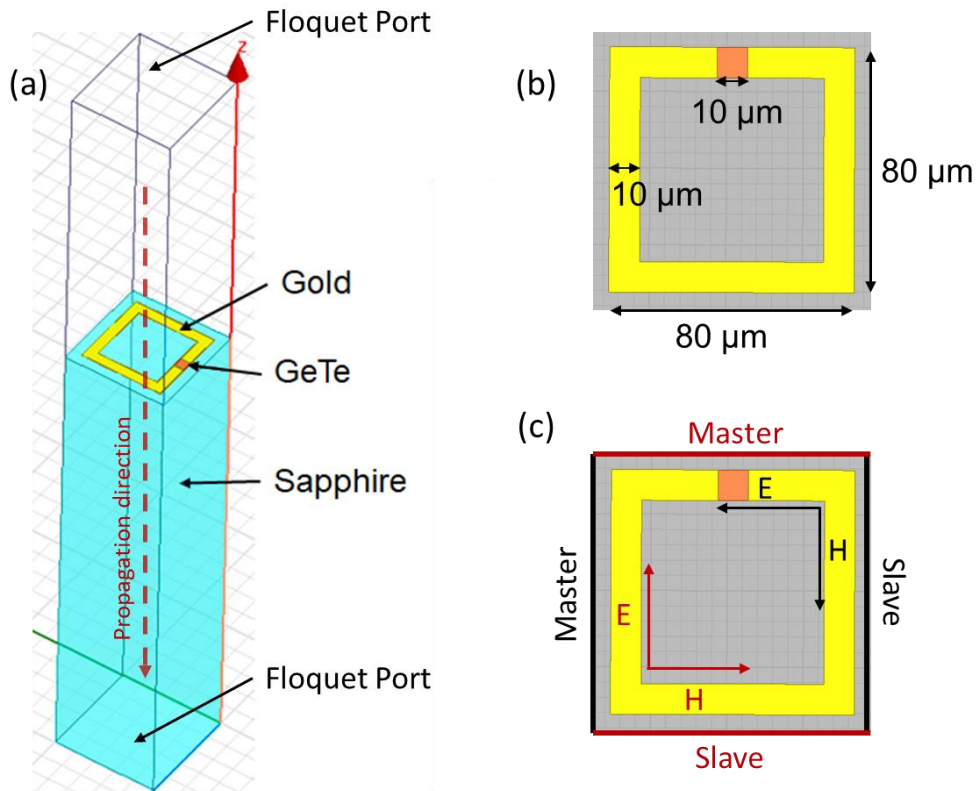
Figure III-16 : (a) Unitary cell of the hybrid metamaterial obtained on a c-cut sapphire substrate with (b) dimensions and (c) boundary conditions of the unit cell

Figure III-17 shows the simulated THz transmission of the metamaterial for both polarizations of the electric field and for both states of the GeTe (metallic and insulating). Based on the results presented in the previous chapter, we used a THz conductivity around 220 kS.m^{-1} for the GeTe crystalline (metallic) phase and around 200 S.m^{-1} for the GeTe amorphous phase in the simulations.

(a)   (b)
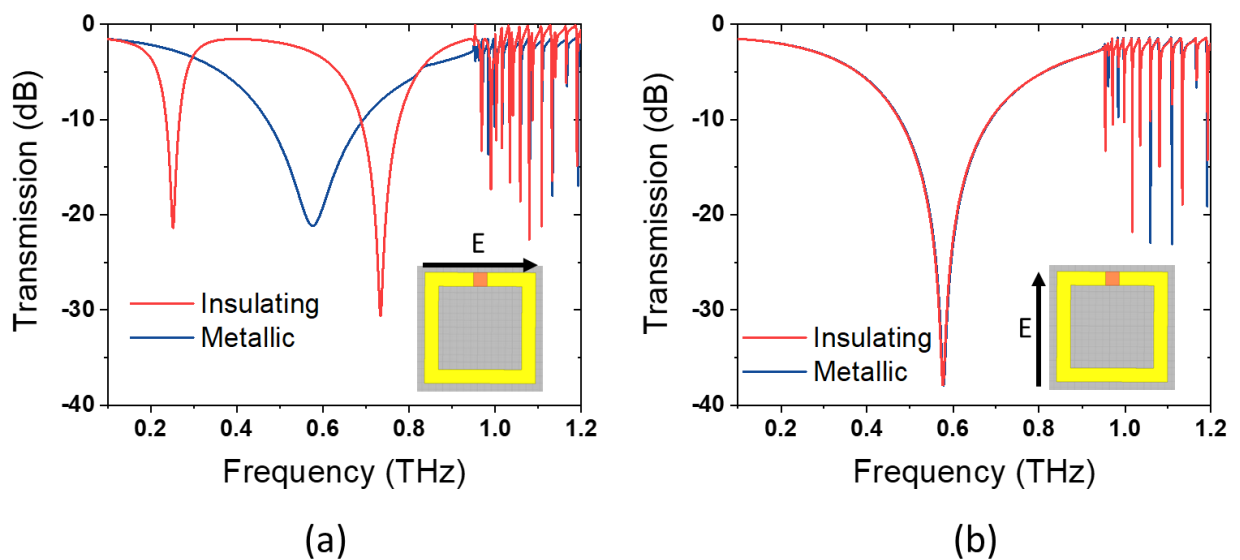
Figure III-17: Simulated THz transmissions of the GeTe-based SRR for a polarization of the electric field parallel (a) and perpendicular (b) to the gap

For the case in which the electric field of the incident THz beam is polarized parallel to the gap (Figure III-17a), we can notice a real change of the SRR response depending on the state of the GeTe pattern. When the GeTe is amorphous, it is almost transparent to the terahertz waves and the typical resonance of the SRR structure occurs. We observe the first LC resonance at 0.25 THz and the second resonance at 0.73 THz (red curve on Figure III-17). Compared to the previously presented SRR structure, we notice a shift of these two resonances to lower frequencies, due to the decrease of the gap size from 60 µm to 10 µm (equation $III.14$.). When the integrated GeTe is metallic, it shorts the capacitance gap, the LC resonance disappears, and we observe only one resonance at a frequency of 0.57 THz, corresponding to the mutual coupling between each SRR structure. On the contrary, when the electric field is perpendicular to the gap (Figure III-17b), the specific state of the GeTe does not change the THz response of the metamaterial. We record a unique resonant frequency at 0.57 THz which corresponds to the same resonance as in the wave polarization state for which the electric field is parallel to the gap and the GeTe is in the metallic state (Figure III-17a). However, if we compare both polarizations of the electric field when the GeTe in the gap is metallic, the resonance has a lower amplitude and quality factor when the electric field is parallel to the gap than when it is perpendicular. This is due to the presence of GeTe in the gap which is not a perfect metal. To observe the effect of the conductivity on the resonance strength, on Figure III-18 we simulated the response of the SRR structure for different conductivity values of GeTe.
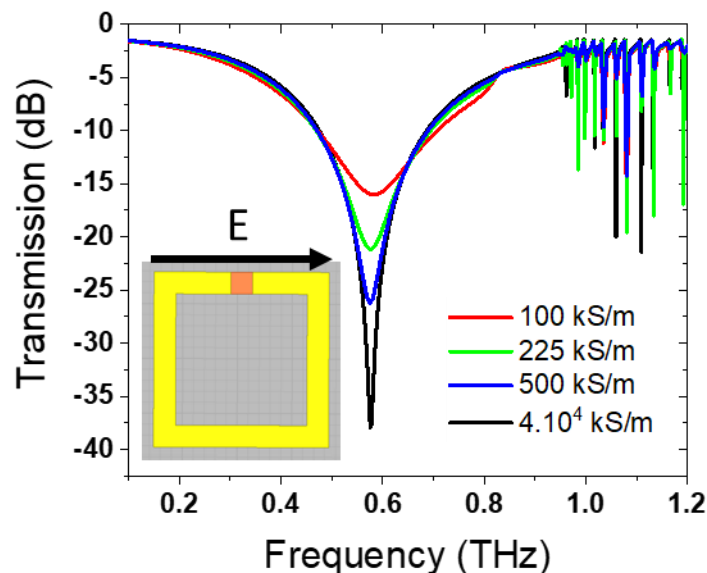
Figure III-18: THz transmission of the GeTe-based SRR for a polarization of the electric field parallel for different value of GeTe conductivity.

As we can see when the conductivity of the GeTe increase, the metallic loses decrease and lower the damping factor (equation (***III.7***)) and the transmission at the resonance decreases.

To better understand the response of the metamaterial, we plot on Figure III-19 the electric field distribution in the SRR structure at different frequencies corresponding to the recorded resonances, for both polarization of the incident THz waves (different orientations of the electric field) and for amorphous and crystalline GeTe.
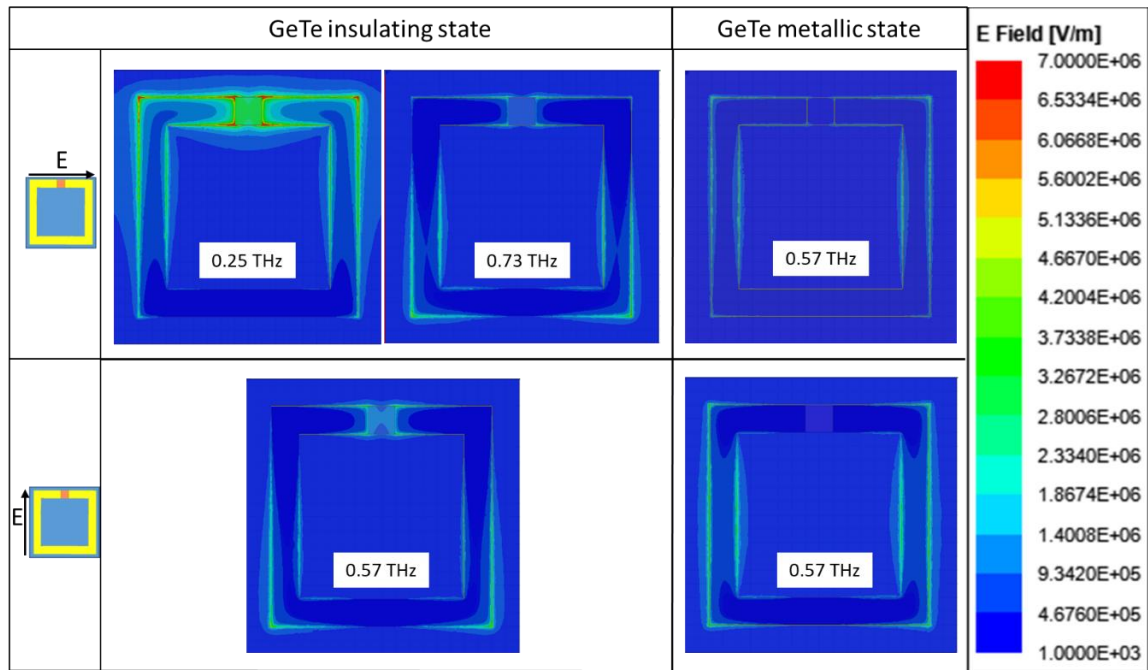
Figure III-19: Electric field distribution in a SRR unit cell of the metamaterial at different resonant frequencies

For the amorphous (insulating) GeTe case, the electric field distribution is different, depending on the resonance frequency. In the case where the electric field is parallel to the SRR gap, for the resonance at 0.25 THz, we observe a strong confinement of the electric field in the gap of the SRR. It confirms the LC resonant behavior of the structure. For the second resonance at 0.73 THz the electric field is not confined in the gap but on the metallic lines of the ring, it corresponds to a horizontal electric quadrupole mode [24]. When the electric field polarization is perpendicular to the gap, for the resonance at 0.57 THz the electric field is distributed on the metallic lines of the SRR and corresponds to a plasmonic resonant mode as similar to an electric dipole mode [25].

When the GeTe is crystalline (metallic), it closes the SRR gap and we observe a confinement of the electric field on the surface of the two vertical arms of the SRR for both polarizations of the electric field implying a similar resonance mode. However, in the case of a perpendicular polarization, we notice a stronger electric field on the surface of the two vertical

arms as expected from the plots on Figure III-17. As explained before, the metallic GeTe is not a perfect metal and has more losses than gold. Consequently, when the electric field is parallel to the gap all the electric field is not confined on the surface of the two vertical arms of the SRR and losses are observed. The resonance observes at 0.57 THz can be due to the mutual coupling of the line between each SRR of the array.

We have simulated two other different configurations of the unit cell to assess the influence of its structure on the response of the metamaterial. We simulated a SRR with an asymmetric gap by moving the 10-µm long GeTe pattern by 10 µm to the left (Figure III-20a). In the case (Figure III-20b), we reduced the overall size of the SRR from 80 µm x 80 µm to 50 µm x 50 µm.
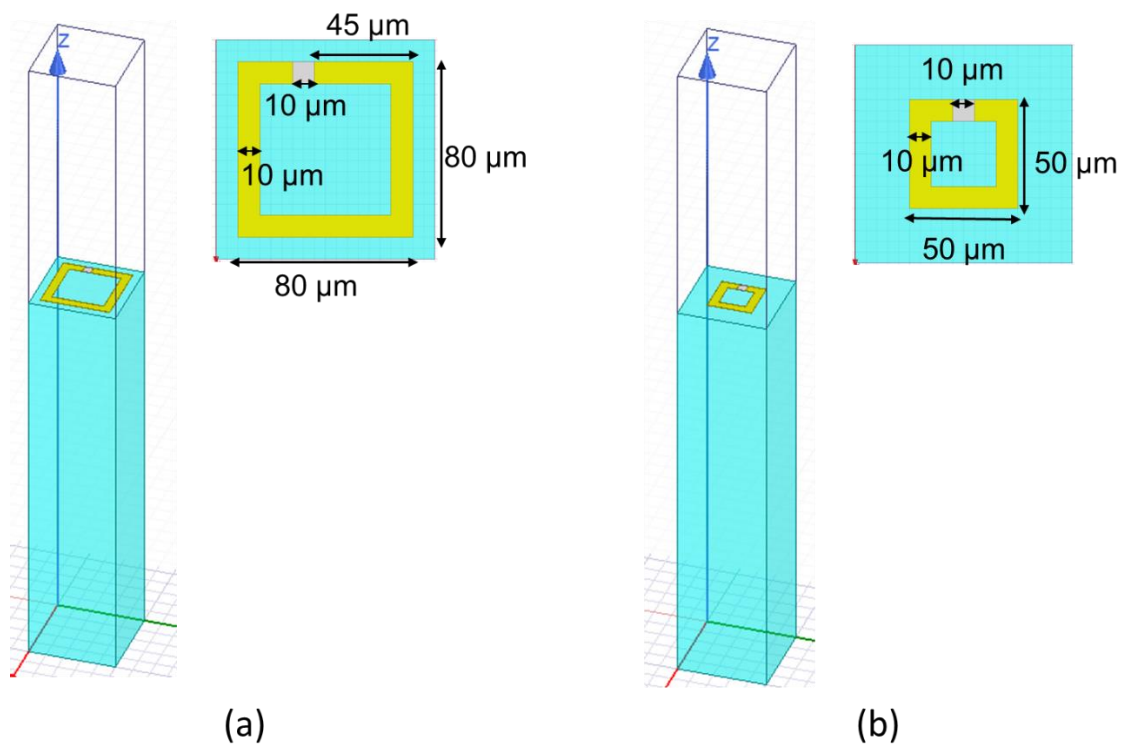
Figure III-20: (a) Schematic of the unit cell of the asymmetric SRR and (b) schematic of the unit cell of the SRR with smaller dimensions

We simulated the THz transmission of both SRR structure for a polarization of the electric field parallel to the gap because this case is inducing the largest change in the THz transmission for the different states of the GeTe (Figure III-21).
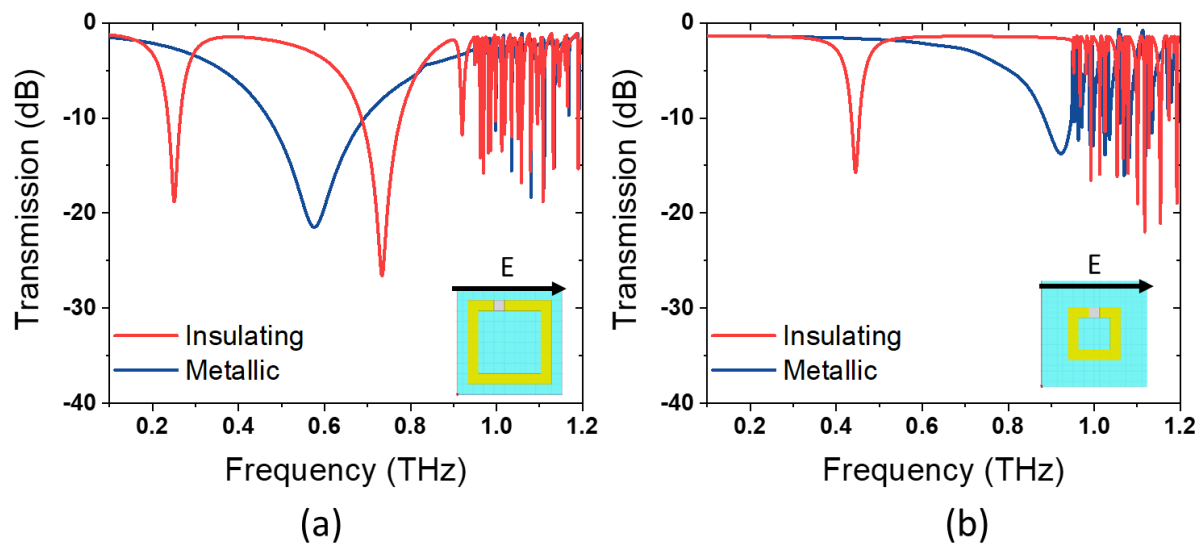
Figure III-21: Simulated transmission of the asymmetric SRR structure (a) and for the small SRR structure (b) for a polarization of the electric field parallel to the gap

The simulation results show that an asymmetric gap does not induce a variation in the SRR response compared with the symmetric design, we observe the same resonances at 0.25 THz and 0.73 THz when the GeTe is amorphous and at 0.57 THz when the GeTe is crystalline. On the contrary, when we decreased the dimension of the metallic SRR structure, we can observe a shift of the resonances towards higher frequencies. When the GeTe is amorphous, the LC resonance shift from 0.25 THz to 0.44 THz. These results are in agreement with the theory and equation ($III.14.$). When the size of the ring is reduced, the inductance of the system is decreasing and thus, the resonant frequency value is increasing. The same shift is also observed when the GeTe is crystalline. By changing the dimension of the ring, we change the coupling between each SRR and thus the resonant frequency.

Thus, it is theoretically possible to tune the response of a metamaterial structure using GeTe pattern integrating in their gap. We can foresee realizing hybrid metamaterials consisting in a metallic SRR integrating GeTe patterns in their gap for the realization of reconfigurable THz devices.

3.2.2. Realization of the hybrid GeTe-metal metamaterial

In order to validate the design approach and the simulation results of the four studied SRR structures, they were fabricated using classical microfabrication technologies, in a clean room environment. The different metamaterial devices were fabricated on the same c-cut sapphire substrate using two principal steps: first, the deposition and patterning of the GeTe and secondly the realization of the metallic structure, fabricated in gold, using a lift-off procedure (Figure III-22).
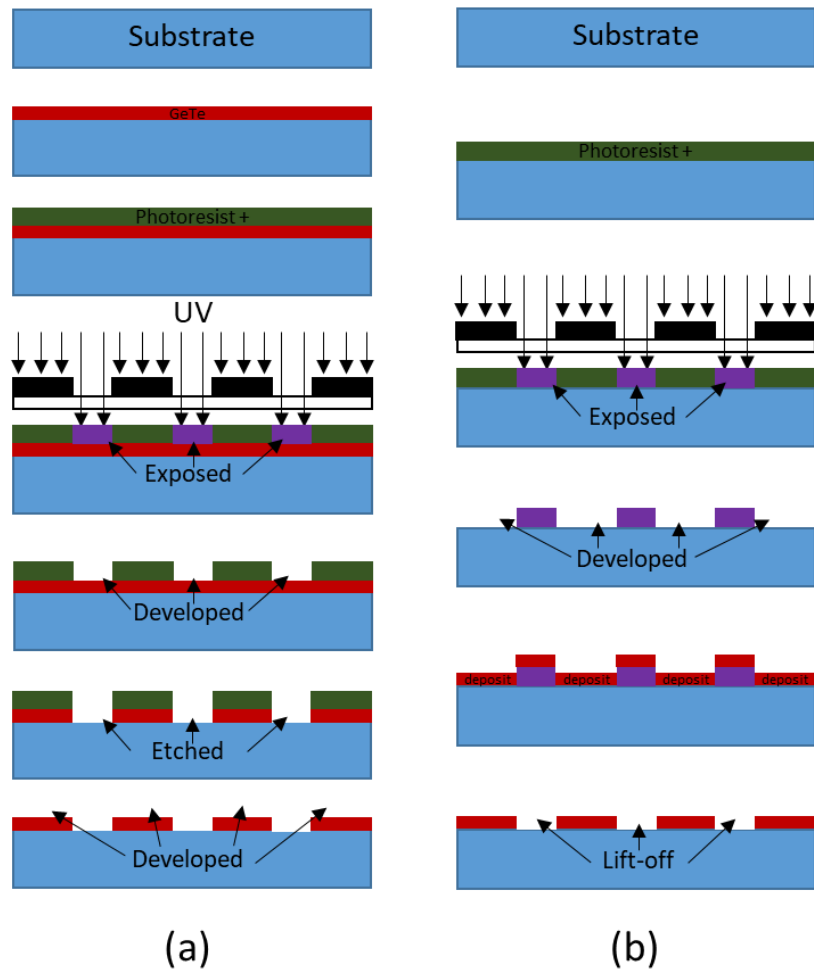
Figure III-22 : (a) Illustrations of the steps of GeTe pattern etching using a positive photoressit and (b) of the lift-off process using a negative resin for the fabrication of the metallic structure of the metamaterials.

As explained in the previous chapter, the GeTe was fabricated using DC magnetron sputtering. After the GeTe film deposition, several steps of photolithography are required to obtain the desired GeTe patterns. In our case we used a wet etching process whose protocol is as follows (Figure III-22a):

- Deposition of positive photoresist S1813 on the GeTe film by spin coating with 4000 RPM during 40s;

- Photoresist heating at 110°C for 1 minute on a heating plate;

- UV exposure during 20 s of the photoresist through a contact lithographic mask which is defining the GeTe patterns;

- Developing of the photoresist in a diluted micro-developer solution;

- Annealling for 1 minute at 110°C;

- Wet etching of the GeTe through the obtained photoresist mask;

- Total UV exposure of the remaining resist followed by a developer bath to remove the masking photoresist.

After the deposition of the GeTe, we proceeded to the realization of the metallic structures of the metamaterials having a bilayer structure, of 300-nm gold layer grown on a 30-nm titanium one (adhesion layer). The metallic parts have been obtained using a lift-off process using the following protocol (Figure III-22b):

- Deposition by spin coating of negative photoresist AZ5214E at 4000 RPM during 40s;

- Photoresist heating at 105°C for 1 minute;

- UV exposure for 3.5 seconds of the photoresist through a contact mask defining the metallic structure;

- Reverse annealing at 120 °C for 1 minute;

- Total UV exposure of the sample for 20 seconds;

- Developing of the photoresist using a pure developer (MF 26A)

- Electron-beam deposition of the 30-nm titanium layer following by the 300-nm thick gold layer;

- Photoresist lift-off process using an acetone bath

- Cleaning the sample in isopropanol and deionised water and drying using a dry air blower

The fabricated hybrid metamaterials having different SRR topologies are shown on Figure 3.3.
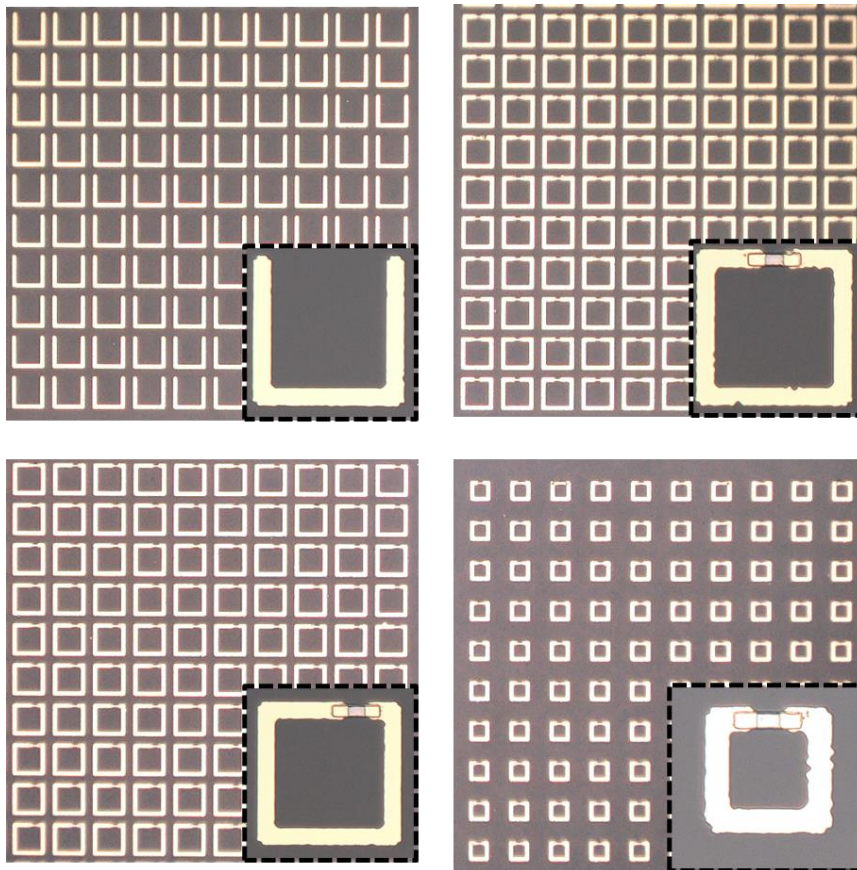
Figure III-23 : Optical microscopy images of the realized gold SRR Structures integrating GeTe in their gap with a close-up look at one unit-cell

When we measured the dimension of the realized structure, we observed slight differences with the theoretical dimensions of the SRR, notably, for the smallest SRR where a variation around 1 µm is observed in the line length. The realized structures were further characterized using THZ-TDS in the frequency band from 0.1 to 1 THz.

3.2.3. THZ characterization of the fabricated devices

3.2.3.1. Characterization of the SRR structure using thermal activation

The THz performances of the metamaterials with as deposited amorphous GeTe were evaluated using the THz TDS system presented in the second chapter. Then, we crystallized the GeTe patterns by heating the whole structure using a heating plate and characterized the SSR structures after cooling using again the THz TDS.

The first investigated SRR structure is a simple metallic metamaterial without GeTe (Figure III-24).
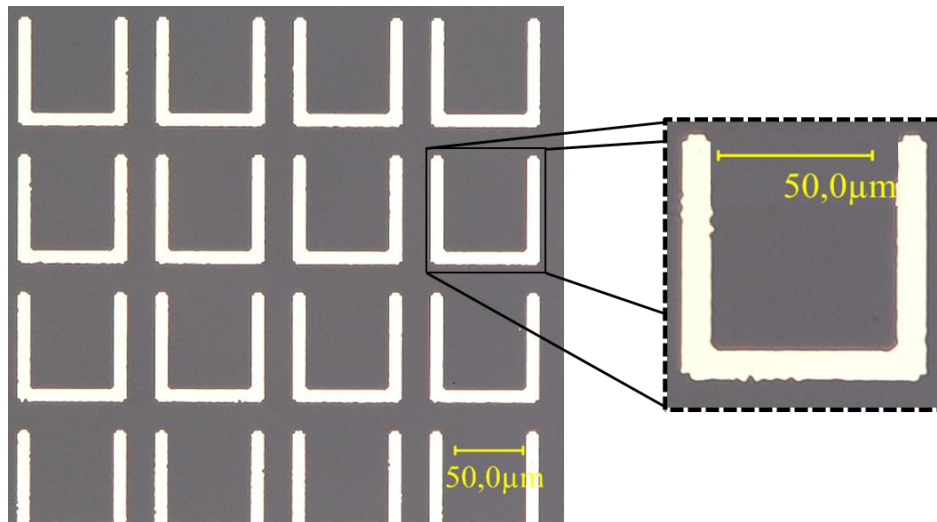
Figure III-24 : Optical image of the fabricated SRR metamaterial array and the corresponding unit cell with a 60 µm gap and not integrating GeTe patterns

We have measured the normalized THz transmission of the structure for a polarization of the electric field perpendicular and parallel to the gap (Figure III-25).
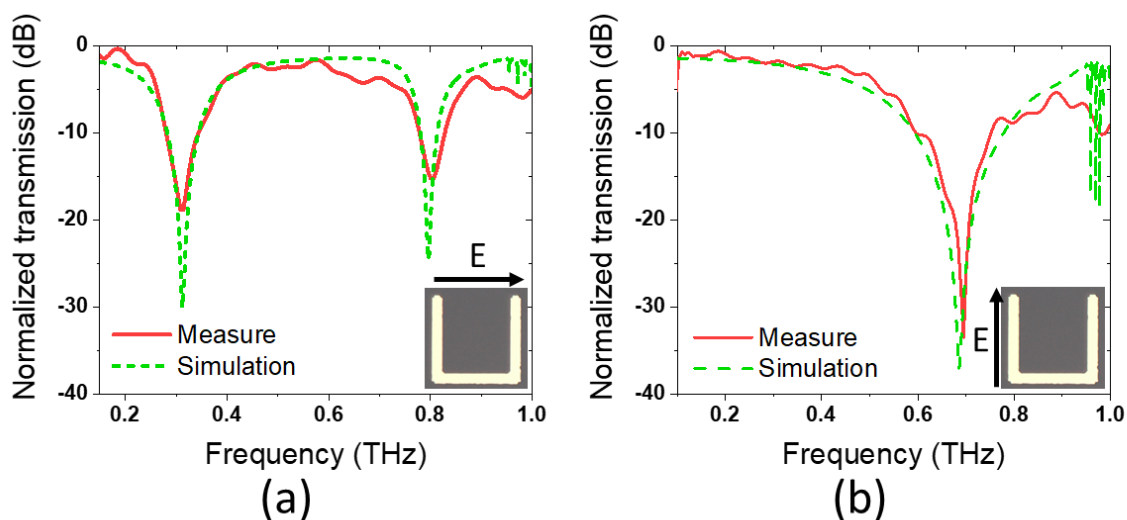
Figure III-25 : Measured and simulated normalized transmission of the SRR for an electric field (a) parallel to the gap and (b) perpendicular to the gap

As observed from Figure III-25, the measurements are agreeing very well with the simulation. When the electric field is parallel to the gap we observe the similar resonances in the transmitted THz spectra, at 0.3 THz and at 0.8 THz. However, the amplitudes of the measured resonances are weaker than the simulation. Thus, at 0.3 THz, the transmission is around -20 dB for the measurements whereas it is around -30 dB for the simulation. This difference can be explained by a lack of resolution of the THz TDS system due to the treatment on the THz-TDS data. As explained in chapter II, in order to minimize the Fabry-Perot effect, we "cut" the end of the Thz-TDS data and replaced it by artificial zeros. If this method allows the suppression of oscillations in the frequency dependent transmission spectra, the data are

smoothed by the treatment and the amplitudes of very narrow resonances can be reduced. When the electric field of the incident THz waves is perpendicular to the gap, we observe also a good agreement between the measure and the simulation. For both polarizations of the incident waves, we observe a decrease of the transmission after 0.9 THz. This decrease can correspond to the plasma resonance frequency of the metamaterial which is not as resolved as for the simulations because of the treatment on the THz-TDS data.

The optical image of the symmetric SRR with GeTe patterns is shown in Figure III-26.
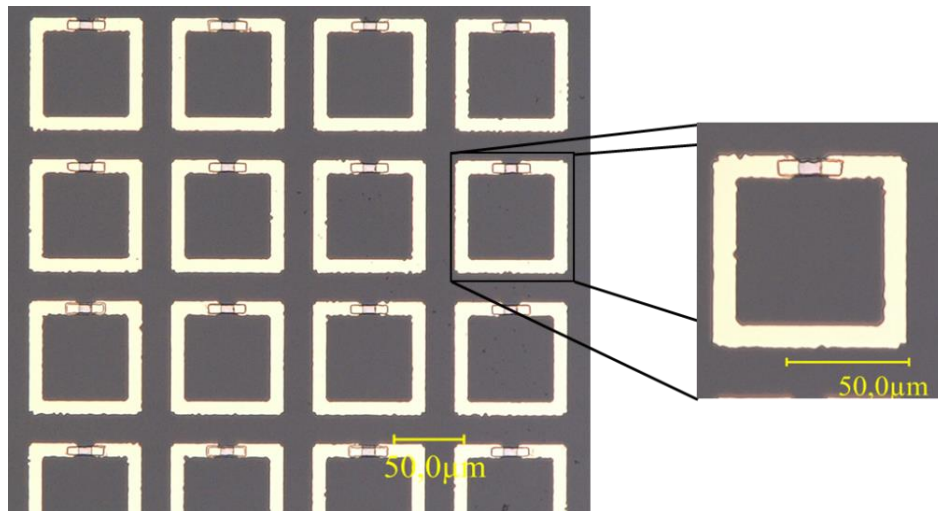
Figure III-26 : Optical image of the fabricated hybrid metamaterial and the corresponding unit cell with a symmetric structure

In Figure III-27 the transmission for amorphous GeTe is shown for a polarization of the electric field parallel and perpendicular to the gap of the SRR structure. When the GeTe is amorphous, it is transparent to the THz waves and, as expected from the electromagnetic simulations, the normal response of the SRR structure occurs (Figure III-27). When the electric field is parallel to the SRR gap we can observe a first LC resonance and a second resonance. For both polarizations, we also observe a decrease of the THz transmission for frequencies higher than 0.9 THz, corresponding to a possible higher order plasmonic resonance [26].
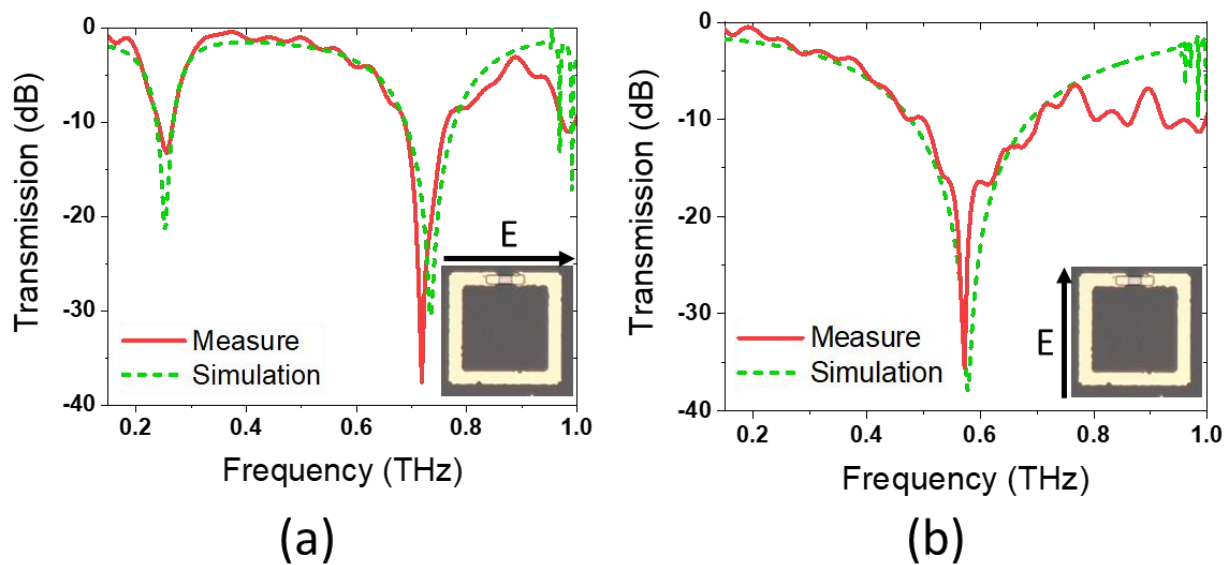
Figure III-27: Measured and simulated normalized THz transmission of the SRR integrated amorphous GeTe for (a) an electric field parallel to the SRR gap and.(b) for an electric field perpendicular to the SRR gap.

The GeTe patterns were crystallized by heating the material during 30 min at 300°C using a heating plate, to ensure a complete crystallization of the GeTe. The THz transmission of the SRR structure integrating a crystalline GeTe pattern is shown on Figure III-28. We can clearly see the modification of the SRR responses compared to the amorphous case (disappearance of the LC resonance), which highlights the principle of tunability of this structure under the effect of a thermal control. In this case, we may observe a pretty good agreement between the measurement results and the simulations, the conductivity of the GeTe crystalline film seems to be correctly evaluated. Thus, the integration of chalcogenide PCMs in a metallic SRR structure allows a modulation of the incident THz waves of 25 dB at 0.75 THz.
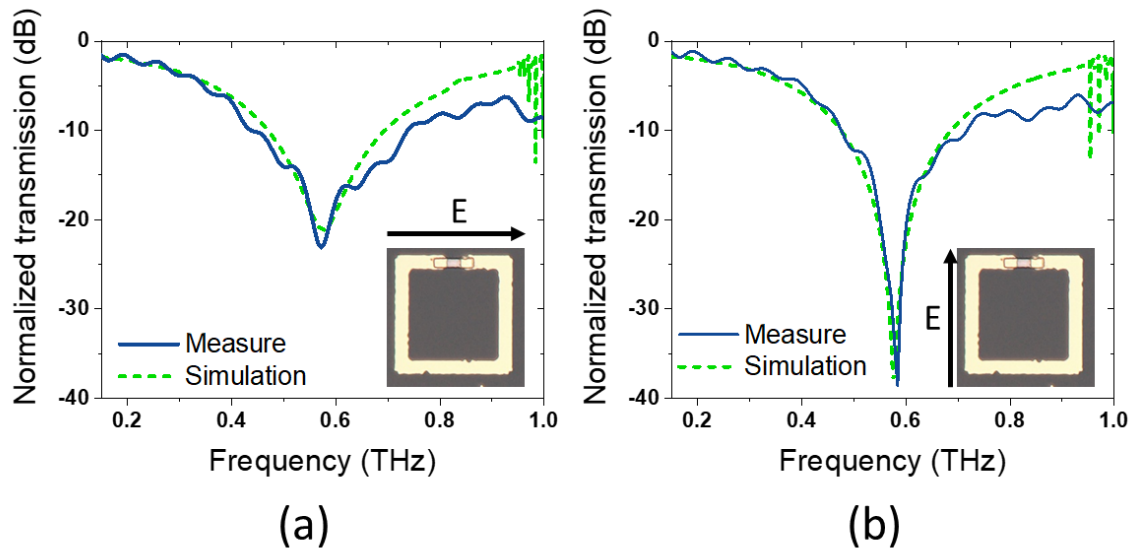
Figure III-28 : Measured and simulated normalized transmission of the SRR with crystalline GeTe in the gap for (a) an electric field parallel to the gap and (b) for an electric field perpendicular to the gap.

The presented results confirm that the integration of a GeTe pattern does not influence the response of the SRR metamaterial when the electric field is perpendicular to the gap. For the following hybrid metamaterials we will therefore present only the cases where the electric fields of the incident waves are parallel to the SRR gaps.

On the Figure III-29, the optical image of an asymmetric SRR structure and the close-up image of the unit cell is presented.
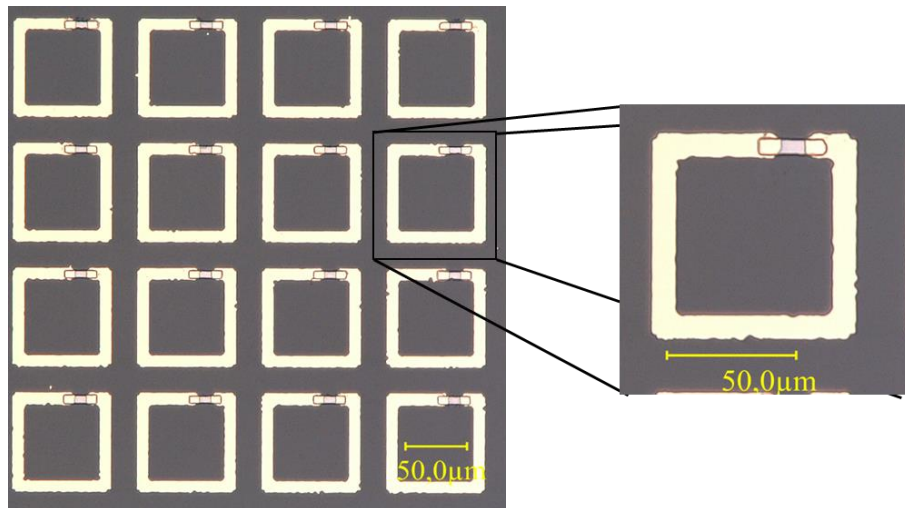
Figure III-29: Optical image of the fabricated hybrid SRR metamaterial and the corresponding unit cell with an asymmetric structure

The simulated THz transmission for the SRR integrating an amorphous GeTe pattern (Figure III-21a) is in a good agreement with the measurements (Figure III-30), with the exception of the same shift of the resonant frequencies as in the previous case. Similarly, when the GeTe is crystalline the LC resonance disappears, and a unique resonance appears at 0.57

THz. Compared to the previous symmetric SRR, no real change in the THz transmission is observed, the same LC resonance occurs at 0.25 THz.
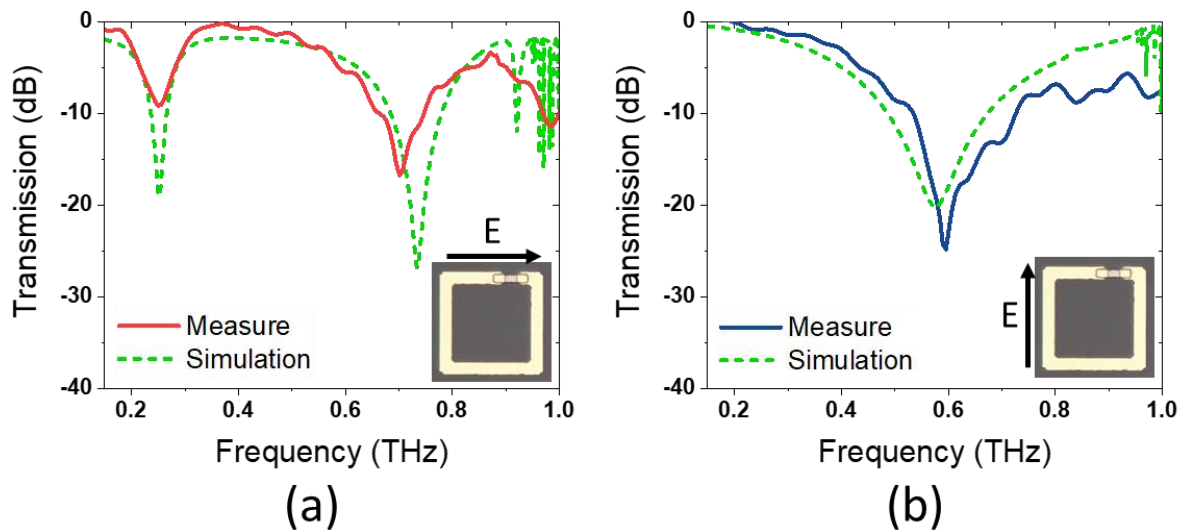
Figure III-30 : Measured and simulated normalized transmission of the asymmetrical SRR integrating a GeTe pattern for an electric field parallel to the gap with (a) amorphous GeTe. and (b) crystalline GeTe

The last studied hybrid metamaterial is the SRR with a gap of 10 µm filled with GeTe but with lower dimensions, of 50 x50 µm². The optical microscopy image of the fabricated structure is shown on Figure III-31.
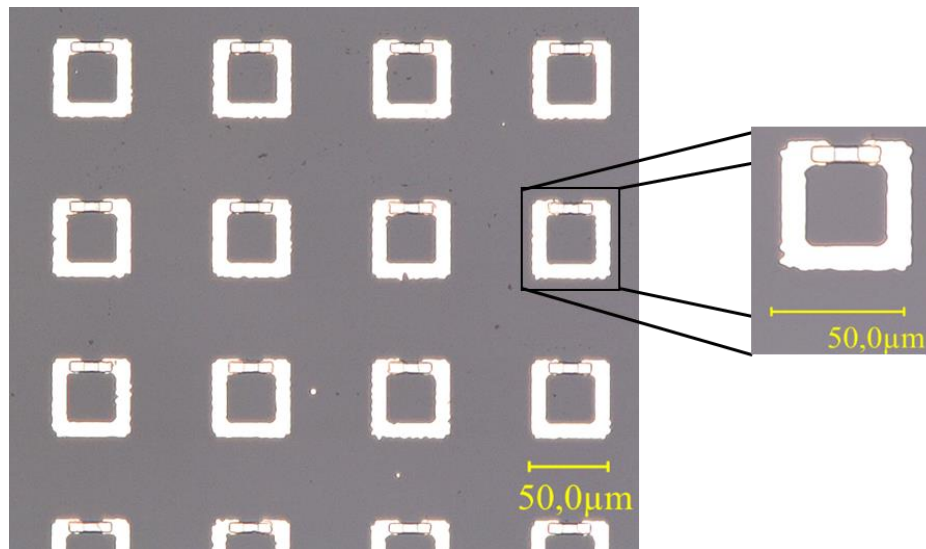
Figure III-31: Optical image of the fabricated metamaterial integrating a 10-µm long GeTe pattern and 50 x50 µm² dimensions and the corresponding unit cell.

The THz transmissions of the hybrid SRR structure for an electric field parallel to the gap when the GeTe pattern is in the amorphous or in the crystalline phases are shown on Figure III-32. As expected from the simulation results, we observe an increase of the resonant frequency when the size of the SRR decrease. However, we can notice a shift of the measured LC resonance compared to the simulation results. The LC resonance of the measured device

occurs at 0.46 THz whereas the simulated resonance occurs at 0.44 THz. This difference can be explained by an error in the extracted conductivity value of the amorphous GeTe. As explained in the design part, the LC resonance is corresponding to a high concentration of the electric field in the SRR gap where is integrated the GeTe pattern. Thus, the GeTe pattern and more precisely its permittivity seems to have a high impact on the position and the amplitude of the resonance. For this particular SRR structures the GeTe takes a larger place in the structure, influencing on a larger extent the overall SRR response, which can explain this shift was not observed with the previous SRR. Additionally, due to the small size of the SRR structure, the response is more sensitive to dimensional errors coming from the fabrication process.
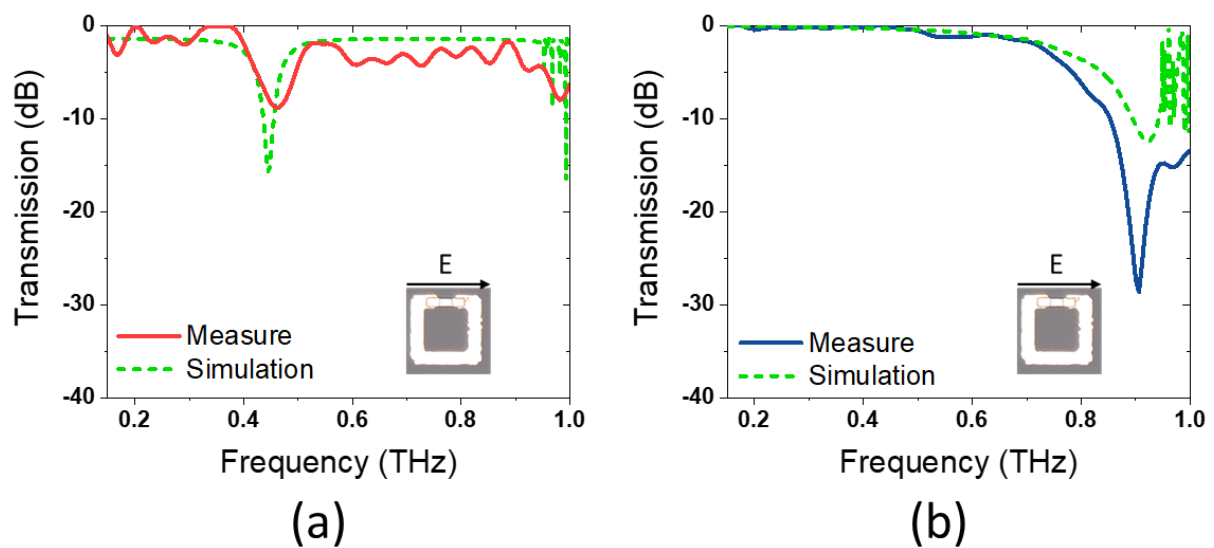
Figure III-32: Measured and simulated normalized transmission of the 50 x50 μm² hybrid SRR for an electric field parallel to the gap integrating GeTe patterns in(a) an amorphous state. and (b) a crystalline state

When the GeTe pattern is crystalline, we observe, as expected, a unique resonance at 0.9 THz. The simulation and the measurement results are in fairly good agreement.

Thus, we have demonstrated SRR structures with a strong variation of the THz transmission, depending on the specific state of the integrated GeTe patterns. For a symmetric SRR (line length of 80 μm and gap of 10 μm) at 0.75 THz we achieve a variation between amorphous phase and crystalline phase around 25 dB, at the state of the art in the domain [26, 27].

3.2.3.2. Optical activation of the fabricated metamaterials structures

We have demonstrated the possibility to integrate GeTe in a metamaterial structure and to modify its response to THz waves, using thermal heating to crystallize the integrated GeTe patterns. Yet, the proposed system is not completely reconfigurable since it is not

possible to reverse the transition of the GeTe patterns by simple direct heating. Therefore, in this section we propose to study the possibility to use the optical activation presented in Chapter II to modify the response of the hybrid SRR structure in a reversible way, i.e. modifying the GeTe material from amorphous-to-crystalline and, reversible, from crystalline to the amorphous state.

We realized the same previous SRR structures on c-cut sapphire substrate. To crystallize the GeTe patterns, we employed the direct irradiation of the GeTe using pulses from an excimer KrF laser with a wavelength of 248 nm and a pulse duration of 35 ns.
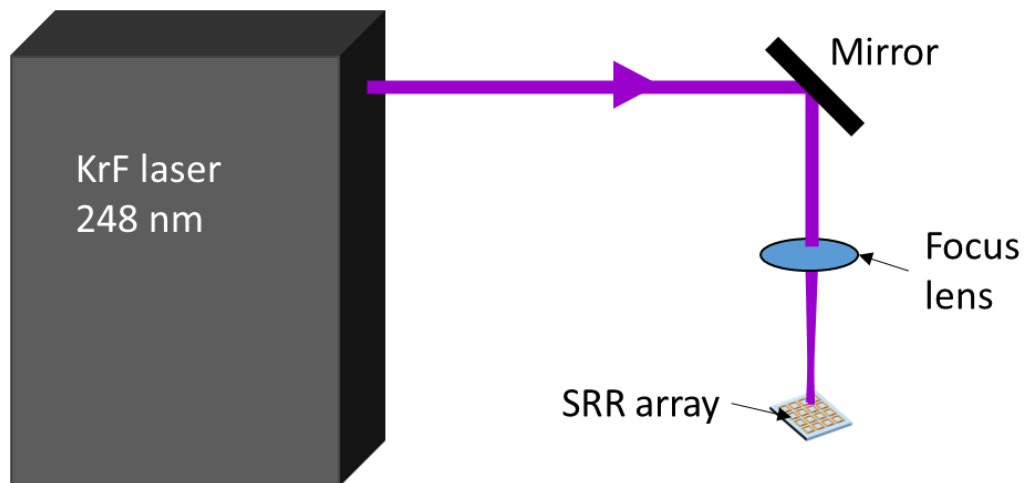
Figure III-33: Schematic of laser exposure process of a SRR structure

Laser pulses with energy densities around 90 mJ/cm^2 were employed for transforming the GeTe from the amorphous to the crystalline state while the reverse transition requires energy densities in the range 185-190 mJ/cm^2. The THz transmission of the symmetric SRR structure with side dimensions of 80 μm and a gap filled of 10 μm GeTe pattern is shown on Figure III-34, comparatively, for the thermal activation and laser activation schemes.
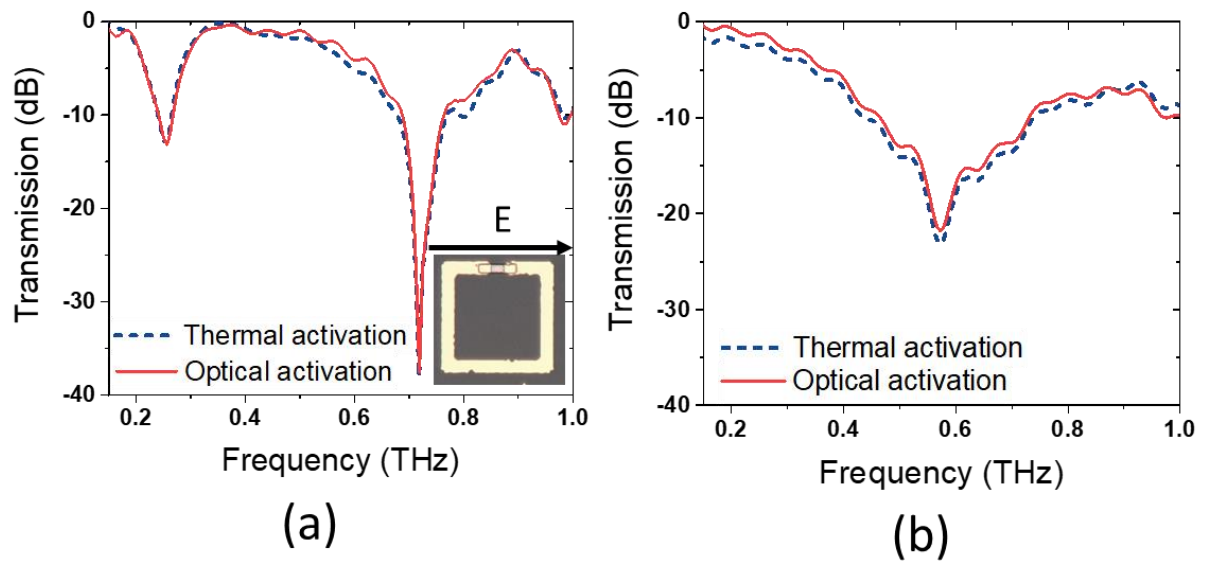
Figure III-34: Measured normalized transmission of the SRR using thermal and optical activation schemes in the case of (a) amorphous GeTe and (b) crystalline GeTe

As we can observe from the results presented on Figure 3.19, by using the optical activation scheme we achieve a modulation of 25 dB at 0.7 THz, as good as the thermal activation when the GeTe goes from amorphous to crystalline phase. Thus, it is possible, by using successive UV laser pulses with correct energy (as discussed in Chapter II), to switch the hybrid SRR structure between two different states.

3.2.3.3. Effect of the substrate on the SRR resonance

To observe the effect of the substrate on the resonance of the SRR structure, we realized the same SRR structure on silica instead of sapphire-c substrate. The performances of the realized devices are similar to the previous devices obtained on sapphire substrates, except the position of the THz resonance peaks (Figure III-35).
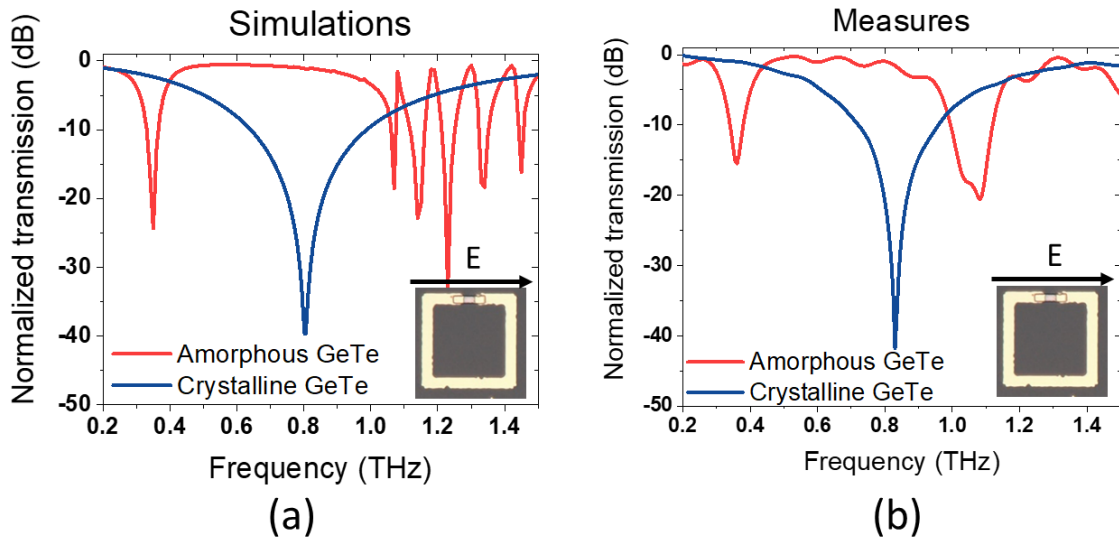
Figure III-35: Simulated (a) and measured (b) THz response of GeTe-based SRR device fabricated on SiO2 substrate.

When the GeTe pattern within the SRR gap is amorphous, it is almost transparent to the THz waves and the normal LC resonance of the SRR structure occurs at around 0.35 THz. When the GeTe is crystalline, it shorts the gap of the SRRs and the LC resonance vanished, a different resonance appearing at 0.85 THz which corresponds to the mutual coupling between each of the thus modified SRR structures. Compared to SRR deposited on sapphire substrate, in the case of SRR deposited on silica substrate, a resonance frequency shift to higher frequency is observed (from 0.25 THz to 0.35 THz). It is due to the different dielectric constants of the silica substrate (real permittivity of ~3.7) compared with the sapphire one real (permittivity around 9.8 in the direction perpendicular to the substrate surface).

To conclude this study, the integration of a GeTe pattern in a SRR structure allows to bring a tunable functionality to the overall metamaterial. The results obtained for the different structures we realized and studied suggest that it is possible to obtain THz response modulation at specific frequencies by choosing the correct dimension of the structure. We have also highlighted the possibility to use optical activation to actively tune the response of the SRR structure. Finally, the high transmission modulation (25 dB) and the non-volatile switching of this structure is very attractive for the development of low consumption and compact THz devices such as reconfigurable filters for fast high-frequency, beyond 5G, telecommunications.

3.3. All dielectric GeTe-based devices

In the previous part we demonstrated the possibility to realize hybrid THz devices composed of a metallic metamaterial structure integrated chalcogenide PCMs patterns. Regarding the strong contrast in THz amplitude signals transmitted through a GeTe film prepared in two different states (crystalline and amorphous) and presented in Chapter II, we

can consider realizing structures made only of GeTe (without additional metallic structures). The realization of all-dielectric structures (realized only with GeTe) offers new interesting and promising opportunities for developing active THz reconfigurable devices. Notably, polarizer devices have critical roles in imaging and wireless communication applications. In this part we proposed to study different polarizer structures made of GeTe.

3.3.1. Design and fabrication of GeTe polarizers

A wire-grid polarizer structure lets the waves with a polarization perpendicular to the wire-grid pass while the waves with a polarization parallel to the grating are blocked. The performance of a polarizer are mainly determined by the period, line width and depth of the grid elements[28]. We designed four different polarizers made of GeTe with different line widths and periods. Three polarizers have the same period P of 10 µm but different wire width w of 2, 3 and 5 µm (denoted as P1(10/2), P2(10/3) and P3(10/5) respectively). The last polarizer has a period of 6 µm and a width line of 3 µm (denoted as P4(6/3)). The dimensions and the fill factors (defined as the ration between the line width and the period) of the four different polarizers are summarized in Table III-1.

Table III-1: Dimensions of the four realized polarizers

	Period P (µm)	Line width w (µm)	Filling factor (w/P)
P1	10	2	0.2
P2	10	3	0.3
P3	10	5	0.5
P4	6	3	0.5

The principle of operation and the structure of the four realized polarizers are shown in Figure III-36**.**
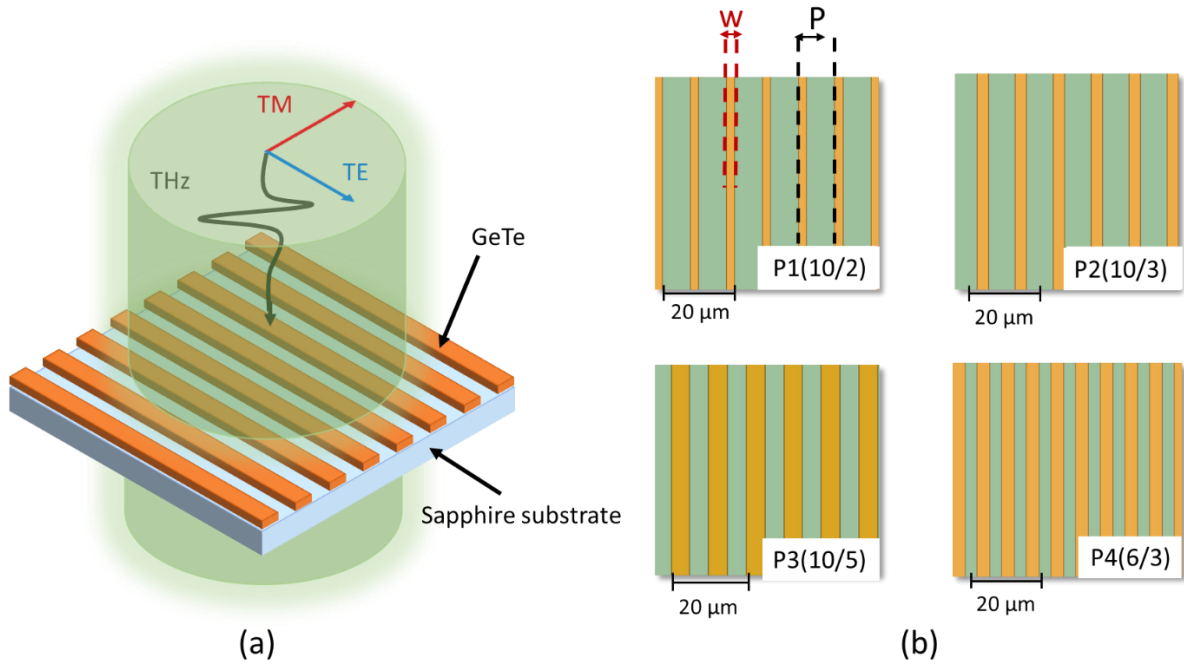
Figure III-36: (a) Schematic of the polarizer structure (b) Schematic of the four different GeTe polarizers (P1, P2, P3, P4) with different period P and line width w (P µm /w µm)

Firstly, the simulation of the different polarizer structures were realized using HFSS software. The simulation was realized using master/slave type boundaries on the structure, the propagation is orthogonal to the polarizer and the electric field is either parallel to the grating (TE polarization) or perpendicular to the grating (TM polarization). The simulated results for the four different polarizers with crystalline GeTe are shown in Figure III-37.
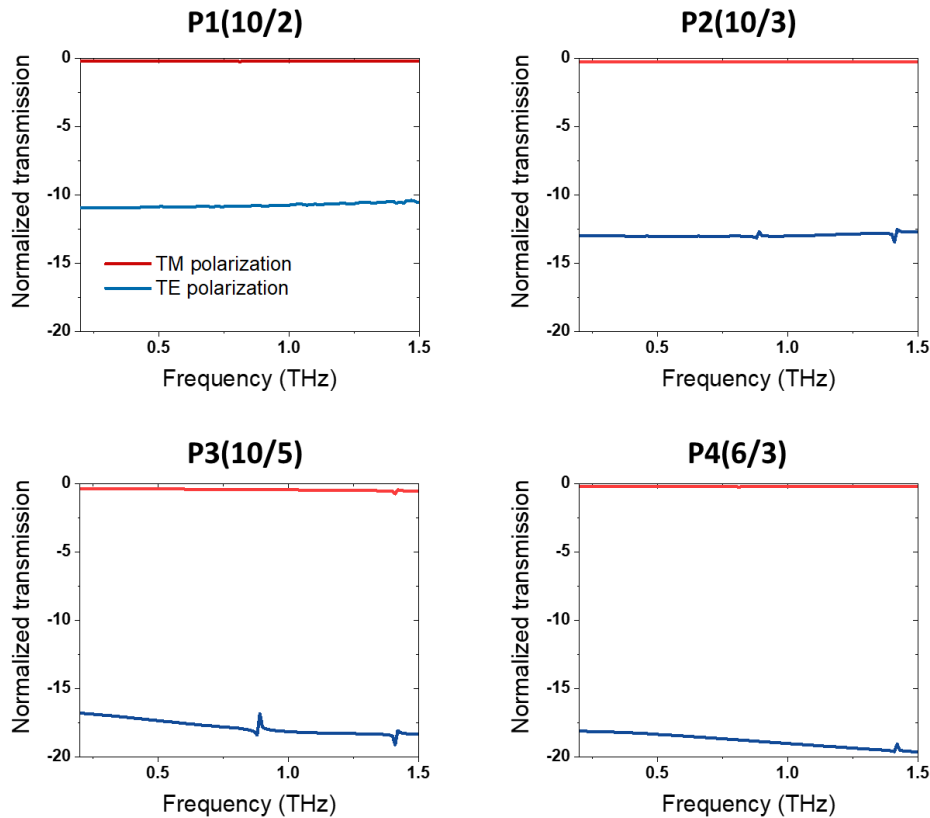
Figure III-37: Simulated THz transmission for both TM and TE polarization of the four polarizers with crystalline GeTe (P1, P2, P3, P4) with different period P and line width w (P µm /w µm).The small spikes around 0.8 and 1.4 THz come from artefact simulation.

When in the amorphous phase, the GeTe is insulating and the structure is almost transparent to the terahertz waves. As expected, no polarization effect could be observed. In the crystalline case, the GeTe is metallic and it is introducing a polarization effect to the incident THz waves. For each structure, the TM polarization transmission (perpendicular to the grating) is unchanged whereas the TE polarization transmission (parallel to the grating) decreases drastically.

If we look in detail, for the first polarizer P1 (P=10 µm and w=2µm) we observe a decrease of the transmission from -0.22 dB for the TM polarization at 1 THz, to -10.77 dB for the TE polarization. If we increase the width of the lines to 3 µm, the THz transmission of the TM polarization is not modified. However, the THz transmission of the TE polarization decreases to -13 dB. If we further increase the width line until 5 µm by keeping the same period (P3) the THz transmission of the TE polarized waves decreases to -18.1 dB. Thus, by increasing the fill factor of the polarizer (defined as the ratio of the width of a single wire to the period of the wire grid structure), we can increase the performance of the polarizer structure. On the last polarizer (P4), we kept a fill factor of 0.5 and we reduced the period from 10 µm to 6 µm. By decreasing the period of the polarizer, we can further decrease the TE transmission

of the polarizer to -19 dB. Thus, gratings with a small period are more adapted to realize high performance THz polarizers.

3.3.2. Fabrication and THz characterization of the polarizers

The 250 nm GeTe polarizer structures on sapphire c substrate (Figure III-38) were realized using the lift-off procedure presented Figure III-22. The transmission of the realized polarizers was measured using the previously presented THz-TDS system.
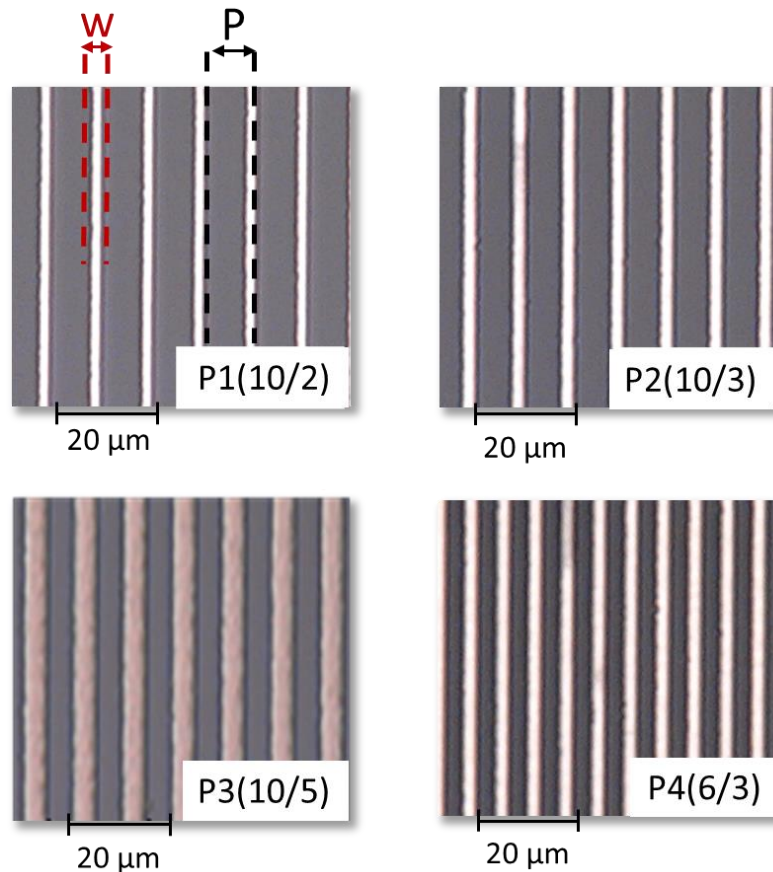
Figure III-38: Close-up optical image of the four different GeTe polarizers (P1, P2, P3, P4) with different period P and line width w (P µm /w µm)

On Figure III-39 is shown a close-up image and the transmission of the P2 polarizer when the GeTe is amorphous. As explained before, in the amorphous phase the GeTe is transparent to the terahertz waves and does not change the response of the incident waves. As expected, no significant difference can be observed in the THz transmission of the two TM and TE polarizations.
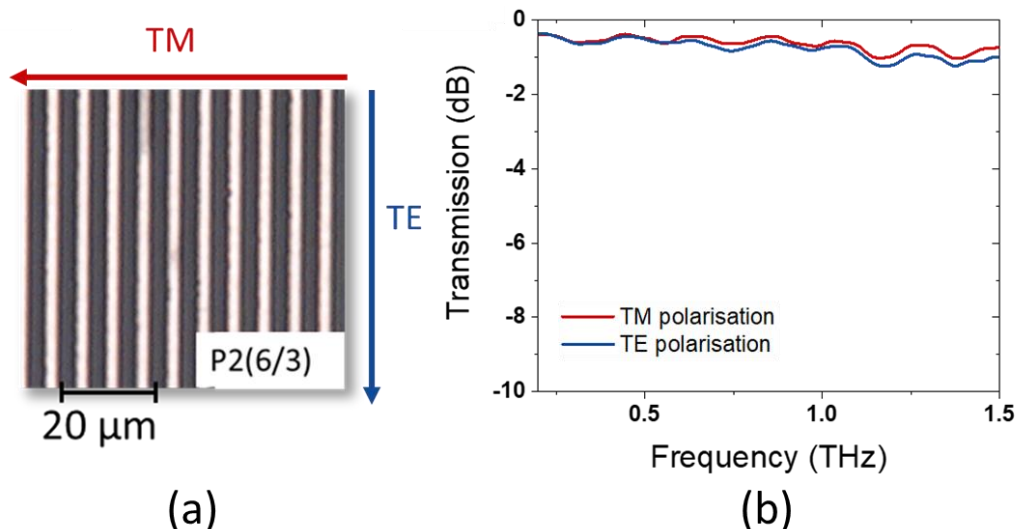
Figure III-39: (a) Optical image of a polarizer structure realized solely with amorphous GeTe with a line width of 3 µm and a period of 6 µm and (b) the corresponding normalized transmission for TE and TM polarization of the incident THz wave.

The same measures were realized on the three other structures and we found the same results, both TM and TE THz waves are transmitted with identical results. We crystallized the GeTe structures by direct heating the whole structure at 300 °C, on a heating plate. The measured THz transmission of the four crystallized GeTe polarizers are shown on Figure III-40**.**
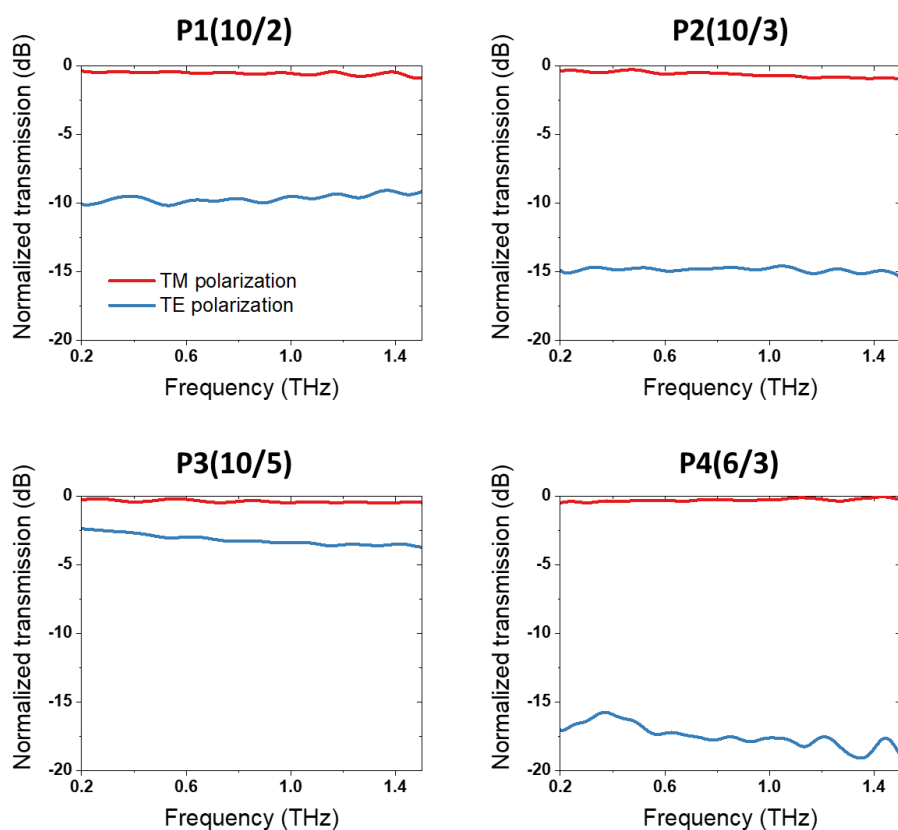
Figure III-40: Measured THz transmission for both TM and TE polarization of the four polarizers

Due to a problem during the fabrication of the P3 polarizer, the device was defective and presented degraded characteristics. If we compare the results for the other polarizers with the simulations, we observed a similar behavior. Thus, by increasing the fill factor and decreasing the period of the polarizer, we can achieve polarization performances with better contrast between the TM and TE polarized waves. For the best polarizer P4, a contrast of 16.5 dB is observed between TE and TM polarizations. This value is slightly different from the simulation and can be due to the small variation in the dimension of the fabricated lines and periods within the device but also to the error in the crystalline GeTe conductivity value. In Figure III-41, the transmission simulation for TE polarization of a polarizer P4 (6/3) for different conductivity value of crystalline GeTe is presented.
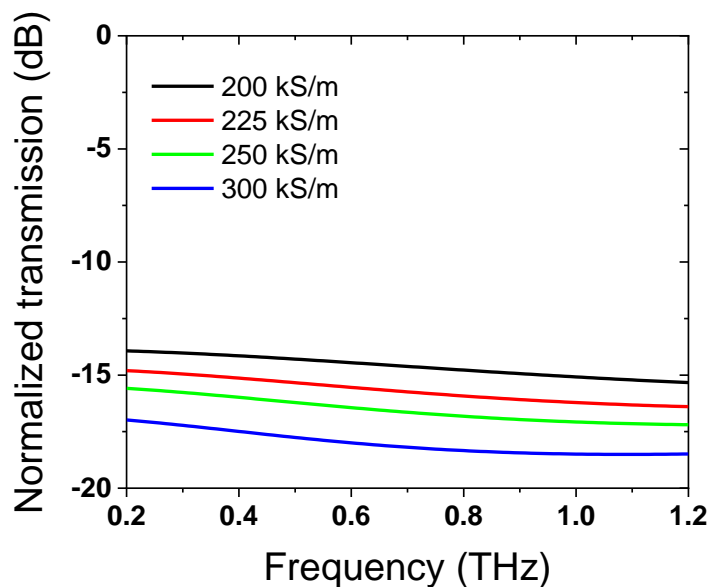
Figure III-41: Simulation of THz transmission for TE polarization of a crystalline GeTe polarizer (P4 type) for different values of conductivity.

As we can see, when the conductivity increases from 200 kS/m to 300kS/m the TE THz wave transmission decreases from -15 dB to -18.5 dB at 1 THz. We found a simulated transmission closer to the measured transmission for GeTe conductivity value of 250 kS/m (instead of the 225 kS/m used in the initial simulation).

If the thermal activation does not allow the reversal of the transition, as for SRR structure, the optical activation of GeTe material using specific laser pulses can be a solution to actively tune the response of the GeTe-based polarizers. In Figure III-42 the THz transmission of the P2 polarizer with a period of 10 μm and a line width of 2 μm based on GeTe crystallized using both optical activation and thermal activation schemes is presented.
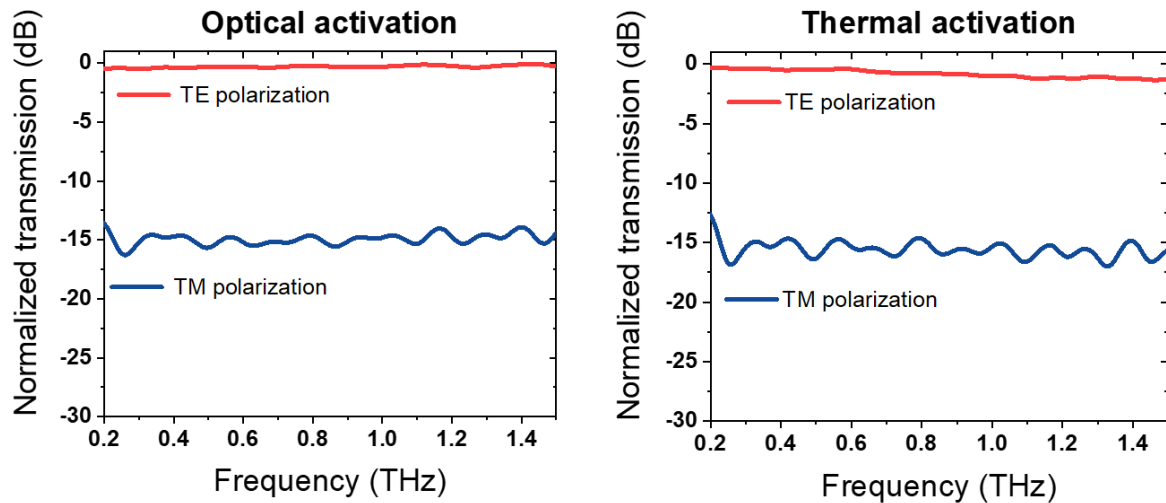
Figure III-42: Comparison of the THz transmission of two GeTe P2-type polarizers with a period of 10 µm and a width line of 3 µm crystallized using optical activation and thermal activation

As observed, the performance of the polarizer is similar, independent of the activation method. We can conclude that optical activation is a reliable method to actively modify the response of a GeTe THz structure.

We compared the performance of GeTe-based polarizers with similar structures fabricated using metallic lines (Au/Ti- based structures). The gold lines-based polarizers were realized using the lift-off process and the e-beam evaporation of a gold/titanium (250 nm/ 10 nm) film on c-cut a sapphire. The measured THz transmissions of the gold polarizer for structures with the same characteristics as described in Table III-1 and in Figure III-36 is shown in Figure III-43.
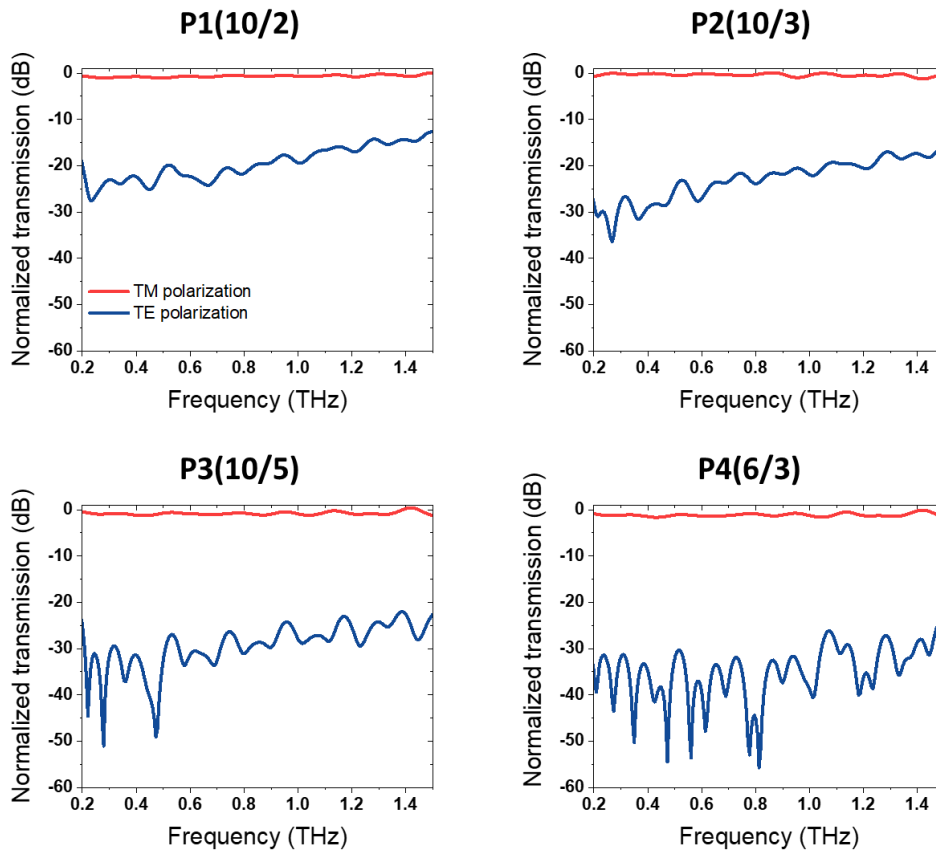
Figure III-43: Measured THz transmission for both TM and TE polarization of the four types of gold-based polarizers

As expected, we observed the same behavior as the polarizers realized using solely GeTe, which confirms the metallic nature of the crystalline GeTe. When the period is kept constant and the fill factor is increased from 0.2 (P1 polarizer) to 0.3 (P2 polarizer) and then to 0.5 (P3 polarizer), the TE polarization level is decreasing from -20 dB to -30 dB at 1 THz which confirms that better performance/contrast can be achieved by increasing the fill factor. As seen previously with the GeTe polarizer, gratings with a small period are preferable for obtaining a better performance [29]. If we keep the same fill factor and decrease the period until 6 µm (P4), we can further decrease the TE transmission below -40 dB at 1 THz. In the case of P4-type device, the signal is noisier because we reach the limit of detection of the THz-TDS system. Comparatively, gold-based polarizers have far better performances than similar GeTe-based devices. This is expected because gold is a perfect metal at THz frequencies and has better conductivity (around 8.10^6 S.m^{-1} at 1 THz) than GeTe. Consequently, a better reflection of THz wave is observed for the TE polarization. The best gold polarizer presents a contrast between the two polarizations superior to 40 dB. Nevertheless, gold structures are fixed and passive structures whereas a PCM structure can be tuned as desired by completely or partially activate the GeTe patterns using optical activation.

In conclusion, we demonstrated for the first time to the best of our knowledge the possibility to realize an all dielectric (metal free) reconfigurable THz device using solely chalcogenide PCM which presents a broadband, high extinction ratio (16.5 dB) between the TE and TM polarization when in crystalline phase and an optically induced non-volatile transition. Chalcogenide materials allow introducing new approaches to realize fast (nanosecond timescale) planar reconfigurable THz devices such as frequency-selective surfaces, reconfigurable spatial modulators, power limiters.

3.4. THz polarizers based on metallic GeTe structures fabricated by optical writing within a bare amorphous GeTe film

3.4.1. Principle and fabrication of the device

We demonstrated before the possibility to realize all-dielectric reconfigurable THz devices using laser activation. These devices represent a real interest for the realization of reconfigurable devices. Nevertheless, they are limited in functionalities due to the fixed, engraved GeTe structure, which cannot be changed. With the development of beyond 5G communications, low consumption and compact devices are highly desired for the development of THz transmission lines [30, 31]. The previous approach has demonstrated the possibility to realize all dielectric reconfigurable THz made of GeTe, however the GeTe was structured beforehand using photolithography which limited the reconfigurable device to a single function. Here we are proposing a lithography free method to realize reconfigurable THz devices based on optical activation to engrave specific metallic GeTe structures in a bare amorphous GeTe film. Lithography free method allows high degree of freedom, not limited to only one GeTe metallic structure, but multiple GeTe crystalline structures can be successively written and erased in a GeTe amorphous matrix. Additionally, by getting rid of the lithography fabrication step we considerably reduce the fabrication costs. This method opens a new path for the realization of multifunctional THz devices, one amorphous GeTe film may replace several components of a THz transmission line such as filters and polarizers.

The principle of the laser exposure experiments is shown on Figure III-44. To write a crystalline metallic structure in the amorphous film, we exposed the GeTe film to a KrF UV (248 nm) laser beam through a contact mask placed above the film. The crystalline patterns can then be erased by exposing the whole structure to a high energy laser beam.
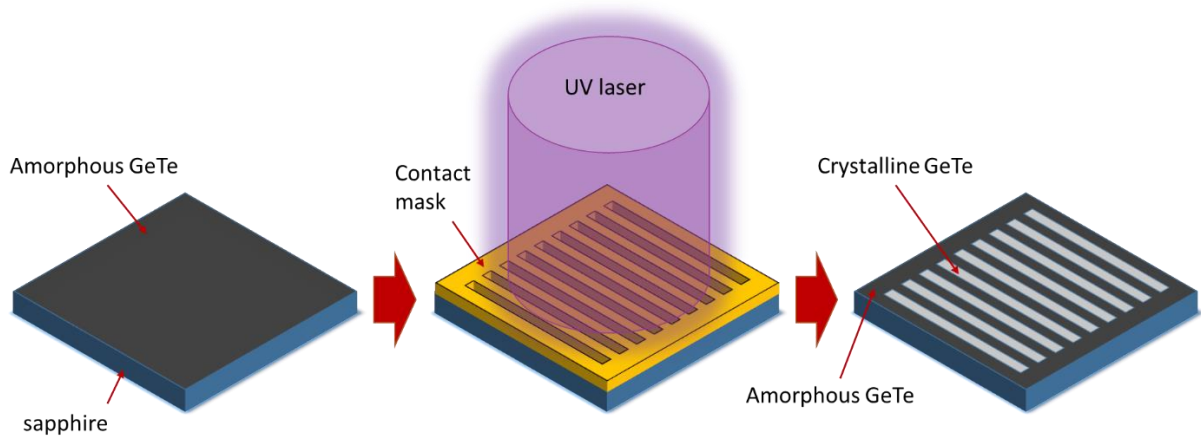
Figure III-44: Principle of 2D laser printing of a metallic structure on an amorphous GeTe film through a contact mask

In order to demonstrate the feasibility of this approach, we realized a 250 nm GeTe film on a c-cut sapphire substrate following the same process as the previously described GeTe film deposition. We realized four gold-based masks on a UV transparent sapphire substrate using electron-beam deposition and a lift-off process.Three masks have the same period P of 10 µm but different wire width w of 3, 8 and 5 µm (denoted as P1'(10/3), P2'(10/8) and P3'(10/5) respectively) and the last mask has a period of 6 µm and a width line of 3 µm (denoted as P4(6/3)). The design of a contact mask corresponds to the complementary polarizer design (Figure III-45).
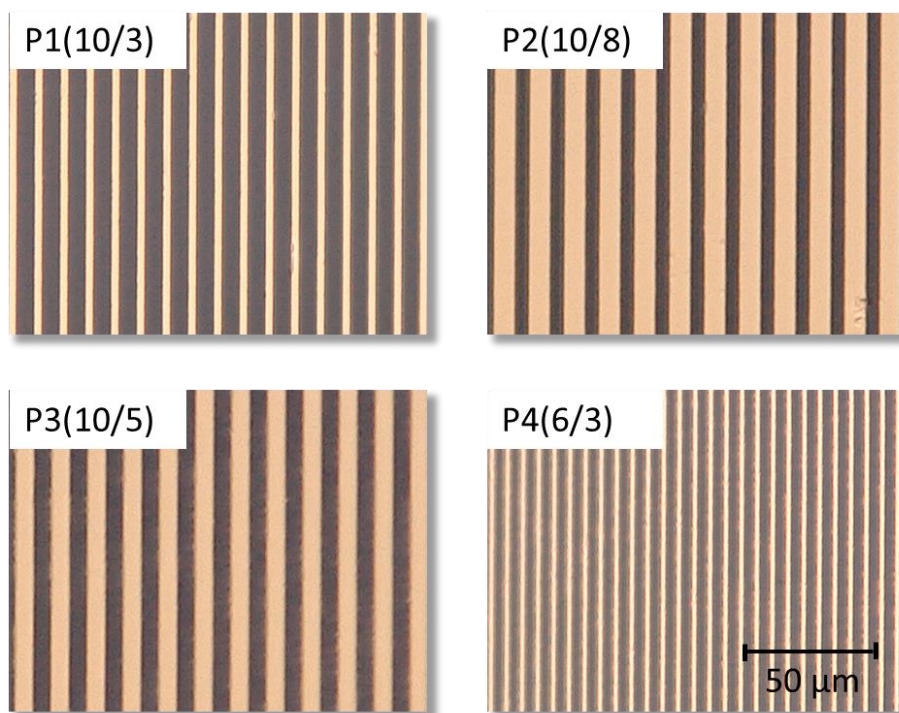
Figure III-45: Optical image of the four contact masks polarizers (P1, P2, P3, P4) with different period P and line width w (P µm /w µm)

By irradiating the amorphous film through the fabricated gold masks we obtained four polarizers composed of an alternation between amorphous GeTe lines and crystalline GeTe lines shown in Figure III-46.
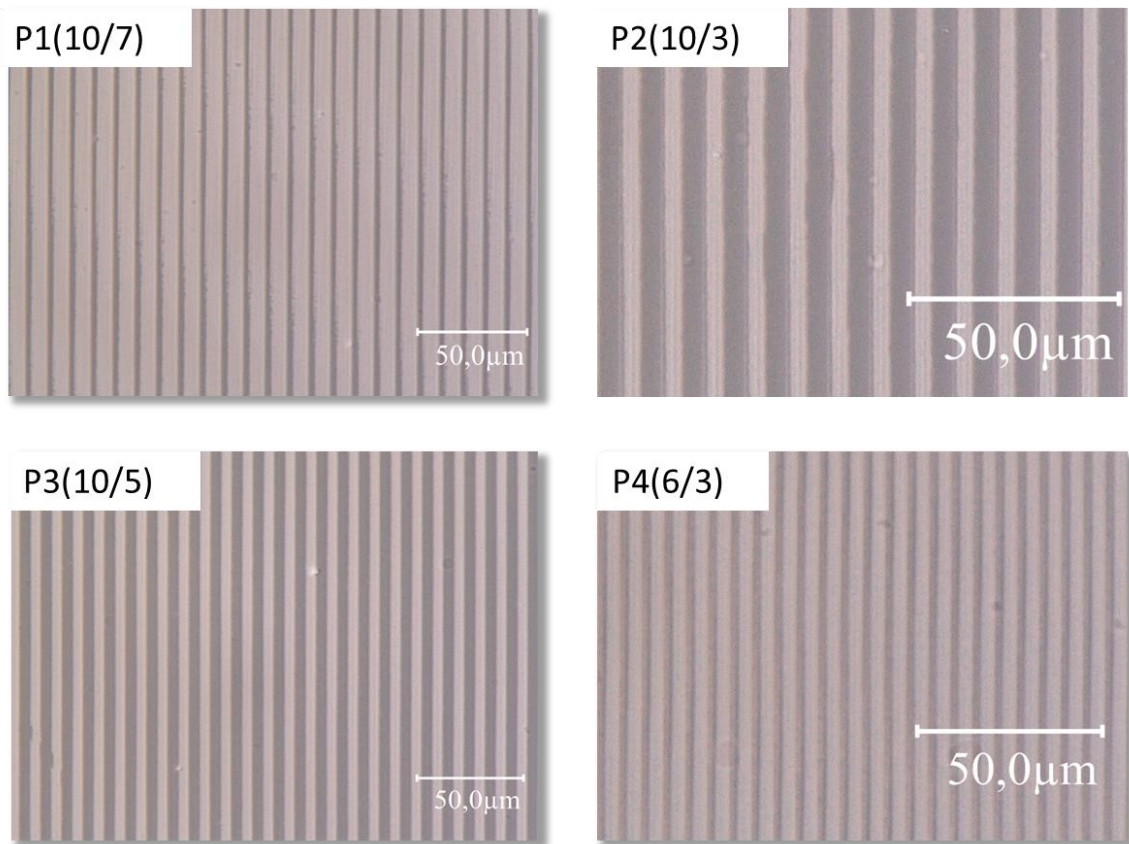
Figure III-46: Optical image of the four laser written polarizers (P1, P2, P3, P4) with different period P and line width w (P μm /w μm)

When we measured the dimensions of each polarizer, the width of the metallic lines is larger than expected. The dimension of each polarizer is summarized in Table III-2. During optical activation, the laser heats the material to a high temperature and as we have noticed inChapter II when performing multiphysics simulations of the interactions between the laser pulse and the GeTe film, a phenomenon of thermal diffusion occurs in the GeTe film. Consequently, the GeTe near the exposed area will be heated and if the temperature is high enough the amorphous GeTe becomes crystalline, leading to larger metallic lines.

Table III-2: Dimension of the realized GeTe polarizer structures

Polarizer name	Period (µm)	Theoretical metallic GeTe line width (µm)	Measured metallic GeTe line width (µm)
P1	10	7	7.5
P2	10	3	3.5
P3	10	5	5.2
P4	6	3	3.4

3.4.2. Characterization of the polarizer devices based on laser inscribed crystalline GeTe structures

We measured the transmission of the four fabricated polarizers using the THz-TDS system. The results are shown in Figure III-47 for each polarizer.
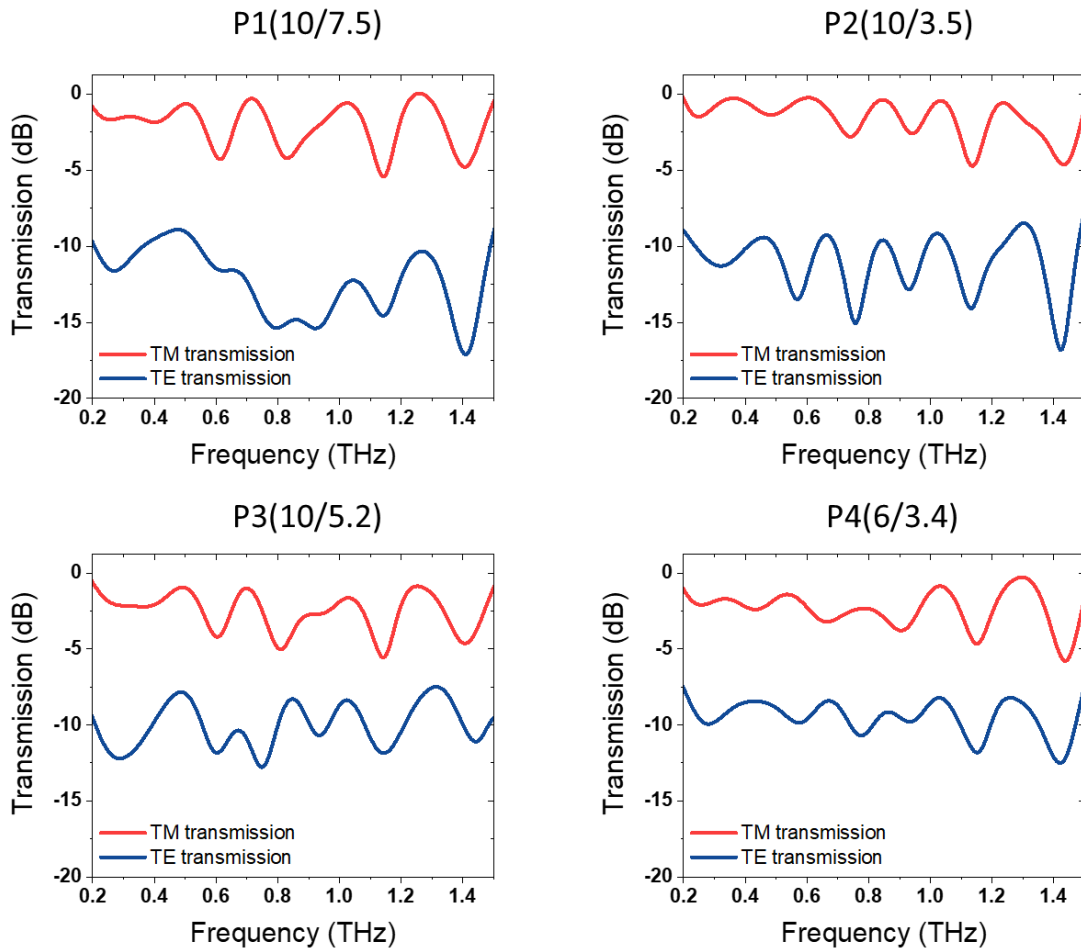
Figure III-47: Measured THz transmission for both TM and TE polarization of the four laser-written polarizers (P1, P2, P3, P4) with different period P and line width w (P µm /w µm)

If we compare with the previous polarizers realized using the lithographic method (Figure III-40), the performances of the polarizers decrease. For example, if we look at the performance of the polarizer P4 Figure III-40 with a period of 6 µm and a line width of 3 µm, the transmission of the TE polarization was strongly absorbed, with a transmission equal to -19 dB at 1 THz. If we write a similar crystalline GeTe structure in a bare amorphous GeTe film (P4-type polarizer), the transmission of the TE polarization decreases to -10 dB and we have a dynamic between TE and TM polarization of only 6.5 dB at 1 THz. Additional we can observe oscillation of the transmission depending on the frequency. This difference can be explained by the difference observed in the dimensions of the lines but also a difference in the conductivity of metallic GeTe because of incomplete crystallization of the film. Indeed, the optimizations of laser exposure in Chapter II were realized with a direct exposure of bare amorphous GeTe film deposited on a sapphire substrate. Here we realized laser activation through a contact mask deposited on a sapphire substrate which changes the activation conditions. Indeed, the sapphire substrate of the contact mask placed beneath the GeTe layer reflect and absorb a part of the incident laser pulse which decreases the power on the film surface. Additional, during previous optimization the film surface was in contact with air. Here,

the film surface is in contact with a mask (composed of a thin gold film grown on a sapphire substrate) which does not have the same thermal dissipation coefficient. Consequently, during laser activation, the heating and cooling time of the GeTe film will be different and it can explain an incomplete crystallization of the GeTe film. The best performances were obtained for the polarizer P1-type structure. For this device, the transmission of the polarizer varies from -0.7 dB to -12.5 dB at 1 THz.

Thus, even if this method is not completely optimized and needs further investigation to control the thermal diffusion and the reversible writing of GeTe crystalline structures, we demonstrate the possibility to inscribe functional THz devices using laser activation of selective areas in bare amorphous GeTe films, without any photolithographic step. This photolithographic free method can considerably decrease the fabrication cost and time of THz devices.

Conclusion

Along this chapter, we have demonstrated the strong potential of GeTe film for the realization of reconfigurable and multifunctional THz devices.

In a first part, we realized hybrid planar THz metamaterials integrating GeTe patterns in its structure, which allows to bring a tunable functionality to the overall metamaterial. The control of the specific structural phase of the GeTe patterns using a laser beam allows the reconfigurability of the metamaterial. By choosing the correct dimension of the structure, it is possible to obtain response modulation over a broadband of frequencies. We demonstrated a metallic symmetric single SRR structure (with a period of 100 µm and line length of 80 µm) integrating a GeTe patch in its 10 µm gap which can achieve modulation of 25 dB around 0.7 THz. The non-volatile switching of this structure is very attractive for the development of low consumption and compact THz devices such as reconfigurable filters for fast high-frequency, beyond 5G, telecommunications.

In a second part, the good contrast of GeTe THz properties between the amorphous and the crystalline state allowed us to design and prove for the first time to the best of our knowledge an all-dielectric THz structure made of GeTe which can actively control the polarization state of the incident THz wave. We realized a wire grid structure which presents a broadband response and a high extinction ratio when in metal-like phase (up to 16.5 dB for a period of 6 µm and line width of 3 µm) and is almost transparent in the amorphous phase, using an optically- induced non-volatile transition. These results open a new way to realize fast (nanosecond timescale), flat reconfigurable THz devices such as polarizers, lenses, waveplates, frequency-selective surfaces, reconfigurable spatial modulators or power limiters.

Finally, we demonstrate a new photolithographic free approach to manipulate the THz waves by using laser writing of metallic GeTe in a bare amorphous GeTe. Photolithography is cost intensive and needs a high level of expertise to handle the instrumentation. With the proposed method we demonstrated the possibility to easily inscribe a metallic structure which can be subsequently erased to inscribe a new metallic structure with a different functionality in the amorphous GeTe film. If at this stage this specific method is not totally optimized, we demonstrate the first step toward the possibility to realize multifunctional THz devices based on solely PCMs for the realization of compact and low consumption THz systems.

The performances of the GeTe-based THz devices demonstrate the high capacity of phase change materials to control the properties of THz waves. The approaches presented in this chapter offer a great reconfiguration flexibility for multifunctional manipulation of THz waves and can be easily adopted for implementing optical reconfiguration techniques capable to activate PCM structures within a particular THz device on large areas or on specific regions

(using raster scanning or optical excitation of precise elements within the device) in order to program precise, on-demand functionalities of THz waves such as arbitrary spatial profile of intensity, phase, and/or polarization distribution. The proposed approaches based on non-volatile optically controlled multi-operational THz devices integrating PCMs open a new path for devices developments in the THz domain like field-programmable metasurfaces, all-dielectric coding metamaterials with multifunctional capabilities for THz field manipulation.

References chapter III

1. Cai, W. and V. Shalaev, *Optical Metamaterials*. 2010, New york: Springer Science+Business Media.
2. Veselago, V.G., *THE ELECTRODYNAMICS OF SUBSTANCES WITH SIMULTANEOUSLY NEGATIVE VALUES OF ϵ AND µ.* Soviet Physics Uspekhi, 1968. **10**(4): p. 509-514.
3. Wong, Z.J., et al., *Optical and acoustic metamaterials: superlens, negative refractive index and invisibility cloak.* Journal of Optics, 2017. **19**(8): p. 084007.
4. Smith, D.R., et al., *Composite Medium with Simultaneously Negative Permeability and Permittivity.* Physical Review Letters, 2000. **84**(18): p. 4184-4187.
5. Holloway, C.L., et al., *A double negative (DNG) composite medium composed of magnetodielectric spherical particles embedded in a matrix.* IEEE Transactions on Antennas and Propagation, 2003. **51**(10): p. 2596-2603.
6. Jylhä, L., et al., *Modeling of isotropic backward-wave materials composed of resonant spheres.* 2006. **99**(4): p. 043102.
7. Grbic, A. and G.V. Eleftheriades, *Overcoming the Diffraction Limit with a Planar Left-Handed Transmission-Line Lens.* Physical Review Letters, 2004. **92**(11): p. 117403.
8. Pendry, J.B., et al., *Extremely low frequency plasmons in metallic mesostructures.* Phys Rev Lett, 1996. **76**(25): p. 4773-4776.
9. Pendry, J.B., et al., *Low frequency plasmons in thin-wire structures.* Journal of Physics: Condensed Matter, 1998. **10**(22): p. 4785-4809.
10. Pendry, J.B., et al., *Magnetism from conductors and enhanced nonlinear phenomena.* IEEE Transactions on Microwave Theory and Techniques, 1999. **47**(11): p. 2075-2084.
11. Shelby, R.A., D.R. Smith, and S. Schultz, *Experimental Verification of a Negative Index of Refraction.* 2001. **292**(5514): p. 77-79.
12. Zaichun, C., *2D and 3D terahertz metamaterials : design, fabrication and characterization*. 2011, National University of Singapore.
13. Padilla, W.J., et al., *Electrically resonant terahertz metamaterials: Theoretical and experimental investigations.* Physical Review B, 2007. **75**(4): p. 041102.
14. Zhou, J., et al., *Saturation of the Magnetic Response of Split-Ring Resonators at Optical Frequencies.* Physical Review Letters, 2005. **95**(22): p. 223902.
15. Gorkunov, M., et al., *Effective magnetic properties of a composite material with circular conductive elements.* The European Physical Journal B - Condensed Matter and Complex Systems, 2002. **28**(3): p. 263-269.
16. Pendry, J.B., *Negative refraction makes a perfect lens.* Phys Rev Lett, 2000. **85**(18): p. 3966-9.
17. Kim, M. and J. Rho, *Metamaterials and imaging.* Nano Converg, 2015. **2**(1): p. 22.
18. Khorasaninejad, M., et al., *Metalenses at visible wavelengths: Diffraction-limited focusing and subwavelength resolution imaging.* 2016. **352**(6290): p. 1190-1194.
19. Schurig, D., et al., *Metamaterial Electromagnetic Cloak at Microwave Frequencies.* 2006. **314**(5801): p. 977-980.
20. Cui, T.J., et al., *Coding metamaterials, digital metamaterials and programmable metamaterials.* Light: Science & Applications, 2014. **3**(10): p. e218-e218.
21. Ulrich, R., *Far-infrared properties of metallic mesh and its complementary structure.* Infrared Physics, 1967. **7**(1): p. 37-55.
22. Tao, H., et al., *A metamaterial absorber for the terahertz regime: design, fabrication and characterization.* Opt Express, 2008. **16**(10): p. 7181-8.
23. Devapriya, A. and S. Robinson, *Investigation on Metamaterial Antenna for Terahertz Applications.* Journal of Microwaves, Optoelectronics and Electromagnetic Applications, 2019. **18**: p. 377-389.

24. Fu, X., et al., *Mode jumping of split-ring resonator metamaterials controlled by high-permittivity BST and incident electric fields.* Scientific Reports, 2016. **6**(1): p. 31274.

25. Okamoto, T., et al., *Dependence of LC resonance wavelength on size of silver split-ring resonator fabricated by nanosphere lithography.* Optics Express, 2012. **20**(21): p. 24059-24067.

26. Kodama, C.H. and R.A. Coutu, *Tunable split-ring resonators using germanium telluride.* Applied Physics Letters, 2016. **108**(23): p. 231901.

27. Zhengli, H., et al., *Tunable Terahertz Filter and Modulator Based on Electrostatic MEMS Reconfigurable SRR Array.* IEEE Journal of Selected Topics in Quantum Electronics, 2015. **21**(4): p. 114-122.

28. Yamada, I., et al., *Terahertz wire-grid polarizers with micrometer-pitch Al gratings.* Optics Letters, 2009. **34**(3): p. 274-276.

29. Yamada, I., et al., *Terahertz wire-grid polarizers with micrometer-pitch Al gratings.* Opt Lett, 2009. **34**(3): p. 274-6.

30. Akyildiz, I.F., J.M. Jornet, and C. Han, *TeraNets: ultra-broadband communication networks in the terahertz band.* IEEE Wireless Communications, 2014. **21**(4): p. 130-135.

31. Elayan, H., et al. *Terahertz communication: The opportunities of wireless technology beyond 5G*. in *2018 International Conference on Advanced Communication Technologies and Networking (CommNet)*. 2018.

Conclusion and perspectives

Conclusion and perspectives

The main objective of the research realized during this thesis was to investigate the terahertz capabilities of phase change materials under optical activation for the realization of reconfigurable THz devices.

In the **first chapter**, we have presented the high potential of terahertz waves for telecommunications, security and medical imaging applications. We emphasized for these applications the need for reconfigurable terahertz devices such as filters, spatial light modulators, frequency selective surfaces, which allow controlling the properties of electromagnetic waves such as their amplitude, phase, polarization and/ or spatiotemporal distribution of their wave fronts. We have identified different methods to realize reconfigurable devices which may allow the optimization of terahertz systems by reducing the size, the energy consumption and the costs integration in smart systems to further development of Beyond 5G or imaging technologies.

In a second time, we have focused our work on phase change materials (PCM) which present a reversible, non-volatile phase transition on nanosecond timescales from an amorphous (insulating) state to a crystalline (metallic) state, triggered by different external stimuli (thermal, electrical, optical). We noted that the simplicity of fabrication and their bistability make PCMs very promising materials for the realization of low consumption devices. Among the different PCMs compositions, GeTe is a very promising candidate for the realization of reconfigurable terahertz devices compared to other PCM compounds. GeTe has a more stable insulating phase and one of the best electrical conductivity in crystalline (metallic) phase, with a difference of 5 to 7 orders of magnitude of resistivity change between the amorphous and crystalline phases. Additionally, the optical-induced switching of GeTe between its two states is abrupt and fast, at the nanosecond timescale.

In the terahertz domain, the potential of PCMs as agile elements for controlling the propagation of THz waves has been shown but the evidence of functional devices capable with full reconfiguration capabilities is still lacking.

The **second chapter** presented the realization and the characterization of GeTe thin films in the perspective to realize reconfigurable devices. We show that GeTe films realized using the DC magnetron sputtering technique present a variation of resistivity of more than 6 orders of magnitude (from 2573 Ω.cm to 3.43 x 10^{-4} Ω.cm for 250 nm thick films), with non-volatile characteristics. Using the THz-TDS system, we evaluated the broadband variation of GeTe THz properties and confirmed our choice to use GeTe for the realization of reconfigurable THz devices. Thus, the THz normalized THz transmission of a GeTe film can

decrease by 97 % between the amorphous and the crystalline states. In order to initiate the phase change of GeTe films, we use UV laser pulses (248 nm) with pulse duration of 35 ns and different laser energies. Optical activation allows a fast, reversible phase change process and simplifies the fabrication process of the potential devices, by avoiding the integration in the device's design of polarization lines (when using the electrical activation) which may alter its overall responses. We have demonstrated for the first time to the best of our knowledge in the THz domain, the possibility to successively switch GeTe films grown on a sapphire substrate between their amorphous and crystalline phases on large areas.

In **chapter III**, we used the optical switching properties of GeTe to realize reconfigurable terahertz devices. We presented a hybrid planar THz metamaterials integrating GeTe patterns in its structure, which allows bringing a tunable functionality to the overall metamaterial. We demonstrated the possibility to actively control the resonances of a split-ring resonator (SRR) THz metamaterial, in bistable way, over a large range of frequency by changing the states of the integrated GeTe patterns. We modulations of the THz transmission as high as 25 dB around 0.7 THz.

Considering the good conductivity contrast between the amorphous and crystalline states of GeTe, we demonstrate for the first time, to the best of our knowledge, an all-dielectric reconfigurable THz device based solely on GeTe that can achieve strong modification of the polarization of incident THz waves. We realized a wire grid structure which presents a broadband response and a high extinction ratio when in the GeTe is in the metal-like phase (up to 16.5 dB)) and which is almost transparent in the amorphous phase. The proposed approach opens a new way for the realization of non-volatile, flat reconfigurable THz devices such as polarizers, lenses, waveplates, frequency-selective surfaces, reconfigurable spatial modulators or power limiters for compact and low consumption THz systems.

Finally, we proposed a new photolithographic-free approach to manipulate the THz waves by using laser writing of metallic GeTe patterns in a bare amorphous GeTe layer. The proposed method using a contact mask, demonstrated the possibility to easily inscribe a GeTe metallic structure which can be subsequently erased to inscribe a new metallic structure with a different functionality in the amorphous GeTe film. If at this stage this specific method is not totally optimized and needs further development, we demonstrate the first step toward the possibility to realize multifunctional THz devices based on solely PCMs for the realization of compact and low consumption THz systems.

To consolidate the reliability of PCM films and improve reconfigurability performances of THz devices presented in chapter III, we propose several perspectives to these researches.

Future integration of PCMs in terahertz systems requires improving the reliability and performances of the devices during optical activation. As a first step, the integration of a heat-sink dielectric thin film between the substrate and the PCM layer will allow a better control of the heating and thermal quenching mechanisms for the amorphization process of PCMs. In a second step, after a large number of optical irradiation cycles we can expect the apparition of chemical degradation of the active film. For future realization of robust devices supporting reversible switching over many cycles, the addition of a thin passivation layer on the PCM surface to avoid interactions between the film and the atmosphere during the phase change will be required. The doping of the PCM film without degrading its properties can also reduce the microscopic structural degradation of the film due to the successive optical cycles and further increase the lifetime of PCM based devices.

Regarding the optical laser system, the use of contact masks to inscribe metallic structures in a bare amorphous GeTe can be difficult to integrate in a terahertz system. A solution, which is currently under investigation at XLIM, consists to use a laser-based raster scanning system that allows real time writing, erasing and rewriting of specific patterns on the bare amorphous GeTe film or hybrid PCMs/metal surfaces (Figure 48). This system used a pair of deformable mirrors to scan and focus a 532-nm laser beam on the PCM film surface. The power and the shape of the laser beam can be adapted to match the specific energies required for the state changes in the PCM layer.
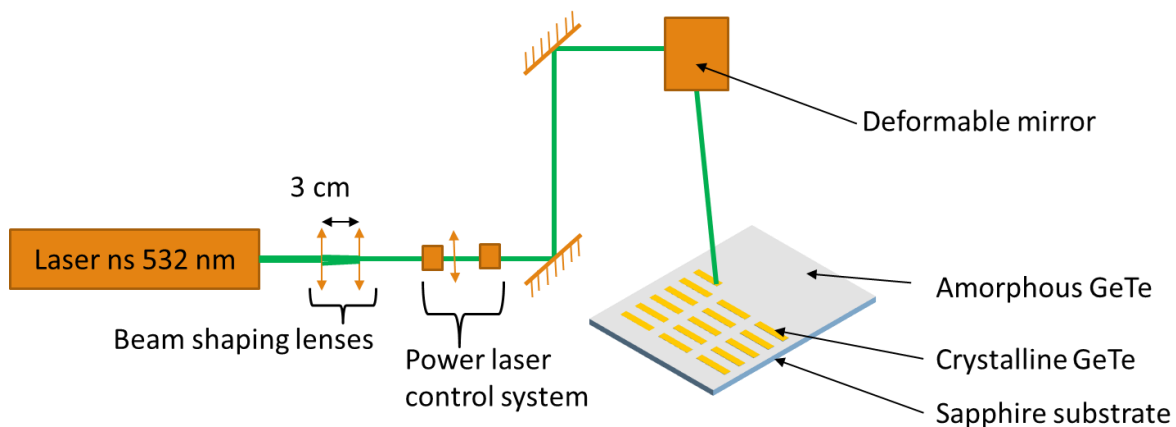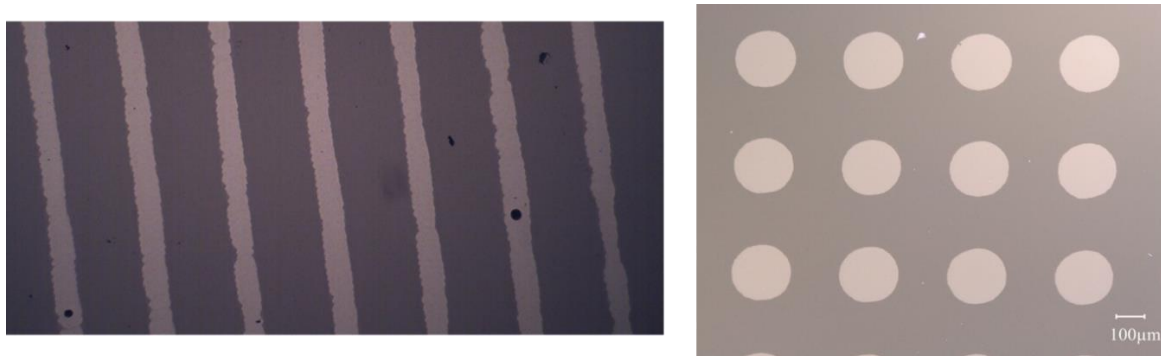

Figure 48 : Schematic of the proposed laser raster scanning system implemented at XLIM for the implementation of THz multifunctional devices.

The first tests on this laser activation scheme, realized on amorphous GeTe layers are very promising for the development of future multifunctional and rewritable devices (Figure 49).

Figure 49 : Optical images of metallic GeTe structures inscribe in a bare amorphous GeTe film using the laser raster scanning system.

By using the laser raster scanning system, the smallest size of the inscribe metallic line is only limited by the wavelength (Rayleigh criterion) and, due to the small size of the laser beam area (at the μm scale), the require power to achieve complete phase change of the PCM film is relatively low (around 10 mW). As a next step, for increasing the degree of integration, one can imagine using small laser diodes close to the PCM film, in the same manner employed for the optical inscription of CD-RW or conveying the laser beam using optical waveguides embedded with the PCM-based device.

The next phase will be the design and implementation of more complex demonstrators such as modulators or reconfigurable filters made solely of PCM whose global properties can be tuned (operating frequency, polarization) using the previously developed laser irradiation system. This approach will allow to propose in the future a new method to realize low consumption, reliable devices for a plethora of THz applications (imaging, testing, sensing or telecommunications).

Published work and conferences

Papers:

- M. Pinaud, G. Humbert, S. Engelbrecht, L. Merlat, B. M. Fischer, A. Crunteanu, "Terahertz Devices Using the Optical Activation of GeTe Phase Change Materials: Toward Fully Reconfigurable Functionalities." *ACS Photonics 2021*

Conferences:

- M. Pinaud, G. Humbert, B. M. Fischer, S.Engelbrecht, A. Crunteanu. "Reconfigurable Terahertz Functions using Phase Change Materials", *Journées du GDR, May 29-31st, 2018*, Montpellier, France. (Oral)

- M. Pinaud, G. Humbert, A. Crunteanu, S. Engelbrecht, L. Merlat, B. M. Fischer. "Optical activation of Phase Change Materials (PCM) for reconfigurable Terahertz devices". *Meeting of young scientist,* 31 march - 01 april 2019, Frankfurt, Germany. (Poster*)*

- M. Pinaud, G. Humbert, A. Crunteanu, S. Engelbrecht, L. Merlat, B. M. Fischer. "Phase Change Materials for reconfigurable Terahertz devices". *French-German THz Conference,* 02-05 April 2019*,* Kaiserslautern, Germany. (Oral)

- M. Pinaud, G. Humbert, S. Engelbrecht, L. Merlat, A.Crunteanu, B. M. Fischer. "Optical Reconfigurable Terahertz Devices using Phase Change Materials" *44th International Conference on Infrared, Millimeter and Terahertz Waves, IRMMW-THz,* 1-6 September 2019 - Paris, France. (Oral)

Matériaux à changement de phase (PCM) pour la réalisation de dispositifs térahertz reconfigurables

Les dispositifs multifonctionnels sont essentiels pour le développement de nouveaux appareils connectés intégrant de nouvelles applications dans tous les aspects de la vie quotidienne (réalité augmentée, réalité virtuelle, voitures à conduite autonome, villes intelligentes, etc.). Cependant, leur développement nécessite encore des fonctions agiles efficaces opérant dans le domaine térahertz. Les matériaux à changement de phase à base de chalcogénure avec des réponses large bande, des transitions non volatiles et réversibles entre les phases isolantes (amorphes) et conductrices (cristallines) ont été étudiés avec succès comme éléments agiles dans des applications photoniques ou électroniques.

Dans ce manuscrit, nous proposons d'utiliser le tellurure de germanium (GeTe) comme élément agile pour la réalisation de dispositifs térahertz optiquement reconfigurables. Pour cela, nous avons démontré le contrôle optique d'états spécifiques du GeTe et caractérisé ses propriétés térahertz. L'excellent contraste des propriétés térahertz du matériau dans les deux états a été utilisé pour réaliser un métamatériau hybride basé sur des structures métalliques de type « split ring resonator » (SRR) intégrant des motifs de GeTe pouvant réaliser une modulation induite optiquement des ondes térahertz incidentes. Nous démontrons également la faisabilité de dispositifs térahertz entièrement diélectriques à base de GeTe présentant une réponse à large bande et des modulations élevées de la réponse térahertz. Ainsi, cette approche hautement fonctionnelle basée sur des dispositifs térahertz multi-opérationnels non-volatils contrôlés optiquement et intégrant des PCMs ouvre une nouvelle voie pour le développement de dispositifs dans le domaine térahertz comme les métasurfaces programmables ou les métamatériaux de codage entièrement diélectrique avec des capacités multifonctionnelles pour la manipulation du champ térahertz.

Phase change materials (PCM) for reconfiguration of terahertz devices

Multifunctional devices are crucial for the development of new connected devices integrating new applications in all aspects of daily life (augmented reality, virtual reality, self-driving cars, smart cities, etc). However, their expansion is still requiring efficient agility functions operating in the terahertz domain. Chalcogenide phase change materials with broadband responses, non-volatile and reversible transitions between insulating (amorphous) and conducting (crystalline) phases were successfully investigated as agile elements in photonics or electronics applications.

In this manuscript, we proposed to use germanium telluride (GeTe) PCM as an agile element for the realization of optically reconfigurable terahertz devices. For that, we demonstrated optical control of specific states of the GeTe and characterized its terahertz properties. The excellent contrast of the material's terahertz properties in the two dissimilar states was used to realize hybrid metamaterial based on split-ring-resonator metallic structures integrating GeTe patterns which can achieve optical-induced modulation of incident terahertz waves. We also demonstrated the feasibility of all dielectric GeTe-based terahertz devices presenting broadband response and high modulations of the terahertz response. Thus, this highly functional approach based on non-volatile optically controlled multi-operational terahertz devices integrating PCMs opens a new path for devices developments in the terahertz domain like field-programmable metasurfaces, all-dielectric coding metamaterials with multifunctional capabilities for terahertz field manipulation.